

Model Driven Design Optimization and Gait Selection  
of Compliant Foldable Robots

by

Mohammad Sharifzadeh

A Dissertation Presented in Partial Fulfillment  
of the Requirements for the Degree  
Doctor of Philosophy

Approved March 2021 by the  
Graduate Supervisory Committee:

Daniel M Aukes, Chair  
Thomas Sugar  
Wenlong Zhang

ARIZONA STATE UNIVERSITY

May 2021

## ABSTRACT

This dissertation studies the methods to enhance the performance of foldable robots manufactured by laminated techniques. This class of robots are unique in their manufacturing process, which involves cutting and staking up thin layers of different materials with various stiffness. While inheriting the advantages of soft robots – low weight, affordable manufacturing cost and a fast prototyping process – a wider range of actuators is available to these mechanisms, while modeling their behavior requires less computational cost. The fundamental question this dissertation strives to answer is how to decode and leverage the effect of material stiffness in these robots. These robots’ stiffness is relatively limited due to their slender design, specifically at larger scales. While compliant robots may have inherent advantages such as being safer to work around, this low rigidity makes modeling more complex. This complexity is mostly contained in material deformation since the conventional actuators such as servo motors can be easily leveraged in these robots. As a result, when introduced to real-world environments, efficient modeling and control of these robots are more achievable than conventional soft robots. Various approaches have been taken to design, model, and control a variety of laminate robot platforms by investigating the effect of material deformation in prototypes while they interact with their working environments. The results obtained show that data-driven approaches such as experimental identification and machine learning techniques are more reliable in modeling and control of these mechanisms. Also, machine learning techniques for training robots in non-ideal experimental setups that encounter the uncertainties of real-world environments can be leveraged to find effective gaits with high performance. Our studies on the effect of stiffness of thin, curved sheets of materials has evolved into introducing a new class of soft elements which we call Soft, Curved, Reconfigurable, Anisotropic Mechanisms (SCRAMs). Like bio-mechanical systems,

SCRAMs are capable of re-configuring the stiffness of curved surfaces to enhance their performance and adaptability. Finally, the findings of this thesis show promising opportunities for foldable robots to become an alternative for conventional soft robots since they still offer similar advantages in a fraction of computational expense.

## DEDICATION

*I dedicate this to my mother and father, who have always made any possible scarifies  
for the sake of their children.*

## ACKNOWLEDGMENTS

*I feel blessed to be able to follow my path toward Ph.D.; I received a great deal of support and assistance in the way. I would like to first thank my God who has blessed me with the power to overcome challenges I faced during my academic journey.*

*I would first like to thank my supervisor, Professor Daniel M. Aukes, whose expertise was invaluable. He convincingly guided me to be professional and do the right thing even when the road got tough. Without his persistent support, the achievements of this dissertation would not have been realized.*

*I would like to express my appreciation to my committee members, Prof. Thomas Sugar, and Prof. Wenlong Zhang for their valuable guidance and comments.*

*I would like to acknowledge my colleagues, specifically, I would like to recognize the assistance that I received from Yuhao Jiang, Azadeh Doroudchi, Roozbeh Khodambashi, Amir Salimi Lafmejani, and Dongting Li.*

*In addition, I would like to thank my parents and my family for all their sacrifices. You have been always there for me. Finally, I could not have completed this journey without the support of my loving wife, Azadeh.*

## TABLE OF CONTENTS

	Page
LIST OF TABLES .....	x
LIST OF FIGURES .....	xi
CHAPTER	
1 INTRODUCTION .....	1
1.1 Problem Definition .....	2
1.2 Background .....	6
1.2.1 Foldable robots .....	6
1.2.2 Modeling and Control of Soft Robots .....	9
1.2.3 Directional & Variable Stiffness .....	12
1.3 Methodology & Contributions .....	16
2 INCREASING THE LIFE SPAN OF FOLDABLE MANIPULATORS ...	23
2.1 Introduction .....	23
2.2 Laminated Techniques and Their Challenges .....	26
2.3 Laminated Mechanism Stiffness & Durability .....	28
2.3.1 Hinge Durability .....	28
2.3.2 Delamination .....	29
2.3.3 Stiffness compensation .....	30
2.4 Case Study of 2-DOF Spherical PM .....	31
2.4.1 Kinematic Synthesis .....	31
2.4.2 Design .....	33
2.4.3 Manufacturing .....	35
2.4.4 Manipulation .....	36
2.5 Discussion .....	38

CHAPTER	Page
3 DYNAMIC MODELING VIA CHARACTERIZATION OF FOLDABLE HINGE .....	40
3.1 Introduction.....	40
3.2 Model Generation .....	43
3.2.1 Importing from PopupCAD .....	45
3.2.2 Obtaining the Dynamic Model .....	45
3.2.3 Adding kinematic constraints and initial conditions .....	46
3.2.4 Integration and solving .....	47
3.3 Hinge Characterization.....	48
3.3.1 Experimental setup .....	49
3.3.2 Material Test .....	50
3.3.3 Repeatability Test .....	51
3.3.4 Modeling Single Pendulum System .....	52
3.3.5 Identification of Damping Coefficient & Stiffness .....	53
3.4 Model Verification .....	57
3.5 Results & Discussion .....	59
4 COMPENSATION OF MATERIAL DEFORMATION USING ADAPTIVE CONTROLLER .....	63
4.1 Introduction.....	64
4.2 Workflow.....	68
4.3 DNN hyper-parameters .....	71
4.4 2DOF Spherical Parallel Mechanism .....	72
4.4.1 Inverse Kinematics .....	73
4.4.2 Forward Kinematics & Workspace .....	74

CHAPTER	Page
4.5	Tuning DNN hyper-parameters ..... 74
4.6	Control ..... 76
4.6.1	Pre-trained Model ..... 76
4.6.2	Control via Transfer Learning ..... 77
4.7	Model-free Controller ..... 80
4.8	Discussion ..... 82
5	IDENTIFICATION & CONTROL IN THE PRESENCE OF UNCER- TAINTIES ..... 86
5.1	Introduction ..... 86
5.2	Maneuvering Strategies & Experimental Setup ..... 89
5.3	Design & Prototyping ..... 92
5.4	Identification & Model Extraction ..... 93
5.5	Controller Design ..... 99
5.6	Conclusion & Future work ..... 103
6	TRAINING FIRE IN THE PRESENCE OF UNCERTAINTIES ..... 105
6.1	Introduction ..... 106
6.2	Fish-inspired Robot for Extreme Environments ..... 110
6.2.1	Design and Manufacturing of Robotic Fish ..... 111
6.2.2	Pectoral Fin: 2-DOF Mechanism ..... 112
6.3	Training the Robotic Fish ..... 113
6.3.1	Training Workflow ..... 113
6.3.2	Experimental Setup ..... 116
6.3.3	Convergence Adaption Matrix Evolution Strategy ..... 116
6.3.4	Selection of Pectoral Fin Attachment ..... 118



CHAPTER	Page
6.4 Results .....	119
6.4.1 Turning .....	119
6.4.2 Swimming Forward .....	122
6.5 Discussion .....	127
7 LEVERAGING VARIABLE STIFFNESS OF CURVATURE-INDUCED BEAMS IN DEVELOPING SOFT ROBOTS .....	131
7.1 Introduction .....	131
7.1.1 Role of Curved Beam Buckling in Locomotion .....	139
7.2 Analysis of Curved Beam in Anisotropic Buckling Wings .....	141
7.2.1 Theoretical Model for Curved Beam Buckling .....	144
7.2.2 FEA Study on Curved Beam Buckling .....	148
7.3 Dynamic Modeling of Buckling Wing Propulsion .....	151
7.4 Experimental Validation .....	154
7.4.1 Case Study I: Wing Flapping in Air .....	154
7.4.2 Case study II: Flapping in Water .....	158
7.5 Tuning Curved Beam Stiffness .....	161
7.5.1 Design & Fabrication .....	162
7.6 Dynamic Modeling .....	166
7.7 Design Optimization .....	168
7.8 Experimental Gait Optimization .....	172
7.9 Discussion .....	175
8 Conclusion .....	178
8.1 Impact & Future Work .....	180
8.2 Publications .....	183

CHAPTER	Page
8.2.1 Journal Papers .....	183
8.2.2 Conference Papers .....	184
8.2.3 Talks .....	185
REFERENCES .....	186
APPENDIX	
A CURRICULUM VITAE .....	204

## LIST OF TABLES

Table	Page
3.1 Hinge Characterization Parameters Used in This Study .....	50
3.2 The Repeatability Test Results in Hinge Characteristics .....	54
3.3 Comparison Between Equilibrium Potions in Simulation and Experiments	60
5.1 List of Propulsion Parameters.....	89
5.2 Different Design & Material Effect .....	94
5.3 Choosing $X$ Basket .....	98
5.4 PID Parameters Values for Different Controllers Reported in the Study	102
6.1 The Tuned Parameters for the CMA-ES Algorithm .....	117
7.1 Torque and Work Generated During Flapping in Air .....	158
7.2 Generated Torques in Simulation and Experimental .....	159
7.3 Parameter Range in Design and Input Optimization .....	170

## LIST OF FIGURES

Figure	Page
1.1 Laminated Techniques Procedure .....	2
1.2 Challenges Associated with Foldable Robots .....	3
1.3 State of the Art Foldable Robots. ....	8
1.4 State of the Art Approaches in Modeling Soft Robots.....	10
1.5 State of the Art Directional and Variable Stiffness Robots. ....	14
1.6 Summary of the Paper’s Chapters. ....	15
2.1 Increasing Laminated Hinge Life Span .....	25
2.2 FEA Study on Simple and Castellated Hinges .....	29
2.3 Kinematic Synthesis of the 2-DOF Spherical PM .....	31
2.4 Design Process Using PopupCAD .....	34
2.5 Prototyping the 2-DOF Spherical Parallel Mechanism .....	35
2.6 Different Applications Derived from the Proposed Mechanism. ....	36
2.7 Camera Stabilization Using the Manufactured 2DOF Spherical PM ....	37
3.1 The Case Study of 6-bar Laminated Mechanism .....	42
3.2 Steps for Mathematically Defining Closed-loop Constraints. ....	44
3.3 The Proposed Model of The Hinge .....	49
3.4 Flex Layer Material Tensile Test .....	52
3.5 The Repeatability Test in Behavior of a Simple Hinge .....	53
3.6 The Effect of Different Cross-sectional Area on Damping Coefficient ...	54
3.7 Effect of Hinge Width on Damping Coefficient and Stiffness of the Hinge	55
3.8 Effect of Hinge Length on Damping Coefficient and Stiffness of the Hinge	56
3.9 Comparison of the Experimental and Modeled Hinge characteristics ...	57
3.10 Pynamics Output Verification Based on 6-bar Mechanism .....	59
4.1 Poor Efficacy of a Laminated 2-DOF Parallel Mechanism Under Load .	64

Figure	Page
4.2	Diagram of the Proposed Workflow . . . . . 69
4.3	The Case Study of 2-DOF Spherical Mechanism . . . . . 71
4.4	Closed-loop Control System Configurations . . . . . 75
4.5	DNN Training By Tracking Errors . . . . . 77
4.6	DNN Training by Inverse Kinematics . . . . . 80
4.7	Discussion . . . . . 82
5.1	Maneuvering Strategy of Tail Movement on Generated Force . . . . . 88
5.2	Test Setup for Identification & Control . . . . . 90
5.3	Forward and Lateral Force Generated by Symmetric Propulsion . . . . . 91
5.4	Prototypes Made to Evaluate Generating Force and Swim Ability . . . . . 93
5.5	Force Generated by Different Fin Propulsion . . . . . 95
5.6	Force Generated by Symmetric Sinusoidal Amplitude Fin Propulsion . . 96
5.7	Force Generated by Sinusoidal Offset and Amplitude Fin Propulsion . . . 97
5.8	Step Response Identification on Generated Thrust . . . . . 99
5.9	Block Diagram of Different Controllers . . . . . 100
5.10	PID Controller Performance . . . . . 101
5.11	Feedforward-feedback Controller Performance . . . . . 102
6.1	FIRE, the Souckermouth Catfish-inspired Robot . . . . . 111
6.2	FIRE's Training Workflow . . . . . 114
6.3	Pectoral Fins' Attachment Selection . . . . . 118
6.4	FIRE's Turn Training . . . . . 121
6.5	FIRE's Large Turning Radius Training . . . . . 123
6.6	FIRE's Swimming Forward Training . . . . . 124
6.7	Forward Thrust Generation by Pectoral Fins . . . . . 127

Figure	Page
7.1 Conceptual Illustration of The Proposed Technique. ....	133
7.2 Comparison Between Different Methods to Achieve Net Thrust in Rowing	136
7.3 The Peg Toy Robot .....	140
7.4 Locomotion of the Robot for Different Stiffness of the Curved Beams ..	141
7.5 The Side View of Our Flapping Wing Designs.....	142
7.6 The Nonlinear Behavior of a Curved Beam .....	143
7.7 Finite Element Analysis on the Curved Slender Beam .....	146
7.8 Dynamic modeling of a wing flapping in water .....	149
7.9 Experimental Setup for Measuring Air Drag Applied to the Wing.....	152
7.10 The Effect of Asymmetric Buckling on a Wing Flapping in Air .....	155
7.11 The Effect of Asymmetric Buckling on a Wing Flapping in Water .....	160
7.12 Utilizing Curved Beams in Rowing and Flapping Swimming Strategies ..	163
7.13 Behavior of Curved Beams with a Short and Long Effective Length....	165
7.14 Dynamic Modeling of the Robot Rowing in Water .....	168
7.15 Design Optimization Using the Dynamic Model .....	171
7.16 Results of the Experimental Gait Optimization.....	173
7.17 Untethered Robot Swimming .....	174

## Chapter 1

### INTRODUCTION

Soft robots have emerged as an alternative to rigid-bodied robots by leveraging soft material properties to gain unique characteristics and accomplish tasks difficult for rigid robots to perform. Some noticeable characteristics include lower weight, lower manufacturing cost, and higher safety in interaction with human and delicate objects. Their ability to change shape helps these robots perform tasks like assisting in surgery or being worn on the human body as assistive devices.

Origami-inspired robots are a class of soft robots distinguished by their foldable features and specific manufacturing techniques. These robots are affordable, light weight, as well as easy and fast to manufacture. One of the most popular methods of manufacturing these robots is through laminate techniques. This process involves cutting individual layers of material, stacking, aligning and fusing individual layers together into a composite, and then releasing the resulting hinged laminate with a secondary cut (Fig. 1.1).

This thesis focuses on preparing foldable robots as platforms for performing tasks in real-world environments. Alongside a discussion of the development of a number of robots, the majority of this dissertation studies the effect of material deformation and stiffness on the performance of these robots when they are subjected to the interaction forces caused by their working environments. The goal of this thesis is to show the potential for foldable robots as a promising alternative to soft robots that are built from cast polymers as well as traditional rigid systems.

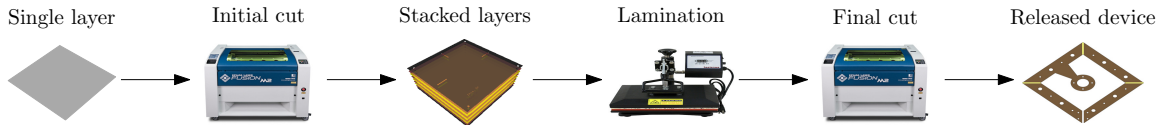


Figure 1.1: Procedure of making a laminated device using heat press and laser cutter as machinery.

## 1.1 Problem Definition

There have been significant advances in the field of soft robotics. There is, however, still a long road ahead for the field of soft robots before they get to the point where their true potential can be realized in order to effectively replace conventional rigid robots. Many unanswered challenges limit soft robots' performance. Three major challenges can be associated with their customary method of actuation, their modeling complexity, and their relatively high compliance. Pneumatic actuation, the most common actuation method for the conventional soft robots, often requires bulky and heavy pneumatic hardware, limiting their capability to move towards untethered mobile systems. Second, the nature of soft robots is also so complex that their modeling, shape, material properties, and design become highly interrelated. This makes closing the design loop for these robots challenging. Finally, the fully soft nature of these robots provides safer mechanisms for interaction with humans and other delicate objects; this, however, limits the maximum forces these systems can exert on external objects.

Foldable robots made with laminate techniques are able to address some of these challenges. These robots can leverage more conventional actuators such as servos; through careful material selection and scaling, they are rigid enough to be modeled with rigid-bodied kinematics and dynamics; finally, their stiffness is easily tuned by material selection.



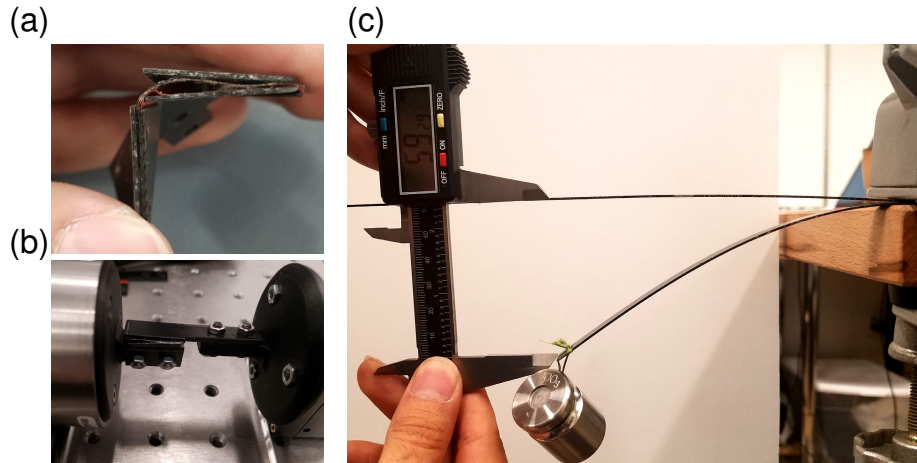


Figure 1.2: Challenges associated with Foldable robots. (a) Delamination. (b) Hinge ripping. (c) Fiberglass beam deformation under load. The beam is 10 mm wide, 140 mm length and 0.762 mm thick.

While there are many benefits to foldable robots, there are some challenges that need to be addressed to improve the functionality of these robots in real-world applications as well:

1. **Stiffness:** Similar to other soft robots, foldable robots tend to deform under load, which can affect their functionality through their interactions with the world. The deformation of these robots can be seen both in their hinges and links. Since flexural hinges are often made from soft materials, they usually permit rotation in unintended directions, e.g. twisting. As explained in chapter 2, in [1], a supported hinge design can be used to reduce the hinge's twist. However, these hinges have a negative impact the life span of hinges when repeatedly deformed over large angles. Through this study, I have used the simple rectangular hinge design and used thicker polyester sheets to reduce unintended rotation. Using fiberglass or carbon fiber as the rigid layers can increase the stiffness and reduce deformation. However, under high loads, thin sheets of any

of the aforementioned materials are likely to experience unintended deformations (Fig. 1.2c).

2. **Modeling complexity:** To avoid deforming the robot's links from the weight of actuators, roboticists tend to use parallel mechanisms in the design of laminated robots. Parallel mechanisms take advantage of multiple pathways to the ground, often making them more rigid and precise than their serial counterparts. Moreover, parallel robots are usually capable of achieving higher speeds because actuators can be proximally mounted on the a slower base chassis, reducing loads on high-speed distal joints and links. However, in the dynamics and kinematics modeling of these robots, parallel mechanisms are more complex to model than robots.
  
3. **Durability:** Using affordable sheets of material can reduce the lifetime of robotic systems. For example, a robot made from cardboard can be permanently deformed and destroyed in minutes. Notable issues impacting lifetime include: (i) Material yield and permanent deformation. (ii) Layer delamination (Fig. 1.2a). (iii) Torn or ripped hinges (Fig. 1.2b). As explained in chapter 2 these problems issues can be addressed by (i) Using higher-end, more durable material like fiberglass as the rigid layer. (ii) Compressing critical points via screws or rivets. (ii) Using multi-layer hinge designs that resist tearing by combining the material properties of different materials in key layers.

Though the above techniques for addressing some of the core issues related to foldable and laminate robots improves their durability and makes them easier to model, the effect of material deformation is still not negligible and should be considered in the modeling and control of laminated robots, especially when loaded or interacting with the world. This is discussed more in chapters 3 and 4.

The majority of this thesis is dedicated to understanding foldable robots' soft nature and their deformation in order to enhance their performance in real-world environments. The proper understanding of these robots can help us to design, model, and control them by closing the loop between design and system behavior in real-world experiments.

The problem with modeling soft robots has been tackled by many researchers through different approaches. In [2], a recent review of soft robots by a collaboration between Harvard University and Carnegie Mellon University, this issue was addressed as one of the "current challenges" in soft robots by stating:

*"In addition to reshaping mechanical compliance and functionality, the use of soft materials also has profound implications on how robots are modelled and controlled. In contrast with autonomous vehicles, humanoid robots and other piecewise rigid systems that have finite degrees of freedom, soft-matter machines and robots are continuous elastic bodies that exhibit infinite degrees of freedom. This introduces new challenges in sensing and proprioception, feedback and adaptive control, path planning and robot intelligence that go beyond the scope of conventional algorithms for robotic autonomy. In most cases, soft robots will be 'unobservable', with incomplete information about their dynamical state and surface interactions. Instead, sensor data will have to be combined with data-driven learning algorithms and computational modelling based on physics engines and finite-element techniques."*

This thesis focuses on extending the functionality of foldable robots while interacting with their working environment by addressing material deformation using data-driven modeling and control methods.

## 1.2 Background

### 1.2.1 Foldable robots

Origami-inspired robots are affordable and light weight, as well as easy and fast to manufacture. Given a competent design, these robots are ideal platforms for experimentally evaluating different design objectives, modeling techniques, control, training, swarm algorithms, and artificial intelligence.

Many foldable robots are made using laminated techniques to achieve different functionalities and goals. Following are some state of the art robots that leverage the advantages of laminated robots, i.e., scalability, low manufacturing cost, lightness, and agility. MilliDelta is a  $15 \times 15 \times 20$  mm robot that weights 430 milligram and is capable of moving a payload of 1.31 gr [3]. Using its piezoelectric actuators, MilliDelta can follow a periodic trajectory at frequencies up to 75Hz (1.3a). A foldable haptic device called FOLDAWAY-Touch is being commercially developed a foldable, portable computer mouse (1.3b). While there is no paper on its commercial design, the primary generations of its design are presented in [4, 5]. In the newer version, presented in [4], they have used a backdrivable MAXON DC as actuator and hall-effect sensors for feedback. The mechanism is then attached to an HTC Vive VR interface for haptic applications. In [6], an origami-inspired miniature robot is proposed for teleoperated surgery (1.3d). The robot has three independent linear actuators and is controlled using a proportional controller. In this study the authors illustrate how using this mechanism in conjunction with a Phantom Omni haptic device to move an operation tool increases the precision in following a desired 0.4 by 0.4 mm square by 68% compared with manual operation of the operation tool.

The Harvard Ambulatory MicroRobot (HAMR) is a cockroach-based quadrupedal microrobot that has evolved over several design cycles (1.3c). The most recent itera-

tion is able to walk on land, swim on the surface of water, sink, and then transition back to land [7]. On the tips of its legs it uses an ElectroWetting Pad (EWP) to keep itself either on the surface of the water or allow it to sink.

Figure 1.3d shows C-Turtle, a laminated robot inspired by sea turtles [9]. The gait is obtained via machine learning, using a sample-efficient reinforcement learning method in both an artificial indoor environment and a natural environment in the Arizona desert.

RoboBee is a laminated, flying, microscale robot (1.3f). Many generations of this robot have been designed; a recent one (RoboBee X-Wing), presented in [10], is a 0.5 gr untethered vehicle that uses small solar panels as a power supply. This robot uses an alumina bridge piezoelectric actuator per two wings that can flap at 165 Hz.

In [12], buckling is used in an origami-inspired structure to produce dual-stiffness joints by pre-stretching the flexible layer during fabrication to induce buckling in the presence of high forces as a mechanical fuse. This characteristic is used in a quadrotor to increase its rigidity and reduce vibration in its flights as well as helping it survive crashes by activation of its embedded fuse (1.3h). The same concept is also used in a gripper to hold an object without overloading it. An origami-inspired quadrotor made by laminated techniques is presented in [11]. In its foldable design, the Foldable QuadRotor (FQR) uses a fifth actuator to retrieve its arm during flights to be able to operate in cluttered environments (1.3g). In wider spaces, it opens its arms to increase stability in aggressive turning maneuvers.

Tribot is the name of a series of millirobots developed at EPFL that are tuned for a variety of applications and functions (Fig. 1.3i). The most recent version is a multi-locomotion robot inspired by the trap-jaw ant [13]. This robot is capable of jumping to an average height of 140.6 mm – 2.5 times its height. It can distance-jump 230 mm and perform a “flic-flac walking” maneuver. This robot uses two SMA

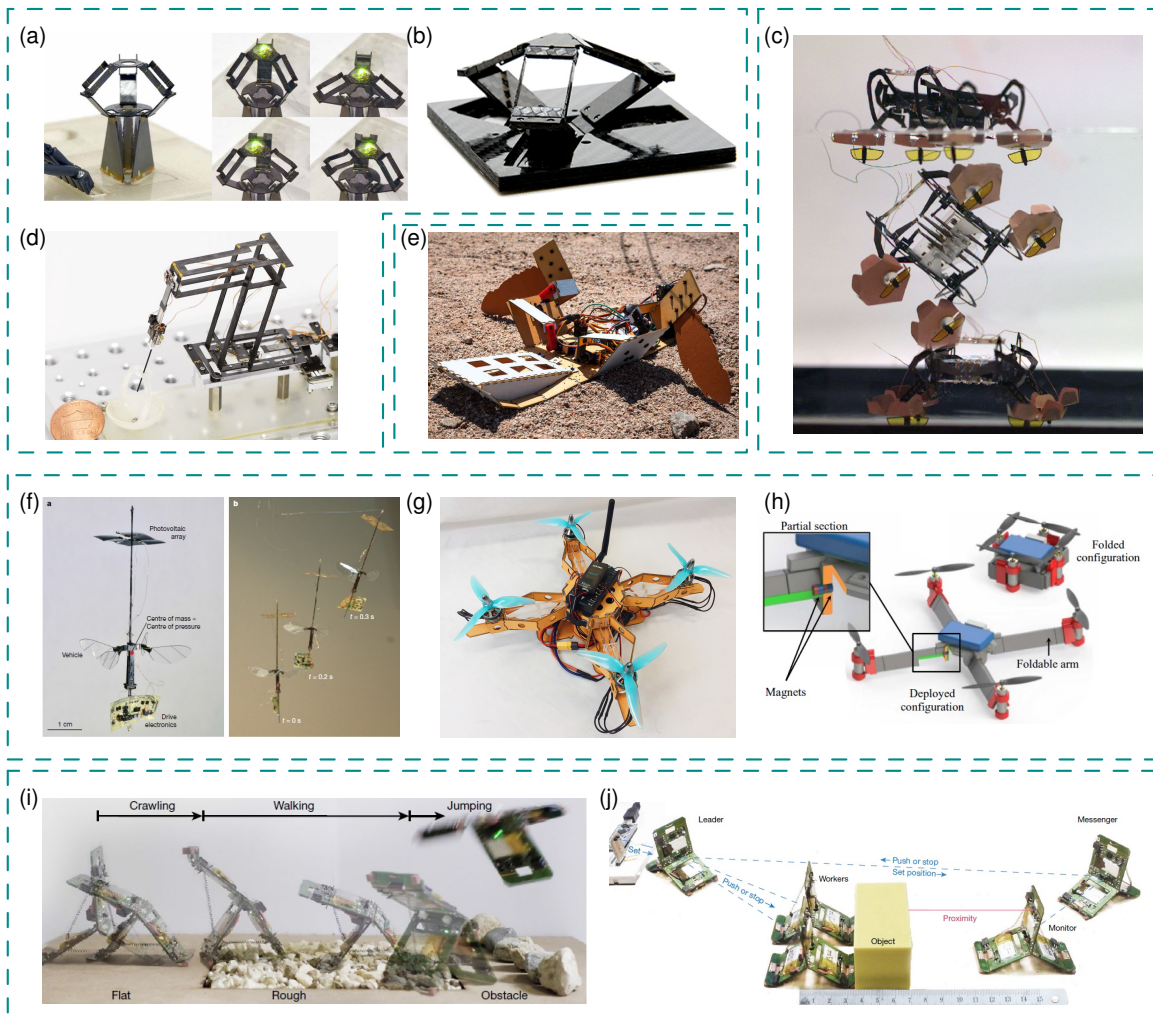


Figure 1.3: **State of the art foldable robots.** (a) MilliDelta [3]. (b) FOLDAWAY-Touch PC mouse[8]. (c) HAMR [7]. (d) Miniature manipulator for teleoperated microsurgery [6]. (e) C-Turtle [9]. (f) RoboBee [10]. (g) FQR [11]. (h) Quadcopter equipped with dual-stiffness origami arms [12]. (i) Tribot [13]. (j) Tribot collaboration[13].

torsional actuators with attached micro-heaters and three SMA spring actuators. As an extension of the functionality of Tribot, they have been used in a team collective labor to move an object (Fig. 1.3j). For this, different types of agents including a leader, two workers, a monitor, and a messenger robot are developed and used. Each agent has a slightly different design and interface circuits installed on it.

### 1.2.2 Modeling and Control of Soft Robots

Laminated techniques, among other manufacturing techniques of robot, are easily scalable. When modeling small foldable robots, material deformation can be reduced by assuming stiff materials at all links. Hence, researchers have been to model the kinematics and dynamics of MilliDelta, FOLDAWAT-Touch, and Tribot using rigid robots modeling methodologies (Fig. 1.4.a-c). The assumption of link rigidity in traditional robots simplifies kinematic expressions, typically localizing highly constrained motion at simple joints and ignoring effects such as backlash and material deformation.

Enlarging the size of these robots or exposing them to high load deforms the materials and prevents us from using rigid modeling assumptions. In contrast, soft matter machines and robots are continuous elastic bodies that exhibit infinite degrees of freedom. This introduces new challenges in sensing, feedback and adaptive control, path planning and robot intelligence [2]. Several different control approaches are proposed and validated by researchers to address this issue.

One of the most precise approaches is using FEA which comes with high calculation costs. In [15], model order reduction of FEM using snapshot proper orthogonal decomposition is proposed to achieve a reduced-order model with lower calculation effort (Fig. 1.4e).

Piecewise Constant Curvature (PCC) approaches are used with different modeling

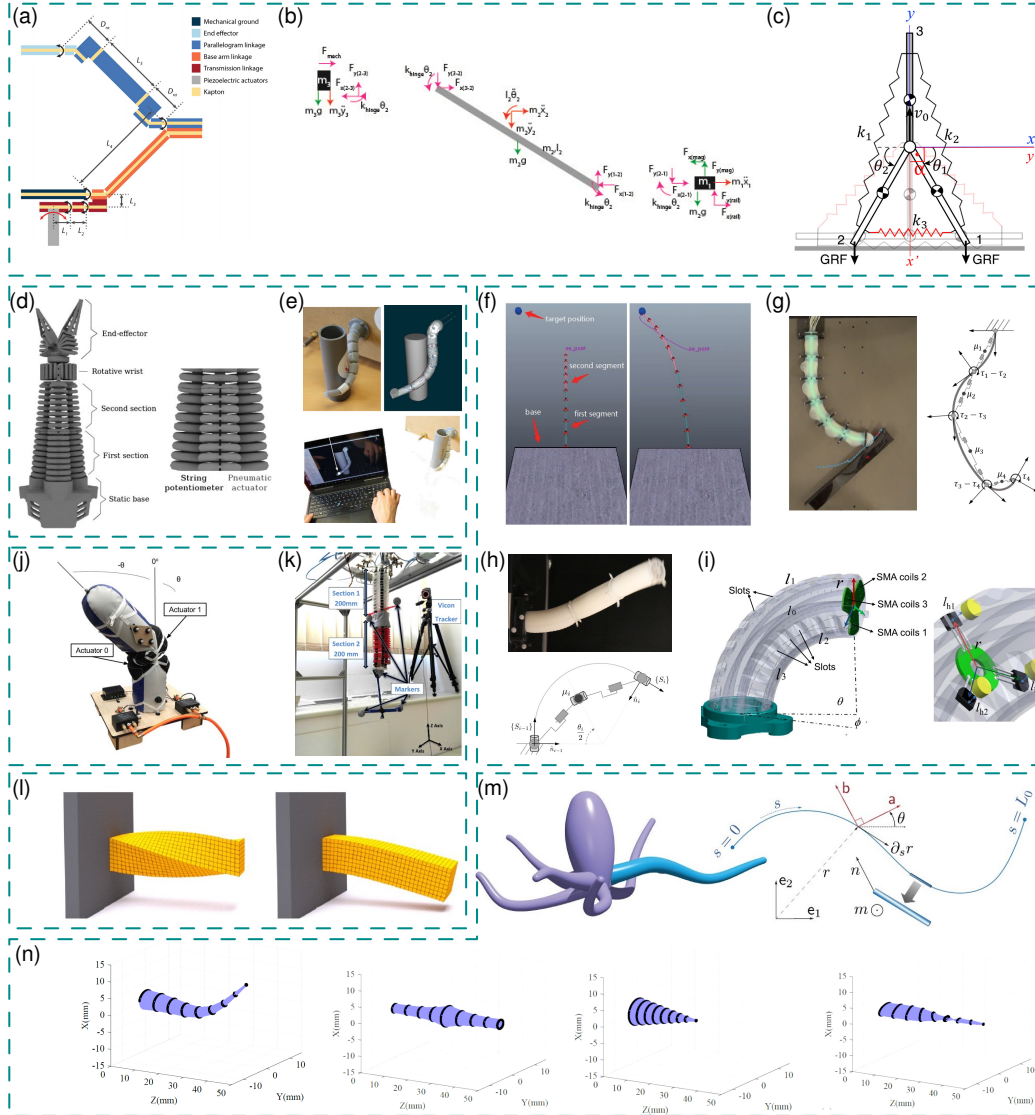


Figure 1.4: State of the art approaches in modeling soft robots. (a) MilliData limb structure and modeling [3]. (b) FOLDAWAY-Touch dynamic modeling [5]. (c) Tribot Modeling [13]. (d) The RobotinoXT by Festo Robotics [14]. (e) Real-time control of the tentacle robot using the reduced-order simulation [15]. (f) PCC modeling using LQR based Gaussian [16]. (g) Soft robot interaction with environment and its PCC modeling [17]. (h) Soft robot controlled in 3D and its PCC robot modeling [18]. (i) Measuring bending of the soft arm and using Hall sensors [19]. (j) A single DOF soft robot platform called grub [20]. (k) Soft manipulator controlled based on model obtained by reinforcement learning [21]. (l) Cantilever modeling via DiffPD [22]. (m) Modeling octopus arms as soft slender rods [23]. (n) Closed-loop control of the configuration of a soft continuum robotic arms [24].



functions to model deformation of soft robots. A linear time-varying Gaussian model is proposed in [16] for dynamic modeling (Fig. 1.4f). This model alongside an LQR based Gaussian controller and a Kullback–Leibler divergence policy is used to get the robot’s end-effector to a point after some iterations while taking care of both dynamics control and path planning. A soft robotic arm driven by SMA coil (Fig. 1.4i) is controlled using a PID controller; curvature is measured using Hall sensors under the assumption of constant curvature of each segment [19]. Santina et al. dynamically controlled a planar soft robotic arm while it was interacting with the environment (Fig. 1.4g) by following a PCC approach and modeling each segment by a rigid RPPR limb [17]. The study is extended to 3D by modeling each segment with an RRPRRRRPRR rigid limb in [18] (Fig. 1.4h). In both cases the masses, stiffnesses and damping coefficients of each limb are experimentally identified. A variable length multisection continuum robot is proposed and experimentally modeled and controlled in [25, 26].

A combination of PCC and FEA model-reduction policy is proposed in [14]. Results obtained from their soft robot (Fig. 1.4d) show that the combined policy is more precise than PCC and faster, but less accurate comparing with FEA.

Machine learning approaches are also used in the modeling and control of these robots. In [20], the rotation of a one-degree-of-freedom pneumatically actuated joint is controlled using a model predictive controller based on deep neural networks (Fig. 1.4j), while no interaction with the world is addressed. Reinforcement Learning is used for dynamic control of a pneumatically actuated soft robotic manipulator [21] (Fig. 1.4k). For forward dynamic modeling, a class of dynamic recurrent neural networks called a nonlinear autoregressive network with exogenous inputs (NARX) is constructed. This network is single-layer, composed of 35 neurons with Tan-sigmoid and linear transfer functions in input and output, respectively.

A fast simulator, named DiffPD, is proposed in [22] that implements the finite element method by voxelizing objects (Fig. 1.4l). This paper features fast, efficient differentiable soft-body simulator, inspired from projective dynamics [27] that can solve contact forces by analyzing a linear complementarity problem based on the assumption that contacts occur on a small number of nodes.

A compliant mechanics environment for controlling soft robots is presented in [28] to model the full advantage of body compliance via the Cosserat rod model. The authors have recently developed a software package, namely, *Elastica*, as an open-source simulation environment for soft, slender rods that can bend, twist, shear and stretch such as octopus arms (Fig. 1.4m).

In [24], a novel model-based, inverse dynamic control is proposed for dynamically controlling bending, torsion, shear, and extension deformation in soft continuum robotic arms (Fig. 1.4n). This is done by implementing a decentralized controller, in which the gain matrices can be defined in terms of the physical and material properties of distinct cross-sections of the robot arm, on the geometrically exact Cosserat rod model. This structure facilitates its application on continuum robot arms composed of independently controllable segments that have local sensing and actuation, such as the arm presented in [29].

### 1.2.3 *Directional & Variable Stiffness*

Recently, a new topic in soft robotics that is getting more attention looks at the use of variable stiffness mechanisms to increase the performance of soft robots. Although the adaptability of soft robots addresses the limitations of many rigid systems, this compliance can also limit functionality, control authority, or frequency response. For example, while a soft gripper can handle delicate objects like an egg more safely than a rigid gripper, it lacks the ability to hold heavy objects. In [30], a gripper is

introduced which, first, actuates tension cables to bend its fingers in order to grasp an object. It then uses a pneumatically actuated layer-jamming mechanism to stiffen the fingers so they can grasp objects they otherwise would be unable to (Fig. 1.5a). Tuning stiffness, both actively and passively, is emerging more in robotic platforms as a way to enhance these robots performance. In [12], curved beams are used in a novel quadrotor (Fig. 1.5b) as mechanical fuses to reduce the robot’s body stiffness in a collision and minimize damages. Baek et. al uses curved beams as a one-side folding mechanism in a gliding robot inspired by the wings of a ladybird beetle [31]. The passive nonlinear stiffness of curved beams enables the wing to be folded into a size that is one-eighth of its deployed area, yet, due to the behavior of the curved materials, its wings are able to deploy in 466 ms (Fig. 1.5c). In [32], a variable stiffness soft continuum robot arm is introduced that uses three tendons alongside its origami structure to bend, expand and contract (Fig. 1.5d). It also leverages three pre-pressurized air-tight chambers filled with pre glass beads to increase the stiffness of the arm when compressed. She et al. has developed a tunable stiffness robotic arm for safe human-robot interaction in [33]. This arm is able to actively tune its links stiffness from stiff to compliant by changing the curvature of two parallel guided beams embedded in the linkage of the arm (Fig. 1.5e).

In [34], variable stiffness through layer jamming of reconfigurable laminates is presented (Fig. 1.5f); among other applications, the authors have shown that the ability to change stiffness on demand enhances the thrust generated by a laminated fishtail when its swimming environment changes between open water to confined channels. An underactuated limb design is proposed in [35] that incorporates hysteretic, pre-curved joints to change their response during loading and unloading (1.5g). In [36], a novel concept is introduced that shows pinching thin-walled tubular structures to induce highly directional changes in their stiffness (Fig. 1.5h). Through both FEA and

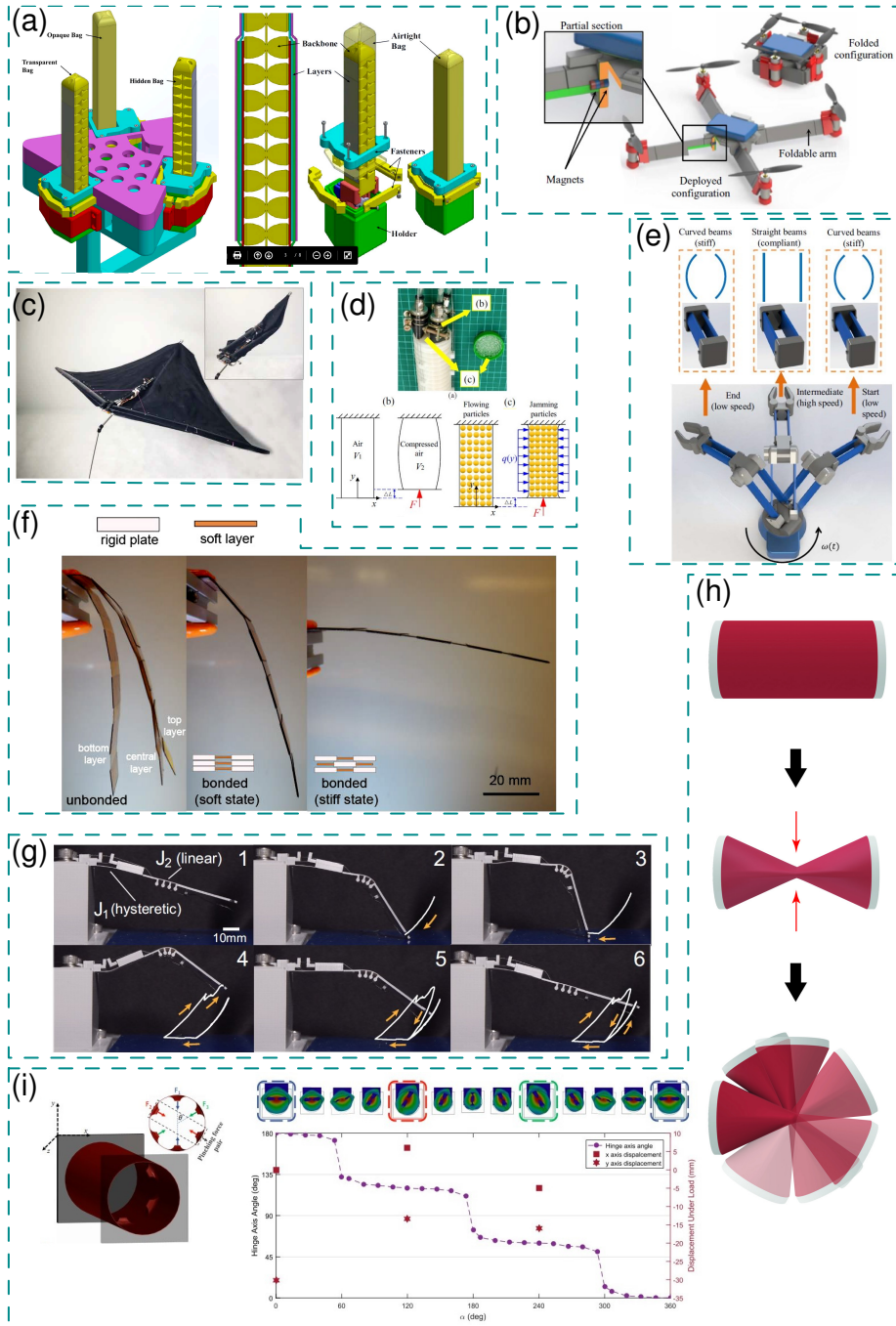


Figure 1.5: State of the art approaches towards use of directional and variable stiffness. (a) Variable stiffness gripper [30]. (b) Quadcopter equipped with dual-stiffness origami arms.[12]. (c) Ladybird beetle-inspired glider [31]. (d) Variable stiffness soft arm [32]. (e) Tunable stiffness arm [33]. (f) Origami-inspired layer jamming [34]. (g) Underactuated limb through curved beams [35]. (h-i) Pinched tubes for directional variable stiffness [36]. (h) Concept of pinching thin-walled tubular structures. (i) Changing direction of the flexible hinge.

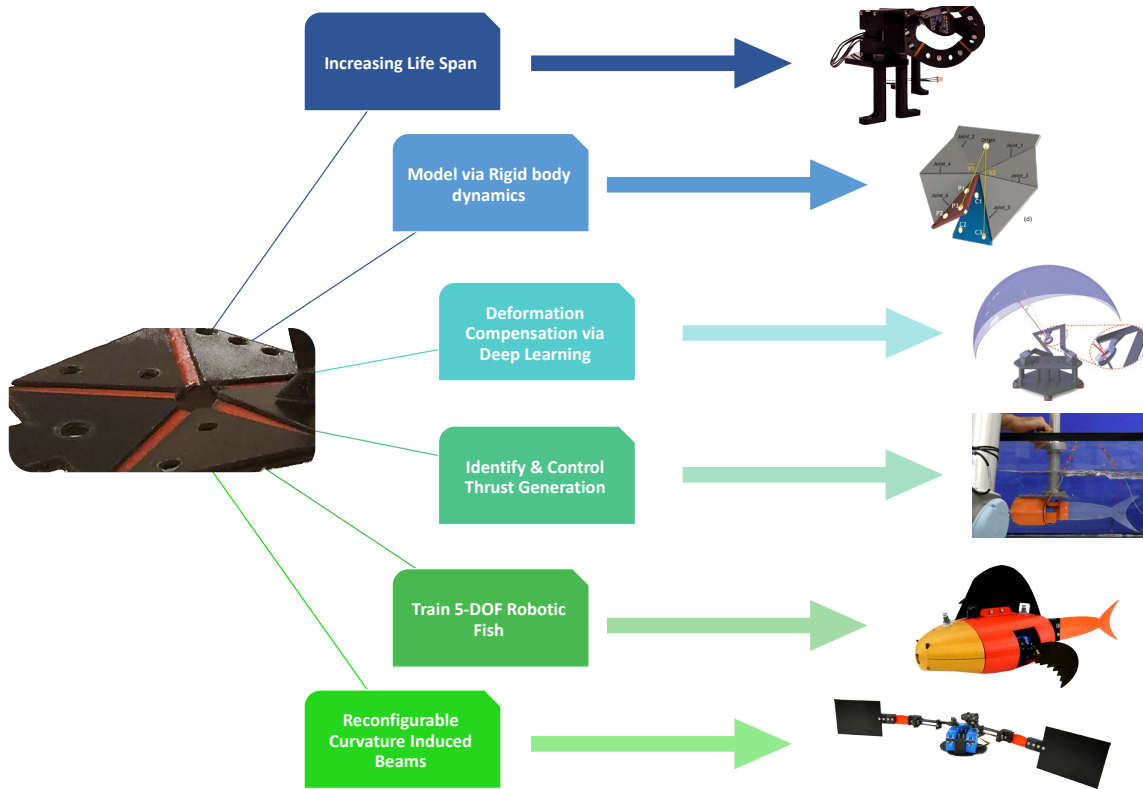


Figure 1.6: Summary of the paper's chapters.

experimental tests, the efficacy of the concept is validated. We first study the relationship between the pinching force and tube deformation. Then, we provide insights into how the combination of multiple pinching forces can be used to orient the major axis of deformation and resulting flexure hinge (Fig. 1.5i). Finally, we experimentally evaluate the suitability of the resulting hinge for use as a joint, i.e., its low stiffness and high displacement under load. The final prototype is capable to generate and recover flexure hinges at multiple orientations around the radial axis of thin-walled tubes on demand.

### 1.3 Methodology & Contributions

This thesis covers the development of different foldable mechanisms with various objectives and working environments (Fig. 1.6). The common aspect shared between all the robots included in this thesis is their need to interact with their working environments. This often results in nonnegligible material deformations. This is addressed, in this thesis, through a focus on modeling and control of these robots' interactions with the world via machine learning techniques. Hence, I have been considering the effect of material deformation through all case studies presented herein. This a unique characteristic of my work compared to other foldable robots mentioned in the background that are design to be small in order to avoid material deformation and in most cases, their interaction with the real-world has not been the addressed.

#### 1. *Increasing the lifespan of foldable robots* (Chapter. 2)

- **Focus:** This study addresses some challenges associated with foldable robots while focusing more on enhancing the lifespan of these robots so they can be used in real world tests.
- **Case Study Robot:** A 2-DOF parallel mechanism at a relatively small scale that preserves the robot's rigidity.
- **Novelty of Study:** A 5-layer flexible hinge composite is introduced as an affordable way to increase the lifespan of the foldable robots. By proposing some ideas to address other challenges in foldable robots, i.e. layer ripping and delamination, a 2-DOF spherical parallel mechanism is fabricated and used to show the advantages of laminated techniques in developing foldable robots. As a case study, this robot is used as an affordable camera stabilizer.

2. *Modeling laminated robot dynamics based on hinge characterization and assumption of rigid links*<sup>1</sup> (Chapter. 3)

- **Focus:** In this study, I have performed a thorough study on hinge characterization for modeling the stiffness and damping coefficients of laminated hinges made from polyester. This is a part of a bigger effort aimed to provide a dynamic modeling engine for laminated robots.
- **Case Study Robot:** The most complicated robot used as a case study in this robot is a 6-bar mechanism which is a spherical robot with three rotational degrees of freedom.
- **Novelty of Study:** We have experimentally validated an extension of Pynamics that can model a closed-loop (Parallel) mechanism. While we assumed that the links are rigid, we modeled the stiffness and damping of flexible Polyester hinges while addressing the effect of air damping on the mechanism.

3. *Compensation of Material Deformation in Soft Robots (Chapter. 4)*

- **Focus:** I present a data-driven modeling approach for compensating for material deformation in soft robots used in closed-loop control.
- **Case Study Robot:** A centimeter-sized 2-DOF Spherical Parallel Manipulator Fabricated via Laminate Processes.
- **Novelty of Study:** In this paper, we propose a workflow for compensation of the material deformation effect on the kinematics of a soft robot by using

---

<sup>1</sup>This study is conducted with an equal contribution between me and Roozbeh Khodambashi. I was responsible for running the tests and hinge characterization while he was in charge of extending the dynamic engine (Pynamics) initially developed by Prof. Aukes

a Deep Neural Network (DNN). In this workflow, we discuss how to tune the DNN's hyper parameters for best performance toward the material deformation of the soft robots under loads.

- **Novelty of Developed Robot:** I have developed a centimeter-scale 2-DOF Spherical Parallel. This mechanism is made by laminated techniques which have resulted in affordable and easy manufacturing process.

4. *Modeling and control of the thrust generation in still water by a laminated sheet sinusoidal propulsion as robotic fish caudal fin* (Chapter. 5)

- **Focus:** This study focuses on the possibility of modeling the thrust of a robotic fish's caudal fin when it is fixed in a small tank and subjected to reflected currents from tank walls. This study originates from a need to have a robot interact with underwater objects and apply force to them. Since the goal environment is a relatively small environment, the robotic fish experiences turbulence from reflected water currents.
- **Case Study Robot:** I have developed a robotic fish that uses a flexible caudal fin as the propulsion system. This fin is made by laminating layers of polyester sheets together. After evaluating the effect of the fin's shape and thickness, the generated thrust is measured and controlled.
- **Novelty of Study:** In order to overcome the challenges caused by material and environment uncertainties, I followed an experimental approach to provide a data-driven model for the generated thrust. First, I have spanned the gait's parameter space to identify a feasible and controllable sub-space that is resistant to uncertainty. Then, I modeled, identified and controlled



the thrust generated by the caudal fin propulsion within that feasible subspace.

5. *Training a 5-DOF robotic fish in the Presence of Uncertainties Caused by Material Deformation and Working Environment* (Chapter. 6)

- **Focus:** In this study, we identify ways to search through a high-dimensional space of a robot's actuation parameters when there is uncertainty caused by both material deformation and the working environment. This study is motivated by extending the aforementioned fish design to add two pectoral fins. This results in a robotic fish with 5 degrees of freedom and a gait parameter space with a higher number of dimensions. This study switches its approach from modeling to training. The goal of the proposed training procedure is to identify a set of gait parameters that perform well against a user-supplied performance objective while producing repeatable results over many cycles in different environments.
- **Case Study Robot:** I have developed a fish-inspired robot, which combines one caudal and two pectoral fins. The resulting five degrees of freedom may be described with a high-dimensional set of locomotion/gait parameters.
- **Novelty of Study:** I have developed strategies for identifying high-performing sets of gait parameters with an online learning strategy (CMA-ES). Our lab setup often differs from the intended goal environment in key ways (turbulence, water speed, type of data-collection setup, i.e., force instead of trajectory). This has also led to new strategies for identifying gait parameter sets that have a high degree of correlation in performance

between the lab and the intended operating environment. These efforts have resulted in a design and optimization workflow for robots that works well in niche environments, while permitting the majority of development, data collection, and characterization in the lab.

- **Novelty of Developed Robot:** A novel fin design based on a 2-DOF spherical mechanism is introduced. Its fabrication is facilitated by laminate design concepts that minimize manufacturing costs typically associated with spherical, parallel mechanisms.

## 6. *Leveraging Variable Stiffness of Curvature-induced beams in Developing Soft Robots* (Chapter. 7)

- **Focus:** Understanding soft material stiffness can be beneficial for designing robots. In this study, a novel concept for using curvature to obtain anisotropic buckling is presented. I demonstrate that tunable preferential buckling during symmetric flapping results in positive net thrust by reducing the drag associated with the recovery stroke while keeping the drag high in the power stroke. In this study, we first validate the efficacy of curvature induced buckling for locomotion in different media. Then, we develop a swimming robot that can switch between different swimming gaits, e.g. rowing, flapping and undulation, by adding a mechanism to actively adjust the buckling limits.
- **Case Study Robot:** The final prototype is a swimming vehicle that uses curvature-induced buckling for thrust generation and can switch between rowing, flapping, undulation, and turning swimming gaits.
- **Novelty of Study:** This study explores the concept of leveraging curved beams and their preferential buckling in producing positive net thrust

through symmetric input gaits. This study illustrates how using this concept reduces the complexity of the system design and control for locomoting through fluids such as air or water.

- **Novelty of Developed Robot:** The robot introduced in this study is the first robot that uses curvature-induced buckling for cyclic thrust generation. The swimming robot made using this concept is capable of reaching an average speed of 0.33 m/s using a symmetric swimming gait with two fins. Furthermore, our results demonstrate that a single buckling fin can be used to produce rotation. Also, by adding a mechanism to actively tune the buckling limits of the curved beams, the swimming robot can switch between different swimming gaits, e.g. rowing, flapping and undulation.

These studies have migrated toward data-driven modeling in order to remain tractable unlike computationally expensive FEA-based approaches for modeling material deformation and environment interaction, e.g. hydrodynamic in swimming robots. However, few workflows exist that help researchers with experimentally obtaining the desired data-driven models. It is safe to say that when dealing with black-box identification, researchers often report their chosen parameters and algorithms without explaining the reason for their selections. For example, I have not been able to find a paper proposing a procedure for selecting the number of hidden layers in a deep neural network.

In the body of this dissertation, along with new ideas and design concepts, novel workflows are proposed and used that can help other roboticists in similar research. I believe one of my main contributions is tackling this issue by introducing different workflows that can help researchers follow a procedure to perform their black-box or gray-box identification. This includes training robots for working in real-world

environments while saving time and energy by designing and carrying out effective experiments in a lab test setup.

## Chapter 2

### INCREASING THE LIFE SPAN OF FOLDABLE MANIPULATORS

This chapter addresses the advantages and challenges of laminated manufacturing techniques, specifically mechanism durability. The goal is to evaluate how laminated techniques may be used to replicate the performance of more traditionally manufactured robotic manipulators. We propose a novel fabric-polyester hinge design with an improved life-span. We additionally provide an overview of the design and construction workflow for a small laminated 2-DOF spherical parallel manipulator for use as a camera stabilizer.

#### 2.1 Introduction

Taking advantage of laminating techniques in the construction of robots can result in considerable savings with regard to fabrication cost and time, but the challenges caused by this technique must be addressed. This study aims to demonstrate the feasibility of fabricating robotic manipulators via laminated techniques by tackling the issues of durability, an artifact of the laminate fabrication methodology itself. We propose a fabric-polyester hinge that increases the life span of laminated devices. This hinge layer consists of a polyester layer laminated between two fabric layers. Using this technique, a 2-DOF spherical parallel mechanism has been designed and built. This mechanism is both affordable and durable, with an embedded IMU sensor. While installing an IMU on mechanisms is fairly common, embedding the required circuit via easy and affordable manufacturing processes and the demonstration of using the embedded sensor can be beneficial to researchers.

Many construction methods exist for manipulators, but only a few groups inves-

tigate the use of laminate techniques for making multiple degree-of-freedom robotic manipulators, such as the delta robots presented in [37, 38]. These papers focus on high-speed manipulators at the millimeter and centimeter scale, respectively. Laminate fabrication techniques have been applied to a broad number of kinematic applications for locomotion, however. Planar four-bar mechanisms have been demonstrated in flapping-wing applications [39], and 5-bar spherical linkages have been previously used to drive 2DOF leg joints in micro-robotic walking applications [40]. A class of mechanisms known as Sarrus linkages have been used in linear actuators [41] and assembly scaffolds [42].

In general, the mechanisms fabricated with laminated techniques can be characterized as low-mass, small-scale devices for which material deformation due to payload is negligible or ignored, or devices that use exotic materials or less-accessible processes to reinforce links and eliminate the issues that accompany compliant end-effectors [10, 37]. Additionally, since this process is still used primarily within research settings, few papers focus on design issues such as mechanism lifetime or durability with a small number of exceptions [43, 44, 45, 46].

The case study for this project is a two degree-of-freedom(DOF) spherical parallel manipulator [47]. Parallel mechanisms leverage multiple pathways to the ground to achieve similar rigidity and precision to their serial counterparts, often with lighter components. Parallel robots are also often able to achieve higher end-effector speeds due to the fact that actuators can be proximally mounted on the fixed chassis, reducing loads on distal joints. These benefits make parallel mechanisms a rich area for research. Specific implementations include the Gough-Stewart platform [48, 49], Delta robot [50], 3RRR Parallel Planar Robot [51, 52], and the 3-Degree-of-Freedom (DOF) decoupled parallel robot [53, 54].

A number of studies have studied this mechanism’s workspace for the purpose of

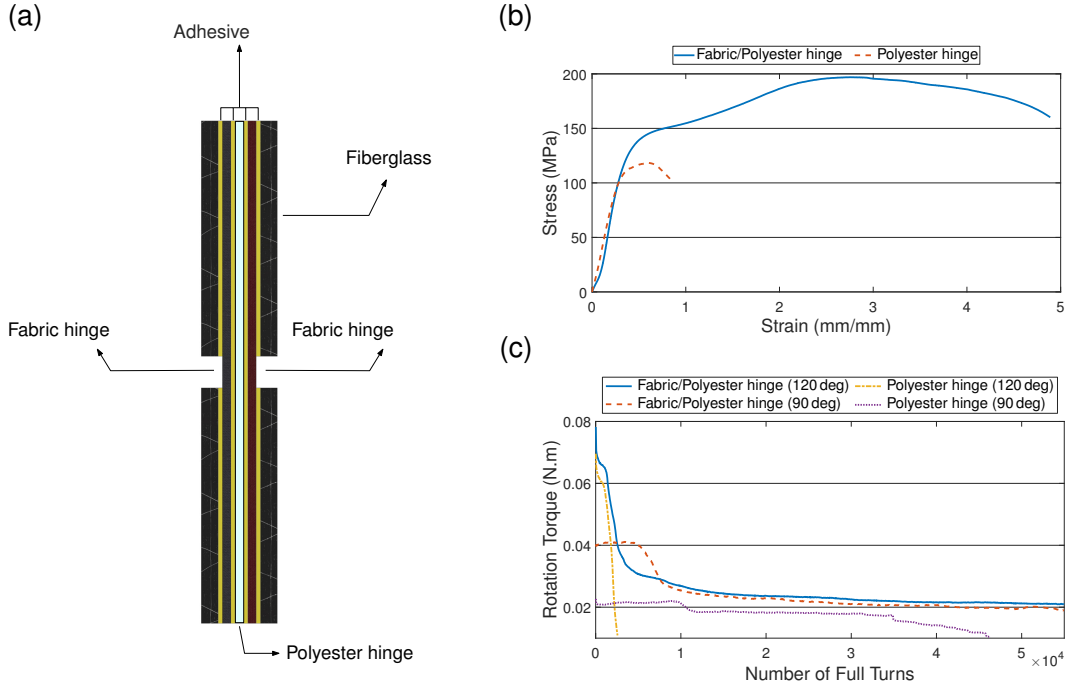


Figure 2.1: **Increasing laminated hinge life span.** (a) Layup of the proposed fabric-polyester hinge. (b) Tensile test data of polyester and fabric-polyester hinge. (c) Life span study on the hinges.

optimization[55, 56], understanding its singularities[57], and computing its forward and inverse kinematics [47, 58] and dynamics. This mechanism has been used for applications such as camera stabilization [59] and object tracking [60]; two such manipulators have also been used in tandem in an active vision system [61]. While none of the research on this particular mechanism uses laminated fabrication techniques for construction of the manipulator, they demonstrate the general usefulness of this manipulator.

The chapter is organized as follows: Section 2.2 describes the laminated fabrication technique and the challenges associated with it. In Section 2.3, we introduce solutions for increasing laminated mechanisms' stiffness and life span. A 2-DOF spherical parallel manipulator is then introduced based on the above mechanism; its design

and fabrication is then discussed in Section 2.4. The study concludes with some remarks and suggestions for future work indicated by obtained results in Section 2.5.

## 2.2 Laminated Techniques and Their Challenges

A typical laminate layup consists of material layers which each perform separate functions based on their material properties. This includes rigid materials, which can be used to form rigid kinematic links, flexible materials, which can be used to create flexure joints at desired locations, and adhesive material, which is used to selectively join neighboring material layers into a monolithic mechanism. One commonly-used layer ordering is (rigid, adhesive, flexible, adhesive, rigid). The symmetric order of these materials with the rigid material on the outside is thought to reduce peeling and delamination between layers. The rigidity of the laminate can be tuned by adjusting the thickness of the rigid layer, switching to a stiffer material, or adjusting its planar offset from the layup's medial axis. Additionally, other material layers like copper can be added to the layup for conducting electricity.

A large number of materials including cardboard, acrylic, fiberglass, carbon fiber – even aluminum or steel – can be used as a rigid layer, as long as they are compatible with the available cutting techniques – water-jet, laser, etc – and bond well with available adhesives. The material type and thickness of the rigid material provides a vast design space in which one can balance rigidity, weight, cost, and durability.

The adhesive layer is responsible for gluing the rigid and flexible layers to each other, and should be selected based on adhesive compatibility with neighboring materials. The flexure layer is used in order to provide a rotational joint in laminated devices. Thus, it must be cuttable and robust against tearing and high forces, as well as exhibit a long lifetime. Many polymers and thin metals may be used; in our study we have selected polyester as an affordable, machinable, and flexible material.



There are, however, drawbacks to using laminate techniques for manipulator construction. One limitation is the finite range of flexure hinges, which are ultimately limited to  $\pm 180^\circ$ , and even less when considering the thickness of the laminate. While using a ball bearing solves the problem in conventional mechanism designs, laminate mechanisms are not able to continuously rotate about an axis, playing an important role in the design of laminate mechanisms. The length of the hinge region ('L' in Fig. 2.2) can be increased to improve range of motion to reach the theoretical  $\pm 180^\circ$  limit, but this sacrifices hinge stiffness. Shorter hinge regions result in stiffer hinges and smaller ranges of motion.

Another consideration is the torsional stiffness of hinges. Long, narrow hinges can easily twist along axes other than the intended joint axis. This condition is commonly mitigated by widening hinges or using "castellated" designs [62].

Durability of the laminated material is another important consideration, and is more often associated with low-cost materials such as cardboard and plastic. While this can be addressed in rigid links by using higher-performance materials like fiberglass or carbon fiber, the durability of flexure hinges is more challenging. For this layer we seek strong, flexible materials that go through desired deformations but do not break easily [63]. The alternative is to use material like fabric, which trades off torsional stability for lifetime. Delamination is often observed in laminate mechanisms and can have a significant impact on device life span. This occurs when torsional stresses or compressive forces exceed inter-layer pressure limits, causing laminate layers to separate or peel.

## 2.3 Laminated Mechanism Stiffness & Durability

This section addresses two important issues currently limiting laminated robot functionality, namely durability and stiffness.

### 2.3.1 Hinge Durability

As an affordable flexible material, we use polyester as the flexible layer in our laminated mechanisms. Thin polyester hinges easily tear, especially in high-stress situations. Hinge durability can be increased by using thicker material, but this adds unwanted rotational stiffness and damping.

In this study a new hinge design is proposed to address the issues previously discussed which impact lifetime and durability. This design consists of a polyester sheet laminated between two layers of fabric using adhesive (Fig. 2.1a). Figure 2.1b demonstrates the result of a tensile test performed on a fiber-polyester hinge and a polyester hinge with the same design. The results confirm the higher fracture strength of the fiber-polyester hinge. Moreover, the similar initial slope of the plots confirms the consistency of stiffness between the two designs, meaning that the hinge stiffness is mostly affected by the polyester hinge.

A lifespan test has been carried out to show how the fabric-polyester hinge can endure more rotation before failing. Figure 2.1c shows the torque required to rotate the hinge across a large number of rotations for both the fiber-polyester and polyester hinges. Two different cases are studied in this test. In the first case, each rotation consists of a motion between  $\pm 90^\circ$ . In the second case, the rotation is increased to  $\pm 120^\circ$  exposing the hinge to higher tension, as rigid parts collide with mounting attachments during this motion. The results, seen in 2.1c show that, in the presence of torsion, the polyester hinge quickly tears (2500 cycles), while the fabric-polyester

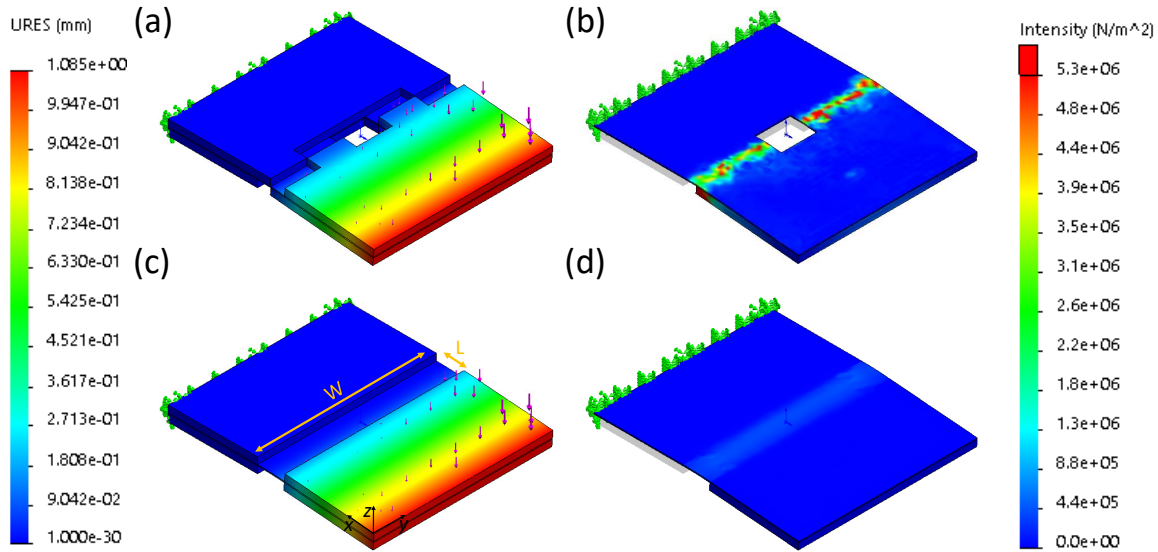


Figure 2.2: **FEA study on simple and Castellated hinge for an uneven distribution of load.** (a) Under load deformation of Castellated hinge. (b) Stress intensity through the flex layer for Castellated hinge. (c) Deformation of the simple hinge under uneven load. (d) Flexible layer stress density for the simple hinge.

hinge endures more than 50,000 cycles before failure.

This fabric-polyester hinge introduces higher strength compared to a polyester hinge. As a result, there is no need to increase polyester sheet thickness, which would result in higher joint stiffness and damping. This independence between life span and dynamic behavior is desirable, as each can thus be tuned separately.

### 2.3.2 Delamination

Although utilizing materials or adhesives with high peel strength is one solution to reduce delamination, other strategies may be used to reduce its occurrence mechanically, via pressure applied to critical points. This is made possible by cutting holes in the laminate near the ends of each hinge and using mechanical constraints like rivets or other connectors to apply pressure to the layers. Though additional

hardware can decrease the range of motion via interference, this can be mitigated by adding corresponding clearance holes so that hardware does not interfere with joint motion, as illustrated in Fig. 2.5a.

### 2.3.3 *Stiffness compensation*

In general, using thinner sheets of material will decrease system stiffness within laminated mechanisms. While this can be mitigated several ways in rigid layers, increasing the stiffness of hinges can negatively impact the dynamic behavior of mechanisms, e.g. requiring higher torques and bigger actuators to move the joints. One of the biggest issues observed in these devices hinges are joints which twist along undesired axes under torsion. While reducing hinge length can stiffen a hinge against such torsional non-idealities, this decreases the joint’s range of motion. Previously, alternative ‘castellated hinge’ designs have been proposed in [62]. This design reduces unwanted twist by effectively reducing the length of the flexure joint, but exhibits higher stress as well as a range of motion less than  $\pm 180$  degrees.

Figure 2.2 shows a Finite Element Analysis (FEA) for a simple and castellated hinge, highlighting the difference in how these two hinges resist torsional loads due to uneven force distributions on the distal end. The load is concentrated at the bottom-right corner of the hinges in Figure 2.2 using the following equation:

$$F(x, y, z) = (x + (5 - y)) \tag{2.1}$$

In this analysis the magnitude of the load ( $|F|$ ) is adjusted between the two designs in order to make hinge rotation equal. The results show that while twist is reduced in the castellated hinge (Figs. 2.2a&c), the magnitude of the load is nearly 12 times higher than the simple hinge. In addition, the castellated hinge has higher stress on

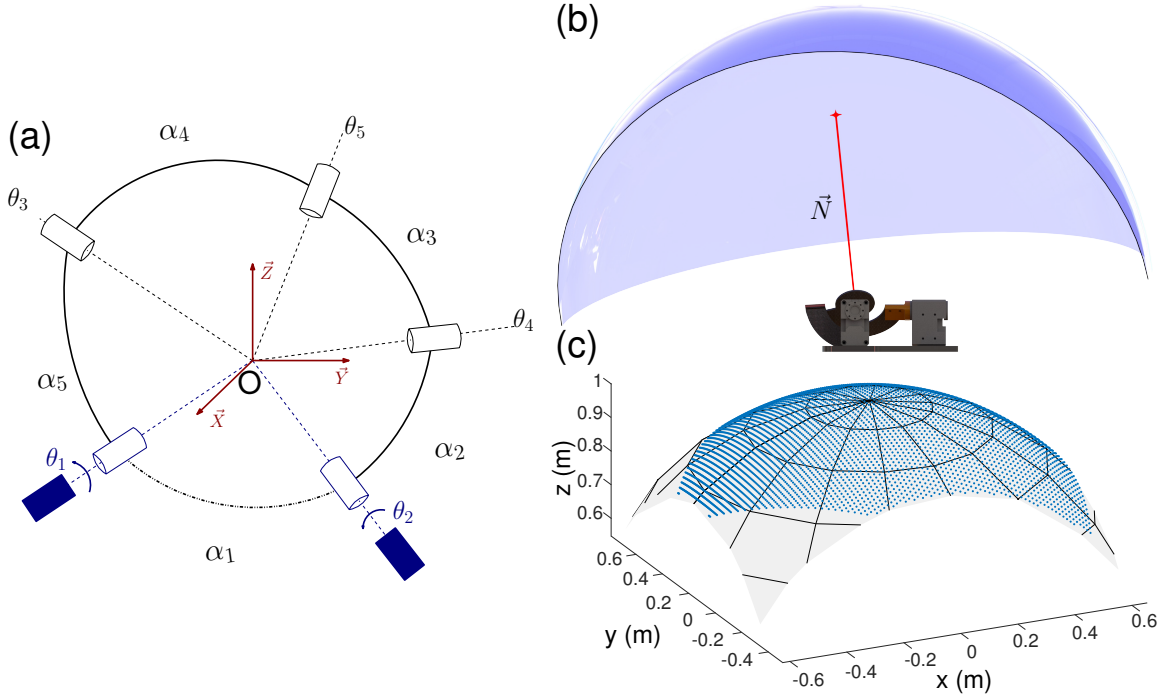


Figure 2.3: **Kinematic synthesis of the 2-DOF Spherical PM.** (a) The 2 DOF rotational linkage design. Dashed lines represent the rotational axes while solid lines represent rigid links. The dashed dotted line corresponding to  $\alpha_1$  represents fixed ground. (b) Illustration of the end-effector orientation by using projection of a virtual laser beam on a sphere. (c) Workspace of the 2-DOF Spherical PM.

its edges (Figs. 2.2b&d) which can damage the hinge over time and decrease its life span.

## 2.4 Case Study of 2-DOF Spherical PM

### 2.4.1 Kinematic Synthesis

The system under study, first introduced as two degree-of-freedom spherical orienting device in [64] consists of 5 rigid links connected by hinges, as shown in Fig. 2.3. The axes of all hinges meet at a single point (Point O) forming a spherical linkage.

The loop closure between the two distal, rotational links requires three constraint equations, resulting in a two degree-of-freedom system. By co-locating the output position of the output link's (the end-effector) at the spherical mechanism's origin, the motion of the system can be considered effectively grounded, permitting the output motion of the end-effector to be represented as pure rotation.

The transmission which relates the actuator's motion to the end-effector's rotation may be computed using design parameters ( $\alpha_i$ ) and the rotation between adjacent body frames ( $\theta_i$ ), making the length scale of each link immaterial. Prior work by Ouerfelli et al demonstrates mathematically that the workspace of the mechanism is maximized if  $\alpha_2 = \alpha_3 = \alpha_4 = \alpha_5 = \pi/2$  [55].

Based on these design parameters, the final design for the robot may be seen in Fig. 2.3a. The mechanism's actuators are aligned along  $x$  and  $y$  axes of the device's chassis (considered the world frame).

Although the angle corresponding to the grounded body ( $\alpha_1$ ) does not affect the workspace of the mechanism, it impacts its singular states. If  $\alpha_1 = 0$ , the mechanism is singular across all inputs. Alternately, if  $\alpha_1 = \pi/2$ , theoretically, the mechanism has minimum singularity within its workspace [55]. Based on that knowledge,  $\alpha_i = \pi/2$  has been selected for all  $\alpha_i$ .

Though the mechanism is a 2-DOF mechanism, its end-effector experiences angular velocities in  $\mathbb{R}^3$  as a function of its two actuated input velocities (even though one of those 3 dimensions is always dependent). This is also reflected in the mechanism's inverse Jacobian matrix as well:

$$\begin{bmatrix} \dot{\theta}_1 \\ \dot{\theta}_2 \\ 0 \end{bmatrix} = \begin{bmatrix} \sin \theta_3 & 0 & -\cos \theta_3 \\ \frac{\cos \theta_5 \sin \theta_3}{\sin \theta_5} & -\frac{\sin \theta_4}{\sin \theta_5} & \frac{\cos \theta_5 \cos \theta_3}{\sin \theta_5} \\ -\cos \theta_3 & 0 & \sin \theta_3 \end{bmatrix} \begin{bmatrix} \omega_X \\ \omega_Y \\ \omega_Z \end{bmatrix} \quad (2.2)$$

where  $\theta_i$  are the hinge angles and  $\omega_k$  are components of the angular velocity of the

end-effector.

We have considered the potential application of a pointing task, e.g. a laser pointer, for the mechanism while formulating its kinematics (Fig. 2.3.b). Being a rotational mechanism, the center of its end-effector only experiences rotation and no translation. For formulating the mechanism kinematics, we consider a vector perpendicular to the plane of the end-effector link, which is co-linear with our “virtual” laser beam vector ( $\vec{N}$ ) shown in Fig. 2.3.b. Based on the global axes’ alignment with servos, the inverse kinematics may be written as:

$$\theta_1 = \tan^{-1}\left(\frac{N_Y N_Z}{N_X^2 + N_Z^2}\right) \quad (2.3)$$

$$\theta_2 = \tan^{-1}\left(\frac{N_X}{N_Z}\right) \quad (2.4)$$

where  $\theta_i$  are the actuator angles and  $N_k$  are the components of the unit vector perpendicular to the end-effector body. In the case of  $N_Z = 0$ , the values of  $\theta_i$  are  $\theta_1 = 0$  and  $\theta_2 = \pi/2$ . The forward kinematics of the robot can then be formulated as:

$$N_Z = \sqrt{\frac{1}{(t_1 + t_1 t_2)^2 + t_2^2 + 1}} \quad (2.5)$$

$$N_X = t_2 N_Z \quad (2.6)$$

$$N_Y = (t_1 + t_1 t_2) N_Z \quad \text{where, } t_i = \tan(\theta_i)_{\{i=1,2\}} \quad (2.7)$$

By using the above set of equations, the workspace of the robot has been obtained and may be seen in Fig. 2.3c.

#### 2.4.2 Design

Figure 2.4 illustrates the design process in popupCAD. Based on this design tool, after designing the mechanism’s main body, the hinges are placed corresponding to the above angles for  $\alpha_i$ , along with any required attachment holes. The software then

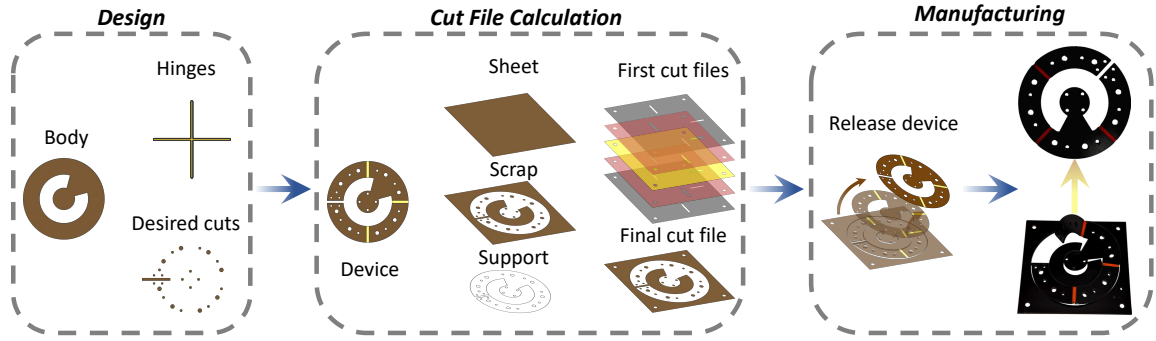


Figure 2.4: Graphical representation of the design process for 2-DOF spherical parallel manipulators using popupCAD.

calculates the final device design, along with the initial and final cut files for each layer.

The 2-DOF mechanism utilizes the fabric-polyester hinge proposed in Section 2.3.1. An IMU is embedded on the mechanism’s end-effector for rotation feedback. A flexible circuit is used to route the electrical connection from the base to the end-effector, so there are no wires affecting the mechanism’s performance. The final device consists of a total of 11 layers, including two rigid fiberglass layers, two fabric layers, one flexible polyester layer, one flexible circuit layer, and five adhesive layers. In order to design the flexible circuit, the final device design is exported from popupCAD as a vector-based DXF file and imported to DesignSpark PCB (As seen in Fig. 2.5c). Using this software, a circuit is routed along the hinge pathway. The circuit is then printed using a Xerox ColorQube 8580 Solid Ink Printer to deposit wax on copper-clad polyimide. Then, the flexible circuit layer is wet-etched and laminated with the rest of the device layers.



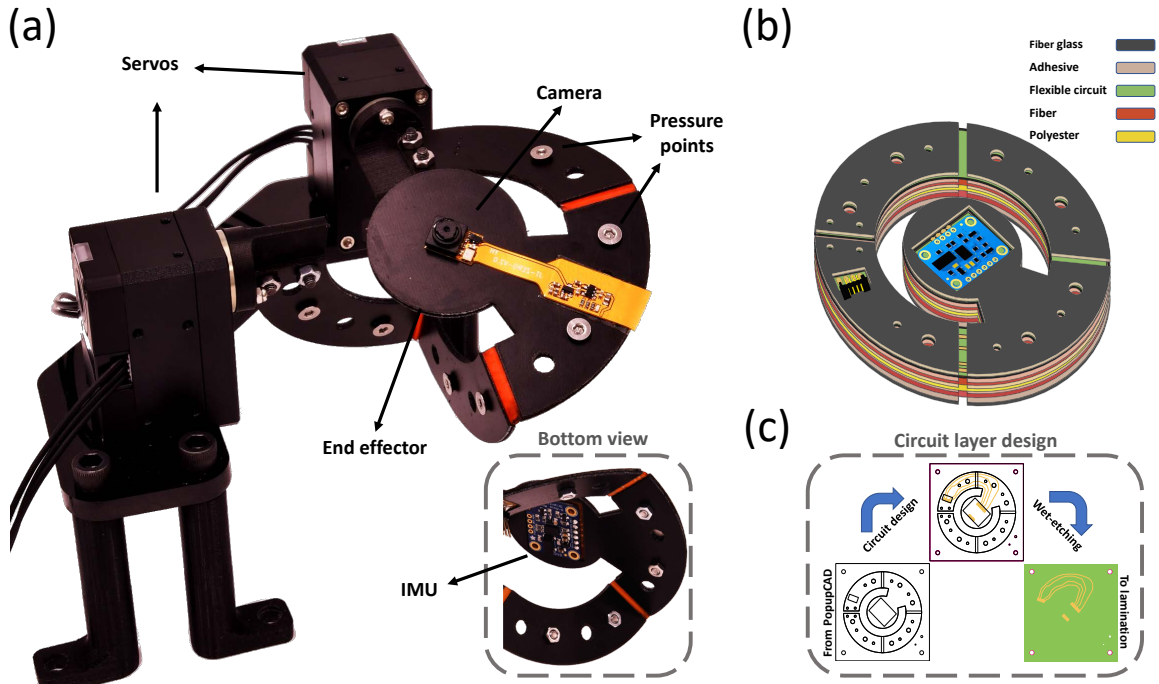


Figure 2.5: **Prototyping the 2-DOF Spherical Parallel Mechanism.** (a) Final prototype and its embedded IMU sensor. (b) Final Design and layers of the prototype. (c) Design of the flexible circuit using prototype design files obtained via PopUpCAD.

### 2.4.3 Manufacturing

Figure 2.5a shows the final prototype with a camera attached to its end-effector. This prototype has been built using 0.03-inch fiberglass sheets as a rigid layer and 0.005-inch polyester sheet as a flexible layer. A heat-activated acrylic adhesive from Drytac<sup>1</sup> is used to bond layers. The flexible circuit layer is copper-coated polyimide from DuPont<sup>2</sup>. Two XM430 Dynamixel DC servos actuate the device. Two custom-made 3D-printed Nylon horns attach and align the mechanism hinges to the servos, as well as act as a safety coupling in the mechanism. The rest of the chassis is made with acrylic.

<sup>1</sup>[www.drytacstore.com](http://www.drytacstore.com)

<sup>2</sup><https://www.dupont.com>

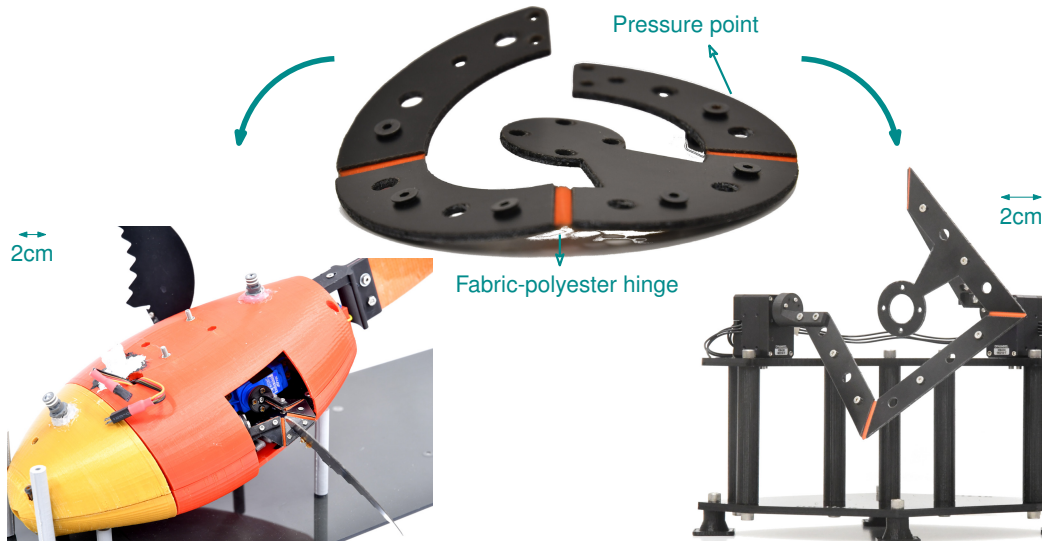


Figure 2.6: Different Applications Derived from the Proposed Mechanism.

#### 2.4.4 Manipulation

The proposed mechanism has been used at several different size scales across different projects within our research. Figure 2.6 shows two exemplar applications. First, this mechanism has been scaled down and used as pectoral fin in a robotic fish (detailed in Chapter 6). The same fabric-polyester hinge with pressure-applying hardware has been responsible for increasing the lifespan of the mechanism to over 9000 runs, each consisting of the robot swimming underwater for one minute (undergoing many individual bending cycles); this demonstrates the hinge’s suitability for underwater applications as well. In another study, the same mechanism has been used at a larger scale to study the performance of compliant laminated mechanisms under load (detailed in Chapter 4). This mechanism has sustained tens of hours of tests over more than 24 months without delamination or tearing. To further demonstrate the advantages of laminated techniques, this 2-DOF spherical mechanism has been used to stabilize a camera mounted on its end effector. This is done based on the orientation feedback from the embedded IMU (Adafruit BNO055). This demon-

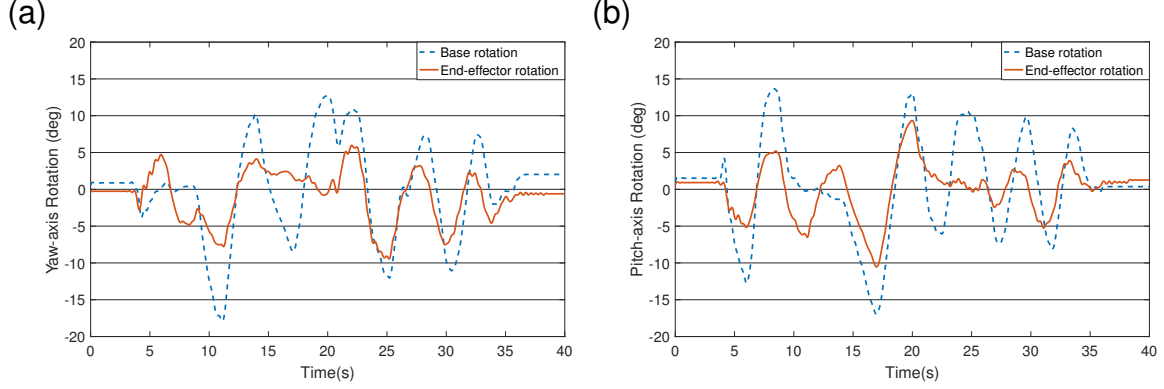


Figure 2.7: **Camera Stabilization using the manufactured 2DOF spherical PM.** (a) Rotations in Yaw-axis. (b) Rotations in Pitch-axis

stabilization is inspired by the study reported in [59], in which Safaryazdi et al. study a number of control approaches for camera stabilization based on the same 2-DOF parallel mechanism albeit manufactured using traditional machining techniques in aluminium.

In order to use the mechanism for camera stabilization, a closed-loop controller is applied, using a linearized kinematic model around  $N_x = N_y \simeq 0, N_z \simeq 1$ . Around this point, Eqs.(2.5), (2.6), and (2.7) can be rewritten:

$$t_i = \tan(\theta_i) \simeq \theta_{i\{i=1,2\}} \quad (2.8)$$

$$N_Z \simeq 1 \quad (2.9)$$

$$N_X \simeq \theta_2 N_Z \quad \rightarrow \quad \frac{N_X}{N_Z} \simeq \theta_2 \quad (2.10)$$

$$N_Y \simeq (\theta_1 + \theta_1 \theta_2) N_Z \simeq \theta_1 N_Z \quad \rightarrow \quad \frac{N_Y}{N_Z} \simeq \theta_1 \quad (2.11)$$

By considering small end-effector orientations about this point, Eqs. (2.10) and (2.11) can be used to describe the linearized kinematic model as:

$$\begin{bmatrix} \psi_1 \\ \psi_2 \end{bmatrix} = \begin{bmatrix} 1 & 0 \\ 0 & 1 \end{bmatrix} \begin{bmatrix} \theta_1 \\ \theta_2 \end{bmatrix} \quad (2.12)$$

$$\text{where, } \psi_1 \simeq \tan(\psi_1) = \frac{N_Y}{N_Z}, \quad \psi_2 \simeq \tan(\psi_2) = \frac{N_X}{N_Z}$$

In this configuration, the inverse and forward kinematics can be modeled as an identity matrix and the orientations of the end-effector in  $x$  and  $y$ -axes become independent from each other. This simplifies the mechanism's inverse and forward kinematics significantly. In this project, we use a simple P-controller to keep the end-effector horizontal. In order to evaluate the controller, another IMU is attached to the mechanism's base and the two signals recorded.

Figure 2.7 shows the orientation of the end-effector vs the mechanism frame when the proposed controller is applied while the mechanism's base is moved randomly by a user<sup>3</sup>. It should be mentioned that the result is similar to the performance of the rigid robot reported in [59] when a similar controller and sensor mounting is used.

## 2.5 Discussion

Laminate devices can often be manufactured faster and cheaper than conventional robots. The construction of our mechanism took less than one and a half hours and cost less than \$30. Interestingly, reducing our mechanism's size not only makes it more rigid, but reduces overall cost. This contrasts with conventionally-fabricated devices, where the cost increases due to the need for tighter tolerances and more precise machining. This makes laminate techniques ideal for mass production of mechanisms at small size scales.

A novel, 2DOF, spherical, parallel manipulator made via laminate techniques has been introduced in this study, based on a class of similar devices manufactured using

---

<sup>3</sup>Shown in this video: <https://youtu.be/IC7SgZzbM9w>

more traditional approaches. The advantages and disadvantages of using laminate techniques have been discussed and several solutions have been proposed to address the non-ideal performance of this device, including both fabrication and modeling techniques. The study subsequently describes the particular design investigated in this study, including a description of the angles used and the specific fabrication choices made. This technique demonstrates steps towards using low cost, durable, laminate, spherical, parallel mechanisms in place of high-precision but more expensive devices. Future work will focus on manufacturing a scaled down prototype that is small, durable, and lightweight to extend the application of next generation to portable devices like gimbals, mobile robots and flying UAVs.

## Chapter 3

### DYNAMIC MODELING VIA CHARACTERIZATION OF FOLDABLE HINGE

This chapter evaluates the possibility of describing laminated mechanisms' dynamic behavior using rigid body dynamics. Laminate mechanisms are a reliable concept in producing low-cost robots for educational and commercial purposes. These mechanisms are produced using low cost manufacturing techniques which have improved significantly during recent years and are more accessible to novices and hobbyists. However, iterating through the design space to come up with the best design for a robot is still a time consuming and rather expensive task and therefore, there is still a need for model-based analysis before manufacturing. Until now, there has been no integrated design and analysis software for designing laminate robots. This chapter addresses some of the issues surrounding laminate analysis by introducing a companion to an existing laminate design tool that automates the generation of dynamic equations and produces simulation results via rendered plots and videos. We have validated the accuracy of the software by comparing the position, velocity and acceleration of the simulated mechanisms with the measurements taken from physical laminate prototypes using a motion capture system.

#### 3.1 Introduction

Robotics is a difficult field for non-experts to enter, as traditional robots are expensive to purchase and require a large amount of analytical skill and technical expertise to design, build, and field successfully. Recently, advances in lower-cost fabrication techniques have made easier for novices to prototype parts and mechanisms quickly and easily using laminate techniques[40, 65]. While manufacturing knowledge has

advanced due to new Computer-Aided Manufacturing (CAM) tools [66, 67], analyzing the motion and performance of such devices has lagged. This often involves understanding the dynamics involved with operating a robot in an unstructured environment – an advanced technique unavailable to many.

This chapter aims at outlining a general method for automatically determining the motion of laminate mechanisms with closed-loop kinematics while simultaneously solving for valid initial conditions. This goal is addressed in several thrusts. In Section 3.2 we describe the fundamentals of the simulation environment along with some of specific modeling decisions made and challenges solved.

Section 3.3 introduces an experimental procedure for obtaining dynamic parameters for the hinges in a simple system and introduces methods of modeling new hinges. Section 3.4 discusses our approach to confirming models with simulation. In Section 3.5, we discuss simulation and experimental results on an extrapolated design and conclude the chapter with thoughts on next steps and future work.

Laminate fabrication processes have made it possible for new generations of millimeter-scale, lightweight, and low-cost robotic mechanisms to be prototyped with ease [40, 65]. These multi-material, multi-layer devices typically feature flexure hinges – composed of Polyimide, Polyester, fabric, etc. – embedded in rigid laminate bodies, which, when exposed at joints, make it possible to create precise mechanisms that rely on material deformation to define the stiffness, damping, and thus, motion of the system. In previous work we introduced PopupCAD [67, 66], a design environment which automates the computations required to manufacture laminate devices. This tool permits object-oriented design methodologies and considers the constraints of laminate fabrication processing steps in order to produce manufacturable laminate cut files. We have also discussed some of the challenges associated with simulation in the past using PopupCAD to generate body and joint information [1], but not pro-



Figure 3.1: A 6-bar laminate mechanism. The experimental setup shows the use of OptiTrack cameras to record the motion of this mechanism.

vided a general solution for kinematics involving loop constraints, a topology often found in laminate systems.

The precision associated with fabrication and the assumption of pin-joint hinges permits many of these structures to be approximated as traditional mechanisms; a variety of work has been done for specific mechanisms to understand resulting kinematics of multi-bar closed-loop systems [68]. With these devices, however, material selection plays a significant role in deflection of these devices, as material bending at hinges can influence the stiffness and damping of the system as a whole [69]. Some approaches have used structural engineering methods to understand system stiffness and to solve the static force balances that these structures can accommodate given external loading [70, 71, 72], while others have looked at higher-order models for flexure hinges [73]. These approaches are useful for understanding quasi-static deformation,



as well as the linearized system stiffness of a given configuration.

Due to inertia, high velocities, and intrinsic damping and stiffness present in the joints, many of the devices being made must be considered dynamic. Kinematic and stiffness-based solutions are not sufficient to understand device motion. While deriving the equations of motion for laminates has been performed for specific devices [74, 75], less has been done to use the properties of laminate systems in order to understand and solve for the motion of devices in general. This is due to several reasons. First, since they are manufactured in a flat state, laminate devices begin in an inherently singular configuration and must be erected into a valid 3D shape on one side or another of a singularity, as discussed in [75].

Due to these singularities, laminate mechanisms often have multiple potentially valid configurations, which must be specified by the user or guessed by an automated system. In addition, laminate mechanisms often form parallel, multi-bar mechanisms. Such loop constraints are difficult to specify in general while maintaining valid and consistent initial conditions across singularities.

### 3.2 Model Generation

We have addressed the issues mentioned in the previous section by introducing a new suite of Python-based tools for simulating rigid-body dynamics in laminates. This functionality is designed to work with several other tools we have previously developed, specifically PopupCAD and Pynamics, a symbolic toolkit for generating equations of motion. Pynamics is particularly useful for several reasons. It can describe vectors using symbolic variables, take time derivatives of vectors in multiple reference frames, and can use Kane’s method to derive equations of motion symbolically. This gives more insight about mechanism motion than numerical methods because one can see the contribution of individual parameters to the evolution of each

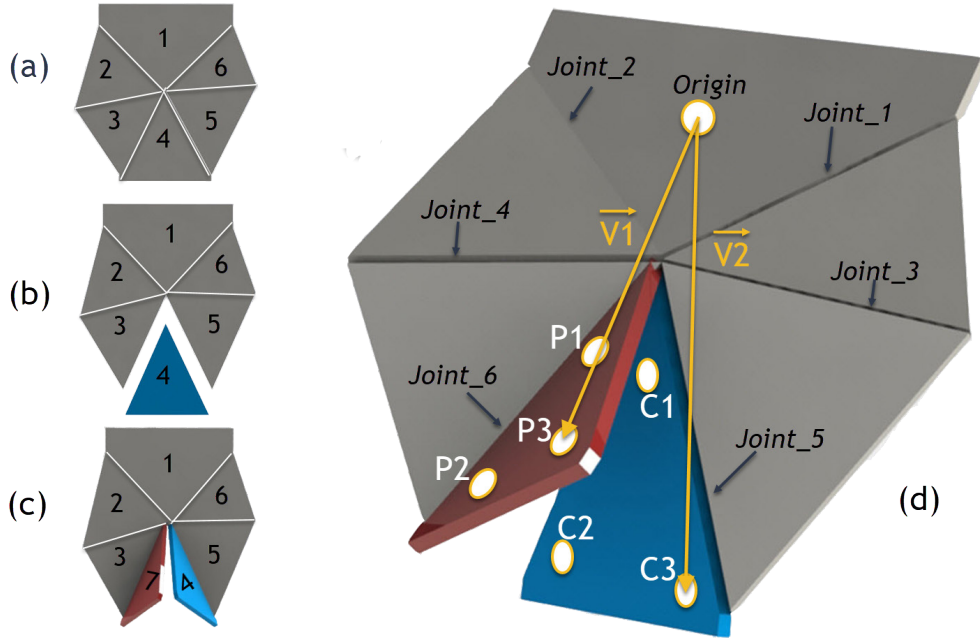


Figure 3.2: The schematic showing the steps for mathematically defining the closed-loop constraints.

state variable.

To merge the capabilities of PopupCAD and Pynamics, we have made the following additions. First, we have made it possible to read PopupCAD classes and extract rigid body information, as well as detailed joint information, making it possible to simulate a device drawn in PopupCAD. Second, we have added the capability to detect and handle open and closed-loop mechanisms automatically, a necessity for laminate devices. We have addressed strategies for determining valid initial conditions. And finally, we have made it possible to render the motion of laminate bodies directly to video or animate 3D motion within a Python-based GUI. Together, these innovations make it possible to simulate a wide variety of laminate mechanisms.

There are four steps required to simulate a laminate mechanism: (i) importing geometry data from PopupCAD, (ii) obtaining the dynamic model, (iii) adding kine-

matic constraints, and (iv) integration and solving.

### 3.2.1 *Importing from PopupCAD*

Dynamics receives geometry data and material properties of laminate layers from PopupCAD as a YAML file. Rigid bodies, hierarchical interconnections of bodies via rotational joints, fixed (Newtonian) bodies and material properties are stored in this file as Python-based classes after the YAML file is read by Pynamics. A hierarchical tree represents the network of connected mechanisms in which rigid bodies are the nodes and the joints connecting them are branches of the tree. Trees are good at representing serial chains of bodies, but do not adequately capture the topology of parallel mechanisms.

For such devices, we discuss adding closed-loop constraints in Section 3.2.3.

### 3.2.2 *Obtaining the Dynamic Model*

A reference frame is created for each body to represent its orientation in space with respect to its parent. The orientation of each body is defined with all axes initially aligned with the base frame. This frame is then rotated along a vector defined by two joint coordinates between the bodies, with  $q$  defining the angular displacement between the two. To clarify this, consider Fig. 3.2a which shows a 6-bar laminate mechanism with each body numbered from 1 to 6. We use this mechanism as a motivating example throughout the study due to its relative complexity, non-symmetric angles, and closed-loop topology. Body 1 is defined in PopupCAD as the fixed Newtonian reference frame. In this representation, body 1 is considered as the parent and body 2 and 3 which are connected to it are considered as the children of this parent. Body 1 is at the top of the hierarchy which is also called the first generation. All bodies connected to body 1 are considered as the second generation.

This hierarchy continues with one branch on the left which contains body 2 and 3, and another branch on the right which contains body 5 and 6. Body 4 is the last body in the hierarchy, which can be either connected to body 3 or 5 as shown in Fig. 3.2b. We describe how this body is treated in the next section while considering kinematic constraints.

### 3.2.3 Adding kinematic constraints and initial conditions

Kinematic constraints used to define the closed-loop mechanisms are introduced using scalar, zero-length constraints obtained from two vectors.

While there are many possible techniques, referring to Fig. 3.2 c, we create a dummy body 7 and attach it to body 3, assigning half of the mass and inertia of body 4 to it. The mass and inertia of body 4 should also be divided by half. In this way we have two rigid bodies attached to the ends of each serial chain that are meant to represent the same single body.

We express the position of three points on body 4 and seven as

$$\left(\vec{V}_2 - \vec{V}_1\right) \cdot \left(\vec{V}_2 - \vec{V}_1\right) = 0, \quad (3.1)$$

where  $\vec{V}_2$  and  $\vec{V}_1$  represent the distance from the origin to two similar points  $C_3$  and  $P_3$  on body 4 and 7, respectively. This comes from the fact that the coordinates of any point on body 4 measured from the fixed reference frame should match the coordinates of the corresponding point on body 7 measured from the same reference frame. A total of three equations representing three non-co-linear points are needed to fully constrain the position and orientation of the bodies together. For multiple loops, the process should be repeated for each loop of the mechanism. However, in this study we have considered mechanisms with only one closed loop, and cannot assume that our method will work without modification when extended to multi-loop

kinematic chains. Next, we add the forces resulting from springs, dampers, gravity and external torques acting on the joints, using parameters supplied by the YAML file. Initial conditions are provided as a vector containing the relative angle between each pair of connected bodies ( $q$ ) and their relative angular velocity ( $\dot{q}$ ). Therefore, in the case of the 6-bar mechanism the vector of initial conditions contains 12 elements. In Sec. 3.2.4 we describe our method for finding a valid set of initial conditions.

### 3.2.4 *Integration and solving*

Since joints in laminate mechanisms are created via flexible material layers, laminate mechanisms typically emerge from fabrication in a singular configuration. After fabrication, an assembly step typically erects a flat laminate into a three-dimensional shape. Resulting mechanisms are then typically constrained or operated in conditions which prevent singularities from occurring. However, for simulation purposes, a set of valid, non-singular initial conditions must be determined in order to integrate. Using a traditional Lagrange formulation to constrain closed-loop mechanisms in the presence of initial-value singularities is a problem, because the introduction of any non-zero initial value in state variables produces a permanent error in position constraints. To reduce this error and to deal with singularities simultaneously, we use Baumgarte’s method [76] which was developed further by Masarati [77].

Using constraint equations with Baumgarte’s method eliminates invalid initial value guesses over successive simulation steps, with the  $\alpha$  and  $\beta$  terms (introduced in [76]) behaving like a second order system to minimize error over successive integrations. Constraint stabilizing is controlled by  $\alpha$  and  $\beta$ -influenced terms, which simultaneously eliminate error and constrain the closed-loop mechanism.  $\alpha$  and  $\beta$  were determined by trial and error for the 6-bar mechanism studied in this study. For these parameters, 300 time steps are needed for the constraint error to approach zero

within desired tolerances.

Simulation of the mechanism occurs in two steps. First, is an initialization step during which the set of constraints are applied and the user provides an initial guess of the initial values. This can be a very rough guess about the value of one of the joint angles, as Baumgarte’s method will produce a valid configuration after sufficient cycles. During the simulation, our algorithm solves for all the angles and a valid configuration is reached eventually. Initial joint angles are used as the initial conditions for the first simulation step. The mechanism is then simulated for 900 time steps to make sure all the error has reached to zero. During this time, the mechanism reaches a valid non-singular configuration under the influence of gravity, joint forces, and initial-value constraints.

The final values of the joint angles from the first step are then fed into the second simulation and used as valid initial conditions to determine the motion of the mechanism. In this second simulation, Baumgarte’s method is not used to increase simulation speed. This is possible because initial error has been eliminated, and what little error gets subsequently introduced is negligible with respect to the valid configuration.

### 3.3 Hinge Characterization

This section describes tracking the motion of a simple pendulum in order to map design variables to stiffness and damping in a parametric hinge joint, for extending simulations to new and more complex systems. Because stiffness and damping are highly dependent on the geometry and material properties of joints, we obtained experimental values for the complex interaction between bending materials operating in real-world conditions where these devices are expected to be used. Doshi et. al [74] retrieves joint parameters by using spring and damping coefficients using a standard

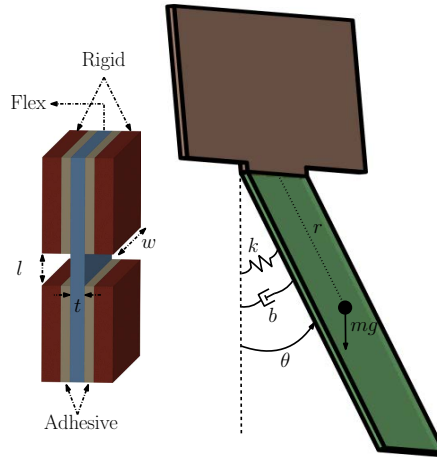


Figure 3.3: The proposed model of the hinge.

second-order system, and applies these to the hand-coded dynamics of a given five-bar mechanism in a vacuum. The methods used in this study work in air and extract model parameters using the dynamic model of our system described in Section 3.3.4. In addition, this study uses different material models in order to more closely match experimental data.

### 3.3.1 Experimental setup

Fig. 3.1 shows the experimental setup for motion data capture. Motion of the mechanism was recorded using two OptiTrack Prime 17W motion tracking cameras at 360 fps rate. Stiffness and damping coefficients were extracted by fitting a model to the recorded data. A variety of prototypes were made by varying the dimensions of the joint. The thickness of the hinge material was kept constant for all prototypes.

We used damped natural oscillations of a simple pendulum to extract damping and stiffness of a single hinge as its design is varied over several design parameters. A Fourier Series (FS) was fitted to each oscillation output and analytic derivations on the fitted FS were applied in order to obtain the angular velocity and angular

acceleration of the pendulum. This method is preferred due to the amplification of noise typically found in derivatives of digital position data.

The hinge layer used in this study was a uniform, rectangular flexible Polyester sheet with the thickness of 0.127 mm. The most important notations used in the characterization of the hinges in this study is shown in Table 3.1. Figure 3.3 illustrates the model considered for the hinges as a single pendulum oscillating, where,  $I_G$ ,  $m$ ,  $r$ , are inertia about the center of mass, mass and distance between center of mass and center of rotation, respectively.

Since the test was conducted in air, drag from the moving body added to the damping of the system. In order to achieve a more precise model, both the material damping  $b_m$  and air  $b_a$  damping was taken in account and the overall damping of the hinges  $b$  was calculated as  $b = b_m + b_a$ .

### 3.3.2 Material Test

As the flexible material has the most important role in hinge characteristics, a stress-strain curve was obtained experimentally for that material. The 0.127 mm-thick flexible polyester used to create flexure hinges was tested according to ASTM D882-12

Table 3.1: Hinge characterization Parameters used in this study

Design Variables	Notation	Dependent Variables	Notation
Hinge Width	$w$	Overall Damping	$b$
Hinge Length	$l$	Stiffness	$k$
Cross-sectional area	$a$	Air Damping	$b_a$
		Material Damping	$b_m$



standard for tensile properties of thin plastic sheeting [78]. Specimens were prepared according to this standard and tightened between two smooth, hard-rubber jaws of the tensile testing machine since serrated grippers created resulted in premature failure of the specimen.

A typical stress-strain curve for the hinge material is shown in Figure 3.4. A line indicating the linear region is shown in red. The toe compensation was made based on the standard in order to remove the effects of take-up of slack and alignment or seating of the specimen at the start of the movement of the jaws. The test was repeated for 11 specimens and the average Young's modulus and yield stress obtained was 4383.27 MPa and 42.84 MPa respectively. Using the yield stress calculated from tensile tests, and referring to the Eq. 3.2, we calculated the maximum allowable load  $F_{max}$  that can be applied to the cantilever beam before it goes under plastic deformation. Having  $F_{max}$ , we then calculated the maximum allowable deflection  $\delta_{max}$  and angle  $\phi_{max}$  using

$$F_{max} = (\sigma_{max} \times b \times t^3)/(6L) \quad (3.2)$$

$$\delta_{max} = (F_{max} \times x^2 \times l)/(2EI) \quad (3.3)$$

$$\phi_{max} = (F_{max} \times x \times l)/(EI). \quad (3.4)$$

The maximum allowable angle of deflection in order to remain in the linear region of the stress-strain curve is 1.96 degrees. The variation in joint angles in real laminate mechanisms are much higher than this value. Therefore, the material used as the flex layer undergoes nonlinear deformation which is considered as a source of error in the analysis of the system.

### 3.3.3 Repeatability Test

As the material shows high nonlinearity in the range of use in our designs, we were interested in understanding the repeatability of the physical system. Figure 3.5

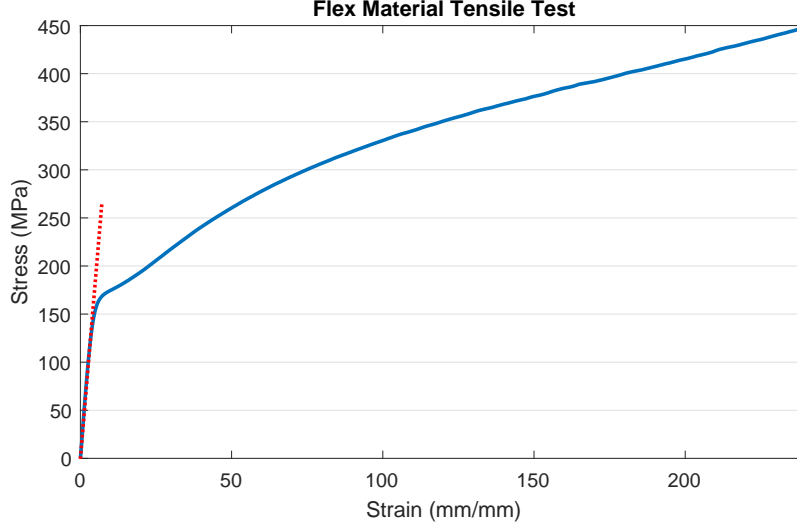


Figure 3.4: Flex layer material tensile test.

depicts the rotation of a laminate pendulum in three tests conducted minutes apart. As shown in the figure, although the oscillations seem close, small differences can be seen in both amplitude and wavelength. In order to provide better insights, the experimentally-derived values of the  $k$  and  $b$  are shown in Table. 3.2. These values were using the methods presented in Section 3.3.4. Based on this data, a considerable noise may be expected in the physical system. To reduce this effect, data from 5 tests were considered for each design.

### 3.3.4 Modeling Single Pendulum System

A single pendulum has been chosen in order to model the oscillation of a simple hinge (Fig. 3.3), as mentioned previously. Moreover, a set of torsion springs and dampers were considered to model the effect of  $k$  and  $b$ . Based on the following model, the equation of motion of a simple hinge can be written as

$$(I_G + mr^2)\ddot{\theta} = -k\theta - b\dot{\theta} - mg\sin(\theta) \quad (3.5)$$

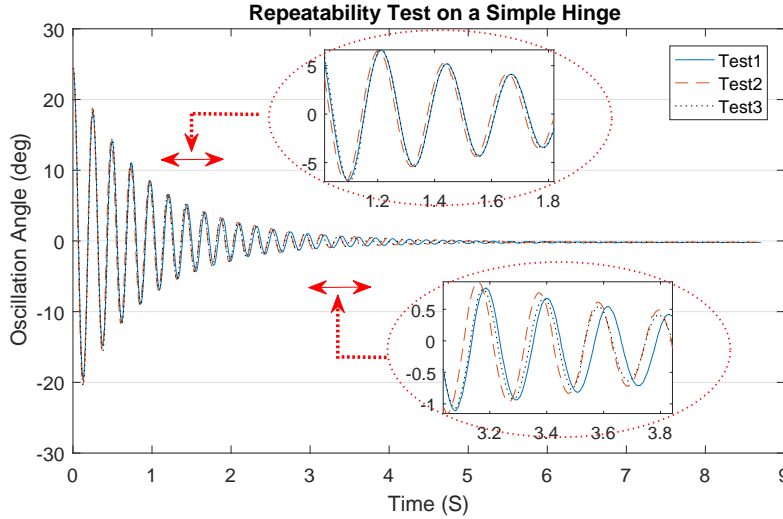


Figure 3.5: The repeatability test in behavior of a simple hinge.

Where the variable notations are consistent with fig. 3.3. Values of all parameters in (3.5) except the stiffness and damping coefficients of the system are provided by either experimental data ( $\theta$ ,  $\dot{\theta}$  and  $\ddot{\theta}$ ) or are extracted from models in PopUpCAD ( $I_G$ ,  $m$  and  $r$ ). A least-squares identification method was used in order to obtain the values of  $k$  and  $b$ . Studying the change in values of the latter criteria by design parameters and finding simple models to explain them is the subject of what follows.

### 3.3.5 Identification of Damping Coefficient & Stiffness

Factors that cause damping and stiffness consist of the hinge layer material being stretched and compressed in oscillation of the hinge. As a result, hinge width and length have play a large role on the latter criteria. For damping, as well as material damping ( $b_m$ ), drag experienced by the body increases the overall damping  $b$  of the system, slowing the system and reducing oscillations faster than when in a vacuum. As air damping can be affected by the cross-sectional area of moving links, it is an important phenomenon to model.

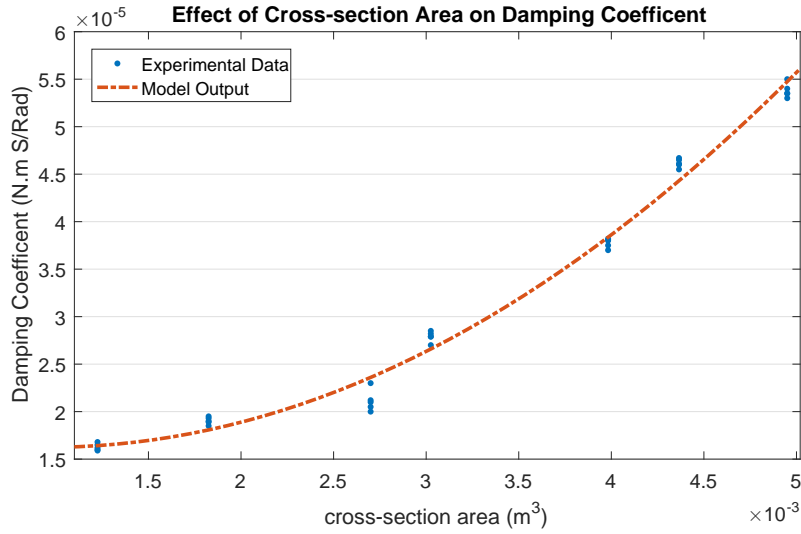


Figure 3.6: The effect of different cross-sectional area on damping coefficient.

### Effect of Air-damping

The effect of air damping was studied by using seven designs where moving bodies had constant hinge designs but differing cross-sectional area. The effect of changing mass due to cross sectional area was accounted for by the  $m$  fed into the simulation for each design. Figure 3.6 depicts the change in the damping coefficient when the cross-sectional area of the moving body is changed. Based on the data, by decreasing cross-sectional area, damping coefficient also decreases. The behavior the system can

Table 3.2: The repeatability test results in hinge characteristics.

Number of Test	Stiffness $k$	Damping Coefficient $b$
1	0.067	$2.791 \times 10^{-4}$
2	0.0701	$2.974 \times 10^{-4}$
3	0.0688	$2.894 \times 10^{-4}$

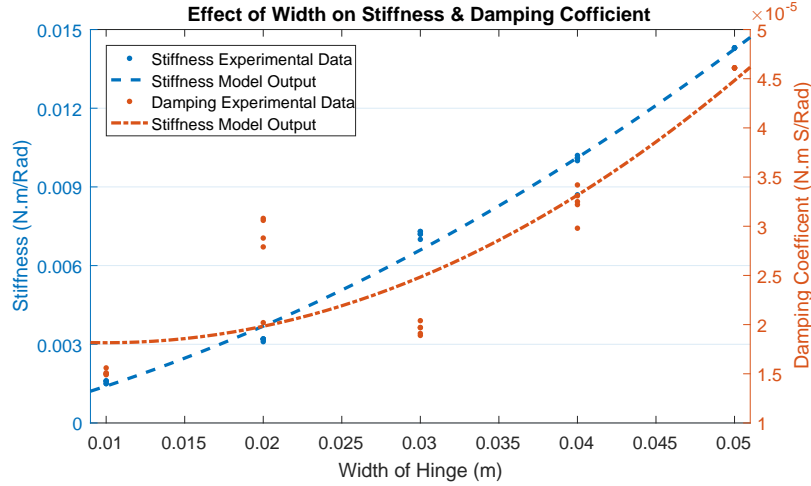


Figure 3.7: Effect of hinge width on damping coefficient and stiffness of the hinge.

be described by following second-order model fitted to the experimental data

$$b = 2.34 \times a^2 - 0.0042 \times a + 1.8e - 5 \quad (3.6)$$

### Effect of Hinge Width

In order to study the effect of hinge width on the value of  $k$  and  $b$ , five specimens with same body design (same cross-sectional area) were built and experimentally tested. In order to minimize the effect of torsion across a wide range of hinge widths, smaller-width hinges were designed with gaps in the middle and constant exterior dimensions across all designs. Figure 3.7 depicts the effect of the hinge width on  $k$  and  $b$ . The second order model for damping and stiffness is given by

$$b = 0.0166 \times w^2 + -3.3197e - 4 \times w + 1.9812e - 5 \quad (3.7)$$

$$k = 3.0857 \times w^2 - 0.1361 \times w + 0.0003 \quad (3.8)$$

Based on the obtained results, an increase in the width of the hinge will increase the damping coefficient and stiffness of the hinge.

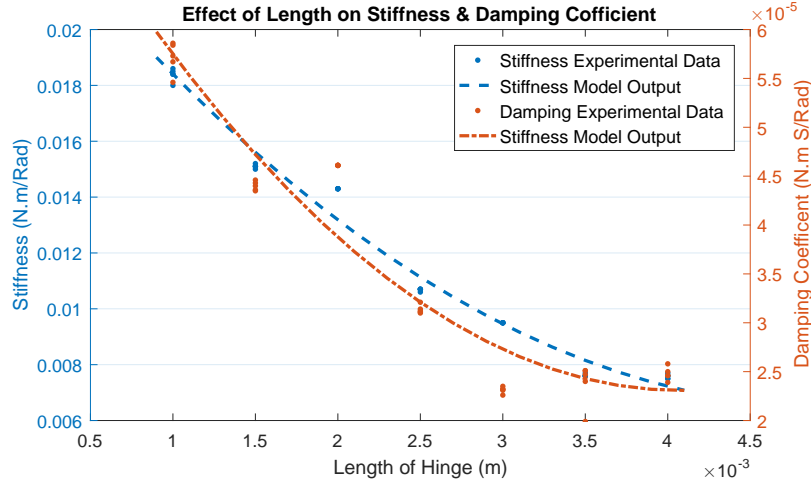


Figure 3.8: Effect of hinge length on damping coefficient and stiffness of the hinge.

### Effect of Hinge Length

The effect of hinge length on  $k$  and  $b$  was studied across five specimens where the total hinge length was increased (Fig. 3.8) which resulted in second order models given by

$$b = 3.6381 \times l^2 - 0.0297 \times l + 8.3506e - 05 \quad (3.9)$$

$$k = 746.6667 \times l^2 - 7.4590 \times l + 0.251 \quad (3.10)$$

The obtained results show a decrease in the value of the damping coefficient and stiffness as length increases.

### Comprehensive Model

A comprehensive model was developed which takes into account all three variables ( $l, w$ , and  $a$ ), permitting one to estimate joint properties throughout a three-dimensional design space. Figures 3.9a and 3.9b depict the predicted  $b$  and  $k$  values vs the exper-

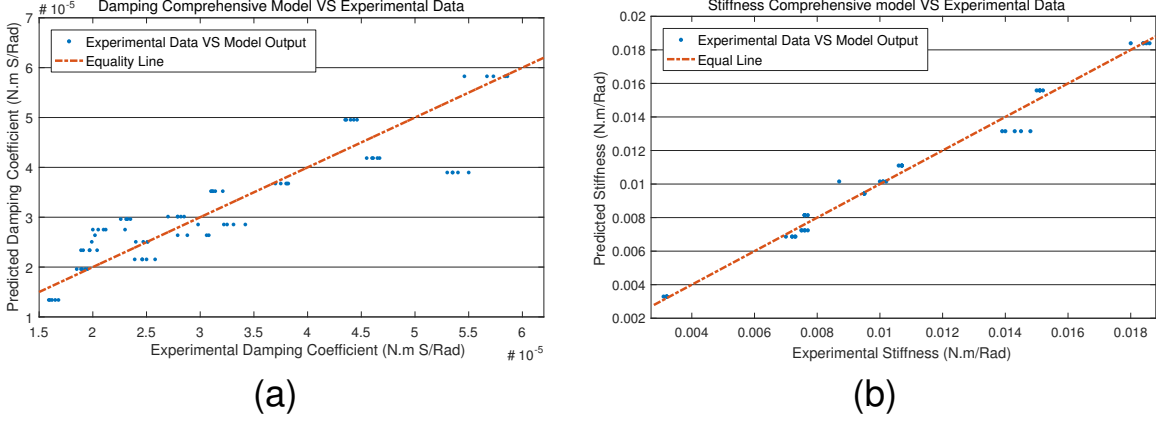


Figure 3.9: Comparison of the experimental and modeled hinge damping coefficient (a) and stiffness (b).

experimental values obtained for all specimen.

$$b = -0.8565 \times a^2 + 0.0129 \times a + 2.0822 \times l^2 - 0.227 \times l + 0.0408 \times w^2 - 0.0023 \times w + 5.0855e - 5 \quad (3.11)$$

$$k = 762.5397 \times l^2 - 7.5305 \times l - 1.4444 \times w^2 + 0.4298 \times w + 0.0073 \quad (3.12)$$

The obtained model for  $b$  has  $2.39e^{-6}$  (4.01%) as the Mean Absolute Error (MAE), while  $k$  values obtained model has  $2.59e^{-4}$  (1.39%) as MAE.

### 3.4 Model Verification

In order to evaluate the output of the Pynamics in comparison to experimental data, a complex case-study was proposed. Models obtained from hinge characterization were used on a six-bar linkage and simulated in Pynamics, as well as prototyped and tested experimentally, then compared against each other. Experiments were conducted in air, which, as previously seen, this could lead to high variability test-to-test. However, it also permits the effect of air to be studied, bringing our hinge models

closer. As discussed in Section 3.2, in order to verify the simulator, a 6-bar spherical mechanism was considered as the case-study (Figs. 3.1 & 3.2).

In order to sample data from mechanism oscillation, the mechanism was positioned in a known initial configuration, released, and allowed to settle into a final static configuration. While sampling experimental data from the single pendulum was straightforward, the data provided by the cameras for this case study demands additional data processing. Motion-tracking cameras require three markers to be mounted to each rigid body. Thus, in order to get the information of position and orientation all the bodies, 18 markers were used to determine the 6 rigid bodies of the mechanism. Marker position and mass information was added to PopupCAD as an additional 2D material layer in order to account for the added inertia.

The raw orientation data provided by the cameras were based on quaternions. In other words, data received from the cameras and Motive SDK were represented as unit quaternions for each rigid body. Since the joint axes for several of the bodies change with respect to the base frame, standard quaternion operations were used to retrieve the angle and axis of each joint over time and compared against the simulation [79]. This was done in order to produce consistent results across the simulation – which reported state variables as the angles between adjacent bodies – and the experiment – which reported the quaternions of each body with respect to the base frame.

The relative quaternion between two adjacent reference frames ( $q_{D_i}$ ) has the following relationship with quaternions of  $i$ th body ( $q_i$ ) and  $(i + 1)$ th body ( $q_{i+1}$ ):

$$q_{D_i} = q_{i+1} * q_i^{-1} \tag{3.13}$$

where,  $(*)$  is quaternion multiplication [79]. As implemented in code, the obtained angle of rotation using the formulation of [79] was always positive and did not change sign when the relative frame displacement went negative; instead the axis of



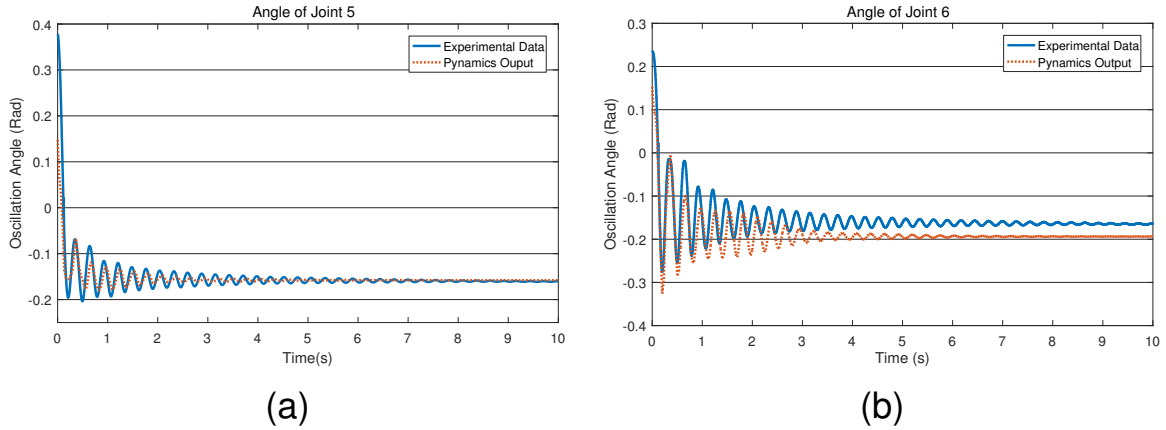


Figure 3.10: Dynamics output verification based on 6-bar mechanism. (a) Dynamics performance regarding  $\theta_5$ . (b) Dynamics performance regarding  $\theta_6$

rotation changed direction. Therefore, in order to achieve a consistent axis and angle of rotation across all time, the direction of the axis was continually monitored so that when the direction of the vector flipped, the rotation angle was negated too.

### 3.5 Results & Discussion

Figure 3.10 illustrates the comparison between simulated and experimentally-recorded joint angles attached to body 4 of the mechanism in Figure 3.2. Despite some error, the simulation was able to properly predict the dynamic behavior of the end effector. In particular the amplitude and wavelength of oscillations were well predicted for  $\theta_5$  and  $\theta_6$ . Table 3.3 compares all of the mechanism's predicted equilibrium angles against experimental data. Small differences between modeled and experimental equilibrium configurations can be seen in this table, as well as in the dynamic plots in Figure 3.10. This is partly due to our experimental method – we used dynamic data to estimate damping and stiffness rather than steady-state force/displacement balances. In addition, material creep, non-uniform material thickness, viscoelastic behavior, and operating in the non-linear part of the stress/strain curve are other

Table 3.3: The equilibrium position of Pynamics output and Experimental results in 6-bar mechanism

Joint	Pynamics (rad)	Experimental data (rad)
$\theta_1$	0.280	0.398
$\theta_2$	0.056	0.113
$\theta_3$	0.431	0.502
$\theta_4$	-0.470	-0.737
$\theta_5$	-0.157	-0.161
$\theta_6$	-0.193	-0.166

significant reasons why this deviation may be present.

In this study, we have developed a suite of tools which permits the dynamic simulation of laminate mechanisms by solving several challenges common across laminate devices. The resulting code integrates well with existing tools, now making it possible for a novice user to easily and quickly generate manufacturing files that are ready to be sent to machining tools with assurance that a design will work. This can help eliminate time consuming and expensive prototyping trials which are otherwise needed to validate designs without the proper analysis. While we have verified our simulations by comparing them to experimental results obtained from a simple pendulum and a spherical 6-bar mechanism, a variety of other open and closed loop designs can be simulated as seen in the accompanying video. This verifies that the automatic generation of closed loop mechanism dynamics is feasible and accurate across a wide variety of designs that are extracted from sketched mechanisms in PopupCAD.

We have characterized the hinges that are an essential part of laminate mechanisms

and extracted the stiffness and damping parameters which are needed for our dynamic simulation environment. Our characterization method is simple and repeatable and therefore can be used to characterize other flexible materials used to manufacture the hinges. We have taken the effect of air damping in our model since many of the laminate mechanisms are operated in air and this makes our simulation results closer to real working conditions of these mechanisms. The hinge parameters can be extrapolated to any new hinge design with different length, width and cross-sectional area.

Our simulation environment automates the task of generating symbolic equations of motion, integrating and solving those equations, and generating numerical and visual output. We have considered laminate mechanisms consisting of serial chains and one closed loop. Future work will include mechanisms with more than one closed loop, topological optimization of kinematics for faster simulation, considering contact between mechanisms and the ground, as well as making it possible to integrate closed-loop controllers into the simulation.

While the use of Baumgarte’s method to eliminate initial-value errors was effective, it requires manual selection of  $\alpha$  and  $\beta$  terms. We hope to migrate to techniques which do not require manual tuning in order to eliminate parameter selection in the future.

Material tests showed that we were using flexure material outside of its linear regime. Further testing is required to determine if the stresses involved would lead to premature failure of these hinges. Future mechanisms may resort to fabrics or thinner materials to minimize stresses in flexure hinges.

With those future improvements, we see this tool being used to assist novice robot designers by optimizing suggested kinematics based on stated performance goals which are then confirmed through simulation. Ultimately, we hope this tool helps to connect design and analysis for novices to make it possible for them to design,

simulate, and prototype complex robots for tasks in unstructured environments.

## Chapter 4

### COMPENSATION OF MATERIAL DEFORMATION USING ADAPTIVE CONTROLLER (CASE STUDY OF 2-DOF SPHERICAL PARALLEL MECHANISM)

In this chapter, we address how to deal with the challenges of working with large scale foldable manipulators using a foldable two-degree freedom spherical parallel robot manufactured with laminated techniques as a motivating example. The slender links typically used within foldable, origami-inspired, and laminate mechanism designs are highly susceptible to deformation under external loading, especially at centimeter scales. At millimeter scales and smaller, laminate devices may often be considered rigid due to dimensional scaling laws, but at larger scales foldable mechanisms enter the territory of soft robots. We show how material deformation under load affects the performance of the robot moving throughout its workspace. We use a supervised deep neural network to model and compensate this deformation; for that, we introduce a workflow to experimentally tune the hyper-parameters and train the deep neural network. Then, we propose using transfer learning between two deep neural network for a closed loop control that uses on-line training to adapt to new deformations. Finally, we experimentally validate its ability to compensate for material deformation when different loads are applied to the robot's end-effector as well as highlighting the efficiency of this workflow in modeling inverse kinematics. Using this procedure, we successfully obtain a closed-loop controller that keeps mean absolute path tracking error under 7 percent across the desired path's corresponding Euler

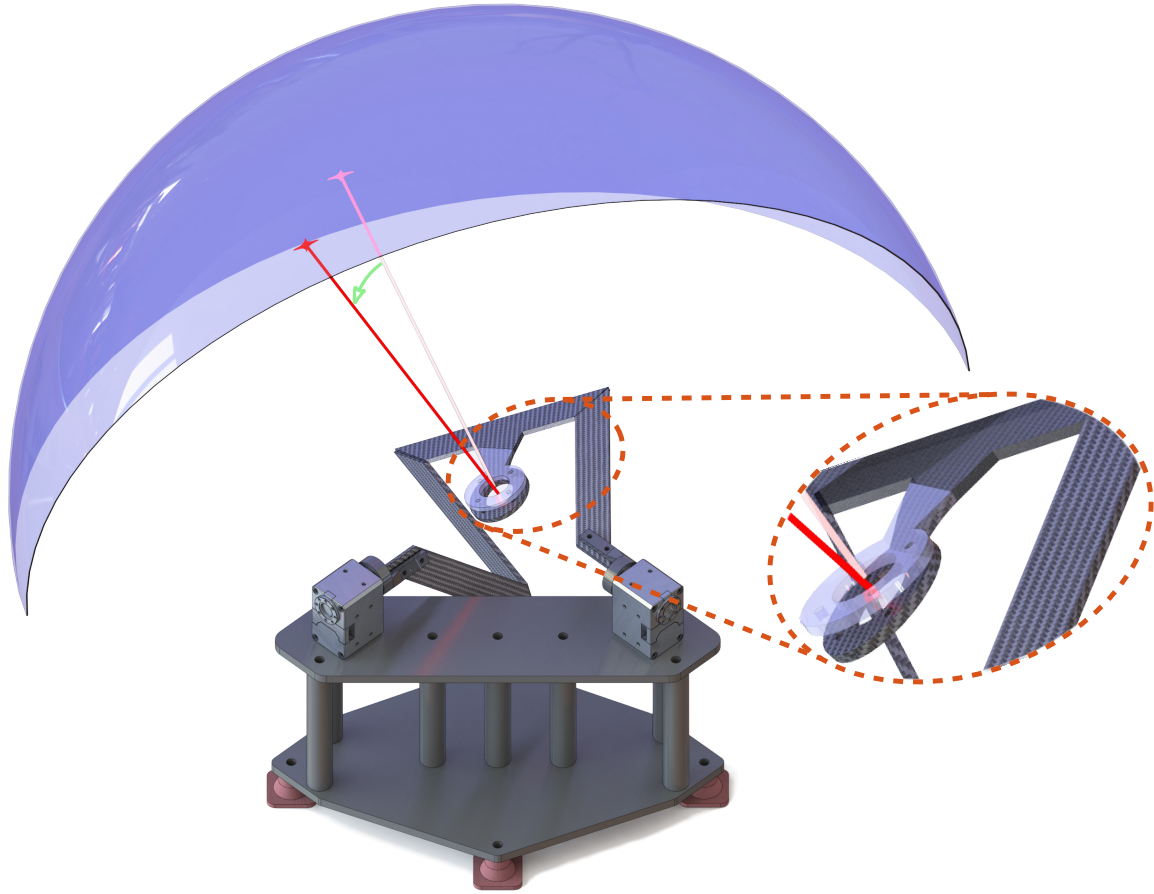


Figure 4.1: Poor efficacy of a laminated 2-DOF parallel mechanism caused by its end-effector deflection.

angles.

#### 4.1 Introduction

Laminate fabrication techniques provide an affordable and rapid alternative to traditional rigid robot prototyping, and have been applied in a variety of micro- and millimeter-scale robotic mechanisms. However, the use of long, slender beams within laminate systems can produce significant amounts of error in end effectors, even when stiffer materials are employed. To address this, parallel mechanisms have often been used in laminate designs to stiffen the devices and permit actuators to be mounted

proximally – lowering end effector load. Despite the improvements in stiffness, in the case of higher loads and larger dimensional scales, traditional kinematic formulations that neglect link flexibility will be insufficient for describing system motion.

The same phenomenon is observed in the field of soft robotics, where computational solutions to the problem of controlling the end effector location under load are based upon subdividing the material into finite number of small elements, which can often lead to a reduction in performance caused by higher computational cost. This has been solved by creating reduced-order Finite Element Analysis (FEA) models which have a limited number of cases been used within controllers. Still however, this is an expert tool in which the order of model reduction affects the precision and relies on domain expertise in order to successfully implement and optimize them on each new design [80, 81, 82, 83].

In contrast with the approaches used to solve soft robotic control problems, the goal of this study is to investigate alternative strategies that simultaneously allow us to represent and solve for the complex inverse kinematics of parallel mechanisms and the position error due to defamation under load for moderately-compliant laminates. This is possible because the motion of laminate robots is still primarily dictated by the geometric relationships of flexure hinges rather than the deformation of stiffer links, making traditional, rigid-link models a good starting point for representing these mechanisms.

In this study, we present a data-driven modeling and control approach for compensating for material deformation and flexibility in large-scale laminate robots under load. By proposing a workflow, we investigate the proper structure for putting a controller together using Deep Neural Networks (DNNs), as well as the impact of different hyper-parameters on the accuracy and precision of our results. We, then, close the control loop by adding a second DNN in the feedback loop and using online training

and transfer learning between two DNNs with the same optimal hyper-parameters. This enables the controller to adapt to new deformation under different loading conditions. Using a 2-DOF parallel mechanism we show how the mechanism performance is negatively impacted under external load in a potential application of a pointing task, e.g. a laser pointer (Fig. 4.1); we then propose a workflow to obtain a closed-loop controller to increase closed-loop system performance.

Soft robots offer the potential to extend the benefits of robotics to applications that have not previously been approachable with rigid robots [84]. However, further progress in the field of soft robots will also increasingly depend on advancements in feedback control, machine intelligence, and computational modeling since the conventional methods in control are not applicable to soft robots with infinite number of degrees-of-freedom [2]. A number of different control approaches have been proposed and validated. One of the most precise approaches is using FEA. In [15], model order reduction of FEM using snapshot proper orthogonal decomposition is proposed in order to achieve a reduced-order model with lower calculation effort. Piecewise Constant Curvature (PCC) approaches are vastly used in numerous studies to model the configuration of soft robots. A linear time-varying Gaussian model is proposed in [16] for dynamic modeling. This model alongside an LQR based Gaussian controller and a Kullback-Leibler divergence policy is used to command the robot's end-effector to a desired point after several iterations while taking care of both dynamics control and path planning. A soft robotic arm driven by a SMA coil is controlled in [19] using PID controller when the curvature is measured using Hall sensors under assumption of constant curvature of each segment. Santina et al. dynamically controlled a planar soft robotic arm while it is interacting with the environment by choosing a PCC approach and modeling each segment by a rigid limb [17]. The study is extended to 3D by modeling each segment with a rigid limb in [18]. In both cases the masses,



stiffnesses and damping coefficients of each limbs must be experimentally identified. A variable length multi-section continuum method is proposed and experimentally validated in [25, 26] A combination of PCC and FEA model-reduction policy is proposed in [14]. Obtained results show that the combined policy is more precise than PCC and faster, but less accurate comparing with FEA. Our strategy is to propose a data-driven approach that has lower computation cost and can achieve higher control frequency while no being effected by larger deformation under loads. Moreover, since laminated robots can be used in conjunction with common actuation strategies such as servos, we can avoid the complex dynamics massociated with modeling pneumatic systems.

Parallel mechanisms are an attractive approach to designing laminate foldable systems. Parallel mechanisms take advantage of multiple pathways to the ground, often making them more rigid and precise than their serial counterparts. Moreover, parallel robots are usually capable of achieving higher speeds due to the fact that actuators can be proximally mounted on the fixed chassis, reducing loads on distal joints. These benefits make parallel mechanisms a rich area for research. Specific implementations include the Gough-Stewart platform [48, 49], 3RRR Parallel Planar Robot [51, 52], and the 2-DOF spherical parallel manipulator [47], which is the case study for this research. Many studies are conducted on this mechanism’s workspace optimization [55, 56], singularities[57], and forward and inverse kinematics [47, 58] and dynamics. This mechanism has also been the basis for camera stabilization [59] and object tracking [60] applications. While none of the research on this particular mechanism includes soft robots, they are proof of the general usefulness of this manipulator.

While there are many construction methods for manipulators, few studies use laminating techniques for making high degree-of-freedom robotic manipulators. Some

recent exceptions include the delta robots presented in [37, 38]. These studies focus on high-speed manipulators at the millimeter and centimeter scales, respectively. Laminate fabrication techniques have already been applied to a broad number of kinematic applications, as well. Planar four-bar mechanisms have been demonstrated in flapping-wing applications [39], 5-bar spherical linkages have been previously used to drive 2DOF leg joints in micro-robotic walking applications [40], and linear motion has been enforced using Sarrus linkages in linear actuators [41] and assembly scaffolds [42].

Neural Networks (NN) have been used to solve a variety of complex problems across a number of fields. Many attempts have been made to apply neural networks to control problems, such as the control of complex, nonlinear plants such as underwater vehicles [85], ships [86], and robotic manipulators [87, 88, 89, 90]. Given the complexity of these nonlinear systems, traditional linear models are often inadequate for system identification and modeling. Neural networks have the capability to characterize those nonlinear relationships directly through the data during the learning process. The results from those attempts have demonstrated the validity of the NN-based adaptive control.

While neural networks have been studied in depth for analyzing both forward kinematic and inverse kinematic problems of rigid robots [91, 92, 93], to the knowledge of authors, NN-based closed-loop control has not yet been introduced for analyzing and compensating the material deformation in foldable or soft robots.

## 4.2 Workflow

The workflow introduced in this study focuses on compensating for error caused by material deformation in foldable robots using DNN. In this workflow, as seen in Fig. 4.2, we also include insights for tuning DNN hyper-parameters to enhance

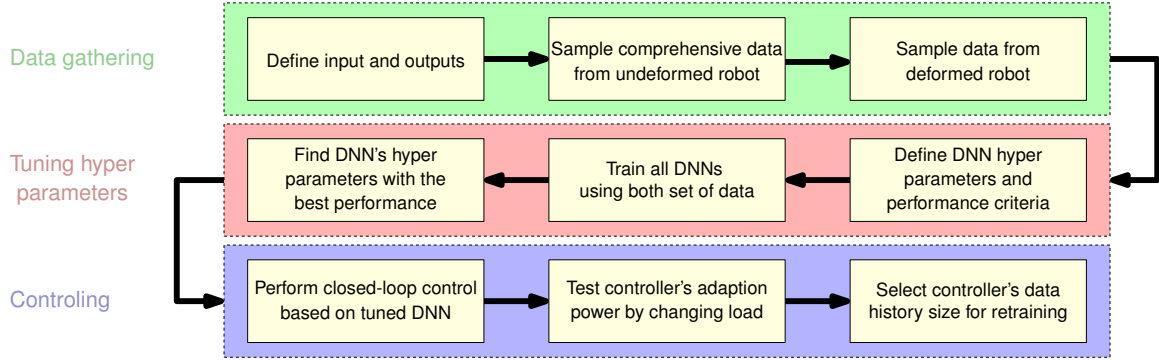


Figure 4.2: **Diagram of the Proposed Workflow**

compensation for material deformation when the system is under load. We propose using the “retraining estimation error” and “retraining time” as the criteria for tuning DNN hyper-parameters such as the “number of hidden layers”, “activation function”, and “optimization solver”. In the proposed workflow, we propose sampling two sets of data from the foldable robot’s inputs and outputs. The first set is a large, comprehensive set of data of the undeformed robot while it is moving through a large portion of its workspace. The second set of data is sampled from the deformed robot. This set is sampled in order to be used in the evaluation of the learning algorithm’s ability to adapt to the material deformation in transfer learning; thus, it can be smaller in size compared to the first set of data. Each set of data is then divided into two subsets of training and test data. The training data is for training the DNN, and the test data is used to evaluate the trained model’s performance.

Among the hyper-parameters of a DNN, our current workflow focuses on selecting the number of hidden layers, activation function, and optimization solver. While the workflow can be extended for other hyper-parameters such as learning rate ( $\alpha$ ), these three hyper-parameters are selected to reduce the study’s complexity and ease its flow. In order to select the best DNN hyper-parameters for modeling the robot’s behavior, the three-dimensional space of these hyper-parameters are spanned in or-

der to evaluate the DNN performance regarding the criteria of estimation error and retraining time.

For each set of hyper-parameters, the DNN is first trained based on the initial set of undeformed motion data. Then, the pre-trained weights are used as to retrain the DNN with the second set of data sampled from the deformed robot. In this workflow, the DNN is retrained several 20 times and the overall retraining time and estimation error of the final DNN are recorded as the DNN retraining time and estimation error, respectively. By repeating the retraining numerous times, we increase the chance of finding the set of DNN hyper-parameters that are most resilient to overfitting. By following these steps, we obtain a DNN-based model that provides the best estimation and is able to retrain and adapt to material deformation in the shortest time while avoiding overfitting.

In order to achieve a high-performance controller, the DNN retraining history – the number of historical samples used for retraining – must also be tuned in order to increase the adaptability of the controller minimize while avoiding overfitting. A larger retraining history increases the adaptation time when a new material deformation occurs but also increases the retraining time and estimation error for robots with complex or non-linear behavior. Smaller retraining histories are insufficient to learn the effect of material deformation, and results in overfitted models incapable of controlling the robot through its whole workspace. Hence, the final step of the proposed workflow is dedicated to experimentally evaluate the performance of the selected DNN in controlling the deformed robot across different retraining history length. We propose considering the “estimation error” and “overfitting issue” as the criteria for tuning the DNN retraining history parameter.

It should be mentioned that the above workflow can be used to effectively model the error between the analytic model of the undeformed foldable robot and the de-

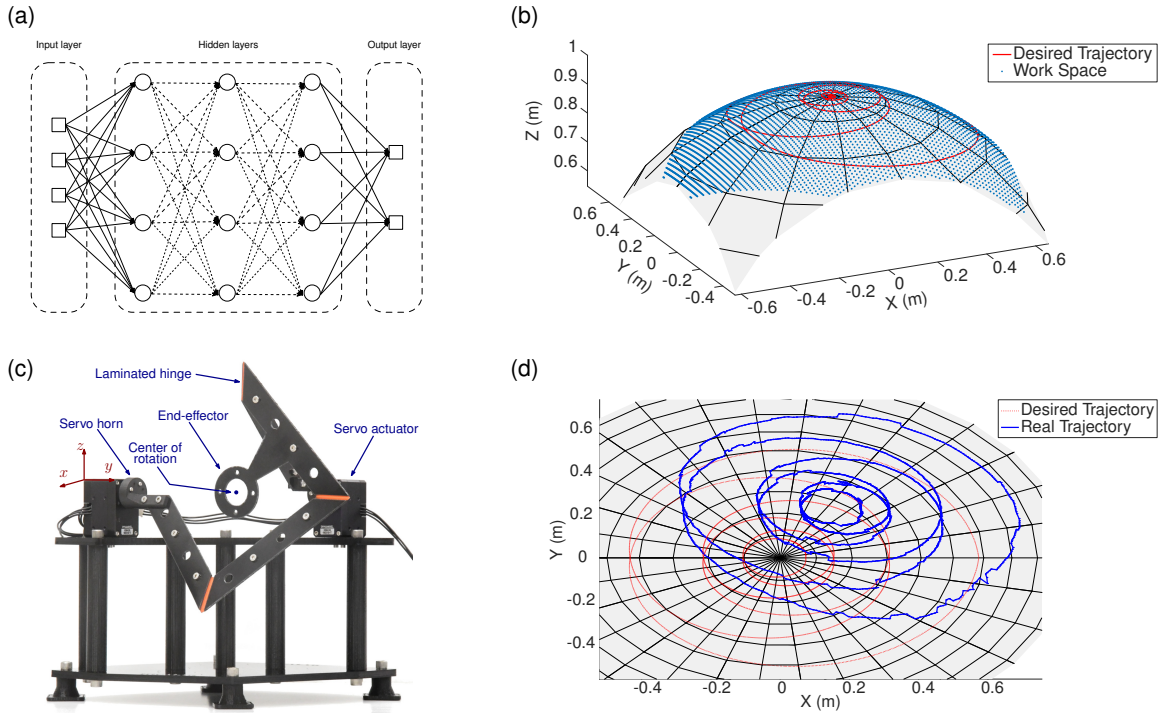


Figure 4.3: **The case study of 2-DOF Spherical mechanism** (a) DNN structure. (b) Robot workspace and the proposed spiral path. (c) Final prototype. (d) Path tracking with open-loop commanding.

formed robot or the overall behavior of the foldable robot. In this study, we have experimentally shown that the proposed workflow is able to provide a controller for a foldable robot by estimating either the material deformation error and the non-linear inverse kinematics.

### 4.3 DNN hyper-parameters

Many neural networks (Fig. 4.3a) utilize the back propagation algorithm for training. The ability to use non-linear activation functions in DNN makes it different from a linear perceptron. Training a NN consist of series of forward and back propagations. The forward propagation estimates the output of NN. With back propagation,

input data is repetitively fed back into the neural network and the error is established by comparing the desired output with the input. This error is then fed back to the neural network to adjust the weights and bias ( $W^T$ , and  $b$ ) so that the error can be reduced and the desired output can be reached. One important hyper parameter of DNN is its neurons activation functions. In this study, the following functions have been studied as the Neural network layers' activation function:

$$\text{Identity: } f(x) = x \quad (4.1)$$

$$\text{Logistic sigmoid: } f(x) = \frac{1}{1 + \exp^{-x}} \quad (4.2)$$

$$\text{Hyperbolic tan: } f(x) = \tanh(x) \quad (4.3)$$

$$\text{Rectified linear unit function: } f(x) = \max(0, x) \quad (4.4)$$

Other important hyper-parameters include the number of hidden layers and the algorithms selected for optimizing weight. In this study, two different algorithms have been evaluated: (i) the quasi-Newton algorithm of Limited-memory Broyden-Fletcher-Goldfarb-Shanno (LBFGS) [94], and (ii) Adam: A method for stochastic optimization [95].

In order to maintain the chapter's flow and reduce complexity, we decided to search only within the three-dimensional space of the above parameters for an optimal set of hyper-parameters. We subsequently fixed the learning rate ( $\alpha$ ) to a small value and considered the number of neurons in all hidden layers consistent with the number of neurons of the input layer (Fig. 4.3a).

#### 4.4 2DOF Spherical Parallel Mechanism

In this study, a 2DOF spherical Parallel Mechanism has been selected as the case study due to its highly non-linear but easily formulated inverse and forward kinematics. This mechanism has already been introduced as two degree-of-freedom

spherical orienting device in [64, 61], and based on kinematic synthesis analysed by Ouerfelli et al. that maximizes the workspace of the mechanism [55].

The device has been constructed using a laminate fabrication process, similar to [96, 42]. The final prototype has been built using 0.03-inch fiberglass sheets as rigid layer and 0.005-inch polyester sheet as a flexible layer. A heat-activated acrylic adhesive from Drytac<sup>1</sup> has been used to bond layers. Figure 4.3c depicts the final prototype. Two XM430 Dynamixel DC servos are used as actuators. Two custom-made Nylon 3D-printed horns are responsible for attaching and aligning mechanism hinges to servos. The servo horns act as a safety coupling in the mechanism. The chassis has been built from acrylic and 3D printed parts.

#### 4.4.1 Inverse Kinematics

Considering the manipulation described in Fig. 4.1 and based on global axes' alignment with servos, the inverse kinematics can be written as:

$$\theta_{a_1} = \tan^{-1}\left(\frac{N_Y N_Z}{N_X^2 + N_Z^2}\right) \quad (4.5)$$

$$\theta_{a_2} = \tan^{-1}\left(\frac{N_X}{N_Z}\right) \quad (4.6)$$

where  $\theta_{a_i}$  are the analytic actuator angles and  $N_k$  are the components of the unit vector perpendicular to the end-effector body. In the case of  $N_Z = 0$ , the values of theta are as follows:

$$\theta_{a_1} = 0, \quad \theta_{a_2} = \pi/2 \quad (4.7)$$

---

<sup>1</sup>[www.drytacstore.com](http://www.drytacstore.com)

#### 4.4.2 Forward Kinematics & Workspace

Accordingly, the forward kinematics of the robot can be formulated as:

$$N_Z = \sqrt{\frac{1}{(t_1 + t_1 t_2)^2 + t_2^2 + 1}} \quad (4.8)$$

$$N_X = t_2 N_Z \quad (4.9)$$

$$N_Y = (t_1 + t_1 t_2) N_Z \quad \text{where, } t_i = \tan(\theta_{a_i})_{\{i=1,2\}} \quad (4.10)$$

By using the above set of equations, the workspace of the robot has been obtained, and a spiral path has been tuned to be inside the workspace of the robot (Fig. 4.3b). The spiral is used to fully traverse the workspace; it is obtained by projecting the normal vector of the end-effector on a sphere with 1 m radius. This spiral has been used through this study as the desired path for tracking. In order to be able to continuously repeat the test, the spiral has been defined to go out and come back into the same point on the workspace sphere.

#### 4.5 Tuning DNN hyper-parameters

As mentioned in the workflow, the first step is to define the input and output of the system. The first goal of our case study is to model the effect of material deformation on the robot's inverse kinematics. The input and output of the model for learning the deformation error have been defined as the quaternion of the end-effector rotation ( $q$ ) and the servos angles' compensation values ( $\tilde{\theta}_1$  and  $\tilde{\theta}_2$ ). These values are obtained by subtracting the values calculated by the analytic inverse kinematics defined in Eqs. (4.5)-(4.7) ( $\theta_{a_1}$  and  $\theta_{a_2}$ ) from the robot servos angles ( $\theta_1$  and  $\theta_2$ ).

In commanding the robot, the DNN estimates the servos' desired compensation values ( $\tilde{\theta}_1^d$  and  $\tilde{\theta}_2^d$ ) for the desired orientation quaternion ( $q^d$ ). These values are added to the desired analytically-obtained servo angles ( $\theta_{a_1}^d$  and  $\theta_{a_2}^d$ ) to obtain the servos



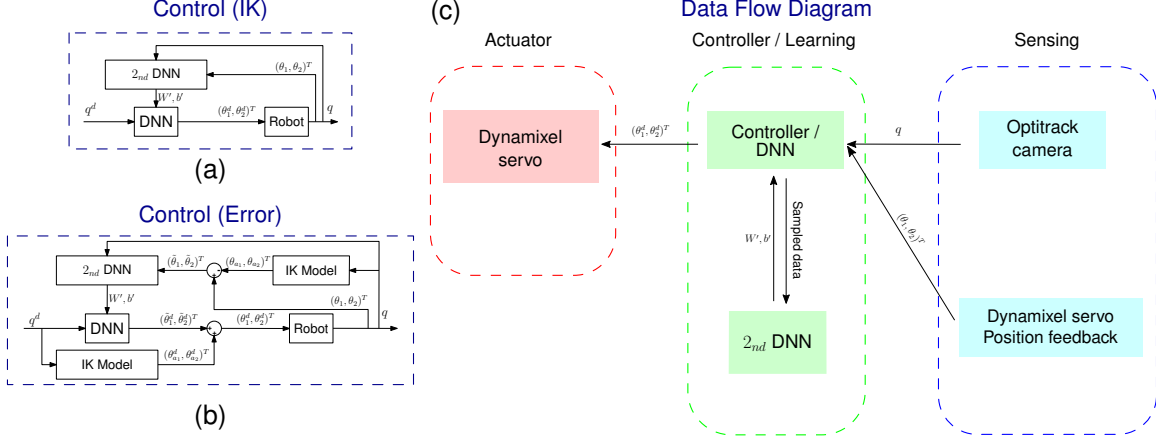


Figure 4.4: **Closed-loop control system configurations.** (a) Diagram of closed-loop control for learning error. (b) Diagram of closed-loop control for inverse kinematics. (c) Data flow diagram.

angles that are used to command the robot:  $(\theta_1^d, \theta_2^d)^T = (\theta_{a_1}^d, \theta_{a_2}^d)^T + (\tilde{\theta}_1^d, \tilde{\theta}_2^d)^T$ . This is shown in Fig. 4.4a.

In the next step, two sets of data from the unloaded (undeformed) and loaded (deformed) system have been sampled in order to tune the DNN hyper-parameters. We consider LBFGS and Adam as the algorithms for weight optimization, and the activation functions of NN as shown in Eqs. (4.1)-(4.4) have been studied for DNN layers.

In order to have a comprehensive study on the effect of number of hidden layers, we consider 154 numbers from a vast spectrum for the number of hidden layers, from 2 to 3000. The layer numbers have been defined as follows:

$$\begin{aligned}
 &\text{Number of Layers}^2: \\
 &\left\{ \{1 : 1 : 100\}, \{100 : 10 : 150\}, \{200 : 20 : 500\}, \right. \\
 &\quad \left. \{500 : 50 : 1000\}, \{1000 : 100 : 3000\} \right\}
 \end{aligned} \tag{4.11}$$

<sup>2</sup>Numbers are shown using the format: {start:step:end}

Figure 4.5a shows the DNN tuning for deformation error. The results do not show a simple, predictable relationship with the number of layers. The overall trend shows that in most cases, training time increases by the number of layers. The Adam algorithm is not capable of finding the global optimum weights for any of the activation functions and gets stuck in a local optimum. While the analytic model is highly non-linear, the identity activation function, which is linear, has a better chance in modeling the system in comparison with the non-linear functions of tangent hyperbolic and logistic sigmoid. Based on the obtained results, the best DNN has three hidden layers, while it is enhanced by LBFGS and identity as optimization solver and activation function, respectively.

## 4.6 Control

### 4.6.1 Pre-trained Model

Figure 4.3d depicts the open loop commanding of the mechanism's actuators based on using the analytic inverse kinematics model presented in (4.5)-(4.7) when there is no load on the robot and the hinges and links are only deformed by their weight. As seen in the plot, the deformation prevented the robot to follow the defined spiral path. The obtained result shows the robot fails to track the Euler angles corresponding to the spiral and it has MAE of 6.370 deg across all three Euler angles.

The pre-trained DNN obtained in the previous section can be used to compensate for error in the unloaded robot. As shown in Fig. 4.5b, the spiral path is followed with higher precision, and the MAE of Euler angles is 1.425 deg. However, this pre-trained DNN is incapable of effective compensation when the system's behavior changes, e.g., when a load has been added to the end-effector. Hence, when a 100 g load is added to the end-effector, the MAE for tracking Euler angles increases to 4.201 deg.

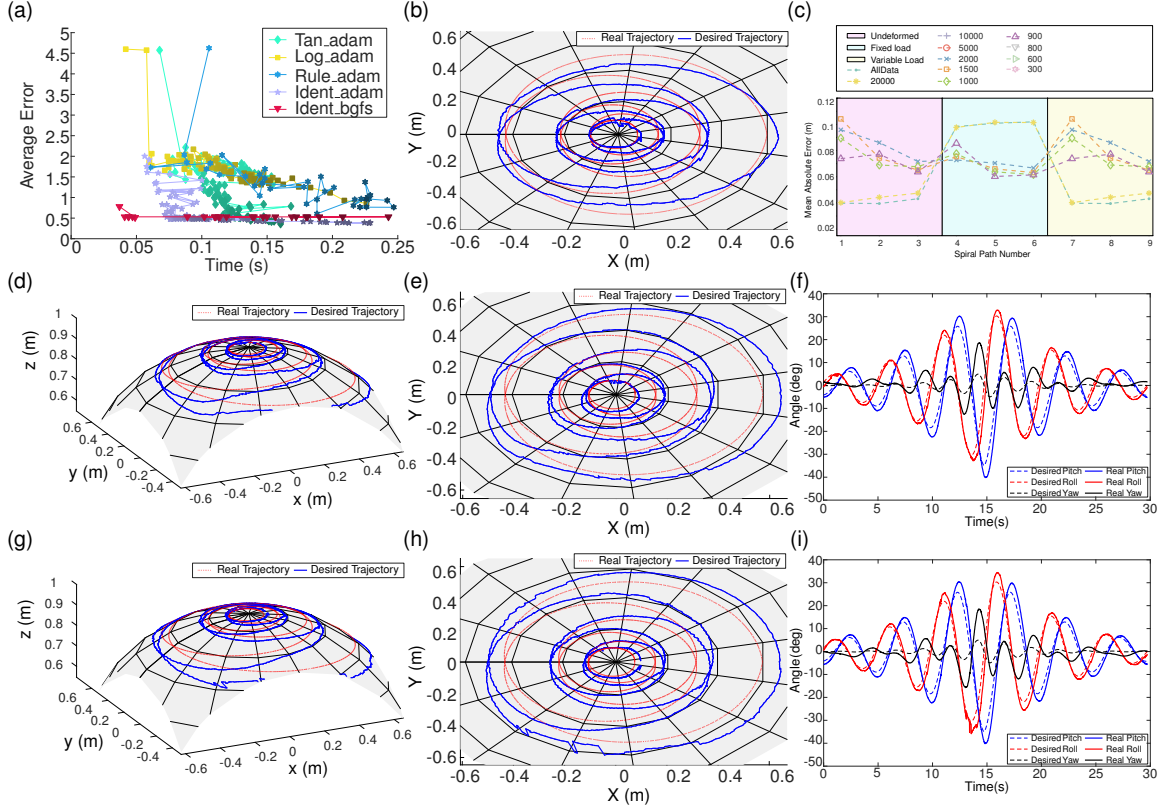


Figure 4.5: **DNN training By tracking errors.** (a) DNN tuning for deformation error. (b) Trajectory tracking by pre-trained DNN. (c) Tuning the retraining history in the control. (d) Path tracking under fixed load in 3D. (e) Path tracking under fixed load in top view. (f) Path tracking under fixed load in Euler angles. (g) Path tracking under variable load in 3D. (h) Path tracking under variable load in top view. (i) Path tracking under variable load in Euler angles.

#### 4.6.2 Control via Transfer Learning

A DNN-based closed-loop controller is proposed to continuously compensate for material deformation while the robot tracks a path under different loading conditions. The obtained results from pre-trained model shows that using the DNN for controlling the robot under changed loading conditions is not effective. However, the results also

prove that the DNN can adapt to the new deformations if it is retrained and updated.

Our next step is to close the feedback loop to include DNN retraining. Utilizing this architecture enables the control system to increase tracking precision when different loads are applied to the end-effector. The diagram of the proposed closed-loop control system is shown in Fig. 4.4a.

In order to use DNN in a closed-loop control system, it should be continuously updated by the most current data sampled from the robot. Since retraining within the main control loop can reduce the controller's frequency and negatively impact the controller's performance, we propose a separate process that retrains a second DNN based on the most current set of data. This second DNN, which has the same hyperparameters as the main DNN, is initialized from the same pre-trained model from the previous section. The task of the second DNN is to continuously retrain using current data and to provide the main DNN with the up-to-date knowledge of system behavior ( $W', b'$  in Fig. 4.4b). In this study, we have used Python's multiprocessing package. The data flow diagram is shown in Fig. 4.4c. In our system, we also have two different parallel processes for getting feedback from tracking cameras and sending commands to the robot's servos, allowing each process to have its own refresh rate. We have synchronized the process in code while making sure that real-time data is sent to the main control loop from other processes. In our experiments, the closed loop control process has an average frequency of 160 hz.

The final step of the workflow is to validate the robustness of the controller while tuning its final parameter (DNN retraining history). We have covered a vast range of retraining history in this study, from unlimited to 300 data points, in order to experimentally find the one with the best performance. It should be mentioned that based on the control loop frequency and definition of the desired spiral path, the robot completes its path once every 30 seconds, during which the controller samples

and processes close to 4800 data points.

In this study, we initially provide both controller’s DNNs with the knowledge of pre-trained DNN obtained in the earlier training step (section. 4.6.1) that considered material deformation (loading). The controller’s performance has been evaluated under different load conditions for each retraining history. We start with the unloaded robot. Then, we add a 100 g load to the robot’s end-effector. Eventually, an 80 g load is also used consisting of small moving masses in a larger container attached to the robot’s end-effector.

Considering that the initial model is derived from the deformed robot, in all three load conditions, we evaluate the controller’s ability to continuously compensate for material deformation.

Figure 4.5c shows the MAE of each controller when tracking a complete spiral path under different load conditions. For better illustration, we only show the errors for the retraining histories that have an MAE under 0.12 m. In order to address the issue of overfitting, we have let the controller follow the path three times for each load condition. Based on the evaluation criteria of estimation error and overfitting, we search for the cases that have the lowest MAE, in which the MAE does not demonstrate any noticeable increment during the three trials. The results show that the retraining history has a significant impact on the performance of the system, such that in some cases, e.g. unlimited retraining history, the controller has high error in some cases, but lower error in others. Evaluation of the defined criteria based on the obtained data reveals that the best retraining history for this case study is 1000 data points. While the 900 data point case often exhibits lower estimation error, the data shows that it overfits the model in some cases (as explained in Sec 4.2). Figures 4.5(d,e), and (g,h) illustrate the desired spiral path and the path the robot takes for different cases of fixed and variable load, respectively. The Euler angles for

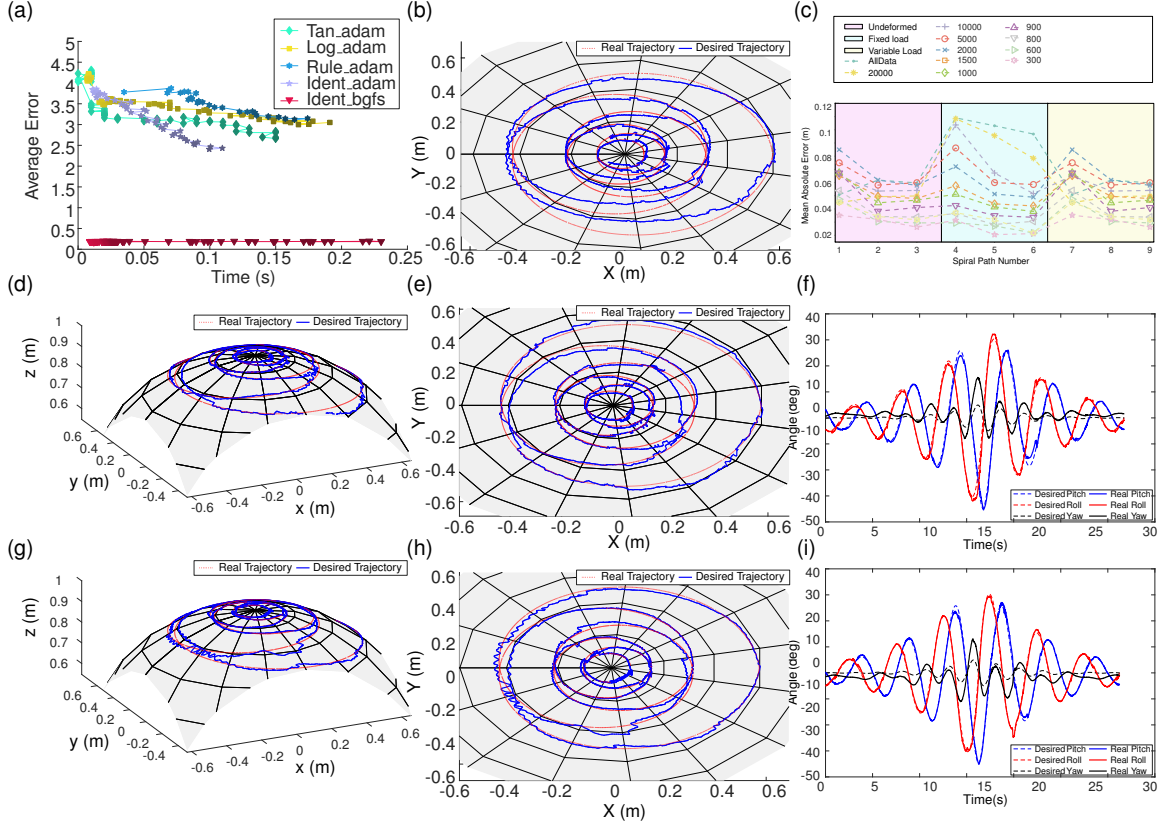


Figure 4.6: **DNN training by inverse kinematics.** (a) DNN tuning for inverse kinematics. (b) Trajectory tracking by Pre-trained DNN. (c) Tuning the retraining history in control. (d) Path tracking under fixed load in 3D. (e) Path tracking under fixed load in top view. (f) Path tracking under fixed load in Euler angles. (g) Path tracking under variable load in 3D. (h) Path tracking under variable load in top view. (i) Path tracking under variable load in Euler angles.

the same paths and load cases are shown in Figs. 4.5f and i, respectively.

#### 4.7 Model-free Controller

We have also considered using a DNN to simply model the full system including kinematics and deformation, rather than using it to model the error as in the previous section. In our case study, the DNN has been used to learn the inverse kinematics of

the 2-DOF spherical parallel mechanism in the presence of material deformation.

Following the workflow for this case, the input of the DNN has been defined as the rotation of the mechanism in quaternion notation ( $q$ ), and the output has been defined as actuator angles ( $\theta_1$  and  $\theta_2$ ). Then, two sets of data for the undeformed and deformed robot have been sampled, and the same hyper-parameters of activation functions ((4.1)-(4.4)) and optimization algorithms (Adam and LBFGS) have been evaluated in DNN tuning. Figure 4.6a shows the DNN tuning for inverse kinematics. Based on the obtained results, the best DNN has two hidden layers, while using LBFGS solver and the identity activation function.

By using the DNN to identify the inverse kinematics of the system, the MAE for the system's output has decreased to 1.341 deg (Figs. 4.6b). However, the pre-trained DNN, does not respond to a new deformation; when a 100 g load is added to the end-effector, the tracking MAE for the Euler angles increases to 3.950 deg. As a result, similar to the previous case, we switch to the closed-loop control mode based on transfer learning between the main DNN and a second DNN with the same hyper-parameters. The control diagram is shown as Fig. 4.4b. In controlling the robot, the input of the DNN is the desired orientation quaternion ( $q^d$ ) and its output is the desired servo command angles ( $(\theta_1^d, \theta_2^d)^T$ ).

Similar to the previous case, the controller's performance has been evaluated under different loading conditions including 0 g (unloaded), a fixed 100 g, and a variable 80 g loads. Figure 4.6c shows the MAE of the controller's performance in tracking a complete spiral path for different loading conditions for the retraining histories that have MAE under 0.12 m. Obtained data reveals that the best retraining history for this case study is 500 data points. The desired spiral path and the path the robot takes for different cases of fixed and variable load are illustrated in Figs. 4.6(d,e), and (g,h), respectively. Figures 4.6f and i, show the Euler angles for the same paths and

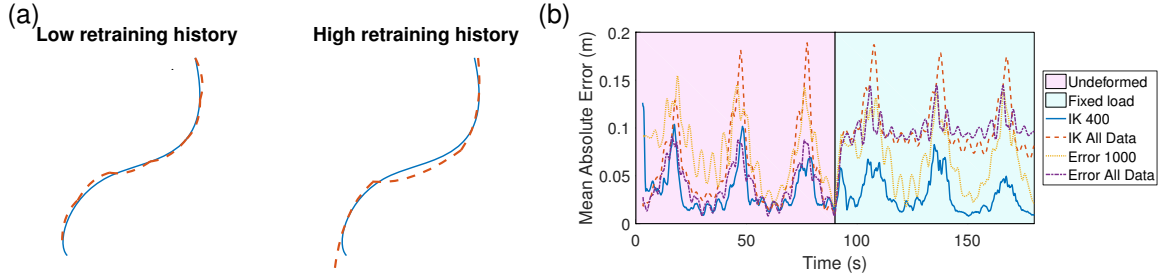


Figure 4.7: (a) Effects of retraining history. (b) Path tracking errors under the optimal scenario.

load cases.

## 4.8 Discussion

The goal of this study is to address the destructive effect of material deformation on foldable robots. We believe that this lack of rigidity often limits the functionality of soft robots as manipulators. Our literature review of these robots confirms this claim – researchers often avoid using large-scale foldable robot as manipulators despite a cheap and fast manufacturing process. In this study, we aim to propose a workflow that can be used to compensate for this deformation across variety of foldable robots. We selected a parallel robot as a case study since one of the most appealing characteristics of this kind of robot is its precision. A 2-DOF spherical parallel robot has been considered in our case study due to its non-linear yet understandable forward and inverse kinematics.

Through this study, we have illustrated that analytic models commonly used for rigid robots are insufficient for controlling large-scale foldable robots (Fig. 4.3d). Hence, we have considered identifying a data-driven approach to describe a system’s behavior using DNN. We have introduced a workflow to tune and train the DNN with a focus on compensating for material deformation. We have shown the effect



of different activation functions, number of hidden layers, and optimization solvers on the estimation error and training time of a DNN, while aiming for a set of hyper-parameters that allows a DNN model to be used in a closed-loop controller. We believe that the optimum parameter set for the DNN is case dependent due to the fact that modeling using a neural network is a black box identification, and there is no analytic formulation to guarantee that a specific set of hyper-parameters would work the best for any case study (we have not anticipated that the linear identity function is the best activation function to model the highly non-linear inverse kinematics of our robot). For example, it is reasonable to assume a robot with more degrees of freedom requires a deeper DNN to model its behavior. However, we experimentally verified that the proposed workflow enables roboticists to find the optimum parameter set for their specific foldable robot. Following the proposed workflow, the optimal number of hidden layers required to learn the deformation and the inverse kinematic the 2-DOF spherical PM are 3 and 2, respectively. The finding that a shallow DNN can be used to describe this system demonstrates the adaptability of the controller by reducing retraining time. This is a testimony of the important role that tuning hyper-parameters plays in DNNs, whereas selecting a different actuation function or optimizing algorithm may require a much deeper DNN to model the system behavior.

The same argument is applicable for other hyper-parameters such as the number of neurons on each hidden layer and learning rate. In this study, focus on a selected set of hyper-parameters, these hyper-parameters were hand-tuned. For our case study, this allowed us to obtain a shallow, well-performing DNN that can effectively adapt to new loading conditions; if that was not the case, one might include the latter two parameters and expand the search for optimal hyper-parameters to a five-dimensional space.

In this chapter, we have also discussed the effect of retraining history on the

control’s ability to adapt to system changes. We have suggested an evaluation of two metrics for estimation error and the issue of overfitting across different loads in order to select the best retraining history. In our case study, the DNN model was built using the linear identity activation function (Eq. 4.1), even though the analytic inverse kinematics model is highly non-linear. We believe that the selected DNN continuously performs a local model fitting of the non-linear model and retraining history adjusts the local curve length. Figure 4.7a illustrates a two-degree demonstration of the effect of the retraining history on the local modeling of the non-linear robot’s model. We believe that a low retraining history produces numerous local models that fit the non-linear curve more precisely. However, changing between these models can produce chatter. Conversely, larger retraining history is smoother but less precise path tracking.

In order to obtain a more general, model-free control algorithm, we have demonstrated the efficiency of the proposed closed-loop controller for modeling the overall inverse kinematics of the foldable robot under load. We have experimentally validated that following the workflow enables us to tune the DNN for this case as well. In fact, this DNN estimator has a better, more consistent performance compared to the alternative of only learning material deformation. In learning only model error, we have seen a 0.1 m/s lag between the desired and experimental Euler angles. We believe that this is due to the higher calculation costs associated with analytical model calculations, as well as a small time difference between calculating the analytic inverse kinematic and estimating the deformation error using DNN. The Learning IK case, does not have this problem and there is no noticeable time lag seen in the data.

Figure 4.7b highlights the path tracking MAE for the unlimited and best retraining histories of the learning IK and learning error cases. The value of the MAE is obtained using a two-second moving window. The results show that in both cases, using an

unlimited retraining history limits the ability of the controller to adapt swiftly to the deformation of the load. Eventually, the best result has been obtained by having a shorter retraining history and using the DNN to model inverse kinematics of the foldable robot. This controller is able to compensate for load-induced deformation in two seconds, which is much faster than other test cases. Based on this study, we encourage researchers to use the proposed workflow to identify competitive, model-free solutions, especially in cases of high open-loop error due to material deformation.

We have demonstrated that using the proposed workflow and utilizing a DNN closed loop controller can give foldable robots higher precision when interacting with loads. This workflow can be used to train the DNN for learning material deformation error or the overall deformed robot's behavior. However, using a neural network to model the system produces lag in order for the model to be retrained, based on historical data. Hence, although the model is able to compensate for deformation caused by static or slowly changing loads, it cannot compensate for error due to dynamic loading with high changing rates. Another limitation of this method is that large deformation can change the workspace of the deformed robot so significantly that the desired path is no longer within the workspace of the deformed robot. This physical limitation cannot be compensated for using any feedback control.

Improving the accuracy of foldable robots can improve their functionality and can even speed up their popularity in the industry. There are many potential future applications of the proposed closed-loop controller. We aim to extend the workflow to include system dynamics and compensate for deformations caused by dynamic loads.

## Chapter 5

### IDENTIFICATION & CONTROL IN THE PRESENCE OF UNCERTAINTIES CAUSED BY MATERIAL DEFORMATION AND WORKING ENVIRONMENT: A CASE STUDY OF FISH-INSPIRED ROBOT

This chapter evaluates the possibility of leveraging a laminated composite as a low-cost caudal fin in a 1-DOF robotic fish. After altering the fin's stiffness and shape, we focus on finding suitable control input gaits that enable us to control the thrust generation.

Many different robots have been designed and built to work under water. In many cases, researchers have chosen to use bio-inspired platforms. In most cases, the main goal of fish inspired robots has been set to autonomously swim and maneuver in an environment that is much larger than the fish's size. In this study, the identification and control of a low-cost fish-inspired robot is studied with the goal of building a mechanism to not only swim in water but to do so in a highly constricted space. The robotic fish under study uses the tail propulsion from its tail as the main source of forward thrust.

#### 5.1 Introduction

Autonomous Underwater Vehicles (AUVs) are widely studied for operating below the surface of the water. Underwater propulsion is one of the main components of AUVs and underwater robots. This type of propulsion is a hard problem to understand analytically due to the highly nonlinear and turbulent nature of the water currents around an object. These turbulent flows result in the loss of energy and therefore energy efficient propulsion systems are of special interest for many researchers.

Evolution provides a variety of successful underwater locomotion examples. Different fish species have developed a variety of mechanisms for underwater propulsion that are energy efficient; many species use their fins to maneuver through the water. Therefore, it is not surprising that fish interests biomechanics researchers for their efficiency and their maneuverability [97]. A fish can make a half-turn in  $1/10$  its length without losing speed, whereas a submarine needs 10 times its length, while slowing down by half to accomplish the same maneuver. Research on robotic fish is mainly focused on dynamic modeling [98, 99, 100, 101] and control [102, 103, 104, 105, 106, 107]. An extensive review and classification of different fish species and marine robots inspired by them is given in [108]. Several other researchers have studied the effect of a certain parameter on the performance of a robot. For example, [109] has addressed the effect of artificial caudal fins on the fish robot's performance. Marchese et al & Zhong et al have used soft materials plus soft robotic fabrication techniques to manufacture a robot fish [110, 111]. In [112], Liu et al study the movement of a carangiform fish and then a robotic fish is controlled based on the obtained results. Turning performance of a robotic fish inspired by a sea bream is studied in [97]. A parametric study of a fish robot performance is carried on in [113]. This study used a 6-meter long water tunnel with flow control over the test tank to provide a known current for robotic fish being studied. A tail consisting of one active joint and two passive joints as well as a flexible caudal fin were studied in this environment. Similar to the previous research, in most cases, conventional robots are unable to replicate specific features of fish locomotion, such as realizing smooth and continuously flexible hulls similar to fish bodies [114], though this issue can be solved using recently-developed laminate manufacturing techniques [115, 116]. Throughout all these studies, the authors have identified an opportunity to address fish-inspired locomotion in the tail using laminate techniques, which have the capability of being able to be rapidly pro-

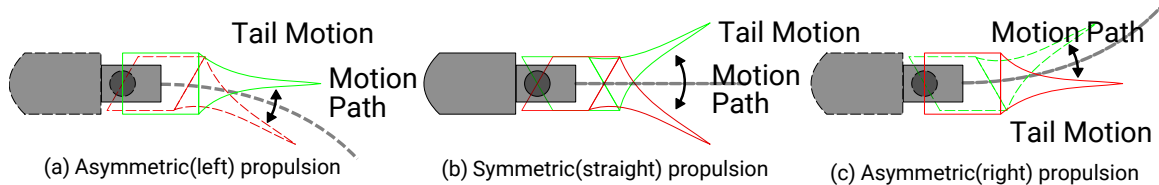


Figure 5.1: Maneuvering strategy and effect of tail movement on generated force

totyped and tested. Using laminate techniques, it is possible to easily add the desired number of passive joints in desired positions, as well as using different materials and thicknesses to achieve desired stiffness.

The main contribution of this study is to investigate the locomotion of a fish-inspired robot swimming in a tight workspace and interacting with environment, while using forward propulsion in a high-flow channel to apply force to an object. This work is motivated by the need for a small, low-power robotic platform which can navigate autonomously in small canals for cleaning, maintenance, and inspection tasks. The focus of this study is to use a tail fin manufactured via laminate fabrication techniques (known as a caudal fin in fish morphology) for locomotion. Laminate fabrication techniques permits iterating rapidly through a complex design space to tune the stiffness and damping properties of soft flexure hinges between a variable number of rigid segments, in order to quickly fabricate and validate an optimal fin design. Laminate fabrication methods are also low-cost, with the structure and tail components (\$5) costing a fraction of the selected actuator (\$55). Even though the laminate platform is novel, the focus of this study is to facilitate a deeper understanding of the control issues at play in small environments and narrow passages.

The study is organized as follows: Section 2 will describe maneuvering strategies as well as test setup construction. In Section 3, design and manufacturing of the robotic fish hardware is discussed. A model of the generated force by robotic fish propulsion has been developed which is presented in section 4. In Section 5, different

Table 5.1: List of propulsion parameters

Symbol	Definition
$a$	Propulsion Amplitude
$b$	Offset in asymmetric propulsion
$f$	Propulsion frequency
$t$	Propulsion time
$\theta$	Angle of servo actuator in propulsion

controllers are designed based on the identified model of the robotic fish. The study concludes with some remarks and suggestions for future work indicated by obtained results.

## 5.2 Maneuvering Strategies & Experimental Setup

In nature, swimming modes of fish can be divided into two main categories, namely caudal fin locomotion and pectoral fin locomotion [117]. In this study, propulsion caused by caudal fin is considered as the main focus of our locomotion strategy. Figure 5.1 shows the locomotion strategy proposed in this study. The fin actuator is commanded to follow the following angle:

$$\theta(t) = b + a \sin(2\pi ft) \quad (5.1)$$

Description of the propulsion parameters are described in Table 5.1 The design goal is to enable the fish to interact with its environment, including vegetation, which may be present in shallow, narrow waterways of the southwestern United States. The interaction can involve pushing an object or cutting a specimen from a plant. The authors believe that this working environment, which contains stationary propulsion

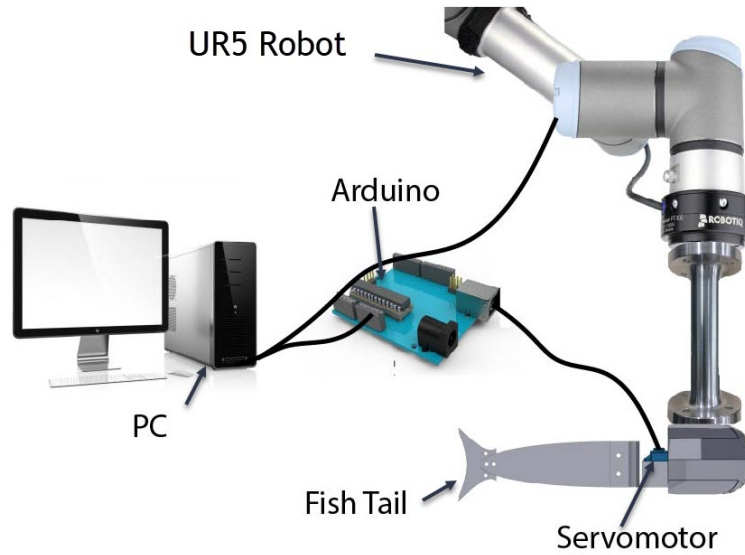


Figure 5.2: Test setup for identification & control

in a narrow canal, is challenging due to reflected waves coming back from canal walls, which can impact sensing navigation by imparting disturbances on the robot caused either by the world or the robot itself.

A test setup has been designed for evaluating the performance of underwater, robotic fish designs by monitoring the thrust generated from undulatory swimming. The design of the test setup is based on the overall strategy for controlling the robot and its working environment. Figure 5.2 shows the experimental setup. The robotic fish is attached to an force-torque sensor (ROBOTIQ FT300) using an aluminum bar. The torque applied by the robotic fish on the sensor through the attachment bar is measured and converted to force by dividing it by the length of the attachment bar (distance of the application point of the force to the origins of the sensor), since the force measurement alone is small relative to the range of the sensor. A  $0.3048 \text{ m L} \times 0.1524 \text{ m W} \times 0.254 \text{ m H}$  water tank is used to model a small canal work environment. The robot is attached to a UR5 robotic arm which can move the fish in the water with constant speed to simulate water current.



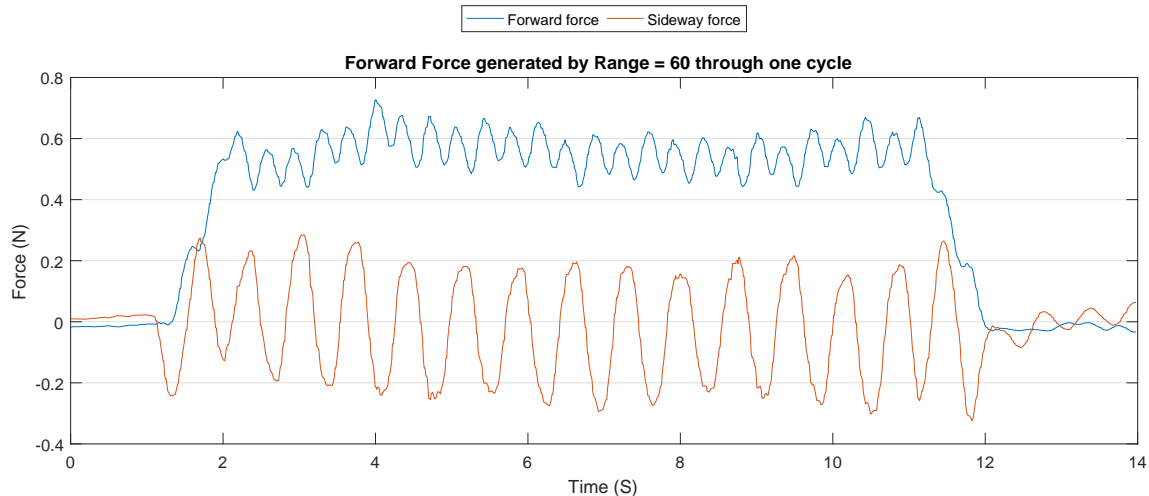


Figure 5.3: Forward and lateral force generated by symmetric propulsion.

An Arduino is responsible for controlling the servomotor. Force and torque data is transferred to the computer through the Modbus protocol. A Python script is responsible for sending motor commands to the Arduino and reading data from the force and torque sensor.

Figure 5.3 shows 10 seconds of raw forward and side-force data for a symmetric undulatory motion with amplitude of 60 deg, in order to provide the reader with insight on the forces generated via fin propulsion. In this study, the forces generated by the fin are split into two main elements corresponding to the fish’s forward and lateral directions. According to this figure, the generated forces are periodic in nature, as was expected due to the undulatory motion of the tail. It can be observed that although the lateral force is changing, the average force produced over a cycle is close to zero due to the symmetric propulsion of the fins. The average forward force is positive although there are periodic variations observed in it. As a result, force-torque data is averaged over a window of specified number of cycles. In this method, the average amount of forward and lateral forces generated by the tail are stored for subsequent use.

### 5.3 Design & Prototyping

In designing the caudal fin, the results of the parametric design study conducted in [113] were considered, specifically the aspect ratio of the end fin. Initially, a laminated design was proposed with one actuated joint and five passive joints to provide the undulatory movement of the fin in the water. The prototype based on this design was built with acrylic (Fig. 5.4a). Initial testing revealed that the thrust generated by the fin was not as high as hoped. The authors believe that the main reason was due to the fact that the tail was heavy and also thick. As a result, for further prototypes, the whole fin was built from sheets of polyester laminated together in different numbers to provide a variety of stiffnesses for evaluation. Individual sheets were laminated together and then cut in a CO<sub>2</sub> laser.

The main components of the robotic fish locomotor are the tail and the actuator which are shown in Fig. 5.4a. A waterproof servomotor was selected based on the torque and speed required to provide thrust via the tail. The motor holder and the body of the fish are made using 3D printed parts. A floating support was made using foam to help the fish to float in water (Fig. 5.4b).

Table 5.2 shows the average amount of force generated in all directions for different fin materials and designs. The result shows an increase in generated force with stiffer material while confirming the assertion made in [113] about producing more force with Larger back fin (Fig. 5.4b). Moreover, the fins were installed and the robot's ability to swim was tested based on observation. One key observation was that as fin stiffness went up, rotation in the tail led to more rotation in the main body of the fish, rendering higher tail forces less useful at generating forward thrust. Thus, a final material thickness of 1.016 mm was used for subsequent fin designs.

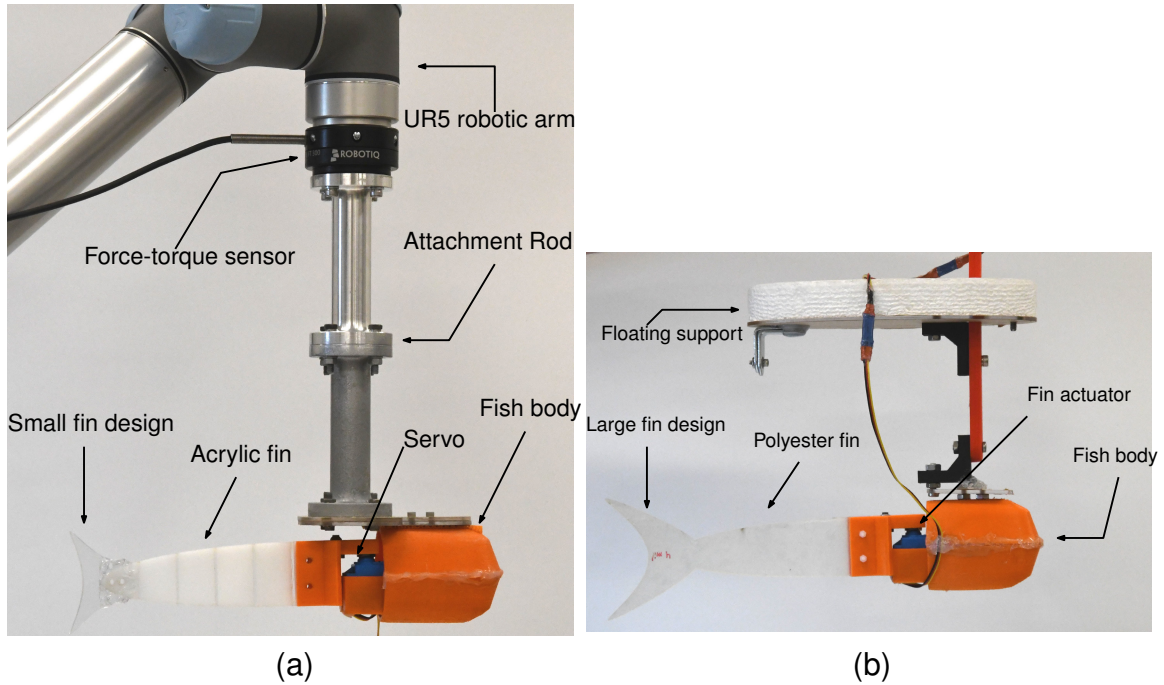


Figure 5.4: Prototypes made to evaluate generating force (a) and swim ability (b).

#### 5.4 Identification & Model Extraction

The goal of this section is to discuss the identification of the magnitude and direction of thrust which can be generated via changing control signals in the robotic fish platform. To this end, providing a model that relates the input and output of the system is studied. According to [113], flapping amplitude and frequency were the two control parameters found most effective at generating forward motion and thrust. Based on our design, placing the servo at the base of the tail, this permits us to select the servo's angle as an input variable. The input to the system is selected to be the amplitude and range of the undulatory motion of the servomotor. Moreover, angular offset from the symmetric plane has the most effect on direction of the generated force (Fig 5.1). As mentioned before, the output of the system is the force generated by the tail propulsion, which is measured by the F/T sensor.

Table 5.2: Different design & material effect.

Material & width (mm)	Fin design	Average generated thrust (N)	Ability to swim
6.35 Acrylic	Small	0.1983	Yes
0.254 polyester	Small	0.2361	Yes
0.254 polyester	Large	0.2647	Yes
0.508 polyester	Small	0.2944	Yes
0.508 polyester	Large	0.3154	Yes
1.016 polyester	Large	0.551	Yes
1.524 polyester	Large	1.157	No

In order to identify the system, the 3 dimensional space of  $a$ ,  $b$  and  $f$  is spanned (Eq. 5.1). To this end, for a known set of  $a$ ,  $b$  and  $f$ , the servomotor is actuated for five cycles and the average forward force and side force are measured. The experiments were performed for  $-20^\circ < b < 20^\circ$ ,  $0 < a < \pm 60 - abs(b)$  and  $0 < f < 82/a$ . The limitations on the values of offset, frequency and range are due to limitations in motor maximum speed and the space limitations of the water tank used for experiments. This results in total of 2292 tests. The average force for each test case is presented in Fig. ?? and Fig. ?? with the values of offset  $b$ , range  $a$  and frequency  $f$  plotted for reference. As illustrated in small zoomed plot in figures, for each test ( $x$  axis data), the servo propulsion parameters are shown(right  $y$  axis) as well as the average value of force generated in forward and lateral directions (left  $y$ -axis).

Based on obtained results, it was found that for the majority of propulsion regimes, the provided force in the forward direction is negative. This means that due to special working conditions, in these regimes the propulsion will result in backward movement.

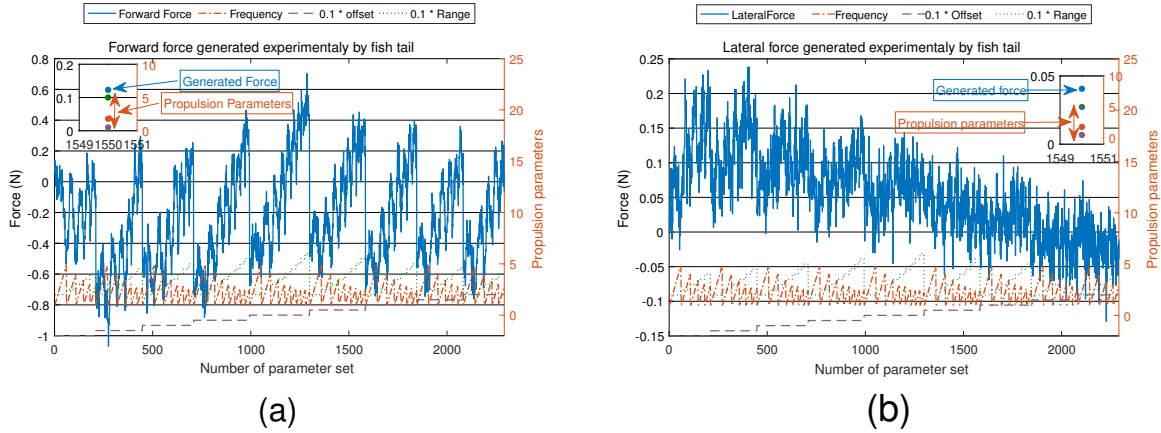


Figure 5.5: Force generated by different fin propulsion in forward (a) and lateral (b) directions. It should be mentioned that  $x$  axis of plots are not time, but is the number of test.

This can affect the fish’s interaction with its environment. In other words, if the fish is used to push an object in a narrow canal with still water, certain command signals will result in the robot failing to apply positive normal forces to desired objects. From a controls perspective, the system is uncontrollable across much of the three-dimensional control space. As a result, in order to control the robot, a proper subspace with a controllable working regime should be selected and identified. As the goal is to interact with the environment, it is convenient to select a working regime in which the forces which are generated are as high as possible. The authors believe that one reason for negative generated forces lies in the reflected waves coming back from tank walls.

The maximum forward force is generated with  $f = 1.4\text{Hz}$ ,  $a = 60^\circ$  and  $b = 0^\circ$ . Searching through the results obtained from spanning the control space, the subspace with fixed propulsion frequency of  $1.4\text{Hz}$  is suitable, while the propulsion amplitude is approximately more than  $20^\circ$ . With the frequency fixed, a second set of experiments

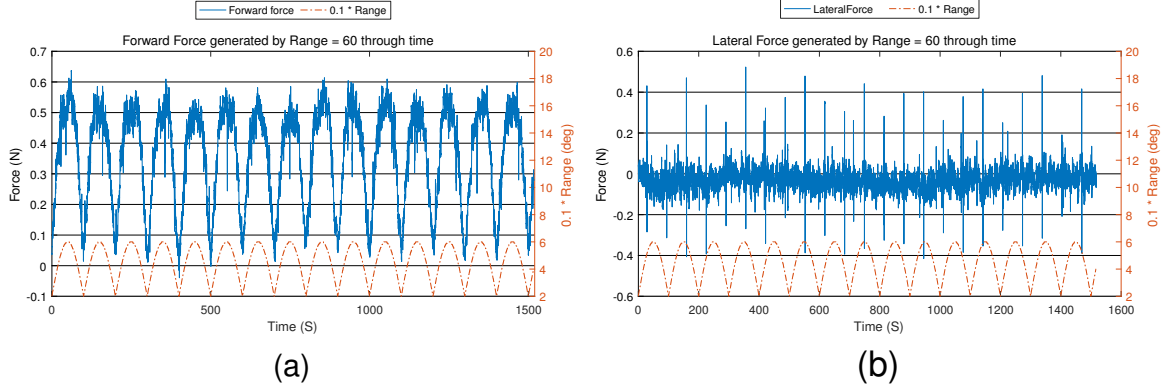


Figure 5.6: Force generated by symmetric sinusoidal amplitude fin propulsion in forward (a) and lateral (b) directions.

was performed to study the dynamic behavior of the output force as a result of other input parameters change. To this end,  $b$  was set to 0 and the range was changed according to a half-wave sinusoidal function according to the following equation:

$$a = 20 + \text{abs}(40 \sin(2 * \pi * 0.005t)) \quad (5.2)$$

The results are presented in Figure 5.6(a) and Figure 5.6(b) for forward and side forces respectively.

The obtained results show a promising, controllable subspace that includes different propulsion regime which are capable of producing different values of force. It should be mentioned that the results show that the lateral force and as a result the angle of produced force is typically zero for symmetric propulsion.

To further understand the relationship between propulsion parameters and generated force, with frequency set at 1.4 Hz, the propulsion range was changed according a half-wave sinusoidal function, while, simultaneously, its offset was changed according

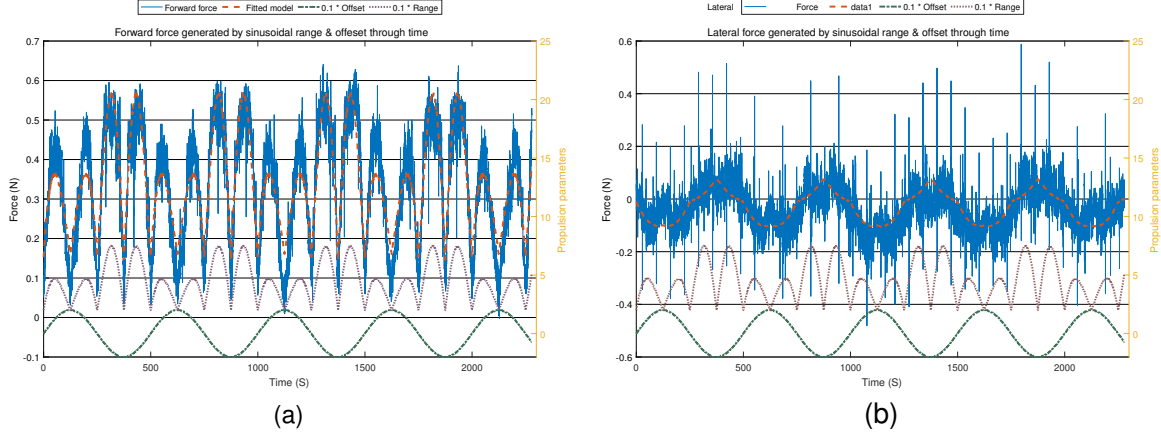


Figure 5.7: Force generated a half-wave sinusoidal range and a full-wave sinusoidal offset input in forward (a) and lateral (b) directions.

to a full-wave sinusoidal function:

$$\begin{aligned}
 \theta &= b + a \sin(2\pi \times 1.4t) \\
 b &= 20 \sin(2 * \pi * 0.002t) \\
 a &= 20 + \text{abs}((40 - b) * \sin(2 * \pi * 0.004t))
 \end{aligned}
 \tag{5.3}$$

It should be mentioned that the frequency of change in amplitude and offset (0.002Hz and 0.004Hz, respectively) were selected differently in order to help with distinguishing their effects. The results are presented in Fig. 5.7a and Fig. 5.7b, showing that the amount of forward force is highly correlated by propulsion range, while the lateral force is mainly effected by the offset of asymmetric propulsion.

In order to model the effect of propulsion parameters on forward and lateral forces, a model was fit to the experimental data using a least-squares approximation plotted in Fig. 5.7a and Fig. 5.7b. In matrix form, this can be represented as the following[118]:

$$\mathbf{Y} = \mathbf{X}\hat{a} \quad \Rightarrow \quad \hat{a} = (\mathbf{X}^T \mathbf{X})^{-1} \mathbf{X}^T \mathbf{Y}
 \tag{5.4}$$

Table 5.3: Choosing  $\mathbf{X}$  basket

Elements	FF MAE	SF MAE
$\{a, b\}$	7.89%	4.19%
$+\{\dot{a}, \dot{b}\}$	7.89%	4.19%
$+\{\ddot{a}, \ddot{b}\}$	7.89%	4.19%
$+\{a^2b^2\}$	7.05%	3.98%
$+\{a^3b^3\}$	4.53%	3.83%
$+\{a^4b^4\}$	4.52%	3.76%
$\{a\dot{a}a^2b\dot{b}b^2\}$	7.89%	4.19%

In order to determine what should be in the basket of the fitted model, different combinations were used (Table 5.3). With considering mean absolute error (MAE) values, it can be concluded that a model with third-order terms provides the best MAE, however, the condition number of  $(\mathbf{X}^T \mathbf{X})$  matrix containing input basket showed that the resulting matrix is close to a singularity and the data are not reliable. As the addition of second order does not improve the model significantly, the best model for the system is considered to be the first order model of  $\{a, b\}$ .

The obtained model for forward force along with the original data is plotted in Fig. 5.7a with  $a$  and  $b$  both changing, while the obtained model for side force along with the original data is plotted in Fig. 5.7b with  $a$  and  $b$  both changing.

The identification results can be summarized by saying that in fixed propulsion frequency of 1.4Hz and propulsion amplitude larger than  $20^\circ$ , the system has a proper behavior with a set of decoupled, linear input-output relations of propulsion amplitude-Force amplitude & propulsion offset-force angle. These results support the principle of a tail-driven robot to control thrust and direction forces.



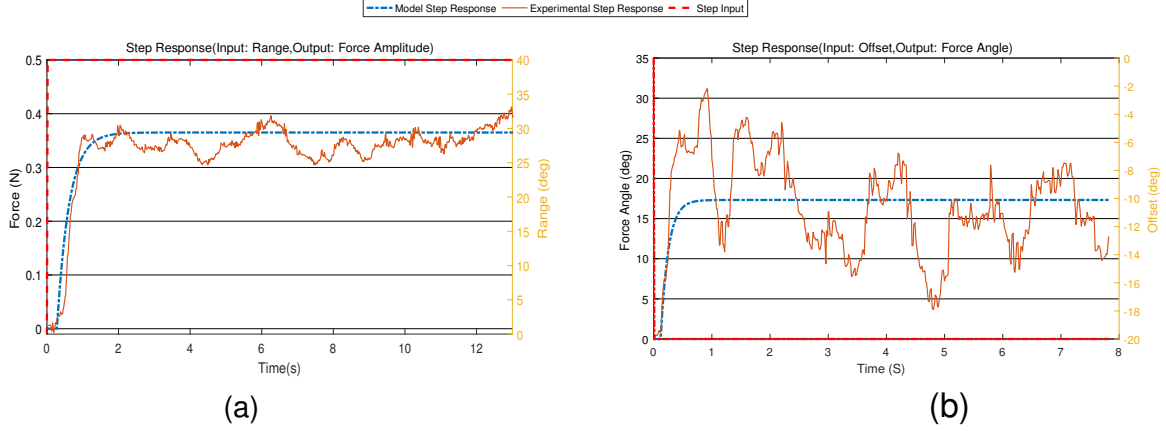


Figure 5.8: Step response identification on generated force amplitude (a) & angle (b) as a function of propulsion amplitude & offset, respectively

## 5.5 Controller Design

While the previous identification results provide a model for the average forces generated by fin propulsion, a dynamic model is also required for control procedures. Hence, the system response to a step input was obtained. For this purpose, the force is represented as magnitude and direction values instead of forward and side force. Regarding force magnitude, propulsion amplitude was set to  $40^\circ$  from stationary and the resulting force magnitude was recorded. In the case of step response identification of force angle, while propulsion amplitude is fixed, the offset was changed from  $0$  to  $-20^\circ$  and the resulting force angle was recorded. Figures 5.8a and 5.8b show the step response tests for the force magnitude and angle respectively.

Based on the obtained results, a first-order transfer function with time delay is fitted to a step response in force magnitude:

$$TF_{\text{Forward force}} = \frac{0.00912e^{-0.28S}}{0.34S + 1} \quad (5.5)$$

Similarly, the same transfer function is fitted on the force direction:

$$TF_{\text{Lateral force}} = \frac{-0.866e^{-0.12S}}{0.13S + 1} \quad (5.6)$$

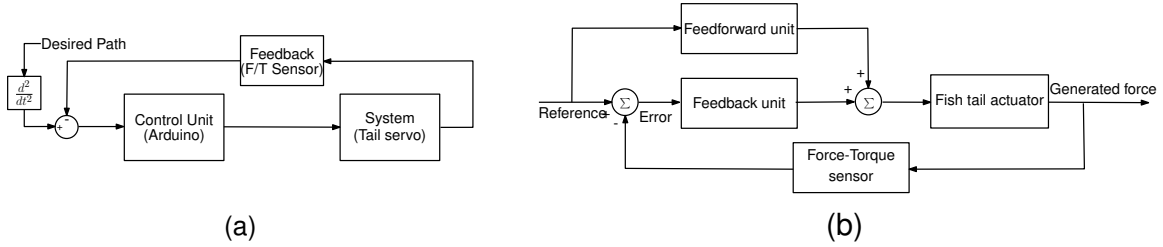


Figure 5.9: Block diagram of the closed-loop controllers proposed in controlling force generated by fin propulsion: feedback controller (a) and feedforward-feedback controller (b).

These transfer functions are used in the system block in the block diagram of Fig. 5.9a alongside the system model for tuning control unit.

Evaluation of the results obtained for the lateral force amplitude (Fig. 5.7a) and force angle (Fig. 5.7b) show that in the studied working environment, the caudal fin propulsion is not able to provide consistently high forces for sharp turns in a narrow canal. This results was also confirmed by a mobile prototype swimming test<sup>1</sup>. As a result, the focus of controlling algorithms is the magnitude of force generated by propulsion.

As mentioned before, the identification and control strategy used in this study is based on the amount and direction of generated force in a full cycle of fin propulsion. As a result, the data received from feedback unit at any time should be averaged over a whole cycle. Hence, a slave parallel process is defined in Python that works alongside of the main Python process and is responsible for determining the average magnitude and direction of the force generated within a single propulsion cycle.

In order to provide a proper controller, the parameters of different PID controllers were tuned using the MATLAB Simulink PID tuning tool in order to be used in control

<sup>1</sup>It should be mentioned that applying controllers robust to uncertainties, such as sliding mode controller, was not applicable due to high noise in feedback force

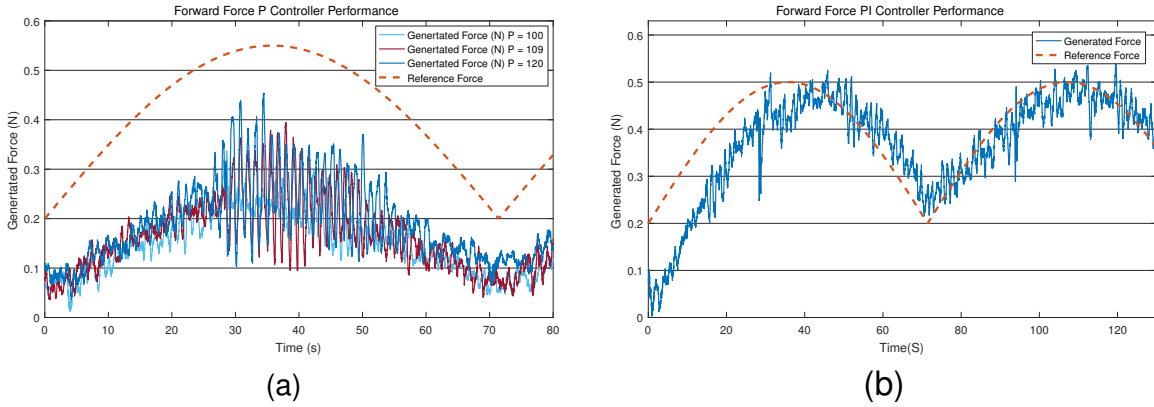


Figure 5.10: PID controller performance: P controller (a) and PI controller (b).

system and then, due to modeling error, tuned more exclusively by experimental tests. A P controller was implemented in the first step. Figure 5.10a shows the generated force when the input reference force is a half wave sine signal. As can be seen, the P controller is not able to track the reference input force and have a considerable error for different gains.

To improve the performance, an integrator was added to the controller. However, the experimental results which are shown in Figure 5.10b show that the system is not able to track the input reference force signal in the first cycle. However, after one cycle, the input tracking is able to follow the reference input force. It should be mentioned that due to high noise in force feedback, the addition of a derivative term to the PID controller had a negative effect in controller performance.

Further improvements were subsequently achieved by adding a feed forward unit which is shown in Fig. 5.9b. To this end, the model obtained from least square identification is used in the feedforward unit. As illustrated in Fig. 5.11a, when the feedforward unit is added to the system, even a simple P controller is able to provide acceptable performance in tracking desired force. However, it can be seen that during more of the cycle, generated force stays slightly smaller than the desired force. In the

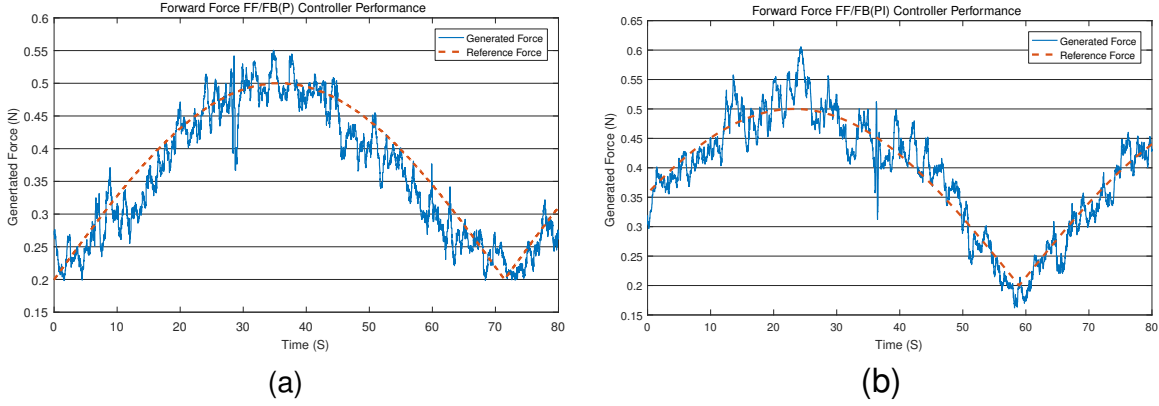


Figure 5.11: Feedforward-feedback controller performance: (a) P controller in feedback. (b) PI controller in feedback.

Table 5.4: PID parameters values for different controllers reported in the study.

Controller	P value	I value	D value
P	100,109,120	0	0
PI	80	0.12	0
FF-P	10.9	0	0
FF-PI	9	0.05	0

controller with both feedforward and PI units, not only is the generated force able to follow the reference input from the first cycle, but its trend matches the desired force more precisely (Fig. 5.11b). The PID parameters for controllers with the highest performances are summarized in table 5.4. Results show a noticeable decrement in the magnitude of PID parameters when the feedforward unit is added, which shows the positive contribution of this unit.

## 5.6 Conclusion & Future work

There are many mechanisms for underwater propulsion. Bio-inspired methods are often more energy efficient, which can be an important consideration in underwater autonomous vehicles. Based on this assumption, a fish inspired robot was designed and built to work in a narrow and shallow workspace such as a small canal.

Our main goal in this research was to find the best control strategy for the navigation of the fish in the canal. For this purpose, a test set up was designed and used for data acquisition and control. Since there are many uncertainties with underwater robotic fish working in narrow canals due to turbulence and hydrodynamic effects, building an accurate analytic model of the system is highly complicated. The methods introduced in this study have been used to identify the relationships between the amplitude and frequency of the tail propulsion and magnitude and direction of the forces generated.

Experimental results show that the model obtained for the generated thrust was linear with a good approximation when the propulsion magnitude varies linearly within the controllable regime. We can conclude that the caudal fin of the current generation of robot is not capable of producing enough consistent lateral force for sharp turns in narrow working environments.

Several linear controllers were tested to find out the best solution for generating directed thrust. The data shows that the PI controller with a feed forward unit is the best strategy to track the reference input force with acceptable accuracy. The obtained results demonstrate that by applying the feedforward feedback controller, it is possible to produce desired amounts of forward force by caudal fin propulsion even in narrow environments.

Biological studies have shown that the pectoral fins are also useful for generat-

ing thrust and are even used as main locomotion for low speed movement in fishes. This addition will permit our team to study simultaneous pectoral and caudal fin propulsion. This study is the focus of the next chapter.

TRAINING IN THE PRESENCE OF UNCERTAINTIES CAUSED BY  
MATERIAL DEFORMATION AND WORKING ENVIRONMENT: A CASE  
STUDY OF FISH-INSPIRED ROBOT FOR EXTREME  
ENVIRONMENTS (FIRE)

In this chapter, laminated techniques are leveraged to build a robotic fish with caudal and pectoral fins. Use of these techniques in manufacturing this mechanism results in a lighter, more affordable solution to underwater locomotion. On the other hand, this study provides the opportunity to deal with cases where laminated mechanisms directly interact with their environment, and where the mechanism's movement contributes to produce locomotion through complex hydrodynamic scenarios.

Fish as a species are evolved to maneuver in variable environments with high efficiency and agility; our strategy supports that goal and contrasts with prior work in that we focus on the interplay between complex fin subsystems as well as non-ideal testing environments in which the effects of turbulence, water flow, and interactions with the environment are present.

We present a novel robotic fish with a pair of two degree-of-freedom pectoral fins and a flexible caudal fin that can be used to maneuver in tight environments and in turbulence. This is made possible by several innovations, including (i) a novel fin design based on a 2-DOF, origami-inspired spherical mechanism; (ii) kinematic modeling of the mechanism's motion and workspace; (iii) a fish-inspired robot design that combines one caudal and two pectoral fins; (iv) strategies for identifying high-performing gaits with an online learning strategy (CMA-ES); and (v) strategies for finding gait parameter sets with a high-degree of correlation between lab and the

intended operating environment.

This study has resulted in a robotic fish that can reach a swimming speed of 0.385 m/s (0.71 body length per second) in forward swimming using its caudal fin, and a near zero turning radius using its pectoral fins.

The highest-performing gaits learned by this design and evolution strategy have been validated in both the laboratory and realistic outdoor settings; the consistently high-performing gaits have then been selected for use.

## 6.1 Introduction

Fish-inspired robots' maneuverability is concerned with the issues of "acceleration and steering characteristics" [119]. While this class of robots offers a novel and interesting mode of locomotion with certain advantages, these platforms can be influenced by a variety of water-based effects, which are difficult to account for in their design and modeling. In this study we describe a robot intended to navigate through a canal system and clear underwater vegetation. This goal is motivated by a recent collaboration with a water utility located in the Phoenix metropolitan area. In order to accomplish these tasks, our robot must be able to work in tight environments and perform tasks that require the platform to exert forces on the world. Due to the size constraints of this underwater environment and the remote nature of the work to be done, we have envisioned small, fish-inspired robots that can leverage the high-efficiency locomotion strategies of fin-based swimming to ultimately solve these challenges in teams. Moreover, we envision the robot to be able to swim close to canal surfaces and perform well even in the presence of surface waves and reflected vortices.

To address the above goals, we have designed and trained a Fish-Inspired Robot for Extreme environments (FIRE). The wide, flat shape of its body is based on the



suckermouth catfish due to this species' ability to swim close to surfaces. We have selected a flexible caudal fin as the primary thrust generation mechanism. In order for the robot to work in tight environments, we have increased its maneuverability by using two bio-inspired pectoral fins with two degrees of freedom (DOF) that, when combined with caudal fin, can be used to create complex patterns of propulsion in six dimensions.

To make this possible, we have used laminate manufacturing techniques to fabricate both caudal and pectoral fins. This has enabled us to easily change the stiffness of the caudal fin and create a mechanism more compact than would have otherwise been possible. In addition, it has allowed us to rapidly iterate through a variety of mechanism design parameters during the prototyping process as well as to reduce the fabrication cost significantly.

Inspired by nature, an evolution strategy (CMA-ES) is used to search through the gait parameter space for different objectives to help the robotic fish swim in three dimensions. A novel experimental setup is designed for evaluating FIRE's performance regarding different gaits in both still and with-current water. Our work in this study contrasts with prior robotic fish that are often designed and tested in ideal environments with few disturbance forces caused by the environment. Many robots in prior literature are designed to mimic and study specific fish morphologies; some focus their study on simplified representations of fish fins with few degrees of freedom, or focus on one specific and complex subsystem.

Having evolved over millions of years, fish and other aquatic animals are endowed with the ability to swim with high efficiency, speed, and agility [120, 121]. Research has focused on robotic fish both in their ability to mimic fish morphology [122, 123, 124] as well as for particular applications such as underwater search and rescue, as well as monitoring fish species [125, 126]. Soft fabrication techniques have been employed

successfully due to fishes' exceptionally large fraction of soft body [127, 128, 129, 126, 130, 131, 7]. Caudal and pectoral fins have been identified as the primary generators of thrust in biological fishes [132]. This had led designers to focus their designs on robots which use these two fin types as their primary source of locomotion.

Caudal fin propulsion is often the primary source of thrust production in robotic fish that are inspired by osteichthyes, or bony fish. Various forms of rigid [122, 133], multi-body [134, 125] and soft [128, 126] caudal fins (or tails) have been studied in order to emulate this propulsion system. Recent studies show that the soft caudal fins produce more effective vortices compared to rigid fins while being significantly simpler than multi-bodies ones [126].

Many mechanisms have been built to emulate the role of pectoral fins of fish in locomotion [135]. Pectoral fins can provide various motions of flapping, rowing, and cupping [136, 132]. Due to the objective of pectoral fins in different fishes, the complexity of these fins varies in different species as well [135]. Pectoral fins have been used in flapping mechanisms for propulsion in rays [137]. This attracted researches to emulate rays' pectoral fins in various studies [129, 138, 135, 139, 140, 141]. Pectoral fins of bluegill sunfish can exhibit much more complex motions including rowing and cupping [136]. Due to high complexity of this pectoral fin, the exact imitation of these motions requires complex, high degree-of-freedom mechanisms [132]. In many studies, pectoral fins have been used alongside caudal fins for gliding, diving and depth control [126, 124, 121, 142, 122, 143].

According to [120], artificial intelligence is integrated in underwater vehicle control with two objectives (i) learning fishlike swimming and (ii) motion optimization. Two methods of bionic learning control and Iterative Learning Control (ILC) have been mainly employed in learning fishlike swimming. The objective in bionic control is to combine the advantages of both trajectory approximation and neural-based control in

order to generate different swimming patterns [144, 145, 146]. ILC is mainly used to achieve real-time control of robotic fish due to the simplicity of the algorithms with model-free properties [147]. Motion optimization is used widely throughout robotics to improve locomotion performance. This method is used toward improving the performance of robotic fish in terms of speed, efficiency and maneuvering control [120]. Different algorithms have been used by roboticists for motion optimization. For example, a combination of dynamic model and Particle Swarm Optimization is used in [148]. Zhou *et al* used Genetic Algorithm (GA) for optimizing maneuver parameters of undulatory swimming of a fish robot [149]. The maximum swimming speed of a robotic fish was obtained by applying a combination of GA and Hill Climbing Algorithm [150].

Evolution Strategy (ES) algorithms are optimization techniques considered as practical alternatives to gradient-based methods which suffer from converging to local optimal solutions [151]. The Covariance Matrix Adaptation Evolution Strategy (CMA-ES) is a type of ES algorithms, known as a stochastic method for numerical optimization of nonlinear and non-convex optimization problems [152]. Using the CMA-ES in practical experiments has many advantages in comparison with other metaheuristic and search-based algorithms. On the other hand, the main disadvantage of the CMA-ES is its computational complexity which originates from the covariance matrix self-adaptation and decomposition in this algorithm [153]. In a recent, similar study conducted in [154], the CMA-ES algorithm has been employed to optimize the controller for travel speed control of a Knifefish-inspired soft robot. The authors of that paper selected CMA-ES algorithm due to its short evaluation time compared to other evolutionary strategies. Using the CMA-ES algorithm to improve convergence rates can have practical benefits in robotic systems as well, including increasing the service life of motors, bearings, and gears, which can be overloaded

during training.

In this study, we introduce (i) a novel fin design based on a 2-DOF spherical mechanism facilitated by laminate design concepts that minimizes manufacturing costs typically associated with spherical, parallel mechanisms. (ii) Kinematic models that allow us to understand the workspace and input-output transforms of this new pectoral fin mechanism. (iii) A design for a fish-inspired robot, which combines one caudal and two pectoral fins. The resulting five degrees of freedom may be described with a high-dimensional set of locomotion/gait parameters. To address this issue, we have also (iv) come up with strategies for identifying high-performing sets of these gait parameters with an online learning strategy (CMA-ES). Our oratory-based experimental testing setup often differs from the intended goal environment in key ways (turbulence, water speed, type of data-collection setup, i.e., force instead of trajectory). This has also led us to (v) develop strategies for finding gait parameter sets that have a high-degree of correlation in performance between the lab and the intended operating environment. These efforts have resulted in a design and optimization workflow for robots that works well in niche environments, while permitting the majority of development, data collection, and characterization in the lab.

## 6.2 Fish-inspired Robot for Extreme Environments.

We have developed and trained a robotic fish capable of swimming in extreme environments (Fig. 6.1a). The robotic fish propels itself by using its pectoral and caudal fins. Due to the ease of manufacturing, we are using a 3D printed PLA body, but our fins and joints' transmissions are built by laminated techniques and may be considered soft.

FIRE is designed to be used in the maintenance of water canals with a width of as low as 3 feet. These canals have high currents and turbulence. In order to train the

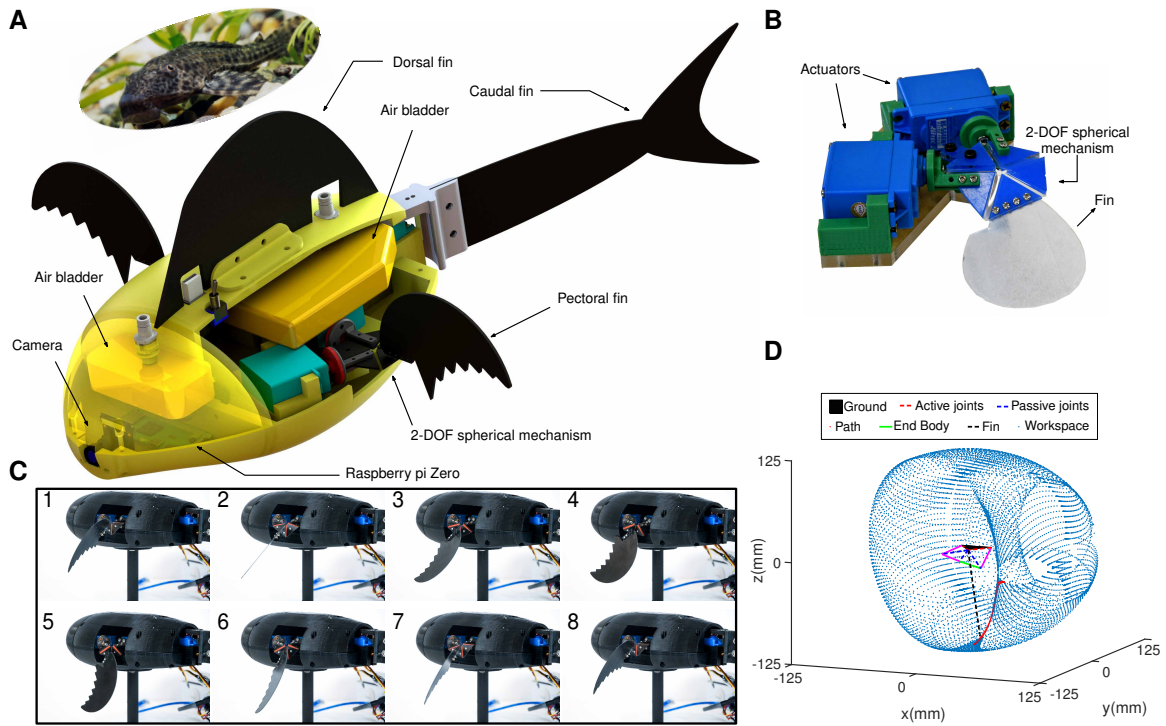


Figure 6.1: **FIRE**, the suckermouth catfish-inspired robot. (a): System overview (photo of suckermouth cat fish is derived from[155]). (b): 2-DOF spherical mechanism exploited in FIRE’s pectoral fins which is built using laminated techniques. (c): Extracted frames of a pectoral fin’s propulsion for turning (result of training in pectoral fin’s attachment selection). (d): Schematics of the pectoral fin’s 2-DOF spherical mechanism, its workspace (blue dots), and end-effector path in previous motion (red dots).

robotic fish to maneuver in this environment, a training workflow has been proposed.

### 6.2.1 Design and Manufacturing of Robotic Fish

FIRE is inspired by the suckermouth catfish due to its similar functionality with our fish robot goal task. These bottom-dwelling creatures, with their wide, flat bodies, are evolved to live and swim along surfaces and feed, while avoiding higher currents

above them. We have mimicked this flat body plan in designing FIRE.

We have embedded three types of fins evocative of a catfish’s pectoral, caudal and dorsal fins. While two sets of pectoral fins are laterally placed in the center of the robotic fish, its caudal fin is placed at its posterior (Fig. 6.1a). A passive dorsal fin is located on the top of the robotic fish to resist body rotation due to caudal fin motion. The pectoral fins are designed so their neutral position mimics the shape of the sucker-mouth catfish fins in a passive state. In designing the robotic fish body, we have reserved space for electronics, a swim bladder for buoyancy, and a sensor suite. At this stage, the bladder is inflated prior to deployment in order to set the fish in a neutrally-buoyant state.

### 6.2.2 *Pectoral Fin: 2-DOF Mechanism*

We have designed and constructed a 2-DOF spherical parallel mechanism (also known as a 5-bar mechanism) to move the pectoral fins (Fig. 6.1b). The advantage of using this parallel mechanism is that the actuators are mounted within the body as opposed to a serial mechanism design; this reduces the torque requirements of our servos while simultaneously permitting a more compact, lower-drag design. This spherical mechanism has been scaled down via laminate fabrication techniques, whose benefits are discussed below. The mechanism is designed to be flat in its neutral state and uses a symmetric design in which the angles between all joints are 72 degrees. This flat, symmetric design permits a more compact design (as opposed to its most popular implementation of this mechanism [55]) as well as enabling us to attach and evaluate a two-body fin.

The two degree-of-freedom mechanism used in FIRE uses laminate techniques for creating a spherical five-bar linkage. Laminate devices are typically manufactured by an iterative process whereby a number of different flat materials are individually cut

and laminated together to create a traditional kinematic mechanism connected by flexure joints. This process has a number of benefits. A number of design variations may be rapidly produced, permitting design variations to be analyzed quickly; second, the low-cost of materials means that such devices can be reproduced quickly and at lower costs than traditional linkages, making this device design compatible with our goal to deploy a low-cost “school” of robotic fish for maintaining water canals.

## 6.3 Training the Robotic Fish

### 6.3.1 *Training Workflow*

Figure 6.2a highlights a workflow we have used to balance the competing needs of testing in a repeatable environment while learning how our device will operate in more realistic settings. This is informed by the current state and limitations of learning algorithms and the time and resources needed to learn motion patterns for complex, high-dimensional systems. The objective of the proposed workflow is to find fin-based gaits that enable the robotic fish to maneuver in various user-specified ways consistently across different environments. This objective is inspired by newborn animals. In animals such as fish and sea turtle hatchlings, which can swim to find food or hide from predators immediately at birth. These animals can move using optimal locomotion patterns without receiving any parental care or training.

An experimental setup has been designed as a non-ideal, extreme environment in which the robot may be mounted. A variety of gaits may be tested on the fish by varying a number of key gait parameters and then measuring the forces produced over a number of cycles (for more details refer to material and methods section). We have adopted a force-torque generation evaluation as the criteria for robotic fish performance, a commonly-used technique for evaluating fish robots’ performance [156,

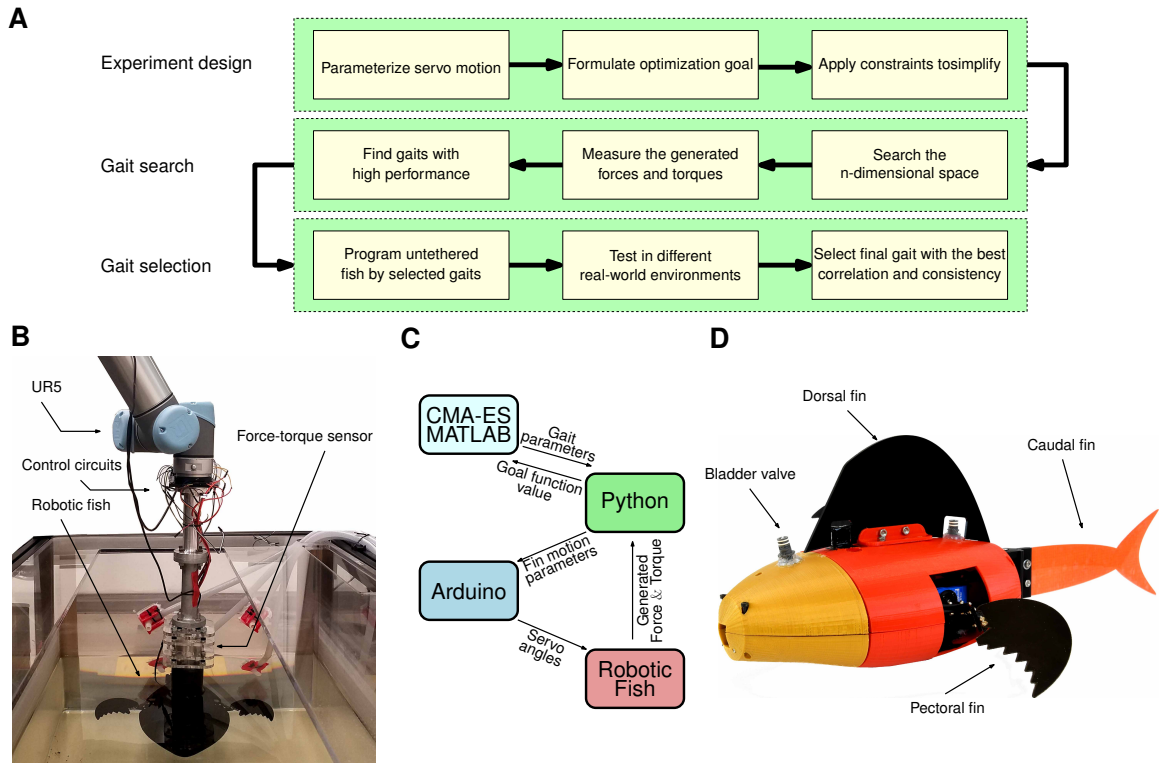


Figure 6.2: **FIRE's training workflow.** (a): Workflow proposed for training FIRE. (b): The experimental setup. (c): Experimental implementation of on-line CMA-ES algorithm. (d):The untethered FIRE.

132].

FIRE's actuators have been commanded to follow sinusoidal patterns. This makes it possible to create motion with a small number of parameters, simplifying the training process.



The servos' commanding signals are defined as:

$$\begin{aligned}
\text{Right pectoral fin: } \theta_1 &= \beta_1 + \alpha_1 \sin(2\pi f_1 t) \\
&\theta_2 = \beta_2 + \alpha_2 \sin(2\pi f_2 t + \phi_1), \\
\text{Left pectoral fin: } \theta_3 &= \beta_3 + \alpha_3 \sin(2\pi f_3 t) \\
&\theta_4 = \beta_4 + \alpha_4 \sin(2\pi f_4 t + \phi_2), \\
\text{Caudal fin: } \theta_5 &= \beta_5 + \alpha_5 \sin(2\pi f_5 t),
\end{aligned} \tag{6.1}$$

where  $\theta_i$  is actuators' angles and  $\beta_i$ ,  $\alpha_i$ ,  $f_i$ , and  $\phi_i$  are the sinusoidal signals' angular offset, amplitude, frequency and phase shift, respectively. There are 17 parameters to control the maneuver of the robotic fish fins.

We have searched the parameter space to find optimal gaits for individual swimming criteria. While the whole space may be searched for a low-dimensional space, we utilize CMA-ES as a way to find ideal parameters in a high-dimensional space for which finding global optimal solutions is nearly impossible.

The goal of the workflow is to find a set of gait parameters that perform well against a user-supplied performance objective and repeatable over many cycles in different situations. Though we prefer to perform testing in the lab, the fish must be able to perform a variety of specialized maneuvers, including turning, diving, and swimming upstream, in a canal where turbulence and current are present. The performance of any selected gait must, therefore, have a high correlation in performance between laboratory experiments and the real-world across many different locomotion goals. Hence, our workflow evaluates more than one top-performing gait for a given maneuver using the untethered FIRE (Fig. 6.2d). The gait with consistently high-performing swimming across lab/outdoor environments is then selected for each swimming criteria.

### 6.3.2 *Experimental Setup*

We have designed an experimental setup that samples the thrust generated by the robotic fish. An ATI mini-40 force-torque sensor has been installed to the distal end of a UR5 robotic arm, which is used to create motion paths. An aluminum extension rigidly connects to the dorsal side of the fish, transmitting torques and forces generated by the robot and its motion through the water back to the load cell. The UR5 itself is mounted next to a fish tank that is 4 feet long, 2 feet wide, and 2 feet deep, and is capable of moving on a straight path with constant speed. This can be used to create a variety of conditions in the water such as simulating an opposing current (Fig. 6.2b).

The size of the tank, the dimensions of the robot, and the speed of the commanded motion paths leads to the generation of nonuniform vortices in the water, which adds noise to the system but helps train the robotic fish for non-ideal conditions. Since these vortices can randomly affect thrust generation, tests are typically repeated for each set of parameters to minimize this effect. The sampling times for each test has been calculated based on the propulsion frequency (period), the range of the UR5's path, and velocity of the UR5's end-effector. By varying the sampling frequency we can maximize the number of gait cycles within the limited range of a single test. The speed of the UR5 is also limited to 0.1 m/s during fin-based locomotion trials and 0.6 m/s when the fins are not actuated.

### 6.3.3 *Convergence Adaption Matrix Evolution Strategy*

The CMA-ES algorithm is known as a powerful optimization algorithm which outperforms other conventional evolutionary heuristic search methods, e.g. Genetic Algorithm (GA) and Particle Swarm Optimization (PSO), specifically for not only

non-convex and ill-conditioned problems but for noisy objective functions [157]. Moreover, it provides a robust and fast search mechanism which makes this algorithm practical for real-world applications [158]. In the CMA-ES algorithm, the next search points in the available search space are obtained by a normal distribution, which is itself determined by the covariance matrix, mean, and standard deviation. The objective function can be represented by its contour lines. This algorithm modifies the covariance matrix so that the normal distribution is fit to the contour lines [159]. Consequently, this strategy increases the likelihood of finding optimal solutions.

In our experimental tests, we have implemented the CMA-ES algorithm to find optimal values for actuators' gaits, i.e.,  $\beta_i$ ,  $\alpha_i$ ,  $f_i$ , and  $\phi$  (Fig.6.2c). These parameters control the search behavior of the algorithm including the parameters listed in Table 6.1. We have tuned the parameters empirically based on experiments and observations so that the CME-AS would find optimal solutions in acceptable time and accuracy ranges. At each iteration, the suggested solutions by the CMA-ES algorithm can appear out of the feasible range of variables restricted by the mechanical constraints and limitations of the servo motors. Hence, we have defined a penalty function in order to exclude non-feasible solutions. The penalty function gradually confines the large search space to the feasible solution space of the problem. Conse-

Table 6.1: The tuned parameters for the CMA-ES algorithm.

<b>Parameters</b>	<b>Value</b>	<b>Parameters</b>	<b>Value</b>
Population size	60	Number of effective solutions	16.57
Number of variables	6	Initial step size	0.67
Maximum iteration	1000	Step size dampening	2.66
Number of parents	30	Learning rate	0.36

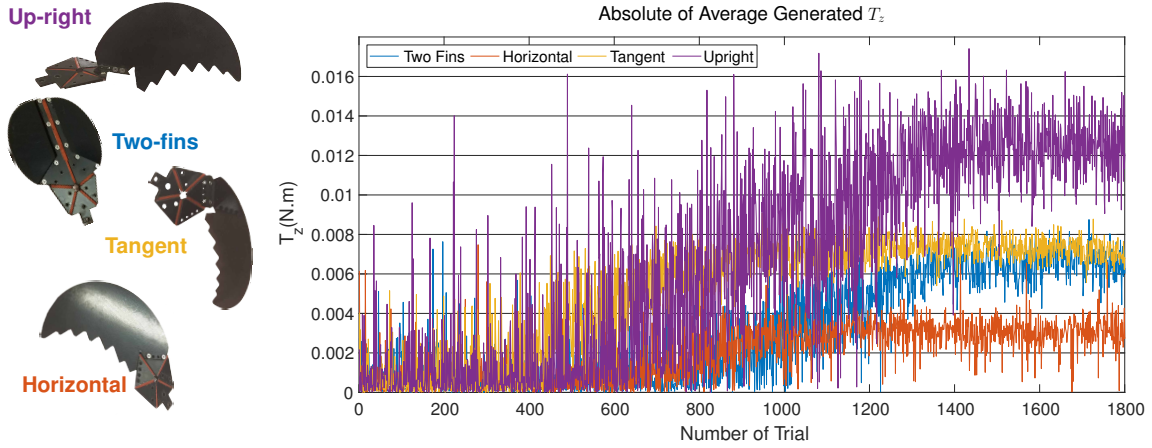


Figure 6.3: **Pectoral fins' attachment selection.** Value of goal function for CMA-ES training trials when UR5 is fixed (simulating still water) for different attachments.

quently, the number of suggested non-feasible solutions decreases as the number of iterations increases.

#### 6.3.4 Selection of Pectoral Fin Attachment

The proposed mechanism for the pectoral fin is a 2-DOF spherical mechanism capable of creating rotation about two axes simultaneously within a finite circular workspace. The fin's attachment to the mechanism to the 5-bar mechanism is important because it impacts the fin's range of motion within that workspace. Hence, three different attachments for the spherical mechanism have been designed, built, and tested. In addition, a two-bodied fin design has been investigated. CMA-ES has been used to train each fin design for maximizing turning torque, and the best fin design has been selected based on the result obtained. Figure S1 illustrates the different fin designs, as well as the results of CMA-ES training for maximizing the turning torque generated by pectoral fins' propulsion.

## 6.4 Results

FIRE can achieve swimming speeds of 0.385 m/s (0.71 body length per second)—using its caudal fin and can perform pure rotation by utilizing its pectoral fins. The turning speed in this rotation is 15.68 deg/s.

### 6.4.1 Turning

Being driven by the goal of maneuverability in tight spaces, a priority for FIRE is to minimize its turning radius. Using its pectoral fins, FIRE can perform a 360-degree turn with a near zero radius. Figure 6.1b illustrates the pectoral fin’s mechanism. The mechanism’s workspace and a sample time-lapse of its motion are shown in Figs. 6.1c and d, respectively. We have concluded in the previous section that the robotic fish cannot perform sharp turns by thrust produced by the caudal fin.

To train the robotic fish for sharp turns, we have carried out a study to maximize the amount of turning torque generated by the pectoral fin’s propulsion. Turning performance has also been used as the selection criterion for selecting the fins’ optimal attachment (for more details refer to material and methods section).

FIRE achieves its best turning performance using both pectoral fins in conjunction with each other. We considered two different cases in our search for the best gait’s parameters. In the case of simulating still water, the UR5 is stationary; however, in the second case, it is commanded to move along a straight path at 0.1 m/s to simulate current. In both cases, the test is repeated three times for each set of parameters.

FIRE’s pectoral fins are parameterized in such a way that their motion is synchronized, but along an opposite path, meaning that when one is moving clockwise, the other one is moving counterclockwise. This is achieved by introducing following

relationships:

$$\begin{aligned} \alpha_1 &= -\alpha_3, & \alpha_2 &= -\alpha_4, & \beta_1 &= -\beta_3, \\ \beta_2 &= -\beta_4, & f_1 &= f_2 = f_3 = f_4, & \phi_1 &= \phi_2 \end{aligned} \tag{6.2}$$

We believe this helps the fins' motions magnify generated torque rather than canceling them out. This assumption also reduces the gait parameter space by half, to seven from fourteen.

Figures 6.4a and b show the turning torques generated in the CMA-ES search for the best gaits in still and moving water, respectively. Based on the peak generated torques and repeatability (marked by red star in Figs. 6.4a and b), 8 unique gaits have been selected for testing in real-world environments by the untethered fish and the best motion gait is selected based on its performance in different environments (marked by green star in Fig. 6.4a). Figure 6.4c illustrates the torque generated through time by the selected gait. Using this motion pattern, FIRE can perform a 360-degree turn with a near zero radius and the average speed of 30.25 deg/s in our two foot wide experimental setup (Fig. 6.4d), despite the presence of turbulence caused by waves reflected by the tank wall. It should be mentioned that the caudal fin is detached to permit FIRE to turn in the tank without hitting walls. Figure 6.4e shows the performance of the same gait in a pool. While the turning speed is reduced to 15.68 deg/sec, the gait motion can reliably turn in the environment, even when it is subjected to turbulence (Movie S1). The authors believe that the slower turning performance of FIRE can be mostly attributed to addition of the caudal and dorsal fins on the untethered robot.

For turning with a larger radius, FIRE can utilize its pectoral fins in conjunction with its caudal fin. While the robot can use the gait selected above in combination with its caudal fin for larger-radius turning, we propose and study a more energy-

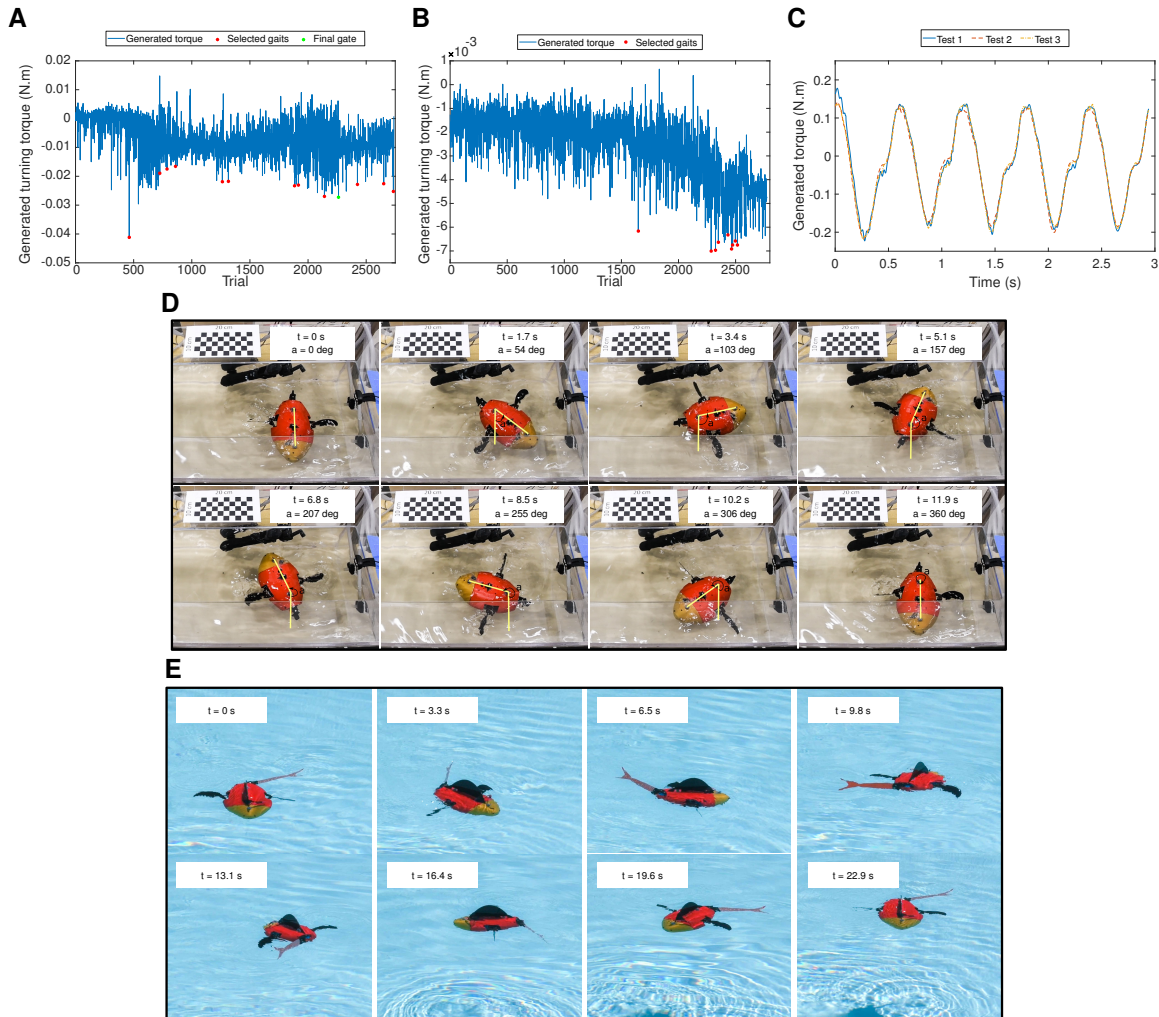


Figure 6.4: **FIRE's turn training.** (a): Value of goal function for CMA-ES training trials when UR5 is fixed (simulating still water). (b): Value of goal function for CMA-ES training trials when UR5 is moving with 0.1 m/s speed (simulating water with current). (c): Turning torque generated in time for selected gait. (d): Extracted frames of FIRE turning in the 2-foot wide tank. (e): Extracted frames of FIRE turning in the pool.

efficient approach to accomplish this goal. In this approach, the robot’s pectoral fins are commanded to move to different fixed configurations, producing different drag forces. This asymmetric drag on the robot’s body enables FIRE to turn gradually, while saving power by avoiding continuous actuation of the pectoral fin servos. As the objective is to find the configuration that maximizes turning torque at various speeds, individual tests are repeated three times per parameter set, once at 0.1, 0.2, and 0.3 m/s each. The cost function has been defined as the summation of average turning torque generated across all three speeds. The selected configuration and the training procedure is shown in Figure S2.

#### 6.4.2 *Swimming Forward*

A series of studies have been run to improve FIRE’s forward thrust generation and swimming speed by finding the best gaits for both caudal and pectoral fins. The next sections discuss several approaches for maximizing swimming speed, including minimizing body drag, optimizing the caudal fin gait, and learning whether the pectoral fins can contribute to thrust generation as well as for turning.

Since we have adopted a force-torque generation evaluation as the criteria for robotic fish performance, each study measures the amount of forces applied to the body of the fish at different speeds using our experimental setup. This measurement enables us to understand the swimming performance of the robotic fish when moving freely. Body drag is measured by commanding the robotic arm to travel the tank length at a number of fixed speeds and at each speed, the average drag force on the body is sampled (Fig.6.6a). It should be mentioned that in this test, all fins are in their neutral configuration ( $\alpha_i = \beta_i = 0$ ).



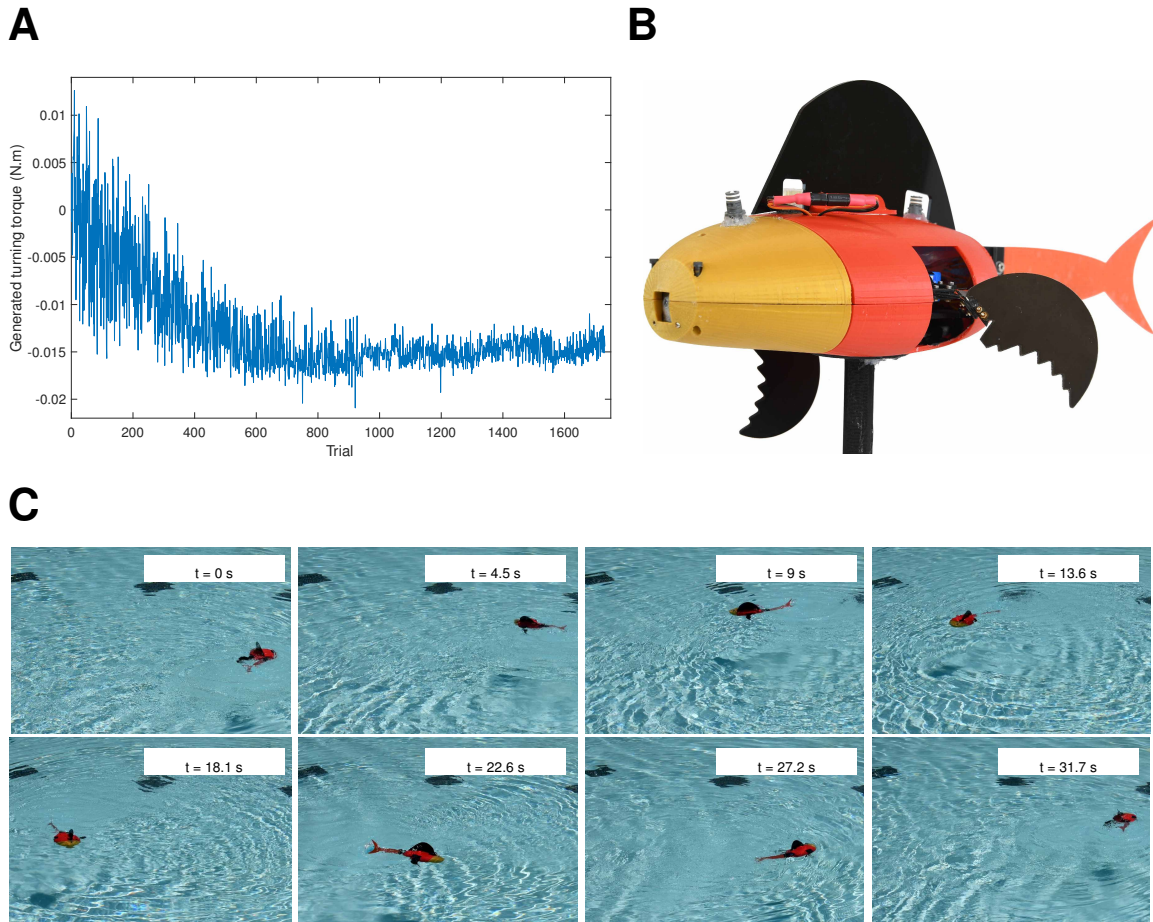


Figure 6.5: **FIRE's large turning radius training.** (a): Value of generated turning torque for CMA-ES training trials when UR5 is moving with 0.1 m/s speed. (b): FIRE in its turn left configuration. (c): Extracted frames of FIRE turning left.

### Body Drag Minimization

The pectoral fin configuration affects the amount of drag exerted on the robotic fish. Our training algorithm has succeeded to reduce the sum of drag to 60 percent across different speeds by finding the optimum configuration of pectoral fins. The obtained results show that the summation of drag value across all speeds has been reduced from 2.5 N in neutral state to 1.5 N in minimum-drag state (Fig. 6.6b). In order to minimize body drag, we can use the training algorithm to minimize drag by finding

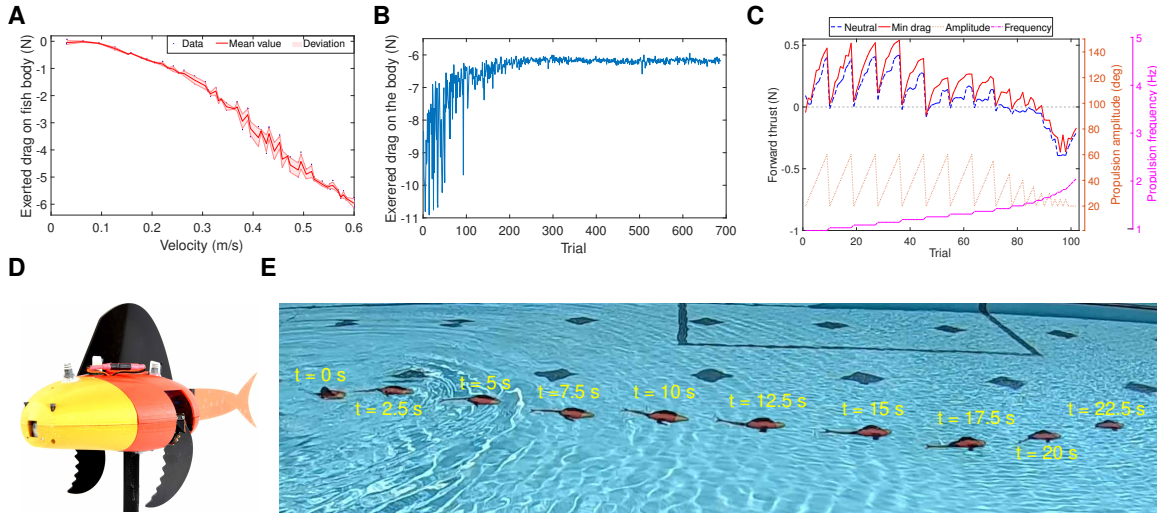


Figure 6.6: **FIRE's swimming forward training.** (a): Value of drag exerted on FIRE's body in different speeds. (b): Value of goal function for CMA-ES training trials in minimizing the drag exerted on FIRE's body. (c): Spanning gait's parameter space for caudal fin thrust generation when the UR5 is moving with 0.1 m/s speed and FIRE pectoral fins are in neutral (blue) and minimum-drag (red) configurations. Gait's amplitude and frequency are shown in orange and pink, respectively. (d): FIRE in its minimum drag configuration. (e): FIRE swimming forward in minimum drag configuration.

fixed servo positions that put both fins in an orientation that minimizes drag. The objective is to find the configuration that produces minimum drag across various speeds that the caudal fin can realistically achieve.

Individual tests are repeated three times per parameter set, once at 0.1, 0.3, and 0.6 m/s each. The cost function has been defined as the summation of average drag exerted on the robotic fish in all mentioned speeds. Figure. 6.6 shows FIRE in its minimum drag configuration.

## Forward Thrust Generation with the Caudal Fin

FIRE can swim forward with the maximum speed of 0.385 m/s by relying solely on its caudal fin (Movie S1 and 6.6e). This mechanism consists of a servo motor moving a flexible, fin-shaped plastic sheet back and forth to produce thrust. Experimental results show that the tail performs best when  $\alpha_5 = 60$  deg and  $f_5 = 1.4$  Hz. Similar to the result reported in [160] the thrust produced by the caudal fin is controllable when  $f_5 = 1.4$  Hz. The results also confirm our prior study [160] that the caudal fin is ineffective for maneuvering in tight spaces. Hence, the caudal fin's motion is therefore set to be symmetric ( $\beta_5 = 0$ ). The three-dimensional space of function parameters ( $\alpha_5$ ,  $\beta_5$ , and  $f_5$ ) has been spanned by measuring the average of sampled thrust produced by the caudal fin across one cycle. This process has been explained in [160] for still water, but this study expands that search by considering the effect of water's opposing currents by simulating water current by commanding the UR5 arm to move at 0.1 m/s. Two different cases of pectoral fin orientations have also been considered throughout the caudal fin study. These cases are neutral and minimum-drag orientations of the pectoral fins. Figure 6.6c illustrates the value of thrust produced by caudal fin based on the gait's amplitude (orange) and frequency (pink) when FIRE pectoral fins are in neutral (blue) and minimum-drag (red) configurations. The maximum thrust produced by the caudal fin increases by almost 15 percent when the pectoral fins have been moved from their neutral to the minimum-drag configuration.

After fitting the drag and thrust generation plots, we can estimate that the caudal fin can achieve a forward velocity of 0.16 and 0.18 m/s when the pectoral fins are in their neutral and minimum-drag configurations, respectively. Considering that the robotic fish has attachments that increase drag during laboratory experiments, the

swimming speed achievable by the untethered robotic fish is expected to be more than the value that has been estimated by matching the body drag and the caudal fin’s thrust generation.

### Forward Thrust Generation with Caudal and Pectoral Fins

The purpose of this next study is to improve forward thrust by utilizing the pectoral fins’ propulsion. The obtained results show that in our current design and configuration, the pectoral fins are not capable of improving the thrust produced by the caudal fin. These results are compatible with Lauder *et al.* observations of pectoral fins’ propulsion being used in low speed swimming [132]. We have considered different cases for this objective. In the initial case, we have performed an unconstrained full search. This has resulted in a gait search in the 16-dimensional parameters space (two for symmetric caudal fin propulsion and two sets of seven variables for each pectoral fin). In this test, the for each set of parameters the test is repeated two times and the UR5 moving speed is 0.1 m/s. The obtained results show that the training algorithm has not converged after one hundred iterations (Fig. S3A). Considering that on average, each iteration takes a hundred minutes, the study has not been carried out for more iterations. Instead, some simplifications have been applied to help the training algorithm to converge. The caudal fin has been set to produce maximum forward thrust and the pectoral fins have been commanded in a way that they have symmetric propulsions (Fig. S3B). This is achieved by introducing following relationships:

$$\begin{aligned}
 \alpha_1 &= \alpha_3, & \alpha_2 &= \alpha_4, \\
 \beta_1 &= -\beta_3, & \beta_2 &= -\beta_4, \\
 f_1 &= f_2 = f_3 = f_4, \\
 \phi_1 &= \phi_2
 \end{aligned}
 \tag{6.3}$$

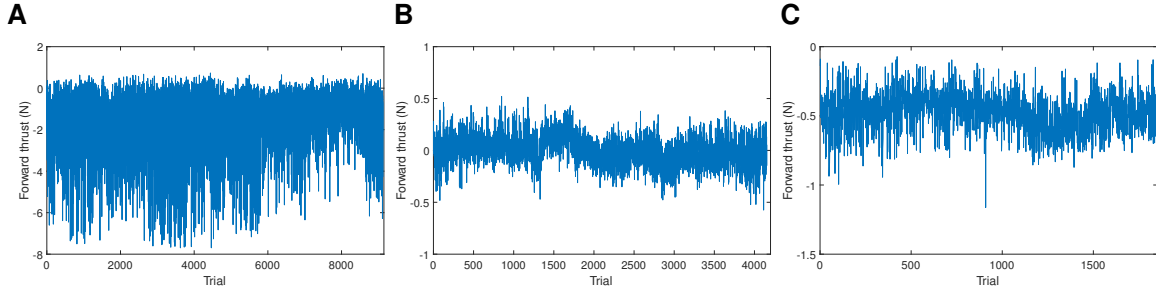


Figure 6.7: **Forward thrust generation by pectoral fins.** (a): Unconstrained full search (16-dimensional space). (b): Pectoral fins’ symmetric propulsion when the caudal fin is actuated by its best motion gait. (c): Pectoral fins’ symmetric propulsion when the caudal fin is not actuated

For each set of parameters, the test is repeated three times while the UR5 moving speed is set to 0.1 m/s. The obtained results show that all tested gaits have values less than the thrust achievable by the caudal fin alone. Finally, another case has also been studied to evaluate the ability of the thrust generation of swimming with the pectoral fins with the caudal fin disabled. The highest performing gait is only capable of overcoming FIRE’s body drag when the UR5 is commanded to move the fish at 0.1 m/s speed (Fig. S3C). This result shows that the symmetric pectoral fins’ propulsion can produce only limited forward thrust in certain circumstances; the maximum speed achievable is around 0.1 m/s.

## 6.5 Discussion

In this study, we have introduced a robotic fish that can utilize complex gait patterns via two 2-DOF pectoral fins and one caudal fin to swim in extreme environments. This is accomplished with a new two degree-of-freedom pectoral fin mechanism, whose parallel architecture permits all actuators to be integrated within the body of the fish, maintaining a more bio-inspired and lightweight fin design as well as

a more streamlined body. We have carried out a comprehensive series of gait selection studies across all five degrees of freedom via a novel experimental setup design that uses a robotic arm to simulate water current. The six-dimensional set of forces and torques generated by the fins' motion has been used as the criteria for evaluating locomotion performance across a number of different goals. By parameterizing actuator motion as a set of sinusoidal functions, a thorough search has been performed using an on-line evolution strategy to find the best sets of propulsion parameters for different maneuvering objectives.

In addition to the platform design and gait selection, we have trained FIRE for use in extreme environments. To do so, we have trained the fish in a non-ideal lab setup and then we have followed up the training by evaluating the top-performing gaits in different real-world environment. Finally, we have selected the final gait that shows high repeatability in its performance. We believe that this method has advantages over performing the whole training in the real-world environment, because it avoids extra complexity of automating repeatable tests in real-world environments. In contrast to previous fish-inspired robotic platforms, the approach proposed in this study can be used to train robotic fish for extreme environments in a compact and efficient lab setup. Also, this method avoids the extra cost and labor lies within production of an out-door experimental setup. Performing an in-lab training alone cannot guarantee a good performance regarding real-world tests, however, these are the reasons behind the proposed training workflow that pairs the advantages of using machine learning in an non-ideal lab setup, and the real-world validation to find gaits that work well in a variety of environments that feature disturbances, currents, and reflected waves.

While this training approach has been effective, some challenges should be addressed. First, due to uncertainties caused by the non-ideal testing environment,

data is not always repeatable. To address this we have repeated the tests more than one time for each set of gait parameters. To improve repeatability we must let the water settle between subsequent trials to minimize the effect of vortices produced by previous trials. Both of these factors increase the total run time and result in relatively long training tests that can take a day for parameter sets with a low number of dimensions (in the range of one to three) and a week for parameter sets with a high number of dimensions (in the range of seven to ten). Another consideration is that the training failed to converge within an acceptable time for cases that have parameter sets with more than ten variables. This has been addressed in current work by introducing constraining relations between gait parameters to reduce the size of parameters' space. Currently, these relationships are manually established; future work should use experimental design techniques in conjunction with machine learning to automate this process.

Although pursuing data-driven approaches in the presence of disturbances is challenging, this study shows that modern training algorithms such as CMA-ES are capable of finding sub-optimal gait parameters for robots in non-ideal environments, as long as they are used in combination with external validation such as that provided by our workflow as well as focusing constraints that are crafted to limit the dimensionality of the search.

Knowing the advantages and limitations of this training workflow has provided us with the opportunity to explore a variety of different body shapes and scales as well as different fin mechanisms and attachment strategies. Being validated by the obtained results for different cases of this study, this approach shows high repeatability in final results. These advantages are achieved by combining the evolution strategy training with our unique experimental setup. In contrast with prior work, using the robotic arm instead of a water tunnel in our force-measurement approach not only helps the

robotic fish to train in a noisy environment but also helps keep the experimental setup compact enough to fit in a typical laboratory setting.



## Chapter 7

### LEVERAGING VARIABLE STIFFNESS OF CURVATURE-INDUCED BEAMS IN DEVELOPING SOFT ROBOTS

This chapter explores a technique to leverage curved surfaces for producing preferential buckling that can be used to create forward thrust in flapping-wing devices and simplify the complexity of swimming devices like those mentioned in prior chapters. We present a novel concept for using anisotropically buckling beams in robot locomotion, facilitated via an analytical and finite-element-based analyses. We demonstrate that with symmetric flapping inputs from a motor, buckling beams can be used to generate forward thrust, power, and work while reducing the drag associated with the recovery phase of the flapping gait. Our analysis includes experimental data that measures the forces produced by wings flapping in air and water. The results show a clear difference in the work produced between buckling and non-buckling curved beams and shows that the average force and work produced by buckling wings over a number of cycles with symmetric flapping is nonzero. This has been demonstrated on a new, two-fin swimming robot that, through the use of this phenomenon, is capable of reaching an average speed of 0.1 m/s. This work makes it possible for simple motor inputs to produce complex swimming gaits through careful consideration during the mechanical design phase for swimming robots.

#### 7.1 Introduction

This study explores the role curved surfaces and local buckling can play in the generation of asymmetric locomotion forces for swimming and flapping robots. More specifically, we study how curved slender beams buckle preferentially in one direction

under symmetric motor inputs, utilizing this phenomenon to design flapping fins and wings that produce forward thrust and net positive work. We further seek, through a knowledge-based exploration of the design and gait parameters key to understanding this effect, how to exploit the phenomenon of one-sided buckling to create complex flapping patterns that create positive average work across multiple gait cycles in physical prototypes that demonstrate and validate this effect.

Figure 7.1 illustrates the overall concept of the proposed wing mechanism. In this design, a wing (or fin) is attached to an electric servo via a compliant, curved beam that buckles at two different points along the positive and negative portion of its force/displacement curve, corresponding to opposite and equal sense bending. Fig. 7.1(a) shows that controlling the amount of force exerted on the end of the beam in positive and negative directions can avoid buckling in both directions, permit buckling in one direction, or buckle the beam in both directions.

When actuated in a fluid such as air or water, it is our intent to show that the dynamics of powered, symmetric flapping results in one of three general cyclic flapping patterns for the system in question. The first regime is typified of slow flapping below the buckling limit in either direction, where drag and inertial forces remain low (Fig. 7.1(d)). In this case, the curved beam acts like a simple bending beam; little asymmetric behavior is observed in its flapping path or in the average thrust generated over a cycle (Fig. 7.1(e)). In the second regime – the primary focus of this study – the flapping velocity is sufficient to buckle the beam in the equal-sense bending direction but not in the opposite direction. This results in the beam undergoing large deflections about the buckling point during roughly half of its flapping cycle, which permits the larger surface area of the wing to travel nearly parallel with the direction of motion, rather than perpendicular. This different angle of attack results in reduced drag forces on the wing during the recovery segment of

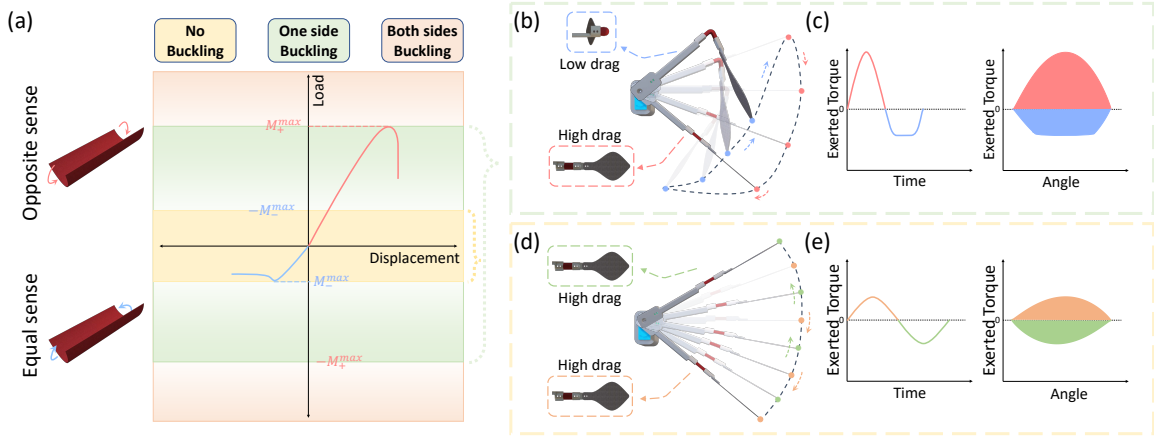


Figure 7.1: Conceptual illustration of the proposed technique. (a) Different regimes of a wing with curved beam. (b) Motion of wing in one-side buckling regime. (c) Torque exerted by the wing on a fixed frame with respect to time and joint angle for one-side buckling regime. (d) Motion of wing in no-buckling regime. (e) Torque exerted by the wing on a fixed frame with respect to time and joint angle for no-buckling regime.

the stroke (Fig. 7.1(b)). As the cycle re-enters the power stroke, drag causes the wing to open back up in the other direction and remain perpendicular to the direction of motion. This difference in overall drag experienced by the wing in power and recovery phases generates non-zero average work over a single flapping cycle, even with a symmetric input from the motor (Fig. 7.1(c)). In the third regime, the beam buckles in both directions due to high torques exerted by the motor that increase the drag and inertial forces experienced at the tip of the beam past the buckling limit in both directions. While also a potentially useful regime, we have observed that, in some cases, buckling in the opposite sense resulted in plastic deformation and rapid failure of the beams. Thus, we have limited our current exploration to the first two regimes in this study.

Many structures in nature utilize flexibility and curvature to enhance locomotion capabilities. In some cases, observations of active curvature or cupping in

fish [161, 162], three-dimensional curvature in batoids [163], and flexible flapping of insect wings [164] has been identified as a strategy proposed for optimizing locomotion efficiency throughout a stroke. Walker et al. suggest that the emergence of rowing vs flapping behavior in biological locomotion is a function of viscosity-dominated forces at low Reynolds numbers [165].

Buckling is also used in the natural world for animal locomotion and other tasks. Camber, deformation, and the “umbrella effect” has been studied in the desert locust [166, 167, 168]; like an umbrella buckling in a gust of wind, hindwing camber has been observed to rapidly invert between up-stroke and down-stroke. Young et al. finds that power economy increases 15% when considering the effect of camber in flapping models [168]. Both [166, 167] identify the buckling of venous structures as the principal mechanism which permits this inversion. Buckling has also been identified as the principal mechanism for successful locomotion in bacterial flagella, [169], arthropod joints [170], and Venus flytraps [171, 172, 173], and is used by ladybird beetles as a mechanism to fold and store wings inside their shell [174].

A basic introduction to buckling is typically found in introductory mechanics of materials texts in engineering. Buckling is typically considered a source of catastrophic failure in structures, and models for buckling [175] are introduced in order to avoid it [176, 177]. However, buckling has several characteristics that make it potentially useful in mechanisms and robotics. First, it does not always imply material yield; rather, small geometric perturbations lead to drastic reductions in load-carrying capacity irrespective of the stress in the material. In general, buckling occurs when a material exhibits a nonlinear and often rapid drop-off in force due to small changes in shape. Once a buckling condition is met, the material deforms quickly, resulting in a new force/displacement curve with a much smaller stiffness coefficient. Sometimes the stiffness coefficient can become negative, leading the device to rapidly reconfigure

to a new stable state; this condition is referred to as a “snap-through instability” in the literature [178, 179]. In the design process, buckling is typically associated with failure and avoided. In some cases – as in a tape spring or tape measure – this condition is exploited. When extended with the curved surface opposing gravity, a tape spring can support its own weight on the order of several feet. When flipped over, however, it collapses rather quickly. In addition, a tape spring is able to be rolled into a small volume without fatigue or failure. Clearly, the material properties, design geometries, and selected camber all play an important role in this device’s operation.

A variety of prior work investigates buckling and snap-through instabilities with regard to its use as a mechanical device. Work by Koh et al. demonstrates a flea-inspired torque reversal mechanism in which energy stored in a spring is released via a small perturbation in the kinematics of a mechanism [180]. In other work a venus flytrap-inspired mechanism utilizes reversible buckling to facilitate rapid inversion between concave and convex states in a SMA-actuated device [181]. In [182], a self-deployed gliding wing is made using characteristics of a curved origami facet. The use of curved facets permits the wing to deploy at its ballistic apex, resulting in an increased gliding range. Jung et al. have also proposed a gripper inspired by a caterpillar’s proleg that uses flexural buckling for adaptive gripping on rugged, uneven surfaces [183]. In [12], an origami-inspired structure is used to produce dual-stiffness joints by pre-stretching and sandwiching a flexible material in a multi-layer structure during fabrication to induce buckling in the presence of high forces, forming a mechanical fuse. Jiang et al. propose a mechanism to reconfigure the stiffness of tubular structures, using pinching to induce highly directional changes in stiffness [36].

In contrast to prior work, which utilizes complex, origami-inspired mechanisms or uses anisotropy for single-use deployment applications, our work seeks to leverage the simplicity of curved slender beams as passive, nonlinear elements in the active gen-

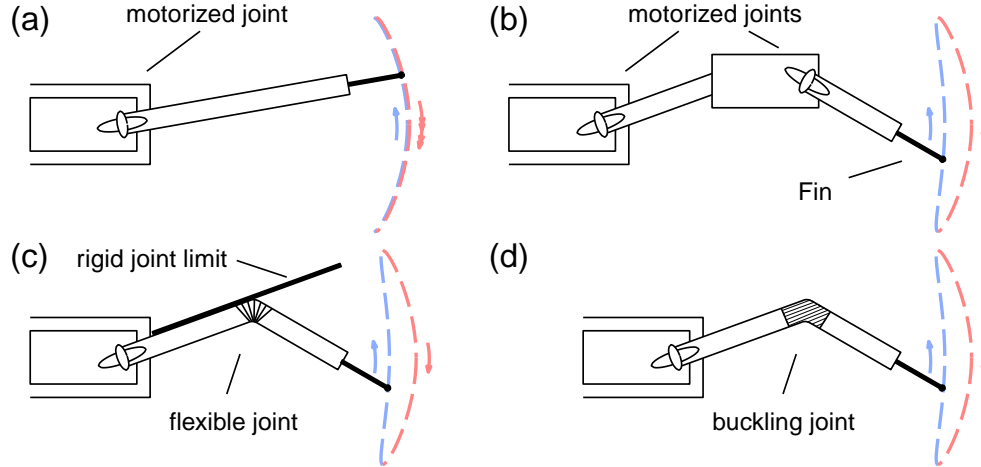


Figure 7.2: **Comparison between different methods to achieve net thrust in rowing.** (a) Variable speed actuation (b) multiple motorized joints. (c) Passive flexible joint in combination with a hard stop. (d) A compliant joint fin enhancing curved beam.

eration of thrust, power, and work via cyclic flapping. Our approach augments prior work in tape spring theory, using FEA to understand and control design parameters such as beam length, curvature, and width to influence the thrust and work generated via symmetric gait patterns. We are motivated by the simplicity of the structures we employ, and our approaches differ from prior analytical methods in that we demonstrate how the nonlinear stiffness produced by such elements is sufficient to describe the dynamic and hysteretic nature of flapping systems in fluid.

Underwater creatures exhibit several fascinating swimming behaviors; among them are feathering, rowing and flapping motions that occur in at least three different phyla. Rowing as a locomotion strategy is characterized by reciprocating motions directed in parallel with the direction of travel, while flapping is typified by motions exerted perpendicular to the direction of travel [184]. Feathering is an alternative to rowing that leverages pitching [185], making this motion more complex to model and

fabricate compared with the planar motions of rowing. Among animals that use a rowing strategy, such as the beach flea [186], backswimmer [187], and copepod [188], fish have been studied more extensively [185, 132]; more robotic platforms leveraging rowing inspired by fish can be found in literature as well. Fish oscillate their paired pectoral fins to generate thrust in their “labriform” swimming mode, and number of approaches are used by roboticists to mimic this style of swimming. In some cases, a faster power stroke and slower recovery stroke produces nonzero net thrust or moment [189, 190] at the cost of potentially increased control complexity and prolonged recovery strokes (Fig. 7.2a). Another approach uses a multi-actuation system to reconfigure for recovery [191, 192] (Fig. 7.2b). This approach introduces the trajectory hysteresis needed but can suffer from higher complexity as well as a heavier and less efficient system. Soft robotic approaches have more recently been used to demonstrate the use of flexible hinges as well. For example, flexible joints or fins are used alongside rigid joint limits to produce positive net thrust and moment (Fig. 7.2c) [193, 194, 195]. The deformation of flexible joints during recovery repositions the fin to reduce drag, while rigid joint limits prevent bending during the power stroke, keeping the fin system better-positioned to push against the surrounding fluid. This approach, while effective at reducing control complexity, is not actively reconfigurable.

In contrast to prior solutions, passive rowing is achieved in this study by taking advantage of the nature of flexible curved beams to preferentially buckle within a rowing cycle (Fig. 7.2d). The fin system design highlighted here produces net thrust and moment through symmetric sinusoidal actuation of a single actuator, resulting in a simple and energy efficient approach. Moreover, the unique characteristics of slender curved beams provides us with the opportunity to tune the system’s dynamic behavior (Fig. 7.12) by altering its stiffness. As demonstrated below, by changing the effective length of a curved beam, we can inhibit buckling unidirectionally or bi-

directionally, enabling us to switch between a rowing gait with a net forward thrust (when actuated as a pair) and a flapping gait, generating lateral thrust. When a pair of such fins are used together, a number of other swimming modalities may be observed as well. This tunability, which is made possible through internal reconfiguration of the buckling beam, splits the use of actuators according to their purpose – power and reconfiguration, permitting us to use machine-learning approaches to find optimal gaits for different swimming modalities in a decoupled fashion, where tuning actuators are first determined, with a subsequent, independent optimization of the power actuator signal.

Our contributions may be summarized as follows. (i) Applying the concept of buckling tape springs for locomotion via flapping in fluids. (ii) Selecting an appropriate analytical framework to understand the effect of buckling in curved beams for use in generating thrust. (iii) utilizing finite-element methods to further study the relationships between design parameters like curvature, length, and width on beam stiffness and buckling limits. (iv) Validated of these relationships in simulation and experimentally, by demonstrating positive nonzero average forces, power, and work (in contrast to regime I introduced above). (v) Introducing a novel robotic platform that leverages this phenomenon to swim in water. (vi) Introducing the concept of using length change to reconfigure the stiffness profile of a curved beam. (vii) Use of this mechanism to switch between rowing and flapping gaits in a mobile robot; (viii) Presenting a new dynamic model that simulates robot swimming by integrating the nonlinear stiffness of curved flexible beam joints; (ix) The use of that model, in addition to an experimental platform, in the optimization of the robot’s design as well as its actuation signal by using an evolutionary approach (CMA-ES). (x) Experimental validation of the forces and trajectories estimated during optimization on a prototype of the proposed platform.



The rest of the chapter is organized as follows. In section 7.1.1, we demonstrate the role of curved beam preferential buckling in locomotion using a robot locomoting through a series of equally-distant pegs. In Section 7.2, we describe a flapping wing design in which the buckling characteristics of curved beams can be studied and tuned. We then study the curved beam by discussing the theoretical underpinnings of our idea in Section 7.2.1; we subsequently introduce a FEA-based model which permits us to study curved beam design parameters (Section 7.2.2). Section 7.3 introduces a dynamic model of our proposed system that validates this phenomenon in water; Section 7.4 describes experimental validation of the concept in air (Section 7.4.1), in water (Section 7.4.2), and in a robot locomoting through a series of equally-distant pegs (Section 7.1.1). In section 7.5 The dynamic model is extended to estimate swimming distance across different designs and actuation signals with an optimization pipeline using CMA-ES. After prototyping the selected design from the prior step, we conduct an experimental search for the actuation signals across rowing, flapping, and undulatory gaits. Finally, based on the obtained results, a swimming robot is fabricated, and its swimming is studied and the chapter concludes in section 7.9 with concluding remarks and a discussion of our planned future work.

### *7.1.1 Role of Curved Beam Buckling in Locomotion*

We aim to show the importance of the curved beam preferential buckling in producing positive net work and helping a robot advance along a series of equally-spaced pegs (Fig. 7.3), even when a symmetric input is commanded to the actuators. Moreover, this case study highlights the versatility of the concept out of a fluid environment.

Figure 7.4 illustrates the locomotion of the peg toy robot across different stiffnesses of the curved beam when the servos are actuated via the same symmetric input.

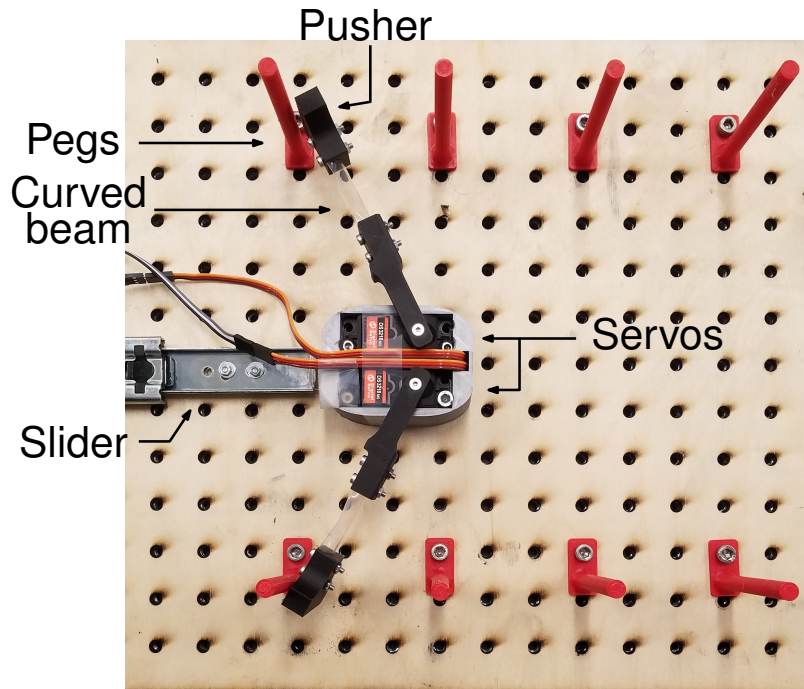


Figure 7.3: The peg toy robot manufactured to show the concept of using curved beam for out-of-fluid locomotion.

Using a thick sheet of material causes the beam to act as a rigid link due to its increased stiffness. In the pegs, the robot moves back and forth between two pegs, since no buckling occurs in either direction (Fig. 7.4a-c). A thin sheet of material exhibits low stiffness, even in curved configurations, acting like a soft hinge that easily bends in either direction. Using thinner material, the robot fails to push itself in either direction due to the compliance of the beam and as a result it does not locomote (Fig. 7.4d-f). Figure 7.4g-i shows the locomotion of the robot when the beam thickness is tuned and the curved beam buckles only in equal sense. In this case, when the arms move forward, the curved beams bend like a soft hinge and help the robot's pusher to pass the pegs, as in the recovery stroke of a swimming gait. When the robot's arms move back, however, the beam acts rigid and, by prohibiting

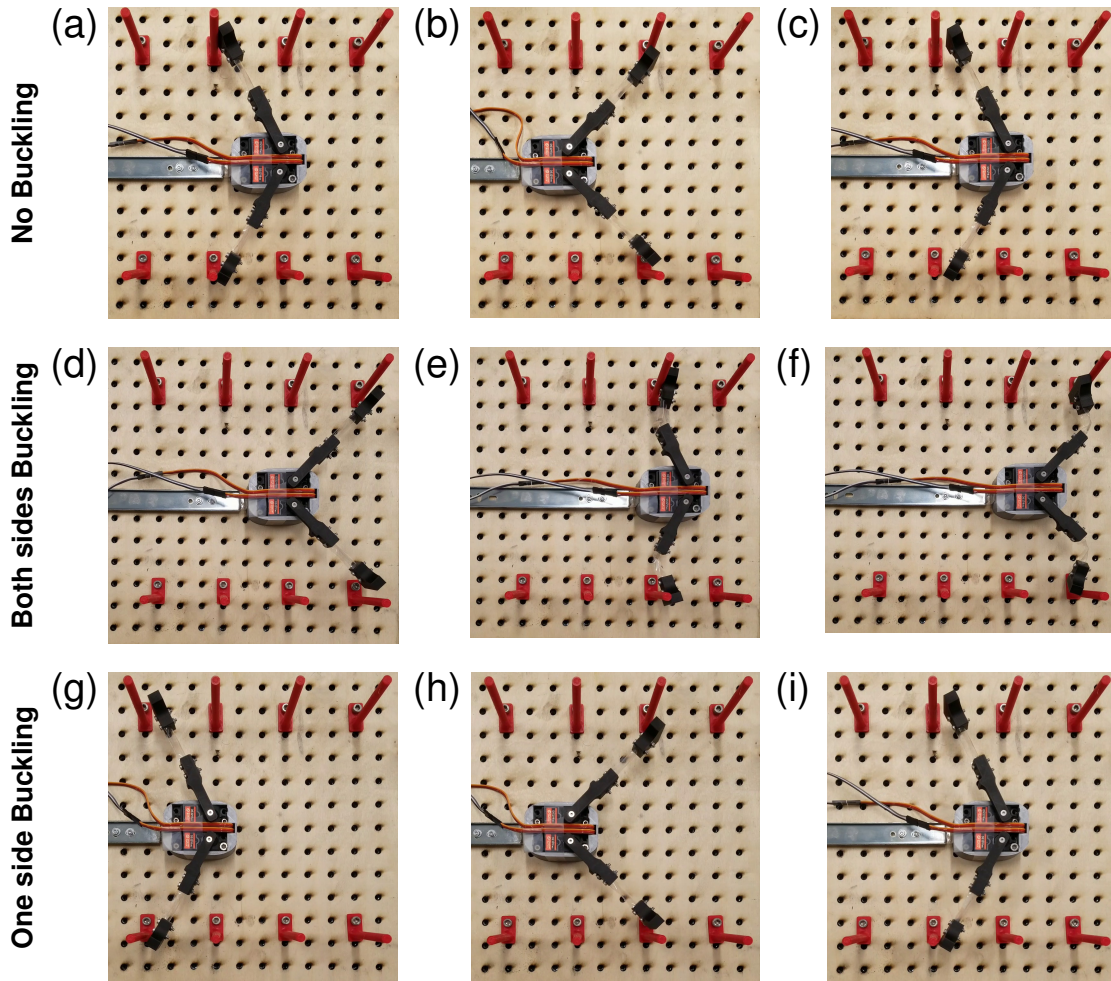


Figure 7.4: **Locomotion of the robot for different stiffness of the curved beams.** (a-c) Low stiffness (thickness = 3 mil). (d-f) High rigidity (thickness = 10 mil). (g-i) Tuned stiffness for directional bending (thickness = 5 mil).

bending, pushes the robot forward, as in a fish's power stroke. <sup>1</sup>

## 7.2 Analysis of Curved Beam in Anisotropic Buckling Wings

This section details the basic components of anisotropic buckling wings. Subsequently, the section focuses on modeling and characterization of curved beams embed-

<sup>1</sup>The results are illustrated in this video: (<https://youtu.be/NE8FUFzxGv8>).

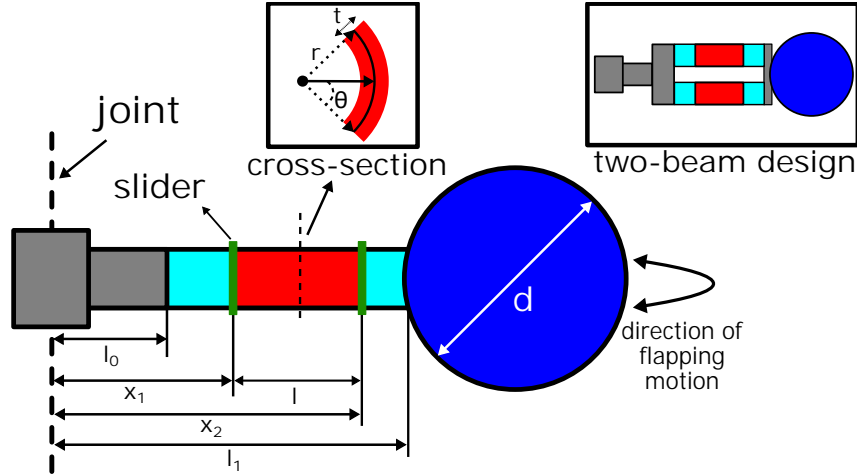


Figure 7.5: The side view of our flapping wing designs, with design and experimental variables labeled.

ded in these wings. In order to split the problem between aerodynamic and buckling domains, a family of relatively simple wing designs composed of a long thin beam connected to a circular flat plate has been considered. This wing is attached to a joint (defined by the heavy dashed line in Fig. 7.5) that may be powered by a motor or transmission. The role of the circular plate is to produce thrust and drag and apply resultant forces and torques through the curved beam to the body of a mobile robot. We assume symmetric propulsion throughout the study, though different gait strategies could be selected and studied. This permits us to study the impact buckling and deflection has on thrust and force production as a function of wing configuration throughout its gait cycle.

We model buckling under the assumption of end-loading conditions consisting of point loads and moments from aerodynamic forces in the distal portion of the wing. The wing seen in Fig. 7.5 comprises several sections: a rigid plastic section of length  $l_0$  (gray), a section of length  $(x_1 - l_0)$  (in cyan), a second interstitial section of length  $(l = x_2 - x_1)$  (red), and a third section of length  $(l_1 - x_2)$  (cyan), which is connected

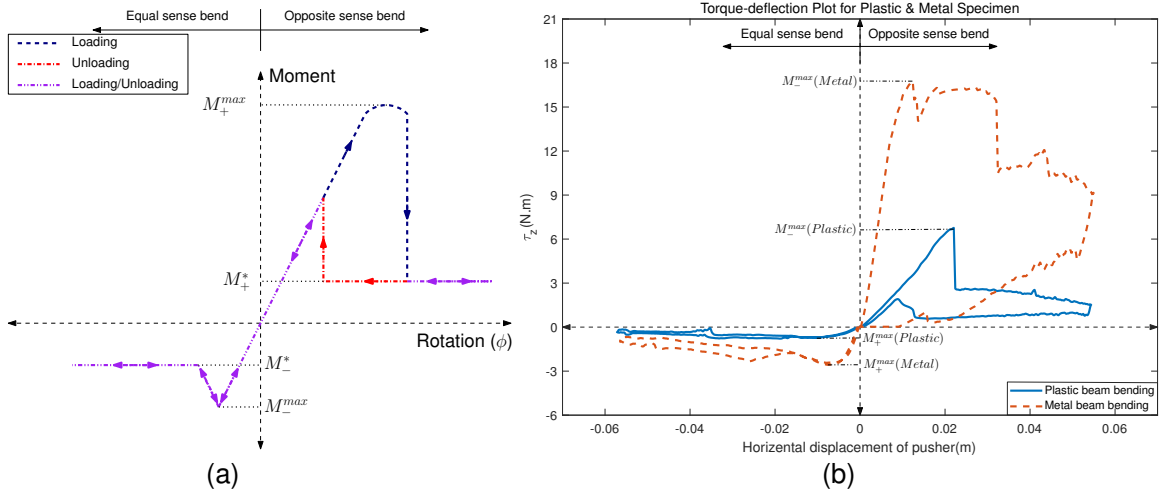


Figure 7.6: The nonlinear behavior of a curved beam derived (a) from theory [196] and (b) from experimental data for a steel and plastic specimen with the same geometry. Both results show a considerable decrease in stiffness after buckling occurrence both in opposite and equal-sense bending.

to a circular plate of diameter  $d$ . The curved beam with thickness  $t$  is curved along its length via two curved plastic sliding attachments located at  $x_1$  and  $x_2$ . These sliders induce a camber to the beam which can be represented as a radius of curvature  $r$ . The cyan and red sections of the wing are made of a single sheet of  $t$ -mm-thick polyester, while the gray portion is a sufficiently rigid 3D-printed plastic.

For the purposes of our design and analysis, we assume that the position of slider 1 and 2 are such that the red portion of the beam is the weakest and buckles first in the presence of flapping forces. Though camber of the wing may be observed along the beam, the circular plate does not exhibit significant curvature due to increased material stiffness.

### 7.2.1 Theoretical Model for Curved Beam Buckling

Two different formulations are most often used to describe the buckling phenomenon of curved beams in the literature, namely the buckling of spherical shells [197, 198] and the behavior of folded tape-springs [199, 196, 200, 201, 202].

In order to understand this phenomenon based on the buckling of spherical shells, Kebabze et al. explain that in opposite-sense bending, pre-stressed, curved material first passes through a flattened state via moments exerted on the shell's edge ( $M_x$  and  $M_y$ ) [198]. Stress ( $\sigma_y$ ) is the direct result of curvature change in the  $y$ -direction, while ( $\sigma_x$ ) is caused by Poisson's ratio. Considering that the material remains in its elastic range during this deformation, the stress distribution through the thickness stays linear and stress distribution can be determined.

This model finds critical buckling stress as a function of curvatures of the two stable phases, i.e., initial longitude curvature and final phase curvature. In our study, the system has no second stable phase. As a result, the value for final phase curvature is unknown and the value for critical buckling moment cannot be obtained based on this system of equations.

The behavior of a tape spring is formulated by Wuest in [201], in which moment-curvature relationships for a tape spring subject to equal and opposite end moments are obtained (Fig. 7.6(a)). As described by Soykasap, end moments can be obtained by integrating of moments about the transverse axis for the whole cross-section of the tape spring by considering the beam as a slightly distorted axi-symmetric cylindrical shell [199]. In this formulation,

$$M = \int_{-s/2}^{s/2} (M_l - N_l w) dy = sD \times \left( k_l + \frac{\nu}{r} - \nu \left( \frac{1}{r} + \nu k_l \right) F_1 + \frac{1}{k_l} \left( \frac{1}{r} + \nu k_l \right)^2 F_2 \right), \quad (7.1)$$

where  $M_l$  and  $N_l$  are the bending moment per unit length and the axial force per

unit, respectively.  $w$  represents out-of-plan deflection, the  $y$ -axis corresponds to the longitudinal direction, and  $k_l$  is longitudinal curvature.  $s$  and  $D$  are the width of the tape spring and bending stiffness, respectively and can be determined by the following equations:

$$s = 2r \sin\left(\frac{\theta}{2}\right) \quad (7.2)$$

$$D = \frac{Et^3}{12(1-\nu^2)}, \quad (7.3)$$

where  $E$ ,  $\nu$  and  $t$  are Young's modulus, Poisson's ratio and tape spring thickness, respectively.  $r$  and  $\theta$  are the initial transverse radius and curvature angle of tape spring, respectively.  $F_1$  and  $F_2$  in Eq. 7.1 are calculated as follows:

$$F_1 = \frac{2 \cosh \lambda - \cos \lambda}{\lambda \sinh \lambda + \sin \lambda} \quad (7.4)$$

$$F_2 = \frac{F_1}{4} - \frac{\sinh \lambda \sin \lambda}{(\sinh \lambda + \sin \lambda)^2} \quad (7.5)$$

$$\text{where } \lambda = \frac{\sqrt[4]{3(1-\nu^2)}s}{\sqrt{\frac{t}{k_l}}} \quad (7.6)$$

The critical buckling moment ( $M_+^{max}$ ), can be calculated by finding the maximum end moment in Eq. 7.1. The ‘‘steady moments’’  $M_+^*$  and  $M_-^*$  referenced in [199] can be calculated by considering that the curved region is approximately cylindrical:

$$M_+^* = (1 + \nu)D\theta \quad (7.7)$$

$$M_-^* = -(1 + \nu)D\theta \quad (7.8)$$

Although  $M_-^*$  and  $M_-^{max}$  are considered different values by [196], they are considered equivalent in other studies, which changes the equal-sense bending curve in Fig.7.6(a) to a simpler horizontal line starting from  $M_-^* = M_-^{max}$  [199]. Additionally, we note that this formulation is limited to the linear regime of the material's stress/strain curve.

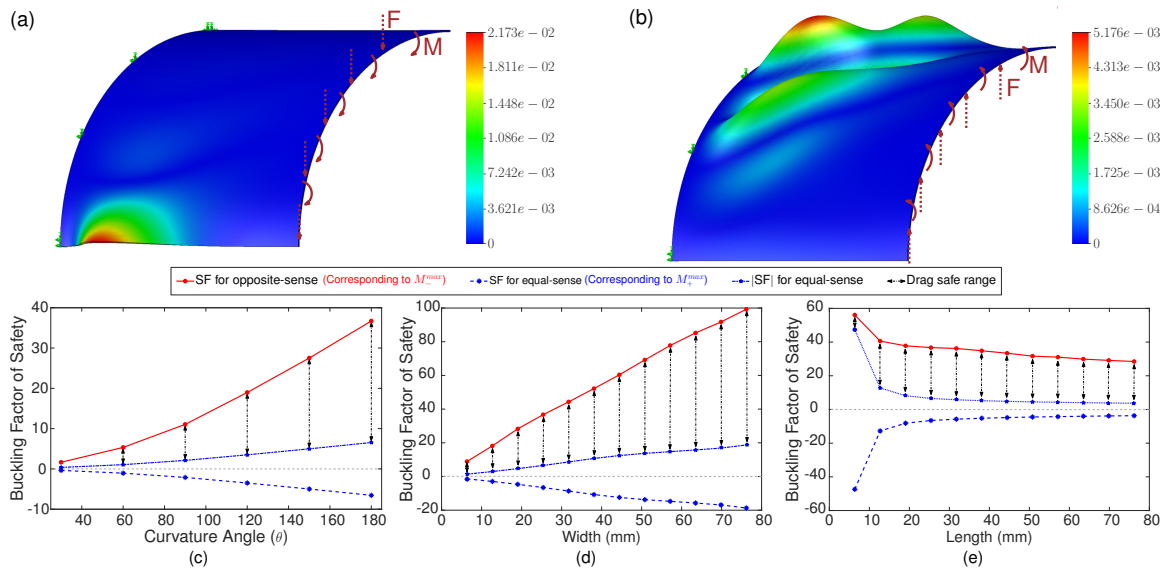


Figure 7.7: **Finite element analysis on the curved slender beam.** Side view of the deformation of a thin beam of dimensions 25.4 mm by 25.4 mm and  $\theta = 180^\circ$  at its critical load in (a) equal-sense and (b) opposite-sense bending. Only half of the symmetric beam is simulated and displayed. FEA results demonstrate the buckling limits as a function of various design parameters in opposite and equal-sense bending, which relate to the differences in load-carrying capability in either direction. (c) The effect of curvature angle ( $\theta$ ). (d) The effect of width ( $r\theta$ ). (e) The effect of length ( $l$ ).

In order to evaluate the theoretical model and provide better understanding of the curved beam, two specimens of a steel measuring tape and a curved polyester beam are considered. Both specimens have the same length ( $l$ ). The polyester specimen is pre-curved so as to have the same radius of curvature ( $r$ ) as the steel specimen. For each specimen, the curved beam is attached at one end to a fixed plate, while a known force is applied to the other end. A force sensor mounted to the output of a linear actuator pushes on the beam via a small, 3D printed contact point. The linear actuator moves back and forth through a 50 mm range in  $10 \mu\text{m}$  increments; applied forces are sampled at each step.



Figure 7.6(b) depicts the result for both specimens in two cases of equal and opposite-sense bending. Both polyester and steel specimens exhibit the buckling behavior predicted in the theoretical model. This may be seen in the sudden drop in the resultant moment at high deflection. The buckling moments in opposite-sense bending ( $M_-^{max}$ ) are much higher than the equal-sense buckling moment ( $M_+^{max}$ ) for both specimens. However, there are some notable differences between the theoretical model and experimental data. In both specimens, the deflection of the specimens in Fig. 7.6(b) does not follow the same path after buckling when forces are removed. This difference is more noticeable in the steel specimen compared to the polyester specimen. In the steel specimen, the values for  $M_+^*$  and  $M_+^{max}$  are different (as predicted in [196]), but in the polyester specimen, they have the same value (as predicted in [199]). The sudden change in the experimental torque/displacement data is believed to be due to out-of plane deformation, pusher slip, and friction. Moreover, in the case of opposite-sense bending, the path during loading and unloading of the polyester specimen is closer to the theoretical model predicted in [196, 199] than the steel specimen. We attribute this to plastic deformation that was observed in the steel specimen. While the theoretical model assumes that the buckling beam does not leave the elastic region, our experiments show otherwise. This can be due to the fact that, like the drag force on the wing, the pusher produces a combination of force and moment on the edge of the curved beam instead of a pure moment. This force-moment combination produces a nonuniform stress distribution on the shell and, in some cases, deforms the plate after buckling in ways not predicted by [196, 199]. This deformation results in permanent damage to the beams if the moment exceeds ( $M_-^{max}$ ). As a result, a safe region must be defined for the moment produced by the wing to ensure that the beam never undergoes opposite-sense buckling.

## 7.2.2 FEA Study on Curved Beam Buckling

In order to customize the buckling behavior of curved beams, various design parameters can be adjusted, including the radius of curvature ( $r$ ), beam width ( $r\theta$ ), beam length ( $l$ ), and other material properties. Finite Element Analysis (FEA) may be used to better understand and tune the relationship between these parameters and the desired buckling conditions. Unlike the analytical formulation, which is based upon uniform geometry and specific loading assumptions, FEA methods permit us to explore a wider range of geometries with more nuanced loading combinations as our use of this technique moves towards design optimization.

We thus study behavior of a slender curved beam, varying the curvature ( $\theta$ ), length ( $l$ ), and width ( $r\theta$ ) of the beam as primary design parameters and monitor the change in buckling factor of safety in linear, eigenvalue-based approach. To simplify the analysis we model half the beam and apply a symmetric constraint for the other half; we use a curvature-based mesh setting with a maximum element size of 0.4 mm and a 0.02 mm tolerance. The proximal edge of the beam is fixed while a load is applied to the distal end. The load is a combination on nominal force and moment (1 N and 1 Nm).

First, we demonstrate how adjusting the camber (or longitudinal curvature) of a beam can be used to alter the beam's stiffness and critical load to produce asymmetric flapping cycles and nonzero thrust. The curvature,  $\theta$ , is defined in Fig. 7.5 so that  $\theta = 0$  corresponds to a flat plate and  $\theta = 180$  produces a half-cylinder. Using the results of an FEA study performed using SolidWorks simulation, seen in Figs. 7.7(a,b), the deflection of a curved beam (of dimensions  $l = 25.4$  mm by  $r\theta = 25.4$  mm by  $t = 1$  mm) loaded in equal and opposite sense differs noticeably.

A further study, shown in Fig. 7.7(c), shows the evolution of the differences in

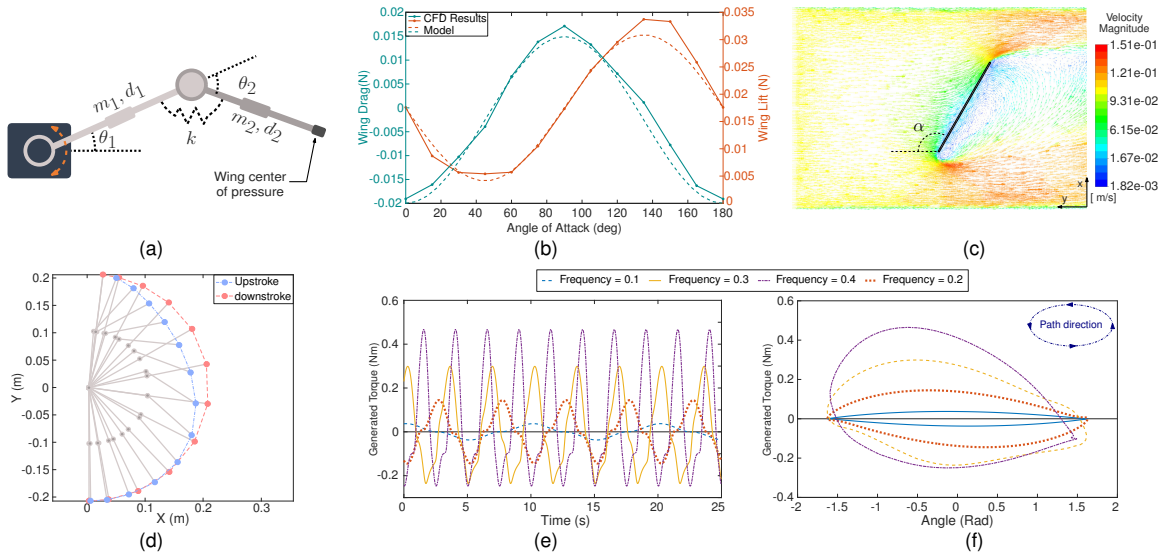


Figure 7.8: **Dynamic Modeling of a Wing Flapping in Water.** (a) Model for the wing system. (b) Comparison between the average values of wing lift and drag between flat plate model (Eqs. (7.9) and (7.10)) and CFD analysis. (c) The velocity magnitude of the water flow in CFD analysis for  $\alpha = 120^\circ$ . (d) Motion of the wing flapping at 0.4 Hz experiencing buckling during the recovery phase. Torque exerted by the wing on the fixed frame with respect to time (e) and motor position (f).

critical load for equal and opposite-sense bending as the curvature of a beam is varied between  $30^\circ$  and  $180^\circ$ . The width ( $r\theta$ ) and length ( $l$ ) of the undeformed half-beam is set to 25 mm in this study, and the resulting critical loads are obtained when loads are applied in the equal and opposite orientation using a linear eigenvalue-based analysis. The results in Fig. 7.7 show the magnitude of the buckling factor of safety in equal-sense (blue) and opposite-sense (red) loading cases. While exceeding the opposite-sense buckling limit leads to plastic deformation and should be avoided (as discussed in the previous section), exceeding the equal-sense buckling force reduces drag in the up-stroke portion of the swimming gait and increases the average thrust produced in swimming gaits without leading to beam failure. The black arrows in

Fig. 7.7 show the magnitude of the difference between critical load in either direction, corresponding to the safe working range for using drag forces to create asymmetric flapping gaits without material failure in the beam.

To further understand the relationship of beam width on buckling point, the curvature ( $\theta$ ) and length ( $l$ ) of the undeformed beam are fixed at  $180^\circ$  and 25.4 mm, respectively, while the width of the beam is varied from 6.4 mm to 76.2 mm. The beam's, radius of curvature ( $r$ ), volume, and mass change as a function of width. Figure 7.7(d) shows the result of this study, where the factor of safety corresponding to both equal and opposite-sense buckling increases as the width of the beam grows. The results also show that the difference in magnitude between equal and opposite-sense buckling limits (black arrows) grows with width.

In order to better understand how beam length ( $l$ ) impacts buckling, we vary the length of the beam from 6.4 mm to 76.2 mm while keeping the curvature ( $\theta$ ) and width ( $r\theta$ ) of the undeformed half-beam fixed at  $180^\circ$  and 25.4 mm, respectively. The beam's volume and mass change as a function of length ( $l$ ) while the radius of curvature ( $r$ ) is held constant. Loading conditions are varied as a function of  $l$  in this since the loading conditions on the buckling portion of the system are defined by the moment and force combination generated by the forces exerted at the distal end of the beam.

The result of this study shows that the buckling limit decreases for both equal and opposite-sense buckling as the length grows (Fig. 7.7(e)). However, the difference between the magnitude of positive and negative buckling limits initially grows and then stays somewhat constant for  $l > 25.4$  mm.

Based on these results, we have selected a curved beam with  $\theta = 180^\circ$  for the rest of the study. The beam length ( $l$ ), width ( $r\theta$ ), and thickness ( $t$ ) remain free design variables that can be tuned in order to maximize the effects of one-sided buckling for

use in conjunction with the drag and inertial forces acting on the fin across fluids of different viscosity. Future work will require a more systematic search for the optimal design through all parameters to find designs which improve performance for criteria such as speed, efficiency, or power.

### 7.3 Dynamic Modeling of Buckling Wing Propulsion

This section describes the dynamic modeling of the system by considering dynamic elements such as wing drag, curved beam stiffness, and rigid body dynamics.

We have modeled the dynamic behavior of a wing system based on these relationships. In this study, a wing system (shown in Fig. 7.8(a)) is connected to the ground at the base of the input joint and the moments exerted on the environment about the rotational axis are recorded similar to our experimental setup in Section 7.4.2. The system is represented by two rigid links with point masses located at their centers of mass, connected by a pin joint and torsional spring, with stiffness coefficient of  $K$ , connected in parallel. The nonlinear stiffness of the spring is represented by three linear regimes; the slopes of each of these regimes have been adjusted to best fit experimental data collected from our prototype introduced in Section 7.4.2 using the methods discussed in Section 7.2.1. The length ( $d_1$  and  $d_2$ ) and mass ( $m_1$  and  $m_2$ ) of each link match the measured values of the in-water prototype from Section 7.4.2.

Using a flat plate model, the forces on a wing due to a fluid are estimated by the equations derived from [203]:

$$F_{w_D} = \rho u^2 A \sin^2 \alpha \quad (7.9)$$

$$F_{w_L} = \rho u^2 A \cos \alpha \sin \alpha, \quad (7.10)$$

where  $\rho$ ,  $u$ ,  $A$ , and  $\alpha$  are the density of fluid, the relative velocity of the plate, the area of the plate, and the angle-of-attack of the wing, respectively.  $F_{w_D}$  and  $F_{w_L}$

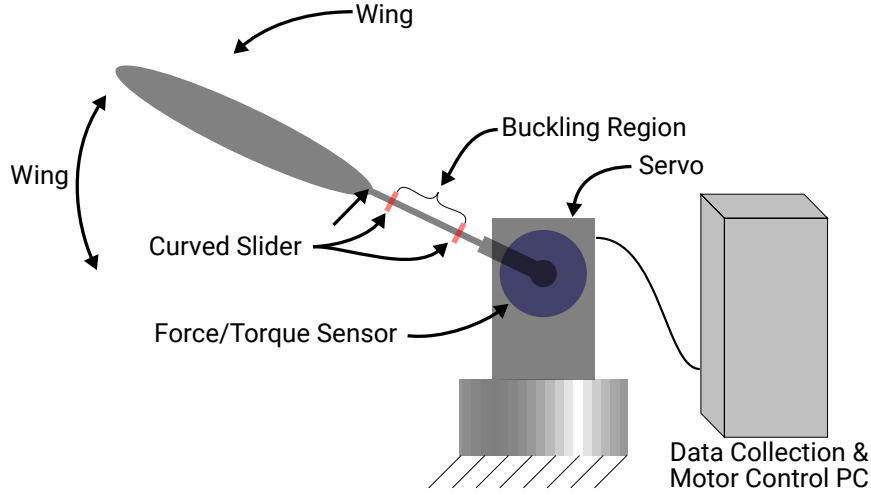


Figure 7.9: Experimental Setup for Measuring Air Drag Applied to the Wing.

correspond to the drag and lift elements of the aerodynamics forces on the plate. This model estimates the total force on a flat plate as:

$$F_w = \rho u^2 A \sin \alpha, \quad (7.11)$$

where  $\alpha$  is 0 when parallel to the flow and  $90^\circ$  when perpendicular (in 2D) [203]. This force is perpendicular to the wing and acts as the aerodynamic load on the curved beam (Fig. 7.1a).

Using Eq. (7.11), we can use the velocity of the plate ( $u$ ) to control the amount of drag force exerted on it, which, in conjunction with the load limits determined by the mechanics of the curved buckling beam (Eqs. (7.1),(7.7),(7.8) and Fig. 7.6(a)), determines whether and under what conditions buckling occurs.

The flat plate model best describes the fluid dynamics of a system when the Reynolds number is low and the system is in the laminar regime. The Reynolds number of a flapping wing in fluid is formulated as follows [204, 205]:

$$Re = \frac{\bar{u}\bar{c}}{\nu}, \quad (7.12)$$

where  $\bar{u}$ ,  $\bar{c}$  and  $\nu$  are the mean translational velocity of the wing tip, the wing mean chord and the kinematic viscosity of the fluid, respectively. For the given flapping system,  $\bar{u} = 2\Phi fR$ , where  $\Phi$  and  $f$  are flapping peak-to-peak angular amplitude and frequency and  $R$  is moment arm to the center of pressure of the wing. For this wing flapping in water, the Reynolds number varies from 1800 to 7200 when the flapping frequencies varies from 0.1 to 0.4 Hz, indicating that the flow regime changes from laminar to turbulent at higher flapping frequencies.

We then compare the flat plate model using a Computational Fluid Dynamic (CFD) analysis on the system wing. In this study, carried out in ANSYS (Fig. 7.8(c)), we have measured the average lift and drag exerted on the wing by uniform water flow with different flowrates as the angle-of-attack varies from 0 to 180°. Figure 7.8(b) shows the CFD analysis results for the flow of 0.1 m/s versus the flat plate model estimation. These plots show the high correlation between the flat plate model and CFD results for the latter speed for which the system is in laminar regime. At the maximum studied flapping frequency, the mean transnational velocity of the wing reaches 0.41 m/s for which, in the worst case, the maximum error between flat plate model and CFD results is less than 15%.

When a sinusoidal torque input is applied to the base joint, the dynamic model demonstrates that the wing system transitions between a non-buckling flapping regime to a one-sided buckling regime (as shown in Fig. 7.1(a)) when the flapping frequency is increased. Figures 7.8(e,f) plot the torque produced across different input frequencies as a function of time and base joint angle. From these data we can see that the wing system transitions from the non-buckling regime to one-sided buckling at around 0.3 Hz. While the maximum positive torque increases with frequency in the power stroke, the torque in the recovery section remains low. The amount of work performed on the environment, in Fig. 7.8(f), also grows with the emergence of buck-

ling. Figure 7.8(d) shows the motion of the modeled wing through a full flapping cycle at 0.4 Hz, behavior which is similar to the in-water flapping behavior shown in Fig. 7.11(b,c).

## 7.4 Experimental Validation

The goal of this section is to experimentally verify the effect of curvature on buckling force for a curved beam, as well as to demonstrate its potential for creating thrust and motion. We have considered two case studies (air and water) to validate our proposed methodology in order to underscore the generality of this concept, using the design principles from the previous section as a design guide.

### 7.4.1 Case Study I: Wing Flapping in Air

In this case study, the air drag exerted on a wing utilizing curved beam buckling is experimentally measured. Our experimental setup is shown in Fig. 7.9. A DC servo is attached to a flapping wing via a 3D printed mount, permitting rapid swapping of different wing designs. Forces and torques generated by flapping are measured with a six-axis ATI Mini40 force/torque sensor mounted to the motor and ground. The servo's position input signal is a triangular wave with a fixed amplitude of  $66^\circ$ ; the frequency is varied in order to change the aerodynamic interactions experienced by the wing.

### **Variable Length (One Beam)**

Two different cases of symmetric flapping are studied to demonstrate the effect of anisotropic buckling. In the first case, the sliders are brought closer together; this shortens the exposed beam length ( $l$ ) and prevents buckling in both directions of flapping and results in similar angle of attack and drag in both up-stroke and down-



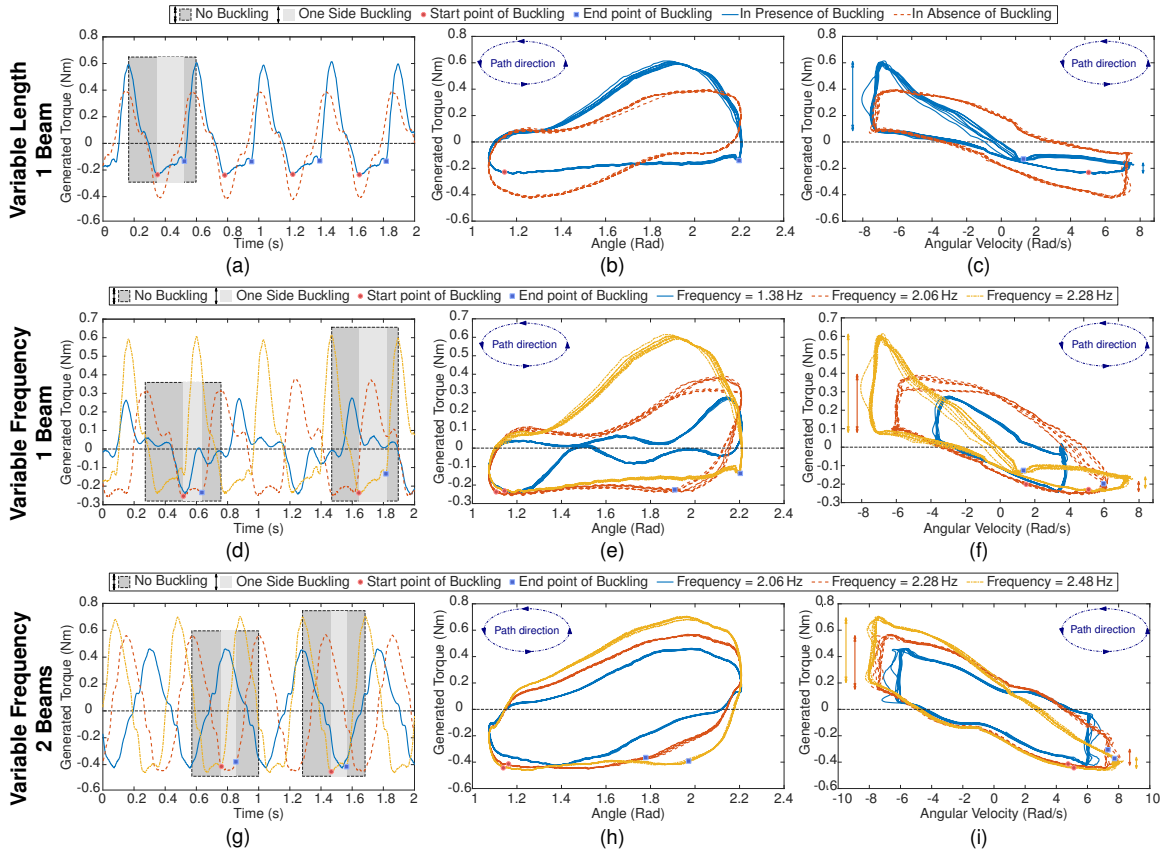


Figure 7.10: **The effect of asymmetric buckling on a wing flapping in air:** (left plots) Torque vs. time, measured over several flapping cycles, (middle plots) position vs. torque; (right plots) velocity vs. torque (a,b,c) One beam with variable effective buckling length that produces no buckling and buckling, respectively. (d,e,f) One beam connected to the wing flapping at 1.38, 2.06, and 2.28 Hz. (g,h,i) Two beams connected to the wing, flapping at 2.06, 2.28, and 2.48 Hz.

stroke (orange line in Figs. 7.10(a,b,c)). In the second case, curved, reinforcing sliders are arranged so that the gap between them is large enough to permit buckling in the equal-sense direction to occur during sinusoidal flapping. This longer buckling region allows the curved beam to buckle under drag forces in equal-sense bending, but is not sufficient to induce buckling in the opposite sense (blue line in Figs. 7.10(a,b,c)).

The start and end points of buckling are illustrated in Figs. 7.10(a,b) using red circles and blue squares, respectively. Non buckling and one-sided buckling regions for a full cycle are also shown using light gray and gray boxes.

Figures 7.10(b,c) show the moment generated by the wing during symmetric flapping as a function of the wing's angle and speed, respectively. The shape of the non-buckling curved beam's work loop is qualitatively symmetric (about torque  $\tau = 0$ ), indicating that the average work – the area of the work loop in the positive  $\tau$  domain minus the area of the work loop in the negative  $\tau$  domain – over several flapping cycles provided by a non-buckling beam (orange) is near zero. In contrast, the buckling beam (in blue) shows an asymmetric path (about torque  $\tau = 0$ ), capable of producing nonzero work in the forward direction. This asymmetry is also noticeable in vertical portion of the blue line in Fig. 7.10(c), shown by vertical double arrows lines, where the positive angular velocity is much smaller compared to the negative side. The above changes in power and work plots show the effectiveness of anisotropic buckling during symmetric flapping in generating non-zero thrust, power, and work.

The results demonstrate that the curved beam produces work in symmetric flapping when it is permitted to buckle. The average torque generated over one flapping cycle increases from 0.009 Nm to 0.165 Nm in the presence of unidirectional buckling (Table 7.1). Though the wing-beam system is not optimized for energy efficiency, the mechanical energy efficiency increases from 1.86% to 29.5%. This is calculated by evaluating the ratio of useful work done over the total work done across a full flapping cycle.

### **Variable Frequency (One beam)**

We next look at the effect of drag on buckling by increasing the frequency of the triangular input signal for the same curved beam. Plots in Fig. 7.10 show the torque gen-

erated via a symmetric flapping gait with respect to time (a,d,g), servo angle (b,e,h), and angular velocity (c,f,i). In Figs. 7.10(d-i), the results for the three flapping rates of 1.38, 2.06, and 2.28 Hz are depicted in blue, red and orange colors, respectively. In these figures we see that the torque generated by each successive increase in flapping speed increases the magnitude of torques experienced in the positive y domain without similar magnitude increases in the negative y domain. This results in work performed on the environment, which can be seen as a clockwise work loop in both the torque vs. servo angle and torque vs. angular velocity plots in Figs. 7.10(e,f). At 1.38 Hz, the beam experiences no buckling, however the faster two cases (2.06 and 2.28 Hz) result in one-sided buckling. The average torque, amount of work done on the environment, and mechanical efficiency are reported in Table 7.1. The data reveal that the buckling duration of a full flapping cycle increases from 25% to 42% in one-sided buckling cases between 2.06 and 2.28 Hz. We note that though the hysteretic gaits obtained here via anisotropic buckling during flapping resembles gaits generated by other techniques such as the split cycle method in [206], the effect in our case is a result of designed system dynamics rather than asymmetric motor inputs.

### **Variable Frequency (Two Beams)**

To address the non-negligible torsional effects visible in the wing during flapping, we stiffened our system in torsion by attaching two beams – 40 mm apart from each other, in parallel – to the wing, as depicted in Fig. 7.5. This reduced the noticeable effects of torsion on long thin beams (as noted by [207]) and produced slightly different torques throughout flapping cycles at different speeds. Figures 7.10(g-i) show the results of this test at 2.06 (blue), 2.28 (red), and 2.48 (orange) Hz, respectively. The results show similar trends and behavior with the previous one-beam case, but because the system is stiffer (due to two beams in parallel), it takes higher velocities (and higher

Table 7.1: Torque and work generated during flapping in air.

Experiment	Frequency (Hz)	Average Torque (Nm)	Work (J)	Mechanical Efficiency	Buckling
Variable	2.28	-0.012	-0.009	1.86%	No
Length	2.28	0.131	0.165	29.50%	One side
1 Beam	1.38	-0.005	-0.005	2.98%	No
	2.06	0.149	0.154	26.73%	One side
	2.28	0.131	0.165	29.50%	One side
2 Beams	2.06	0.004	0.013	2.29%	No
	2.28	0.031	0.019	2.56%	One side
	2.48	0.077	0.095	10.30%	One side

drag) to initiate buckling. This can be seen in the of 2.06 Hz case, which experiences no buckling in contrast to the single-beam trial. The data sampled in the two-beam case are smoother, with less high-frequency noise; this can be attributed both to a reduction in torsional effects as well as the impact of the altered stiffness on the resonant frequencies of the system.

#### 7.4.2 Case study II: Flapping in Water

This concept has also been demonstrated in water, using a RC servo to produce symmetric flapping while measuring the torques produced by the fluidic interactions. Figure 7.11(b) shows frames extracted from a single flapping cycle of a wing with a pre-curved buckling beam. Frames 1-4 represent the recovery stroke of our sinusoidal control signal; frames 5-8 constitute the power stroke. Hysteresis is clearly visible

Table 7.2: Generated torques in simulation and experimental

Frequency	Simulation		Experiment		Buckling
	$\tau_{\min}$ (Nm)	$\tau_{\max}$ (Nm)	$\tau_{\min}$ (Nm)	$\tau_{\max}$ (Nm)	
0.1	-0.04	0.04	-0.04	0.04	No
0.2	-0.14	0.14	-0.14	0.15	No
0.3	-0.23	0.3	-0.13	0.32	One side
0.4	-0.24	0.46	-0.12	0.44	One side

between these strokes, indicating that the dynamic interactions between inertia, drag, and buckling play a role in deforming the beam anisotropically.

In this experiment we use a sinusoidal input signal with constant amplitude and variable frequency to study the impact of flapping speed on buckling and torque. Figure 7.11(c) shows the torque generated for 0.1, 0.2, 0.3, and 0.4 Hz frequencies over several cycles. The results clearly demonstrate the effect of anisotropic beam buckling. The maximum positive torque increases from 0.05 Nm to 0.43 Nm between 0.1 Hz and 0.4 Hz while the negative torque generated during a flapping cycle is limited across all experiments to no less than -0.12 Nm. Table 7.2 shows the comparison between the generated torques in this experiment and values estimated by the dynamic model (Sec. 7.3). The results of the two-beam design are subsequently shown in Fig. 7.5. Though illustrative of the tradeoffs between torsional stiffness and buckling, the results show that increased mechanism stiffness increases the torque that can be supported by the beam in recovery (Fig. 7.11(d)), undesirable from the perspective of gait efficiency. This design requires optimization against other design parameters to simultaneously reduce the effect of torsion and increase efficiency.

Using these results, a water-based robotic platform has been developed that lever-

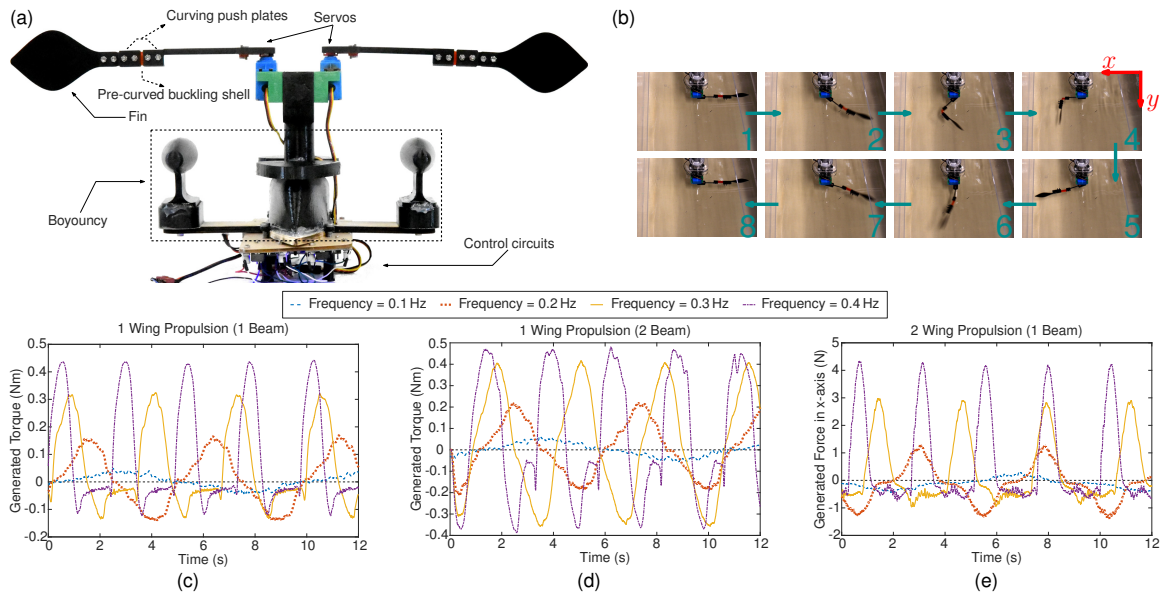


Figure 7.11: **The effect of asymmetric buckling on a wing flapping in water:**

(a) This robotic prototype uses buckling to swim through water. (b) Frames extracted from the propulsion test demonstrate buckling in the recovery stroke and no buckling in the power stroke. (c-e) The effect of various flapping rates on the torque produced on a fixed frame for (c) a one-beam wing, (d) a two-beam wing, and (e) the thrust produced in the  $x$ -axis by two one-beam wings.

ages buckling during flapping. As illustrated in Fig. 7.11(a), the robot uses curved beams to connect to two rigid fins made from 0.76 mm fiberglass sheet. The buckling portions of the links are made from a laminated composite of fabric, adhesive and 0.18 mm-thick polyester, which is used to reinforce the material during buckling.

Based on the properties of the curved beam, if the combination of force and moment experienced at the fin is between the equal and opposite-sense buckling values discussed earlier, the curved beam will buckle unidirectionally, resulting in a different angle of attack, which impacts the lift and drag forces acting on the fin by the fluid. As a result, drag on the robot will be different in power stroke and

recovery stroke, creating a thrust differential over a gait cycle which makes the robot swim forward. The magnitude of forces and moments caused by fin propulsion can be adjusted by controlling the amplitude and speed of the servo movements, size of the fin, length of the beam ( $l$ ), and radius of curvature ( $r$ ).

The left and right fin servos follow a sinusoidal control signal of the form

$$y_i = A_i \sin(2\pi f_i t + a_i) + b_i \quad (7.13)$$

where  $A_i$  represents an adjustable amplitude,  $f_i$  represents the frequency,  $a_i$  represents a phase offset, and  $b_i$  represents an amplitude offset from the neutral point, which is nominally set to  $b_i = 0$  throughout these trials. This symmetric motion about our transverse and bilaterally-symmetric robot guarantees that any forward locomotion can be attributed to the changes in drag caused by the buckling curved beam attached to the fin. Figure 7.11(e) shows the forward thrust generated by symmetrical flapping of the two wings for 0.1, 0.2, 0.3, and 0.4 Hz frequencies.

In water trials, the swimming robot was able to swim with an average speed of 0.1 m/s when  $y_0 = y_1$ . The robot was able to rotate by using only one limb at a time. This is important because a non-buckling fin acts more like a fish caudal fin and causes the robot to move laterally; because of buckling, the fin produces nonzero average torque, resulting in the robot turning.

## 7.5 Tuning Curved Beam Stiffness for Selectable Swimming Gaits

After validating the efficacy of the proposed fin design in producing positive net thrust and locomotion between pegs, in air and in water, the following sections are dedicated to in-depth study on using this concept for enhancing swimming.

As illustrated in Fig. 7.12, rowing is a swimming motion employed by a number of animals via tuned passive biomechanics and active gait strategies. This gait generates

positive net thrust (or moment) by having a higher drag profile in the power stroke compared with the recovery stroke, which is obtained via faster actuation speed or higher effective area. We first cover the advantages of our method in generating positive net thrust and moment compared to other state-of-art methods in producing rowing. We have extended the dynamic model introduced in the previous part of this chapter to model the swimming behavior of the robot. A design optimization has been carried out, using the CMA-ES, to find the design and gait parameters that maximize the robot's forward swimming speed using rowing. Additionally, we show that these curved beams can be actively tuned to alter their behavior on demand for use in swimming applications, and can be used in an underwater robot to switch between rowing and flapping gaits. Finally, a series of experimental gait searches have subsequently been conducted on the resulting optimal design, again using CMA-ES with the goal of finding the optimal gait pattern across a number of swimming strategies such as paddling, flapping, and undulation. By actively altering the curved beam's buckling limits, an untethered robot has been developed that maneuvers in water across each of these swimming strategies. The findings suggest that tuning the preferential buckling limits of curved beams can be an effective and potentially advantageous approach for producing directional thrust and moments.

### 7.5.1 *Design & Fabrication*

This section details curved beams and their nature to buckle preferentially, for use in creating rowing and flapping gaits. A flat, slender, compliant beam shows little resistance towards bending; however, by inducing curvature in it (Fig. 7.12a), the resulting curved beam resists bending in the direction opposing its camber (known as opposite sense bending) more than when the beam is bent in the direction of the beam's camber (equal sense bending). The influence of curvature results in different



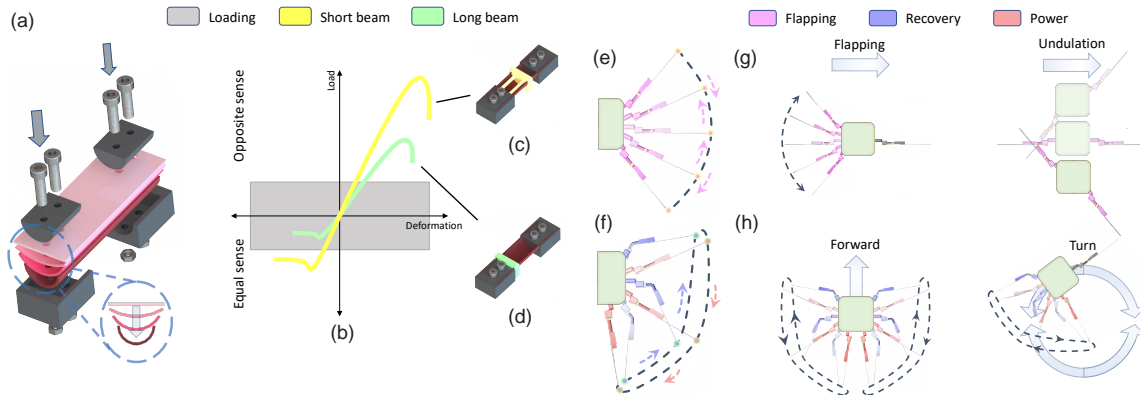


Figure 7.12: **Utilizing curved beams in rowing and flapping swimming strategies.** (a) Curving mechanism. (b) The nonlinear behavior of curved beams. (c) short beam. (d) long beam. (e) flapping gait. (f) Rowing gait. (g) Lateral swimming using one fin flapping gait, and undulation. (h) Forward swimming and turning using rowing gait.

buckling limits in equal and opposite sense bending as well. Furthermore, this phenomenon is also controllable by considering the effective length of the beam (green and yellow lines in Fig. 7.12b). When the beam’s effective length is shorter, both the stiffness and buckling behavior behave more symmetrically, while at the same time, beam stiffness increases.

In this study, we use this controllable, asymmetric buckling behavior to enhance swimming in an underwater robot. We show that by careful consideration during mechanical design, the preferential buckling of curved beams can be used to passively produce a rowing gait even with simple, symmetric inputs. On the other hand, the beam can also be reconfigured to produce flapping gaits. As shown by the green plot in Fig. 7.12b, in the rowing gait regime, the fluid’s dynamic load on the distal end of a properly-sized beam (Fig. 7.12d) overcomes its critical buckling limit in equal sense bending, resulting in the beam undergoing a large deflection during recovery

stroke (blue in Fig. 7.12f). Buckling permits the fin to travel nearly parallel with the direction of motion, rather than perpendicular to it, altering the angle of attack to reduce drag on the fin during the recovery stroke. In the power stroke, however, the fluid’s dynamic load on a properly-dimensioned curved beam does not exceed the critical buckling limit in the opposite sense; the beam consequently remains perpendicular to the direction of motion, maintaining higher drag forces on the distally-mounted fin (red in Fig. 7.12f). Cycles of alternating power and recovery strokes result in a rowing gait that can be used to produce a positive net thrust in the forward direction. In the flapping regime, by shortening and stiffening the curved beam (Fig. 7.12c), the critical buckling limits of the beam – in both equal and opposite sense bending – are larger than the fluid’s dynamic load (yellow plot in Fig. 7.12b), resulting in a flapping gait that primarily produces lateral thrust (Fig. 7.12e).

One of the common formulations to describe the buckling phenomenon of curved beams in literature is the behavior of folded tape-springs [199, 196, 200, 201, 202]. The behavior of a tape spring is formulated by Wuest in [201], in which moment-curvature relationships for a tape spring subject to equal and opposite end moments are obtained. Soykasap states that end moments can be obtained by integrating moments about the transverse axis for the whole cross-section of the tape spring by considering the beam as a slightly distorted axi-symmetric cylindrical shell and provides formulations to calculate the critical buckling moments in opposite and equal sense bending.

In [199], Soykasap’s formulation also assumes that materials are operating in their linear regime and that the loading on the distal end of curved beams is a pure moment. In our case, both material properties of the polyester beam and its loading condition caused by fluid dynamics do not satisfy the assumptions. In [208], we have previously shown that a beam’s curvature influences and can be used to increase the

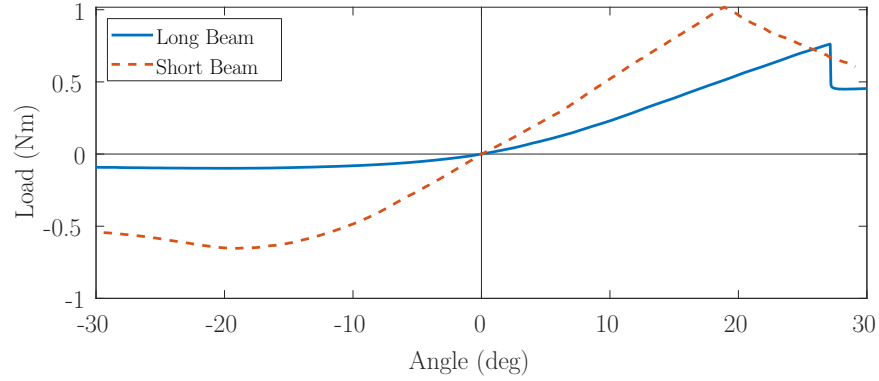


Figure 7.13: Experimental data showing the changing nonlinear behavior of curved beams with a short and long effective length. The positive x-axis represents opposite-sense bending, while the negative x-axis represents equal-sense bending.

difference between opposite and equal sense critical loads using Finite Element Analysis (FEA). We have also shown with FEA in [208] that the opposite and equal-sense critical buckling loads are much closer in value in shorter beams. This has been verified experimentally, by measuring the torque/rotation behavior and identifying the critical loads for the long and short beams corresponding to the device depicted in Fig. 7.12(c, d).

Figure 7.13 shows the nonlinear behavior of two specimens with the same curvature ( $180^\circ$ ) and width (25.4 mm), and with effective lengths of 31.75 and 3.6 mm. In this test, for each specimen, the curved beam is attached at one end to a fixed plate while a known force is applied to the other end. A force sensor mounted to the output of a linear actuator pushes on the beam via a small, 3D printed contact point. The linear actuator moves back and forth through a 50 mm range in  $10 \mu\text{m}$  increments while forces and torques are logged. Since the curved beams are modeled as a flexible hinge, the sampled data is displayed by their equivalent torque and deformation angles in Fig. 7.13. These profiles are used within subsequent models and prototypes in the rest of this study. These data also show that by reducing the

beam length, the critical buckling limit in equal sense bending increases from 0.1 to 0.65 Nm; the limit for opposite sense buckling, however, only increases from 0.76 to 1.02 Nm. Thus, for fluid-dynamic loads between 0.1 to 0.65 Nm, altering the effective length changes the buckling condition from unidirectional to bi-directional, resulting in the gait switching from rowing to flapping.

A slider mechanism has been implemented to alter the effective length of the beam, as illustrated in Fig. 7.16b. The mechanism consists of a rigid slider with a curved slot; when pulled, it prevents deflection by maintaining the beam's curvature, decreasing the length of the portion of the beam available to buckle. The slider's neutral configuration is set by a compression spring as the beam's natural length, which permits one-sided buckling – and thus rowing – at lower forces. To activate flapping, a single actuator pulls both fins' sliders forward via a tendon and pulley system, preventing buckling when the beams are loaded. The curved beam's stiffness in this configuration is both higher and more symmetric (in the equal and opposite sense), as seen in the red dashed line in Fig. 7.13).

## 7.6 Dynamic Modeling

In order to optimize the design of the device for rowing, we next describe the dynamics of the system by considering the contribution of the wing's drag, the curved beam's stiffness (in the long configuration), and the inertial effects of each body. The proposed robot uses two fins attached to the main robot's body at a distance of  $d_0$  (shown in Fig. 7.14a). Each fin is represented by two rigid links ( $d_1, m_1$  and  $d_2, m_2$ ) with point masses located at their centers of mass, connected by a pin joint and torsional spring, with stiffness coefficient of  $K$ , connected in parallel. The nonlinear stiffness of the spring is represented by three linear regimes; the slopes of each of these regimes have been adjusted to best fit experimental data collected from our specimen

in its long effective length configuration (blue in Fig. 7.13).

Using Eq. (7.11), we can use the velocity of the plate ( $u$ ) to control the amount of drag force exerted on it, which, in conjunction with the load limits determined by the mechanics of the curved buckling beam, determines whether and under what conditions buckling occurs. In section 7.3, we showed that, in the worst case, the maximum error between flat plate model and CFD results is less than 15%. Due to the simplicity of the flat plate model, we use it in our simulation to reduce computation time and keep the optimization process tractable. Our simulation is performed with a Python-based dynamics package called Pynamics. This library derives the Equation of Motion (EOM) using Kane’s method [209]<sup>2</sup> which are then integrated using the `scipy.integrate.odeint()` function to determine the system’s state over time. The performance of the model is evaluated by comparing the moments generated by one fin against data collected experimentally. By defining two forces connecting the robot to the ground ( $k_G$  and  $b_G$  in Fig. 7.14a), the forces and moments exerted on the environment about the rotational axis when one fin is actuated may be measured in simulation.

When a sinusoidal input torque is applied to the base joint of a fin, the dynamic model demonstrates that the wing system transitions between a non-buckling flapping regime to a one-sided buckling regime when the input frequency increases. Figure 7.14b plots the torque across different input frequencies as a function of time. From these data, we can see that the wing system transitions from the non-buckling regime to one-sided buckling at around 0.3 Hz, where the maximum positive torque increases with frequency in the power stroke, but the maximum negative torque in the recovery section remains low. Figure 7.14c shows the moments exerted on a force sensor attached to the robot’s main body when similar inputs are commanded to

---

<sup>2</sup>[https://github.com/idealabasu/code\\_pynamics.git](https://github.com/idealabasu/code_pynamics.git).

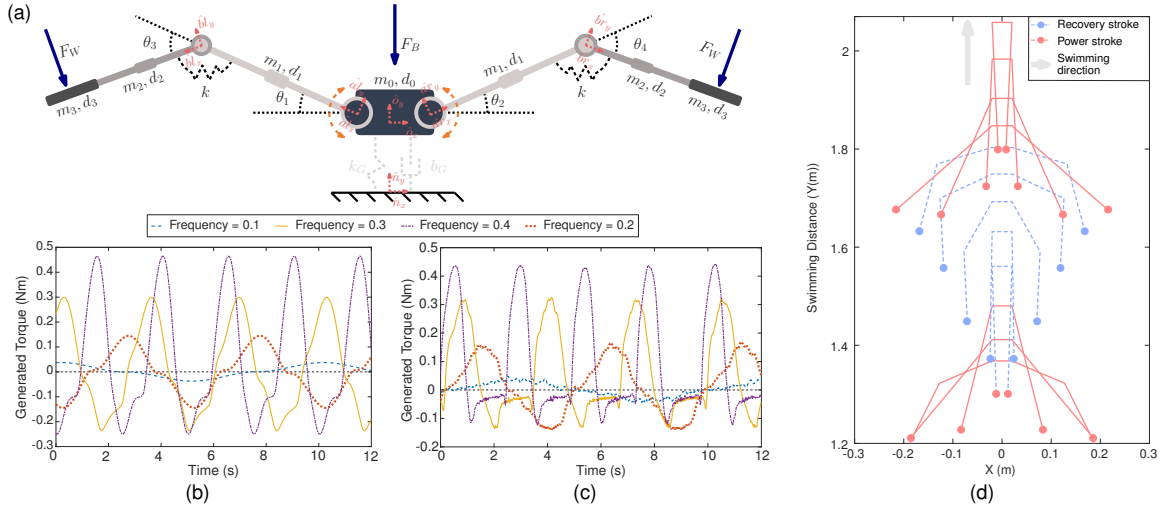


Figure 7.14: **Dynamic modeling of the robot swimming in water with long effective length.** (a) Model for the swimming robot. Torque exerted by the wing on the frame, when the robot is fixed, from simulation (b) and experiment (c). (d) Simulation of robot swimming freely without any constraints.

the robot using our experimental setup explained in (Section 7.8). Table 7.2 data also shows an acceptable correlation between the generated torques in this experiment and the values estimated by the dynamic model. Based on this performance, we simulate the robot swimming by removing the forces holding the robot’s main body ( $k_G = b_G = 0$ ). We also consider a drag force acting on the main body for more realistic simulation. Figure 7.14d shows a time sequence of the robot’s motion when both fins are actuated with a symmetric input gait and robot swims forward; the recovery and power strokes are illustrated in blue and red, respectively.

## 7.7 Design Optimization

Using the dynamic model introduced above, we next seek the design that maximizes forward swimming speed for symmetric rowing gaits. In our optimization, we consider the lengths of the fin’s links and the distance between the robot’s drive mo-

tors as design parameters ( $d_1, d_2, d_3$  and  $d_0$  in Fig. 7.14). The mass of each link is based on measurements of physical prototypes.

Any optimization focusing solely on design parameters would be incomplete; actuator inputs are thus optimized simultaneously. The torques at motorized joints track desired angular trajectories ( $\theta_1$  &  $\theta_2$  in Fig 7.14a) via  $k_G$  and  $b_G$  as mentioned previously. Input signals are supplied as a pair of sinusoidal functions,

$$\begin{aligned}\theta_1 &= \beta_1 + \alpha_1 \sin(2\pi f_1 t) \\ \theta_2 &= \beta_2 + \alpha_2 \sin(2\pi f_2 t + \phi),\end{aligned}\tag{7.14}$$

where  $\theta_i$  is actuator  $i$ 's angle, and  $\beta_i$ ,  $\alpha_i$ ,  $f_i$ , and  $\phi_i$  are the sinusoidal signals' angular offset, amplitude, frequency and phase shift, respectively. In order to have synchronized rowing gaits for the purposes of forward rowing, these parameters are set to  $\alpha_1 = -\alpha_2$ ,  $\beta_1 = -\beta_2$ ,  $f_1 = f_2$ , and  $\phi = 0$ . Based on the design and input gaits parameters introduced above, there are seven parameters affecting the robot's swimming speed. We have selected a numerical optimization approach using an evolution strategy for finding the optimal parameters; while the whole parameter space may be searched for lower-dimensional problems, we utilize CMA-ES as a way to find ideal parameters within this seven-dimensional space, as finding a globally-optimal solution would be neither be feasible nor desirable.

In our optimization process, we define the cost function as negative of the swimming range that robot achieves in 10 seconds. We also introduce the following assumptions and constraints to simplify the optimization process and obtain more realistic results:

**Assumptions** (i) Water drag is applied to the main body and fins ( $F_B$  and  $F_W$  in Fig. 7.14), but not to the links. (ii) Drag is applied to the center of each geometry. (iii) Fins and main body have rectangular cross-sections with 80 and 50 mm widths,

Table 7.3: Parameter range in design and input optimization.

Parameter	Range	Parameter	Range
$d_0$ (mm)	40 - 160	$d_1$ (mm)	30 - 160
$d_2$ (mm)	30 - 160	$d_3$ (mm)	30 - 160
$\alpha$ (deg)	0 - 90	$\beta$ (deg)	-90 - 90
$f$ (Hz)	0.1 - 1.2	$\phi$ (deg)	0 - 359

respectively. (iv) The robot body’s mass, mostly driven by the mass of servos and electronics, is assumed to be constant.

**Constraints** (i) Variables remain within the ranges defined by Table 7.3. (ii) The total length of the robot is under 560 mm (to fit our water tank). (iii) Actuation speed and power must remain within the servo’s nominal speed and power range. (iv) Loads on the curved beam must remain below opposite sense critical load throughout the trial. (v) Design and gait parameters must not collide during actuation.

We have defined a penalty function in order to exclude non-feasible solutions, in which a large positive value proportional to the number of violated constraints is returned. The penalty function gradually restricts the large search space to converge within the feasible solution space of the problem. For feasible solutions, the dynamic simulation runs and the cost function returned.

Figure 7.15a shows the cost function value as well as the evolution of the design throughout the CMA-ES optimization process for the parameter sets that exhibit a noticeable reduction in the cost value. The results converged after 25 iterations, revealing that designs with a smaller distance between the fins ( $d_0$ ) as well as smaller second link length ( $d_2$ ) are preferential for maximizing swimming speed.



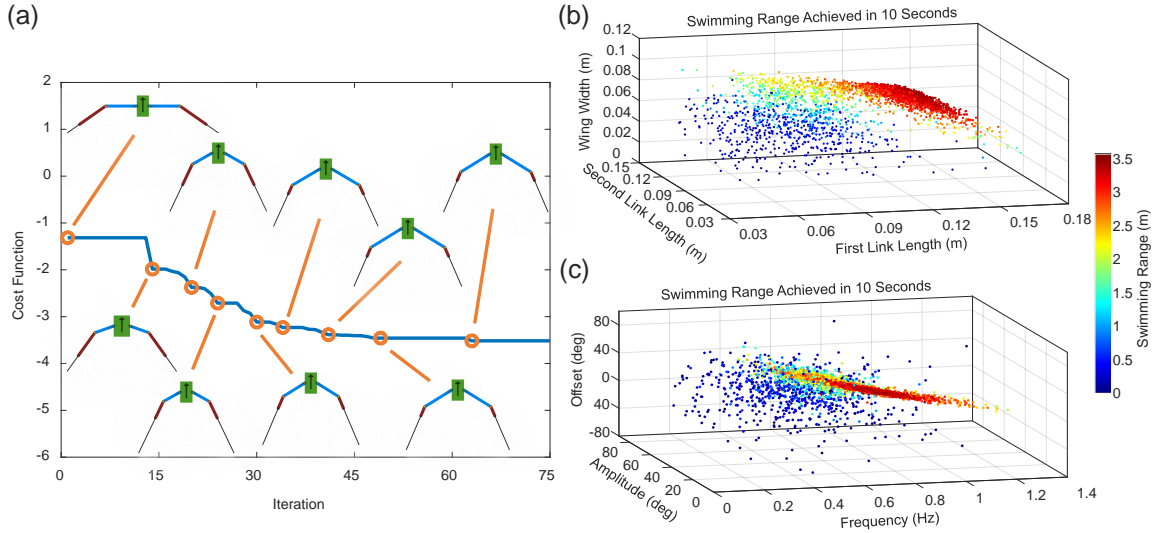


Figure 7.15: **Design optimization using the dynamic model.** (a) The value of optimization cost function and the evolution of the robot design. Feasible parameter sets in the optimization process: (b) Fin system design parameters and (c) input gaits.

Figures 7.15(b,c) show cost function values for feasible parameter sets. The optimal design parameters (in mm) are  $d_0 = 40$ ,  $d_1 = 112.1$ ,  $d_2 = 30.2$ , and  $d_3 = 114.2$ .

We have designed a prototype using the above design parameters (Fig. 7.16b). The lengths of the rigid parts are calculated assuming that the curved beam bends at the midpoint. This assumption is made based on the observation of the curved beam bending underwater. Two Hitec D646WP waterproof servos actuate the input joints; the rigid links are 3D printed from Onyx<sup>3</sup>; the fin is cut from 0.76 mm fiberglass sheets<sup>4</sup>.

<sup>3</sup>markforged.com

<sup>4</sup>acpcomposites.com

## 7.8 Experimental Gait Optimization

This section describes our approach to experimentally search for optimal gaits for various swimming maneuvers using the final prototype, which was based on the optimal results from the prior simulation. The experimental search is essential for closing the gap between simulation and real-world trials due to model estimation errors caused by the flat plate model, as well as the approach used for modeling servo control. To evaluate the performance of each gait, we have prepared an experimental setup (Fig 7.16a) capable of sampling either the thrust and moment generated by the fins, or the swimming distance and speed. A linear carriage running on a rail is installed on the top of a  $4 \times 2 \times 2\text{ft}^3$  tank ( $1 \times w \times h$ ). The robot's position is measured using an OptiTrack motion tracking system. An ATI mini-40 force-torque sensor is attached to the carriage; its distal attachment connects to the robot via an aluminum extension arm that holds the robot underwater. An optimization process is then performed using CMA-ES to find the optimal parameters of each desired gait by determining optimal parameters for control rule (7.14).

**Rowing Gaits** In this optimization process, the robot swims 5 seconds with the buckling beam in its long configuration (Fig. 7.15c); the distance traveled in that time is then measured. A servo and pulley resets the carriage to its initial position at the end of each trial. In order to protect the curved beams from damage due to gaits that exceed a safe operating range, a joint limit is temporarily attached during the optimization process, and optimal gaits are then re-tested once they are determined to be safe. Figure 7.16d shows the swimming distance for the feasible parameter sets in the optimization process. The swimming distance of the best gait is illustrated in Fig. 7.16e. The data show a discontinuous pattern motion. We believe this is caused by high friction and stiction within the linear slider; the generated

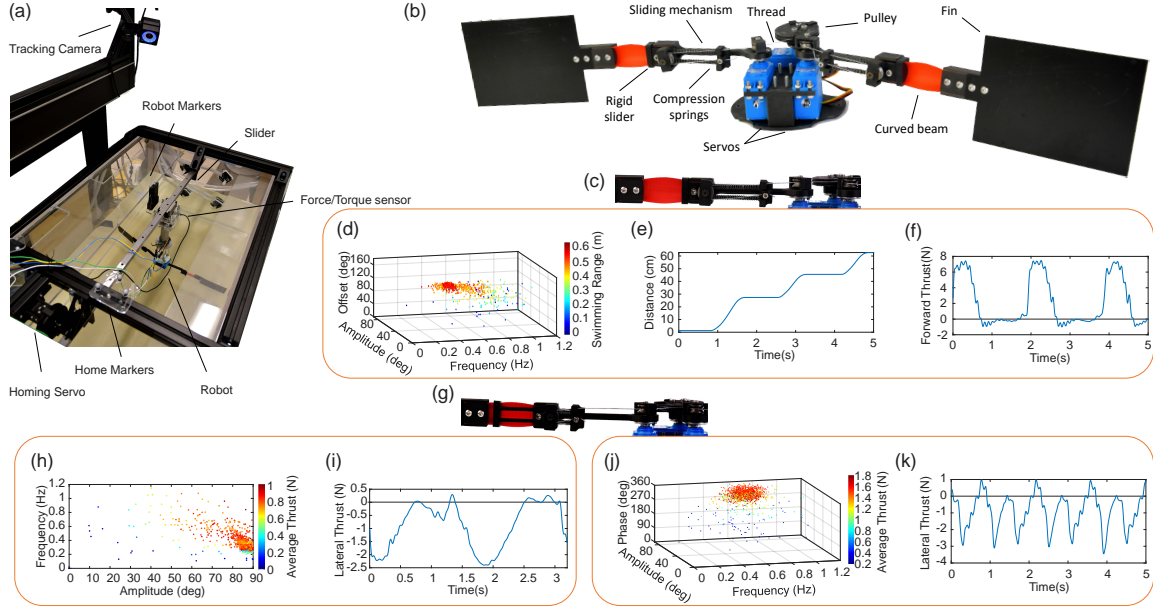


Figure 7.16: **Results of the experimental gait optimization for (c-f) forward swimming, (g-i) lateral swimming, and (g,j-k) undulation.** (a) Experimental setup. (b) Robot's prototype. Sliding mechanism configuration for (c) Long and (g) short effective lengths. (e) Position vs. time for forward swimming. (f,i,k) Thrust forces generated by each gait.

thrust measurements may be seen in Fig. 7.16f. Nevertheless, the data also shows the efficacy of the one-sided buckling of the curved hinge when used in conjunction with optimized input gaits to generate net thrust; the forces generated during recovery stroke are limited to -1 N, while the power stroke achieves 7.5 N thrust at its peak.

**Flapping Gaits** By reducing the effective length of the curved beam (Fig. 7.16g), its stiffness increases in both the opposite and equal-sense directions, changing the buckling beam's behavior, seen in Fig7.13, to be both stiffer and more symmetric. Using this phenomenon, lateral thrusts may be generated by flapping one limb ( $\alpha_2 = \beta_2 = f_2 = 0$ ) with a sinusoidal input while maintaining a neutral offset in the

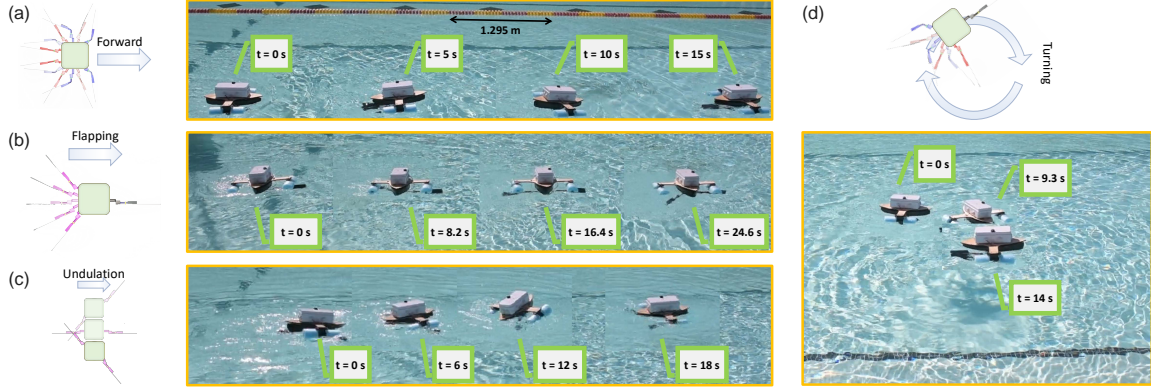


Figure 7.17: **Untethered robot swimming.** (a) Swimming forward using rowing gaits of both fins. (b) Swimming laterally using one fin flapping actuation. (c) Swimming using undulating gait. (d) Turning by rowing gaits of one fin.

other ( $\beta_1 = 0$ ). A new set of optimal gait parameters was obtained by searching through the resulting two-dimensional space of gait parameters, but the lateral thrust found by this approach was unable to overcome rail stiction. We therefore adopted a thrust-based metric (rather than a distance metric) similar to [132]. Figures 7.16(h,i) illustrate the average thrust generated by each gait throughout the optimization as well as the thrust generated by the optimal gait, respectively. The result shows that a flapping gait with relatively large input amplitude ( $\alpha = 87^\circ$ ) and low frequency ( $f = 0.3$  Hz) is optimal.

By commanding both limbs to perform asynchronous, flapping gaits ( $\phi \neq 0^\circ$ ), the robot swimming mode changes to undulation, similar to snakes, eels, and Purcell’s three-link swimmer [210, 211, 212]. We have experimentally searched the three-dimensional space of input parameters related to undulation in order to obtain the highest lateral thrust undulating gait that exceeds the lateral single-limb maximum swimming speed found above. The resulting net thrust generated by each set of gait parameters throughout the optimization is shown in Fig. 7.16j; the optimal gait

generated thrust is shown in Fig. 7.16k.

To address the problem of stiction which we found in the experimental setup, a free-swimming prototype has been constructed by mounting the swimming mechanism to a floating platform that ensures the fins stay underwater, while keeping power electronics above the water. Using the optimal gaits obtained from the experimental search, the untethered robot's performance has been evaluated (Fig 7.17).

Using the optimal rowing gait, the robot achieves a forward swimming speed of about 0.32 m/s (Fig 7.17a); the swimming distance per rowing cycle is around 0.6 m. The robot is also able to turn when only one limb is commanded by the same optimal gait. The turning speed is 25.7 deg/s (Fig 7.17d). When flapping, the untethered robot achieves a lateral swimming speed of 0.17 m/s when only one limb is actuated (Fig 7.17b). When undulating, the robot achieves a swimming speed of 0.16 m/s (Fig 7.17c). It was observed that, while the thrust data is better for an undulating strategy, the swimming speed of the untethered robot was lower than others, which we attribute to the higher drag of the floating platform when rotating. Future work will consider this additional loss of energy in modeling and optimization.

## 7.9 Discussion

This chapter studies the use of buckling curved beams for use in flapping-wing mobile robots moving through fluids. The theory behind this phenomenon is studied analytically, while finite element analysis permits us to look beyond the limited conditions anticipated by prior work and investigate a wide range of buckling shapes and load conditions. The proposed propulsion method has been experimentally validated by measuring the force and work generated by a wing flapping in air and water, in the presence and absence of buckling. Hysteresis due to buckling is clearly visible, and the average force produced via symmetric flapping is positive in the direction of

forward motion. Next, we study how altering the stiffness and buckling limits of slender curved beams enhances swimming maneuverability by providing the opportunity to switch between different swimming gaits. By introducing a dynamic model that simulates the swimming of a robot using this concept, we have performed a design optimization to increase swimming speed. We have also conducted an experimental search through selected gait parameters for swimming strategies that result in a robot that is capable of swimming both forward and laterally as well as turning. The unique characteristics of our fin system, obtained through the use flexible curved beams, not only simplifies the role actuation plays in locomotion, but also helps decouple the role of the actuators between the generation of work and reconfiguration.

In terms of impact, we believe this work will inform the future design and optimization of simple flapping swimmers and flyers. Understanding the nonlinear behavior of buckling curved beams and how geometry influences critical buckling loads permits these systems to be tuned along a spectrum of performance requirements for use in air or water. Knowledge of how hinge geometry affects such response will also lead to simpler, more mechanism-oriented design approaches, and will permit designers to identify coupled wing/beam designs as well as tuned swimming gaits that are optimal across competing criteria like efficiency, power, and speed. We also believe our approach of tuning stiffness and buckling limits, in conjunction with simple actuation strategies, will eventually permit lower-power and more affordable robots to be tuned for specialist jobs in niche environments, while still permitting a wide range of locomotion strategies.

Future work will focus on improving models to include three-dimensional simulation for better understanding the full state of underwater robot dynamics, as well as implementing depth change. This will enable us to consider multiple swimming strategies simultaneously in optimizing the robot's body and fin morphology. We also

plan to continue optimizing the design of curved beam devices for more efficient locomotion by investigating variable stiffness designs as well as multi-material fabrication strategies. Future work will expand this concept further to include terrestrial locomotion and amphibious environments.

### CONCLUSION

Moving from rigid robots to robots built from soft materials opens new possibilities for robotic platforms to perform unique tasks safer and more efficiently. There are, however, some challenges limiting conventional soft robots' performance; among them, three important ones are still unanswered. First, the big bulky and heavy air pressure systems required for pneumatically actuated soft robots limits their mobility and their capability to become stand-alone and untethered. Second, soft robots' modeling, shape, material properties, and design are interrelated and complex that make closing the design loop of these robots challenging for roboticists. Finally, in many cases, a fully soft mechanism provides a safer working environment for human interaction, however, it limits the amount of force it can exert on external objects.

Foldable robots made with laminated techniques can be good alternatives to conventional soft robots since they can leverage regular actuators such as servos. These robot's stiffness is easily tuned by material selection and scaling sizes.

This thesis shows how considering the compliance of soft robots, specifically foldable robots manufactured using laminated techniques, and their deformation enhances their performance in real-world environments. We believe that through careful modeling and control, these robots can be considered as alternatives to both expensive rigid robots manufactured from metals with high precision and conventional soft robots manufactured by molding and curing silicon-based materials. The manufacturing time and cost of these robots are a fraction of the conventional rigid robot's metal machinery. In comparison with conventional soft robots that use pneumatic and tendon-based actuation, the ability to use servo motors in foldable robots reduces



the complexity associated with modeling and control of these robots.

By increasing the life span and selecting correct modeling and control methods, laminated robots presented in this thesis can be leveraged to perform unique tasks similar to other robots manufactured by conventional methods; while being lighter, easily scalable, more affordable, and faster to manufacture.

The majority of this thesis is dedicated to proposing methods to model and control these robots in their interactions with their surroundings. We have presented different data-driven and machine learning approaches to deal with and in fact leverage the deformation of these robots. The proposed methods represent alternatives to the FEA-based and exact geometry modeling approaches such as PCC and Cosserat models, that are computationally expensive, especially in the presence of external force interactions.

The proposed approaches in this thesis are also unique because they are based on experimental setups that account for uncertainties that commonly exist in real-world environments. In other words, in designing experiments and assembling the experimental setups, we have avoided ideal environments with perfect repeatability. We believe that the high repeatability associated with ideal test environments can negatively impact the robot's performance and its capability to perform tasks in the real-world. On the other hand, running tests in the real world can be challenging and difficult to set up and maintain. In this thesis, we showed that non-ideal experimental setups with uncertainties embedded in them are good compromise, especially if they are utilized in conjunction with machine learning techniques. Another distinct characteristic of the proposed methods in this thesis is the use of online optimization. While interacting with the working environment, soft robots tend to experience more deformation. The modeling of soft robots in this case is complicated and computationally expensive, if plausible at all. Online optimization is also useful in the absence

of models that adequately capture system behavior. We leverage automation in designing and running experiments, so the online processes may be carried out without the need for human involvement.

## 8.1 Impact & Future Work

This thesis proposes some solutions to the big challenges associated with foldable robots manufactured by laminated techniques. The use of soft materials in this manufacturing approach imparts a large technical challenge in the design, modeling, and control of high-performing robots made from less-formalized materials.

I believe the methods proposed for training robots to be used in the real-world via machine learning techniques can be used as a roadmap by other experts in the field of robotics. The achievements of this thesis on the Soft, Curved, Reconfigurable, Anisotropic Mechanisms (SCRAMs) that exhibit local reconfigurability will ameliorate the control and actuation difficulties in current soft robot systems in near future, resulting in robots with much higher efficiency and adaptability.

Another important impact of this thesis is presenting a series of technical suggestions that improve the durability of foldable robots even when affordable materials are used to keep the robot's cost low. The ability to develop durable, low-cost robots that are fast to prototype is critical to lowering the barrier to entry for using affordable and accessible robots outside the community of roboticists. These unique characteristics make these robots a perfect asset to be used in education and help to introduce students to the field much sooner. Solutions to fundamental problems in modeling, control, and design of these robots make them more accessible in new domains like farming and undersea exploration.

This thesis contributes to the field of compliant foldable robots by providing some answers to the grand challenges associated with these robots. This field within

robotics is a rich area filled with unlimited opportunities. I would like to conclude this thesis by proposing some suggestions for future work:

**Design & manufacturing:** While manufacturing foldable robots using laminated techniques is fast, there is still room to improve and ease the design process. PopupCAD, the software used in this thesis, helps with designing these robots in 2D and automatically produces cut files efficiently with minimum effort from the user. However, the initial design step of converting a 3D design to a series of 2D ones is still mostly done by the user; a software solution to this step would make the design process more accessible to average people.

**Evolving to smart, adaptable robots:** Robots are often designed and manufactured for a specific task in a pre-defined environment. This limits their performance and should be addressed so the robots can adapt to real-world working environments with different types of uncertainties. As a starting point, we demonstrated how reconfigurability helps to enhance a swimming robot's maneuverability. We also showed the potential of using machine learning for finding gaits suitable for different scenarios in real-world environments. However, future work should address the current limiting factors of machine learning techniques, such as the vulnerability of optimization algorithms to repeatability of systems. The obtained results show that this issue increases the time required for training robots. In general, the common assumption of high repeatability during optimization should be revised. There remains a need for algorithms that consider system repeatability as a factor in finding optimal results. Another step in training the next generation of robots is to enhance their functionality through continuous online training in the field, so the robot constantly updates its knowledge from the environment to refine its design, adapt its decision making or behavior, and switch between gaits as needed. An amphibious robot is a good example; leveraging the methods explained in this thesis, optimal gaits can be found

to enhance the robots' locomotion in water and on land. However, an effective transition between these two gaits needs extensive study that requires extra sensing, online training, and control so the robot learns how to adapt to new environments.

**Extension to other fields:** Introducing these robots to experts of other fields opens the door to new opportunities and challenges. The low manufacturing time and cost associated with origami-inspired and SCRAM devices makes these robots perfect platform for swarm applications. Each robot may be limited in power and performance, but a swarm of these robots are capable of performing more complex tasks. While the latter advantages are mentioned for many foldable platforms, few studies cover implementations of these robots in swarm robotics.

**Environment friendly:** We can propose solutions to real-life problems leveraging the unique characteristics of these robots. For example, using a swarm of these robots in large numbers reduces the impact of one robot and enables the system to complete tasks even if some robot agents fail. While these minimize human involvement, it increases concerns about how the remains of the failed robots would affect the environment. Moving towards organic, environment-friendly materials, sensors and actuators is a necessity for these robots' proper introduction to the real world.

I envision a herd of mobile foldable robots to collaborate and perform various tasks in the real world. Future generations of these robots should be capable of adapting themselves to locomote in different environments, such as water, granular environments, and smooth land, or even jump and glide to pass an obstacle. Ideally, these robots would be made from environment-friendly materials, so in case of failure, they would not be harmful to the environment.

As manipulators, I envision these robots to be used as reliable, human-safe, and affordable alternatives to the rigid robots currently used in industry. These robots can use embedded sensing and actuation to increase their precision and, by performing

a constant evaluation of their performance, they will provide scientists with useful data to iterate the robot’s design and improve over multiple design cycles using data from the field. Wouldn’t it be fun if manufacturing robots finish up the week by manufacturing an improved generation of themselves to be used the next week?

## 8.2 Publications

### 8.2.1 *Journal Papers*

**Sharifzadeh, Mohammad,** and Aukes, Daniel. “Curvature-Induced Buckling for Flapping-Wing Vehicles.” *IEEE/ASME Transactions on Mechatronics* (2020).

**Sharifzadeh, Mohammad,** Jiang, Yuhao, and Aukes, Daniel. “Reconfigurable Curved Beams for Selectable Swimming Gaits in an Underwater Robot.” *IEEE Robotics and Automation Letters* (2021).

Doroudchi, Azadeh, Khodambashi, Roozbeh, **Sharifzadeh, Mohammad,** Li, Dongting, Berman, Spring, and Aukes, Daniel. “Tracking Control of a Miniature 2-DOF Manipulator with Hydrogel Actuators.” *IEEE Robotics and Automation Letters* (2021)

textbfSharifzadeh, Mohammad, Jiang, Yuhao, Lafmejani, Amir Salimi, Nichols, Kevin, and Aukes, Daniel. “Maneuverable Gait Selection for a Novel Fish-Inspired Robot Using a CMAES-Assisted Workflow.” *IOP Bioinspiration & Biomimetics* (Under preparation)

**Sharifzadeh, Mohammad,** Jiang, Yuhao, and Aukes, Daniel. “Compensating for Material Deformation in Foldable Robots via Deep Learning– A Case Study.” *ASME Journal of Mechanisms and Robotics* (Under preparation)

### 8.2.2 Conference Papers

Jiang, Yuhao, and **Sharifzadeh, Mohammad**, and Aukes, Daniel. “Reconfigurable Soft Flexure Hinges via Pinched Tubes.” IEEE IROS (2020).

**Sharifzadeh, Mohammad**, Jiang, Yuhao, Khodambashi, Roozbeh , and Aukes, Daniel. “Increasing the Life Span of Foldable Manipulators With Fabric.” ASME IDETC-CIE (2020).

**Sharifzadeh, Mohammad**, Khodambashi, Roozbeh, Zhang, Wenlong, and Aukes, Daniel. “On Locomotion of a Laminated Fish-inspired robot in a Small-to-size Environment.” ASME IDETC-CIE (2018)

**Sharifzadeh, Mohammad**, and Khodambashi, Roozbeh, and Aukes, Daniel. “An integrated design and simulation environment for rapid prototyping of laminate robotic mechanisms.” ASME IDETC-CIE (2018)

Jiang, Yuhao, and **Sharifzadeh, Mohammad**, and Aukes, Daniel. “Shape Change Propagation Through Soft Curved Materials for Dynamically-Tuned Paddling Robots.” IEEE IROS (2020).

Doroudchi, Azadeh, Khodambashi, Roozbeh, **Sharifzadeh, Mohammad**, Li, Dongting, Berman, Spring, and Aukes, Daniel. “Tracking Control of a Miniature 2-DOF Manipulator with Hydrogel Actuators.” IEEE RoboSoft Conference (2021)

### 8.2.3 Talks

**Sharifzadeh, Mohammad,** Jiang, Yuhao, Justus, Nathan, Jiang, Mingsong, Aukes, Daniel, Gravish, Nick, Harnett, Cindy, and Hatton, Ross. “Breaking the Mold: Challenging Current Paradigms in Soft Robotics.” IEEE RoboSoft Conference (2021) Workshop, April 12, 2021.

**Sharifzadeh, Mohammad,** Lafmejani, Amir Salimi, Nichols, Kevin, and Aukes, Daniel. “Training of Robotic Pectoral Fin Maneuvers Based on the CMAES Algorithm”. 2019 Southwest Robotics Symposium, Arizona State University, Tempe, AZ, Jan. 24-25, 2019.

**Sharifzadeh, Mohammad,** Khodambashi, Roozbeh, Aukes, Daniel, and Zhang, Wenlong. “Experimental identification and control of a fish-inspired laminated robot movement in the water.” 2018 Southwest Robotics Symposium, Arizona State University, Tempe, AZ, Jan. 25-26, 2018.

## REFERENCES

- [1] Daniel M Aukes and Robert J Wood. PopupCAD: a tool for automated design, fabrication, and analysis of laminate devices. In Thomas George, Achyut K. Dutta, and M. Saif Islam, editors, *SPIE.DSS*, page 94671B, may 2015.
- [2] Steven I. Rich, Robert J. Wood, and Carmel Majidi. Untethered soft robotics. *Nature Electronics*, 1(2):102–112, 2018.
- [3] Hayley McClintock, Fatma Zeynep Temel, Neel Doshi, Je Sung Koh, and Robert J. Wood. The milliDelta: A high-bandwidth, high-precision, millimeter-scale Delta robot. *Science Robotics*, 3(14), 2018.
- [4] Satoshi Saga. *Haptic Display — Laser-Emission-Based*. Springer Singapore, 2019.
- [5] Marco Salerno, Amir Firouzeh, and Jamie Paik. A low profile electromagnetic actuator design and model for an origami parallel platform. *Journal of Mechanisms and Robotics*, 9(4):1–63, 2017.
- [6] Hiroyuki Suzuki and Robert J Wood. Origami-inspired miniature manipulator for teleoperated microsurgery. *Nature Machine Intelligence*, 2(8):437–446, 2020.
- [7] Di Chen, Weiping Shao, and Chunquan Xu. Development of a Soft Robotic Fish with BCF Propulsion Using MFC Smart Materials. *Chinese Control Conference, CCC*, 2018-July:5358–5363, 2018.
- [8] 2018. Portable Haptic Interface, <http://http://www.foldaway-haptics.com/>.
- [9] Kevin Sebastian Luck, Joseph Campbell, Michael Andrew Jansen, Daniel M. Aukes, and Heni Ben Amor. From the lab to the desert: Fast prototyping and learning of robot locomotion. *Robotics: Science and Systems*, 13(c), 2017.
- [10] Noah T. Jafferis, E. Farrell Helbling, Michael Karpelson, and Robert J. Wood. Untethered flight of an insect-sized flapping-wing microscale aerial vehicle. *Nature*, 570(7762):491–495, 2019.
- [11] Dangli Yang, Shatadal Mishra, Daniel M Aukes, and Wenlong Zhang. Design, Planning, and Control of an Origami-inspired Foldable Quadrotor. *2019 American Control Conference*, pages 2251–2256, 2019.
- [12] Stefano Mintchev, Jun Shintake, and Dario Floreano. Bioinspired dual-stiffness origami. *Science Robotics*, 3(20):eaau0275, 2018.
- [13] Zhenishbek Zhakypov, Kazuaki Mori, Koh Hosoda, and Jamie Paik. Designing minimal and scalable insect-inspired multi-locomotion millirobots. *Nature*, 28, 2019.



- [14] Thor Morales Bieze, Frederick Largilliere, Alexandre Kruszewski, Zhongkai Zhang, Rochdi Merzouki, and Christian Duriez. Finite element method-based kinematics and closed-loop control of soft, continuum manipulators. *Soft Robotics*, 5(3):348–364, 2018.
- [15] Olivier Goury and Christian Duriez. Fast, Generic, and Reliable Control and Simulation of Soft Robots Using Model Order Reduction. *IEEE Transactions on Robotics*, 34(6):1565–1576, 2018.
- [16] Sheng Huang, Qiyuan Zhang, Zhaoyang Liu, Xueqian Wang, and Bin Liang. Control of a piecewise constant curvature continuum manipulator via policy search method. *2018 IEEE International Conference on Robotics and Biomimetics, ROBIO 2018*, (61673239):1777–1782, 2019.
- [17] Cosimo Della Santina, Robert K. Katzschmann, Antonio Bicchi, and Daniela Rus. Dynamic control of soft robots interacting with the environment. *2018 IEEE International Conference on Soft Robotics, RoboSoft 2018*, pages 46–53, 2018.
- [18] Robert K. Katzschmann, Cosimo Della Santina, Yasunori Tshimitsu, Antonio Bicchi, and Daniela Rus. Dynamic motion control of multi-segment soft robots using piecewise constant curvature matched with an augmented rigid body model. *RoboSoft 2019 - 2019 IEEE International Conference on Soft Robotics*, pages 454–461, 2019.
- [19] Hao Yang, Min Xu, Weihua Li, and Shiwu Zhang. Design and Implementation of a Soft Robotic Arm Driven by SMA Coils. *IEEE Transactions on Industrial Electronics*, 66(8):6108–6116, 2019.
- [20] Morgan T. Gillespie, Charles M. Best, Eric C. Townsend, David Wingate, and Marc D. Killpack. Learning nonlinear dynamic models of soft robots for model predictive control with neural networks. *2018 IEEE International Conference on Soft Robotics, RoboSoft 2018*, pages 39–45, 2018.
- [21] Thomas George Thuruthel, Egidio Falotico, Federico Renda, and Cecilia Laschi. Model-Based Reinforcement Learning for Closed-Loop Dynamic Control of Soft Robotic Manipulators. *IEEE Transactions on Robotics*, 35(1):127–134, 2019.
- [22] Tao Du, Kui Wu, Pingchuan Ma, Sebastien Wah, Andrew Spielberg, Daniela Rus, and Wojciech Matusik. Diffpd: Differentiable projective dynamics with contact. *arXiv e-prints*, pages arXiv–2101, 2021.
- [23] Heng-Sheng Chang, Udit Halder, Chia-Hsien Shih, Arman Tekinalp, Tejaswin Parthasarathy, Ekaterina Gribkova, Girish Chowdhary, Rhanor Gillette, Mattia Gazzola, and Prashant G Mehta. Energy shaping control of a cyberoctopus soft arm. In *2020 59th IEEE Conference on Decision and Control (CDC)*, pages 3913–3920. IEEE, 2020.

- [24] Azadeh Dorudchi and Spring Berman. Configuration tracking for soft continuum robotic arms using inverse dynamic control of a cosserat rod model. In *2021 IEEE International Conference on Soft Robotics, RoboSoft 2021*, page Accepted. Institute of Electrical and Electronics Engineers Inc., 2021.
- [25] Isuru S. Godage, Yue Chen, Kevin C. Galloway, Emily Templeton, Brian Rife, and Ian D. Walker. Real-time Dynamic Models for Soft Bending Actuators. *2018 IEEE International Conference on Robotics and Biomimetics, ROBIO 2018*, pages 1310–1315, 2019.
- [26] Isuru S. Godage, Gustavo A. Medrano-Cerda, David T. Branson, Emanuele Guglielmino, and Darwin G. Caldwell. Dynamics for variable length multisection continuum arms. *International Journal of Robotics Research*, 35(6):695–722, 2016.
- [27] Sofien Bouaziz, Sebastian Martin, Tiantian Liu, Ladislav Kavan, and Mark Pauly. Projective dynamics: Fusing constraint projections for fast simulation. *ACM transactions on graphics (TOG)*, 33(4):1–11, 2014.
- [28] Noel Naughton, Jiarui Sun, Arman Tekinalp, Girish Chowdhary, and Mattia Gazzola. Elastica: A compliant mechanics environment for soft robotic control. *arXiv preprint arXiv:2009.08422*, 2020.
- [29] Azadeh Doroudchi, Roozbeh Khodambashiy, Amir Salimi Lafmejaniy, Daniel M Aukes, and Spring Berman. Dynamic modeling of a hydrogel-based continuum robotic arm with experimental validation. In *2020 3rd IEEE International Conference on Soft Robotics (RoboSoft)*, pages 695–701. IEEE, 2020.
- [30] Yuan Gao, Xiguang Huang, Ishan Singh Mann, and Hai-Jun Su. A novel variable stiffness compliant robotic gripper based on layer jamming. *Journal of Mechanisms and Robotics*, 12(5), 2020.
- [31] Sang-Min Baek, Sojung Yim, Soo-Hwan Chae, Dae-Young Lee, and Kyu-Jin Cho. Ladybird beetle-inspired compliant origami. *Science Robotics*, 5(41), 2020.
- [32] Yujia Li, Tao Ren, Yonghua Chen, and Michael ZQ Chen. A variable stiffness soft continuum robot based on pre-charged air, particle jamming, and origami. In *2020 IEEE International Conference on Robotics and Automation (ICRA)*, pages 5869–5875. IEEE, 2020.
- [33] Yu She, Hai-Jun Su, Deshan Meng, and Cheng Lai. Design and modeling of a continuously tunable stiffness arm for safe physical human–robot interaction. *Journal of Mechanisms and Robotics*, 12(1), 2020.
- [34] Mingsong Jiang and Nick Gravish. Reconfigurable laminates enable multifunctional robotic building blocks. *Smart Materials and Structures*, 2021.

- [35] Mingsong Jiang, Rongzichen Song, and Nick Gravish. Knuckles that buckle: compliant underactuated limbs with joint hysteresis enable minimalist terrestrial robots. In *2020 IEEE/RSJ International Conference on Intelligent Robots and Systems, IROS 2020*, page Accepted. Institute of Electrical and Electronics Engineers Inc., 2020.
- [36] Yuhao Jiang, Mohammad Sharifzadeh, and Dan Aukes. Reconfigurable soft flexure hinges via pinched tubes. In *2020 IEEE/RSJ International Conference on Intelligent Robots and Systems, IROS 2020*, page Accepted. Institute of Electrical and Electronics Engineers Inc., 2020.
- [37] Hayley McClintock, Fatma Zeynep Temel, Neel Doshi, Je-sung Koh, and Robert J Wood. The millidelta: A high-bandwidth, high-precision, millimeter-scale delta robot. *Science Robotics*, 3(14):eaar3018, 2018.
- [38] Jorge E Correa, Joseph Toombs, Nicholas Toombs, and Placid M Ferreira. Laminated micro-machine: Design and fabrication of a flexure-based delta robot. *Journal of Manufacturing Processes*, 24:370–375, 2016.
- [39] Metin Sitti. Piezoelectrically actuated four-bar mechanism with two flexible links for micromechanical flying insect thorax. *IEEE/ASME Transactions on Mechatronics*, 8(1):26–36, 2003.
- [40] A. T. Baisch, O. Ozcan, B. Goldberg, D. Ithier, and R. J. Wood. High speed locomotion for a quadrupedal microrobot. *The International Journal of Robotics Research*, may 2014.
- [41] Ben Goldberg, Onur Ozcan, and Robert J. Wood. Planar Fabrication of a Mesoscale Voice Coil Actuator. In *IEEE Int. Conf. on Robotics and Automation*, Hong Kong, 2014.
- [42] P S Sreetharan, J P Whitney, M D Strauss, and R J Wood. Monolithic fabrication of millimeter-scale machines. *Journal of Micromechanics and Microengineering*, 22(5):055027, may 2012.
- [43] P. Birkmeyer, K. Peterson, and R. S. Fearing. DASH: A dynamic 16g hexapedal robot. *2009 IEEE/RSJ International Conference on Intelligent Robots and Systems, IROS 2009*, pages 2683–2689, 2009.
- [44] Matthew Gardiner. Folding and unfolding a million times over: Longevity, origami, robotics and biomimetics as material thinking in oribotics. *Symmetrion, Symmetries in ORI Bibliography*, 2015.
- [45] Frank Dirksen, Mathias Anselmann, Tarek I Zohdi, and Rolf Lammering. Incorporation of flexural hinge fatigue-life cycle criteria into the topological design of compliant small-scale devices. *Precision Engineering*, 37(3):531–541, 2013.
- [46] Ronit Malka, Alexis Lussier Desbiens, Yufeng Chen, and Robert J Wood. Principles of microscale flexure hinge design for enhanced endurance. In *2014 IEEE/RSJ International Conference on Intelligent Robots and Systems*, pages 2879–2885. IEEE, 2014.

- [47] Xianwen Kong. Forward displacement analysis and singularity analysis of a special 2-dof 5r spherical parallel manipulator. *Journal of Mechanisms and Robotics*, 3(2):024501, 2011.
- [48] Doug Stewart. A platform with six degrees of freedom. *Proceedings of the institution of mechanical engineers*, 180(1):371–386, 1965.
- [49] Amir Salimi Lafmejani, Mehdi Tale Masouleh, and Ahmad Kalhor. Trajectory tracking control of a pneumatically actuated 6-dof gough–stewart parallel robot using backstepping-sliding mode controller and geometry-based quasi forward kinematic method. *Robotics and Computer-Integrated Manufacturing*, 54:96–114, 2018.
- [50] François Pierrot, C Reynaud, and Alain Fournier. Delta: a simple and efficient parallel robot. *Robotica*, 8(2):105–109, 1990.
- [51] Lung-Wen Tsai. Kinematics of a three-dof platform with three extensible limbs. In *Recent advances in robot kinematics*, pages 401–410. Springer, 1996.
- [52] Azadeh Doroudchi, Mohsen Heydarzadeh, Mehdi Tale Masouleh, and Masume Moghimi Esfandabad. An experimental study on open-loop position and speed control of a 3-rrr planar parallel mechanism. In *Robotics and Mechatronics (ICROM), 2015 3rd RSI International Conference on*, pages 176–181. IEEE, 2015.
- [53] CM Gosselin, X Kong, S Foucault, IA Bonev, et al. A fully decoupled 3-dof translational parallel mechanism. In *Parallel Kinematic Machines in Research and Practice, 4th Chemnitz Parallel Kinematics Seminar*, pages 595–610, 2004.
- [54] Mohsen Heydarzadeh, Nima Karbasizadeh, Mehdi Tale Masouleh, and Ahmad Kalhor. Experimental kinematic identification and position control of a 3-dof decoupled parallel robot. *Proceedings of the Institution of Mechanical Engineers, Part C: Journal of Mechanical Engineering Science*, page 0954406218775906, 2018.
- [55] M Ouerfelli and V Kumar. Optimization of a spherical five-bar parallel drive linkage. *Journal of mechanical design*, 116(1):166–173, 1994.
- [56] Li-Jie Zhang, Yue-Wei Niu, Yong-Quan Li, and Zhen Huang. Analysis of the workspace of 2-dof spherical 5r parallel manipulator. In *Robotics and Automation, 2006. ICRA 2006. Proceedings 2006 IEEE International Conference on*, pages 1123–1128. IEEE, 2006.
- [57] Jialun Yang and Feng Gao. Singularity loci of an orthogonal spherical two-degree-of-freedom parallel mechanism. *Frontiers of Mechanical Engineering in China*, 4(4):379, 2009.
- [58] Alaleh Arian, Behzad Danaei, and Mehdi Tale Masouleh. Kinematics and dynamics analysis of a 2-dof spherical parallel robot. In *Robotics and Mechatronics (ICROM), 2016 4th International Conference on*, pages 154–159. IEEE, 2016.

- [59] Alireza Safaryazdi, Mojtaba Zarei, Omid Abolghasemi, and Mehdi Tale Masouleh. Experimental study on the model-based control of a 2-degree-of-freedom spherical parallel robot camera stabilizer based on multi-thread programming concept. *Proceedings of the Institution of Mechanical Engineers, Part C: Journal of Mechanical Engineering Science*, 232(10):1882–1897, 2018.
- [60] Milad Eyvazi Hesar, MT Masouleh, Ahmad Kalhor, MB Menhaj, and Navid Kashi. Ball tracking with a 2-dof spherical parallel robot based on visual servoing controllers. In *Robotics and Mechatronics (ICRoM), 2014 Second RSI/ISM International Conference on*, pages 292–297. IEEE, 2014.
- [61] Eric Samson, Denis Laurendeau, Marc Parizeau, Sylvain Comtois, Jean-François Allan, and Clément Gosselin. The agile stereo pair for active vision. *Machine Vision and Applications*, 17(1):32–50, 2006.
- [62] Neel Doshi, Benjamin Goldberg, Ranjana Sahai, Noah Jafferis, Daniel Aukes, Robert J Wood, and John A Paulson. Model driven design for flexure-based microrobots. In *Intelligent Robots and Systems (IROS), 2015 IEEE/RSJ International Conference on*, pages 4119–4126. IEEE, 2015.
- [63] Larry L Howell, Spencer P Magleby, and Brian M Olsen. *Handbook of compliant mechanisms*. John Wiley & Sons, 2013.
- [64] Clement M Gosselin and François Caron. Two degree-of-freedom spherical orienting device, October 19 1999. US Patent 5,966,991.
- [65] K. Y. Ma, P. Chirarattananon, S. B. Fuller, and R. J. Wood. Controlled Flight of a Biologically Inspired, Insect-Scale Robot. *Science*, 340(6132):603–607, may 2013.
- [66] Daniel M. Aukes and Robert J. Wood. Algorithms for Rapid Development of Inherently-Manufacturable Laminate Devices. In *ASME 2014 Conference on Smart Materials, Adaptive Structures and Intelligent Systems*, page V001T01A005, Newport, RI, USA, sep 2014. ASME.
- [67] Daniel M Aukes, Benjamin Goldberg, Mark R Cutkosky, and Robert J Wood. An analytic framework for developing inherently-manufacturable pop-up laminate devices. *Smart Materials and Structures*, 23(9):094013, sep 2014.
- [68] Daniel M. Aukes, Onur Ozcan, and Robert J. Wood. Monolithic Design and Fabrication of a 2-DOF Bio-Inspired Leg Transmission. In *Third International Conference, Living Machines 2014, Milan, Italy, July 30 - August 1, 2014.*, pages 1–10. Springer International Publishing, Milan, 2014.
- [69] P. Stellman, W. Arora, S. Takahashi, E. D. Demaine, and G. Barbastathis. Kinematics and Dynamics of Nanostructured Origami™. In *Design Engineering, Parts A and B*, volume 2005, pages 541–548. ASME, 2005.
- [70] Tomohiro Tachi. Simulation of Rigid Origami. In *Origami4:Proceedings of 4OSME*, 2009.

- [71] Mark Schenk and Simon D Guest. Origami Folding : A Structural Engineering Approach. In *Origami 5: Fifth International Meeting of Origami Science, Mathematics, and Education.(5OSME)*, pages 291–303, 2011.
- [72] Kazuko Fuchi, Philip R Buskohl, James J Joo, Gregory W Reich, and Richard A Vaia. Topology Optimization for Design of Origami-Based Active Mechanisms. In *Proceedings of the ASME 2014 International Design Engineering Technical Conferences & Computers and Information in Engineering Conference (IDETC/CIE 2014)*, pages DETC2014–35153, Buffalo, 2014.
- [73] Raymond R. Ma, Lael U. Odhner, and Aaron M. Dollar. A Modular, Open-Source 3D Printed Underactuated Hand. In *2013 IEEE International Conference on Robotics and Automation(preprint)*. IEEE, may 2013.
- [74] Neel Doshi, Benjamin Goldberg, Ranjana Sahai, Noah Jafferis, Daniel Aukes, Robert J Wood, and John A. Paulson. Model driven design for flexure-based Microrobots. In *2015 IEEE/RSJ International Conference on Intelligent Robots and Systems (IROS)*, pages 4119–4126. IEEE, sep 2015.
- [75] Brandon H Hanna, Jason M Lund, Robert J Lang, Spencer P Magleby, and Larry L Howell. Waterbomb base: a symmetric single-vertex bistable origami mechanism. *Smart Materials and Structures*, 23(9):094009, sep 2014.
- [76] J. Baumgarte. Stabilization of constraints and integrals of motion in dynamical systems, 1972.
- [77] Pierangelo Masarati. Adding kinematic constraints to purely differential dynamics. *Computational Mechanics*, 47(2):187–203, 2011.
- [78] ASTM International. ASTM D882: Standard Test Method for Tensile Properties of Thin Plastic Sheeting. *ASTM Standards*, page 12, 2012.
- [79] Yavuz Aydin and Serdar Kucuk. Quaternion based inverse kinematics for industrial robot manipulators with euler wrist. In *Mechatronics, 2006 IEEE International Conference on*, pages 581–586. IEEE, 2006.
- [80] Philip Moseley, Juan Manuel Florez, Harshal Arun Sonar, Gunjan Agarwal, William Curtin, and Jamie Paik. Modeling, Design, and Development of Soft Pneumatic Actuators with Finite Element Method. *Advanced Engineering Materials*, (6), 2015.
- [81] Christian Duriez. Control of elastic soft robots based on real-time finite element method. *Proceedings - IEEE International Conference on Robotics and Automation*, pages 3982–3987, 2013.
- [82] Koichi Suzumori, Satoshi Endo, Takefumi Kanda, Naomi Kato, and Hiroyoshi Suzuki. A Bending Pneumatic Rubber Actuator Realizing Soft-bodied Manta Swimming Robot. In *Proceedings 2007 IEEE International Conference on Robotics and Automation*, pages 4975–4980. IEEE, apr 2007.

- [83] Jonathan Hiller and Hod Lipson. Dynamic Simulation of Soft Heterogeneous Objects. 2012.
- [84] Robert J. Webster and Bryan A. Jones. Design and kinematic modeling of constant curvature continuum robots: A review. *International Journal of Robotics Research*, 29(13):1661–1683, 2010.
- [85] Baobin Miao, Tieshan Li, and Weilin Luo. A dsc and mlp based robust adaptive nn tracking control for underwater vehicle. *Neurocomputing*, 111:184–189, 2013.
- [86] Guoqing Zhang and Xianku Zhang. Concise robust adaptive path-following control of underactuated ships using DSC and MLP. *IEEE Journal of Oceanic Engineering*, 39(4):685–694, 2014.
- [87] Ali T. Hasan, N. Ismail, A. M.S. Hamouda, Ishak Aris, M. H. Marhaban, and H. M.A.A. Al-Assadi. Artificial neural network-based kinematics Jacobian solution for serial manipulator passing through singular configurations. *Advances in Engineering Software*, 41(2):359–367, 2010.
- [88] Panchanand Jha and B. B. Biswal. A Neural Network Approach for Inverse Kinematic of a SCARA Manipulator. *IAES International Journal of Robotics and Automation (IJRA)*, 3(1):52–61, 2014.
- [89] Jung Wook Park, Ronald G. Harley, and Ganesh K. Venayagamoorthy. Indirect adaptive control for synchronous generator: Comparison of MLP/RBF neural networks approach with Lyapunov stability analysis. *IEEE Transactions on Neural Networks*, 15(2):460–464, 2004.
- [90] Srinivasan Alavandar and M. J. Nigam. Neuro-fuzzy based approach for inverse kinematics solution of industrial robot manipulators. *International Journal of Computers, Communications and Control*, 3(3):224–234, 2008.
- [91] Ammar H Elsheikh Ezzat A Showaib. Artificial Neural Network Based Forward Kinematics Solution for Planar Parallel Manipulators Passing through Singular Configuration. *Advances in Robotics & Automation*, 02(02), 2013.
- [92] Bassam Daya, Shadi Khawandi, and Mohamed Akoum. Applying Neural Network Architecture for Inverse Kinematics Problem in Robotics. *Journal of Software Engineering and Applications*, 03(03):230–239, 2010.
- [93] D. T. Pham, M. Castellani, and A. A. Fahmy. Learning the inverse kinematics of a robot manipulator using the Bees Algorithm. *IEEE International Conference on Industrial Informatics (INDIN)*, (Indin):493–498, 2008.
- [94] Dong C Liu and Jorge Nocedal. On the limited memory bfgs method for large scale optimization. *Mathematical programming*, 45(1-3):503–528, 1989.
- [95] Diederik P Kingma and Jimmy Ba. Adam: A method for stochastic optimization. *arXiv preprint arXiv:1412.6980*, 2014.

- [96] J P Whitney, P S Sreetharan, K Y Ma, and R J Wood. Pop-up book MEMS. *Journal of Micromechanics and Microengineering*, 21(11):115021, nov 2011.
- [97] Koichi Hirata, Tadanori Takimoto, and Kenkichi Tamura. Study on turning performance of a fish robot. In *First International Symposium on Aqua Bio-Mechanisms*, pages 287–292, 2000.
- [98] Jianxun Wang and Xiaobo Tan. A dynamic model for tail-actuated robotic fish with drag coefficient adaptation. *Mechatronics*, 23(6):659–668, 2013.
- [99] Lei Wang, Min Xu, Bo Liu, Kin Huat Low, Jie Yang, and Shiwu Zhang. A three-dimensional kinematics analysis of a koi carp pectoral fin by digital image processing. *Journal of Bionic Engineering*, 10(2):210–221, 2013.
- [100] Phi Luan Nguyen, Byung Ryong Lee, et al. Dynamic modeling and experiment of a fish robot with a flexible tail fin. *Journal of Bionic Engineering*, 10(1):39–45, 2013.
- [101] Phi Luan Nguyen, Byung Ryong Lee, et al. Dynamic modeling of a non-uniform flexible tail for a robotic fish. *Journal of Bionic Engineering*, 10(2):201–209, 2013.
- [102] Qinyuan Ren, Jianxin Xu, and Xuefang Li. A data-driven motion control approach for a robotic fish. *Journal of Bionic Engineering*, 12(3):382–394, 2015.
- [103] Qinyuan Ren, Jianxin Xu, Lupeng Fan, and Xuelei Niu. A gim-based biomimetic learning approach for motion generation of a multi-joint robotic fish. *Journal of Bionic Engineering*, 10(4):423–433, 2013.
- [104] Mohsen Siahmansouri, Ahmad Ghanbari, and Mir Masoud Seyyed Fakhrabadi. Design, implementation and control of a fish robot with undulating fins. *International Journal of Advanced Robotic Systems*, 8(5):60, 2011.
- [105] Jing Chen, Tianjiang Hu, Longxin Lin, Haibin Xie, and Lincheng Shen. Learning control for biomimetic undulating fins: An experimental study. *Journal of Bionic Engineering*, 7:S191–S198, 2010.
- [106] Kin Huat Low. Locomotion and depth control of robotic fish with modular undulating fins. *International Journal of Automation and Computing*, 3(4):348–357, 2006.
- [107] Zhengxing Wu, Junzhi Yu, Min Tan, and Jianwei Zhang. Kinematic comparison of forward and backward swimming and maneuvering in a self-propelled sub-carangiform robotic fish. *Journal of Bionic Engineering*, 11(2):199–212, 2014.
- [108] S Zimmerman and A Abdelkefi. Review of marine animals and bioinspired robotic vehicles: Classifications and characteristics. *Progress in Aerospace Sciences*, 93:95–119, 2017.



- [109] Seok Heo, Tedy Wiguna, Hoon Cheol Park, and Nam Seo Goo. Effect of an artificial caudal fin on the performance of a biomimetic fish robot propelled by piezoelectric actuators. *Journal of Bionic Engineering*, 4(3):151–158, 2007.
- [110] Andrew D Marchese, Cagdas D Onal, and Daniela Rus. Autonomous soft robotic fish capable of escape maneuvers using fluidic elastomer actuators. *Soft Robotics*, 1(1):75–87, 2014.
- [111] Yong Zhong and Ruxu Du. Design and implementation of a novel robot fish with active and compliant propulsion mechanism. In *Robotics: Science and Systems*, 2016.
- [112] Jindong Liu and Huosheng Hu. Biological inspiration: from carangiform fish to multi-joint robotic fish. *Journal of bionic engineering*, 7(1):35–48, 2010.
- [113] KH Low and CW Chong. Parametric study of the swimming performance of a fish robot propelled by a flexible caudal fin. *Bioinspiration & Biomimetics*, 5(4):046002, 2010.
- [114] David Scaradozzi, Giacomo Palmieri, Daniele Costa, and Antonio Pinelli. Bcf swimming locomotion for autonomous underwater robots: a review and a novel solution to improve control and efficiency. *Ocean Engineering*, 130:437–453, 2017.
- [115] Daniel M Aukes, Benjamin Goldberg, Mark R Cutkosky, and Robert J Wood. An analytic framework for developing inherently-manufacturable pop-up laminate devices. *Smart Materials and Structures*, 23(9):094013, 2014.
- [116] Daniel M Aukes, Önur Ozcan, and Robert J Wood. Monolithic design and fabrication of a 2-dof bio-inspired leg transmission. In *Conference on Biomimetic and Biohybrid Systems*, pages 1–10. Springer, 2014.
- [117] Iman Borazjani and Fotis Sotiropoulos. Numerical investigation of the hydrodynamics of carangiform swimming in the transitional and inertial flow regimes. *Journal of Experimental Biology*, 211(10):1541–1558, 2008.
- [118] Sheng Chen, Stephen A Billings, and Wan Luo. Orthogonal least squares methods and their application to non-linear system identification. *International Journal of control*, 50(5):1873–1896, 1989.
- [119] Jindong Liu and Huosheng Hu. Biological Inspiration: From Carangiform Fish to Multi-Joint Robotic Fish. *Journal of Bionic Engineering*, 7(1):35–48, 2010.
- [120] Junzhi Yu, Ming Wang, Huifang Dong, Yanlu Zhang, and Zhengxing Wu. Motion Control and Motion Coordination of Bionic Robotic Fish: A Review. *Journal of Bionic Engineering*, 15(4):579–598, 2018.
- [121] Xiaobo Tan. Autonomous Robotic Fish as Mobile Sensor Platforms: Challenges and Potential Solutions. *Marine Technology Society Journal*, 45(4):31–40, 2011.

- [122] Wei Wang, Xia Dai, Liang Li, Banti H. Gheneti, Yang Ding, Junzhi Yu, and Guangming Xie. Three-Dimensional Modeling of a Fin-Actuated Robotic Fish with Multimodal Swimming. *IEEE/ASME Transactions on Mechatronics*, 23(4):1641–1652, 2018.
- [123] Saurab Verma and Jian Xin Xu. Analytic Modeling for Precise Speed Tracking of Multilink Robotic Fish. *IEEE Transactions on Industrial Electronics*, 65(7):5665–5672, 2018.
- [124] Junzhi Yu, Zhengxing Wu, Zongshuai Su, Tianzhu Wang, and Suwen Qi. Motion Control Strategies for a Repetitive Leaping Robotic Dolphin. *IEEE/ASME Transactions on Mechatronics*, PP(c):1–1, 2019.
- [125] Dong Xu, Haining Zeng, Xiang Peng, Ziqing Zhao, and Jingmeng Liu. A Stiffness Adjustment Mechanism Based on Negative Work for High-efficient Propulsion of Robotic Fish. *Journal of Bionic Engineering*, 15(2):270–282, 2018.
- [126] Robert K. Katzschmann, Joseph DelPreto, Robert MacCurdy, and Daniela Rus. Exploration of underwater life with an acoustically controlled soft robotic fish. *Science Robotics*, 3(16):eaar3449, 2018.
- [127] Tiefeng Li, Guorui Li, Yiming Liang, Tingyu Cheng, Jing Dai, Xuxu Yang, Bangyuan Liu, Zedong Zeng, Zhilong Huang, Yingwu Luo, et al. Fast-moving soft electronic fish. *Science Advances*, 3(4):e1602045, 2017.
- [128] Andrew D. Marchese, Cagdas D. Onal, and Daniela Rus. Autonomous Soft Robotic Fish Capable of Escape Maneuvers Using Fluidic Elastomer Actuators. *Soft Robotics*, 1(1):75–87, 2014.
- [129] Sung Jin Park, Mattia Gazzola, Kyung Soo Park, Shirley Park, Valentina Di Santo, Erin L. Blevins, Johan U. Lind, Patrick H. Campbell, Stephanie Dauth, Andrew K. Capulli, Francesco S. Pasqualini, Seungkuk Ahn, Alexander Cho, Hongyan Yuan, Ben M. Maoz, Ragu Vijaykumar, Jeong Woo Choi, Karl Deisseroth, George V. Lauder, L. Mahadevan, and Kevin Kit Parker. Phototactic guidance of a tissue-engineered soft-robotic ray. *Science*, 353(6295):158–162, jul 2016.
- [130] Tingyu Cheng, Guori Li, Yiming Liang, Mingqi Zhang, Bangyuan Liu, Tuck Whye Wong, Jack Forman, Mianhong Chen, Guanyun Wang, Ye Tao, and Tiefeng Li. Untethered soft robotic jellyfish. *Smart Materials and Structures*, 28(1):015019, jan 2019.
- [131] Robert K Katzschmann, Andrew D Marchese, and Daniela Rus. Hydraulic Autonomous Soft Robotic Fish for 3D Swimming. In Tsuneo Yoshikawa and Fumio Miyazaki, editors, *Experimental Robotics III*, volume 200 of *Lecture Notes in Control and Information Sciences*, pages 405–420. Springer Berlin Heidelberg, Berlin, Heidelberg, 2016.
- [132] G. V. Lauder, E. J. Anderson, J. Tangorra, and P. G. A. Madden. Fish biorobotics: kinematics and hydrodynamics of self-propulsion. *Journal of Experimental Biology*, 210(16):2767–2780, 2007.

- [133] Junzhi Yu, Zongshuai Su, Zhengxing Wu, and Min Tan. Development of a Fast-Swimming Dolphin Robot Capable of Leaping. *IEEE/ASME Transactions on Mechatronics*, 21(5):2307–2316, oct 2016.
- [134] Junzhi Yu, Min Tan, Shuo Wang, and Erkuai Chen. Development of a biomimetic robotic fish and its control algorithm. *IEEE Transactions on Systems, Man, and Cybernetics, Part B: Cybernetics*, 34(4):1798–1810, 2004.
- [135] Soheil Arastehfar, Chee-Meng Chew, Athena Jalalian, Gunawan Gunawan, and Khoon Seng Yeo. A Relationship Between Sweep Angle of Flapping Pectoral Fins and Thrust Generation. *Journal of Mechanisms and Robotics*, 11(1):011014, 2018.
- [136] George V. Lauder and Peter G. A. Madden. Learning from fish: Kinematics and experimental hydrodynamics for roboticists. *International Journal of Automation and Computing*, 3(4):325–335, oct 2006.
- [137] Valentina Di Santo and Christopher P. Kenaley. Skating by: low energetic costs of swimming in a batoid fish. *The Journal of Experimental Biology*, 219(12):1804–1807, jun 2016.
- [138] Peter A. Dewey, Antoine Carriou, and Alexander J. Smits. On the relationship between efficiency and wake structure of a batoid-inspired oscillating fin. *Journal of Fluid Mechanics*, 691:245–266, jan 2012.
- [139] Chunlin Zhou and K. H. Low. Design and locomotion control of a biomimetic underwater vehicle with fin propulsion. *IEEE/ASME Transactions on Mechatronics*, 17(1):25–35, feb 2012.
- [140] Zonggang Li, Liming Ge, Weiqiang Xu, and Yajiang Du. Turning characteristics of biomimetic robotic fish driven by two degrees of freedom of pectoral fins and flexible body/caudal fin. *International Journal of Advanced Robotic Systems*, 15(1):1–12, 2018.
- [141] R. P. Clark and A. J. Smits. Thrust production and wake structure of a batoid-inspired oscillating fin. *Journal of Fluid Mechanics*, 562:415–429, sep 2006.
- [142] Shiwu Zhang, Yun Qian, Pan Liao, Fenghua Qin, and Jiming Yang. Design and Control of an Agile Robotic Fish with Integrative Biomimetic Mechanisms. *IEEE/ASME Transactions on Mechatronics*, 21(4):1846–1857, aug 2016.
- [143] Yong Zhong, Zheng Li, and Ruxu Du. A Novel Robot Fish with Wire-Driven Active Body and Compliant Tail. *IEEE/ASME Transactions on Mechatronics*, 22(4):1633–1643, aug 2017.
- [144] Xuelei Niu, Jianxin Xu, Qinyuan Ren, and Qingguo Wang. Locomotion learning for an anguilliform robotic fish using central pattern generator approach. *IEEE Transactions on Industrial Electronics*, 61(9):4780–4787, 2014.

- [145] Yonghui Hu, Jianhong Liang, and Tianmiao Wang. Parameter synthesis of coupled nonlinear oscillators for CPG-based robotic locomotion. *IEEE Transactions on Industrial Electronics*, 61(11):6183–6193, nov 2014.
- [146] Qinyuan Ren, Jianxin Xu, Lupeng Fan, and Xuelei Niu. A GIM-Based Biomimetic Learning Approach for Motion Generation of a Multi-Joint Robotic Fish. *Journal of Bionic Engineering*, 10(4):423–433, dec 2013.
- [147] Jing Chen, Tianjiang Hu, Longxin Lin, Haibin Xie, and Lincheng Shen. Learning control for biomimetic undulating fins: An experimental study. *Journal of Bionic Engineering*, 7(SUPPL.):S191–S198, 2010.
- [148] Junzhi Yu, Zhengxing Wu, Ming Wang, and Min Tan. CPG Network Optimization for a Biomimetic Robotic Fish via PSO. *IEEE Transactions on Neural Networks and Learning Systems*, 27(9):1962–1968, sep 2016.
- [149] Chunlin Zhou and Kin Huat Low. On-line optimization of biomimetic undulatory swimming by an experiment-based approach. *Journal of Bionic Engineering*, 11(2):213–225, jun 2014.
- [150] Tuong Quan Vo, Hyoung Seok Kim, and Byung Ryong Lee. Propulsive Velocity Optimization of 3-Joint Fish Robot Using Genetic-Hill Climbing Algorithm. *Journal of Bionic Engineering*, 6(4):415–429, dec 2009.
- [151] Stephane Doncieux, Nicolas Bredeche, Jean-Baptiste Mouret, and Agoston E Gusz Eiben. Evolutionary robotics: what, why, and where to. *Frontiers in Robotics and AI*, 2:4, 2015.
- [152] Nikolaus Hansen. The cma evolution strategy: a comparing review. In *Towards a new evolutionary computation*, pages 75–102. Springer, 2006.
- [153] Mohammad Nabi Omidvar and Xiaodong Li. A comparative study of cma-es on large scale global optimisation. In *Australasian Joint Conference on Artificial Intelligence*, pages 303–312. Springer, 2010.
- [154] Frank Veenstra, Jonas Jørgensen, and Sebastian Risi. Evolution of fin undulation on a physical knifefish-inspired soft robot. In *Proceedings of the Genetic and Evolutionary Computation Conference*, pages 157–164, 2018.
- [155] 2018. Amy E. Robertson, <http://www.npr.org/>.
- [156] K. H. Low and C. W. Chong. Parametric study of the swimming performance of a fish robot propelled by a flexible caudal fin. *Bioinspiration and Biomimetics*, 5(4), 2010.
- [157] Nikolaus Hansen. The cma evolution strategy: a comparing review. In *Towards a new evolutionary computation*, pages 75–102. Springer, 2006.
- [158] Haiping Ma, Dan Simon, Minrui Fei, and Zixiang Chen. On the equivalences and differences of evolutionary algorithms. *Engineering Applications of Artificial Intelligence*, 26(10):2397–2407, 2013.

- [159] Martin Andersson, Sunith Bandaru, Amos HC Ng, and Anna Syberfeldt. Parameter tuned cma-es on the cec'15 expensive problems. In *2015 IEEE Congress on Evolutionary Computation (CEC)*, pages 1950–1957. IEEE, 2015.
- [160] Mohammad Sharifzadeh, Roozbeh Khodambashi, Wenlong Zhang, and Daniel Aukes. On Locomotion of a Laminated Fish-Inspired Robot in a Small-to-Size Environment. In *Volume 5A: 42nd Mechanisms and Robotics Conference*, page V05AT07A071. ASME, aug 2018.
- [161] Brooke Elizabeth Flammang and George V Lauder. Caudal fin shape modulation and control during acceleration, braking and backing maneuvers in bluegill sunfish, *leptomis macrochirus*. *Journal of Experimental Biology*, 212(2):277–286, 2009.
- [162] Khoi Nguyen, Ning Yu, Mahesh M Bandi, Madhusudhan Venkadesan, and Shreyas Mandre. Curvature-induced stiffening of a fish fin. *Journal of The Royal Society Interface*, 14(130):20170247, 2017.
- [163] Valentina Di Santo, Erin L Blevins, and George V Lauder. Batoid locomotion: effects of speed on pectoral fin deformation in the little skate, *leucoraja erinacea*. *Journal of Experimental Biology*, 220(4):705–712, 2017.
- [164] SA Combes and TL Daniel. Flexural stiffness in insect wings ii. spatial distribution and dynamic wing bending. *Journal of Experimental Biology*, 206(17):2989–2997, 2003.
- [165] Jeffrey A Walker. Functional morphology and virtual models: physical constraints on the design of oscillating wings, fins, legs, and feet at intermediate reynolds numbers. *Integrative and Comparative Biology*, 42(2):232–242, 2002.
- [166] Robin J Wootton. Geometry and mechanics of insect hindwing fans: a modelling approach. *Proceedings of the Royal Society of London. Series B: Biological Sciences*, 262(1364):181–187, 1995.
- [167] Simon M Walker, Adrian LR Thomas, and Graham K Taylor. Deformable wing kinematics in the desert locust: how and why do camber, twist and topography vary through the stroke? *Journal of the royal society Interface*, 6(38):735–747, 2008.
- [168] John Young, Simon M Walker, Richard J Bomphrey, Graham K Taylor, and Adrian LR Thomas. Details of insect wing design and deformation enhance aerodynamic function and flight efficiency. *Science*, 325(5947):1549–1552, 2009.
- [169] Reinhard Vogel and Holger Stark. Motor-driven bacterial flagella and buckling instabilities. *The European Physical Journal E*, 35(2):15, 2012.
- [170] Animangsu Ghatak, Abhijit Majumder, and Rajendra Kumar. Hysteresis of soft joints embedded with fluid-filled microchannels. *Journal of The Royal Society Interface*, 6(31):203–208, 2008.

- [171] Alexander G Volkov, Tejumade Adesina, Vladislav S Markin, and Emil Jovanov. Kinetics and mechanism of dionaea muscipula trap closing. *Plant physiology*, 146(2):694–702, 2008.
- [172] Vladislav S Markin, Alexander G Volkov, and Emil Jovanov. Active movements in plants: mechanism of trap closure by dionaea muscipula ellis. *Plant signaling & behavior*, 3(10):778–783, 2008.
- [173] Dieter Hodick and Andreas Sievers. On the mechanism of trap closure of venus flytrap (dionaea muscipula ellis). *Planta*, 179(1):32–42, 1989.
- [174] Kazuya Saito, Shuhei Nomura, Shuhei Yamamoto, Ryuma Niiyama, and Yoji Okabe. Investigation of hindwing folding in ladybird beetles by artificial elytron transplantation and microcomputed tomography. *Proceedings of the National Academy of Sciences*, 114(22):5624–5628, 2017.
- [175] Y. Wang and M. A. Minor. Design and evaluation of a soft robotic smart shoe for haptic terrain rendering. *IEEE/ASME Transactions on Mechatronics*, 23(6):2974–2979, Dec 2018.
- [176] D. Drotman, M. Ishida, S. Jadhav, and M. T. Tolley. Application-driven design of soft, 3-d printed, pneumatic actuators with bellows. *IEEE/ASME Transactions on Mechatronics*, 24(1):78–87, Feb 2019.
- [177] Y. Shin, T. Kim, B. C. Jung, S. Moon, and J. Lee. Development of hybrid vibration isolator by inertial type actuator and wire mesh mount. *IEEE/ASME Transactions on Mechatronics*, pages 1–1, 2019.
- [178] KA Seffen. Mechanical memory metal: a novel material for developing morphing engineering structures. *Scripta materialia*, 55(4):411–414, 2006.
- [179] Anupam Pandey, Derek E Moulton, Dominic Vella, and Douglas P Holmes. Dynamics of snapping beams and jumping poppers. *EPL (Europhysics Letters)*, 105(2):24001, 2014.
- [180] Je-sung Koh, Daniel M Aukes, Brandon Araki, Sarah Pohorecky, Yash Mulgaonkar, Michael T Tolley, Vijay Kumar, Daniela Rus, and Robert J Wood. A modular folded laminate robot capable of multi modal locomotion. In *International Symposium on Experimental Robotics*, pages 59–70. Springer, 2016.
- [181] Seung-Won Kim, Je-Sung Koh, Jong-Gu Lee, Junghyun Ryu, Maenghyo Cho, and Kyu-Jin Cho. Flytrap-inspired robot using structurally integrated actuation based on bistability and a developable surface. *Bioinspiration & biomimetics*, 9(3):036004, 2014.
- [182] Sang-Min Baek, Dae-Young Lee, and Kyu-Jin Cho. Curved compliant facet origami-based self-deployable gliding wing module for jump-gliding. In *ASME 2016 International Design Engineering Technical Conferences and Computers and Information in Engineering Conference*. American Society of Mechanical Engineers Digital Collection, 2016.

- [183] Gwang-Pil Jung, Je-Sung Koh, and Kyu-Jin Cho. Underactuated adaptive gripper using flexural buckling. *IEEE Transactions on Robotics*, 29(6):1396–1407, 2013.
- [184] Jeffrey A Walker and Mark W Westneat. Kinematics, dynamics, and energetics of rowing and flapping propulsion in fishes. *Integrative and Comparative Biology*, 42(5):1032–1043, 2002.
- [185] George V Lauder and Bruce C Jayne. Pectoral fin locomotion in fishes: testing drag-based models using three-dimensional kinematics. *American zoologist*, 36(6):567–581, 1996.
- [186] Seiichi Sudo, Takuya Amano, Atsushi Shirai, and Toshiyuki Hayase. On the motility and locomotive organs of beach flea. *Journal of Aero Aqua Biomechanisms*, 4(1):37–43, 2015.
- [187] Christine Essenberg. The habits and natural history of the backswimmers notonectidae. *Journal of Animal Behavior*, 5(5):381, 1915.
- [188] EDITH SUSANA Fanta. Anatomy of the nauplii of oithona ovalis herbst (copepoda, cyclopoida). *Bolm Zool., Univ. S Paulo*, 1:205–238, 1976.
- [189] Sanaz Bazaz Behbahani, Jianxun Wang, and Xiaobo Tan. A dynamic model for robotic fish with flexible pectoral fins. In *2013 IEEE/ASME International Conference on Advanced Intelligent Mechatronics*, pages 1552–1557. IEEE, 2013.
- [190] Farah A Naser and Mofeed T Rashid. Design, modeling, and experimental validation of a concave-shape pectoral fin of labriform-mode swimming robot. *Engineering Reports*, page e12082, 2019.
- [191] Naomi Kato, Bugi Wiku Wicaksono, and Yoshihiro Suzuki. Development of biology-inspired autonomous underwater vehicle” bass iii” with high maneuverability. In *Proceedings of the 2000 International Symposium on Underwater Technology (Cat. No. 00EX418)*, pages 84–89. IEEE, 2000.
- [192] Patar Ebenezer Sitorus, Yul Yunazwin Nazaruddin, Edi Leksono, and Agus Budiyo. Design and implementation of paired pectoral fins locomotion of labriform fish applied to a fish robot. *Journal of Bionic Engineering*, 6(1):37–45, 2009.
- [193] Sanaz Bazaz Behbahani and Xiaobo Tan. Design and modeling of flexible passive rowing joint for robotic fish pectoral fins. *IEEE Transactions on Robotics*, 32(5):1119–1132, 2016.
- [194] Ashutosh Simha, Roza Gkliva, Ülle Kotta, and Maarja Kruusmaa. A flapped paddle-fin for improving underwater propulsive efficiency of oscillatory actuation. *IEEE Robotics and Automation Letters*, 5(2):3176–3181, 2020.
- [195] Van Anh Pham, Tan Tien Nguyen, Byung Ryong Lee, and Tuong Quan Vo. Dynamic analysis of a robotic fish propelled by flexible folding pectoral fins. *Robotica*, 38(4):699–718, 2020.

- [196] Scott J I. Walker and Guglielmo S Aglietti. Experimental investigation of tape springs folded in three dimensions. *AIAA journal*, 44(1):151–159, 2006.
- [197] Stephen P Timoshenko and James M Gere. *Theory of elastic stability*, 1961.
- [198] E Kebabze, SD Guest, and S Pellegrino. Bistable prestressed shell structures. *International Journal of Solids and Structures*, 41(11-12):2801–2820, 2004.
- [199] Ömer Soykasap. Analysis of tape spring hinges. *International Journal of Mechanical Sciences*, 49(7):853–860, 2007.
- [200] Sébastien Hoffait, O Bröls, Didier Granville, Frédéric Cugnon, and Gaëtan Kerschen. Dynamic analysis of the self-locking phenomenon in tape-spring hinges. *Acta Astronautica*, 66(7-8):1125–1132, 2010.
- [201] Walter Wuest. Einige anwendungen der theorie der zylinderschale. *ZAMM-Journal of Applied Mathematics and Mechanics/Zeitschrift für Angewandte Mathematik und Mechanik*, 34(12):444–454, 1954.
- [202] KA Seffen. On the behavior of folded tape-springs. *Journal of applied mechanics*, 68(3):369–375, 2001.
- [203] John W. Roberts, Rick Cory, and Russ Tedrake. On the controllability of fixed-wing perching. In *Proceedings of the American Control Conference*, number 1, pages 2018–2023. IEEE, 2009.
- [204] John Peter Whitney. *Design and performance of insect-scale flapping-wing vehicles*. PhD thesis, 2012.
- [205] K Mazaheri and A Ebrahimi. Experimental investigation of the effect of chord-wise flexibility on the aerodynamics of flapping wings in hovering flight. *Journal of Fluids and Structures*, 26(4):544–558, 2010.
- [206] Nick Gravish and Robert J Wood. Anomalous yaw torque generation from passively pitching wings. In *2016 IEEE International Conference on Robotics and Automation (ICRA)*, pages 3282–3287. IEEE, 2016.
- [207] John P Whitney and Robert J Wood. Aeromechanics of passive rotation in flapping flight. *Journal of fluid mechanics*, 660:197–220, 2010.
- [208] M. Sharifzadeh and D. M. Aukes. Curvature-induced buckling for flapping-wing vehicles. *IEEE/ASME Transactions on Mechatronics*, 2020.
- [209] Thomas R Kane and David A Levinson. *Dynamics, theory and applications*. McGraw Hill, 1985.
- [210] Ross L. Hatton, Yang Ding, Howie Choset, and Daniel I. Goldman. Geometric visualization of self-propulsion in a complex medium. *Phys. Rev. Lett.*, 110:078101, Feb 2013.



- [211] Edward M Purcell. Life at low reynolds number. *American journal of physics*, 45(1):3–11, 1977.
- [212] Leif E Becker, Stephan A Koehler, and Howard A Stone. On self-propulsion of micro-machines at low reynolds number: Purcell’s three-link swimmer. *Journal of fluid mechanics*, 490:15–35, 2003.

APPENDIX A  
CURRICULUM VITAE

# Mohammad SHARIFZADEH

**Affiliation:** Ph.D. Candidate in Systems Engineering, Arizona State University,  
**Research Associate** Integrating Design, Engineering, and Analysis (IDEALab)  
**email:** sharifzadeh@asu.edu  
**Phone:** 801-889-0887

## Research Interests

Robotics & Mechatronics, Foldable Robotics, Laminated Mechanisms, Soft Robotics, Dynamic & Kinematics Control, System Identification, Analytic Control, Parallel mechanism, and Human-Robot Interaction (HRI).

## Education

*Jan. 2017 - present* **Ph.D.** in Systems Engineering, Arizona State University  
**GPA:** 4/4  
**Research Team:** Integrating, Design, Engineering, and Analysis Laboratory (IDEALab)  
**Dissertation:** Addressing the Effect of Non-rigidity in Soft Robots Interacting with Their Working Environments (Advisor: Prof. Daniel Aukes).  
*Sep. 2013 - Mar. 2016* **M.Sc.** in Mechatronics Engineering, University of Tehran  
**GPA:** 18.4/20  
**Research Team:** Human-Robot Interaction Laboratory (Taarlab)  
**Thesis:** Dynamical Control & Identification of 3-DOF Decoupled Parallel Mechanism (Tripteron) and Constructing a Human-Robot Interaction Interface (Advisors: Prof. Mehdi Tale Masouleh & Prof. Ahmad Kalhor).  
*Sep. 2008 - Jun. 2012* **B.Sc.** in Electrical Engineering (Control field), Shiraz University  
**GPA:** 15/20  
**Thesis:** Designing and Constructing a Buck-Boost Converter with Variable (2-50 V) Output Voltage (Advisor: Prof. Haidar Samet).  
*Sep. 2004 - Jun. 2008* **High School**, Dastgheib high school  
**GPA:** 18.97/20

## Journal Papers

**Sharifzadeh, Mohammad**, and Aukes, Daniel. "Curvature-Induced Buckling for Flapping-Wing Vehicles." IEEE/ASME Transactions on Mechatronics (2020).  
**Sharifzadeh, Mohammad**, Jiang, Yuhao, and Aukes, Daniel. "Reconfigurable Curved Beams for Selectable Swimming Gaits in an Underwater Robot." IEEE Robotics and Automation Letters (2021).  
**Sharifzadeh, Mohammad**, Masouleh, Mehdi Tale, Kalhor, Ahmad, and Shahverdi, Pourya "An experimental dynamic identification & control of an overconstrained 3-DOF parallel mechanism in presence of variable friction and feedback delay." Robotics and autonomous systems 102 (2018): 27-43.  
**Sharifzadeh, Mohammad**, et al. "An experimental study on the direct & indirect dynamic identification of an over-constrained 3-DOF decoupled parallel mechanism." Mechanism and Machine Theory 116 (2017): 178-202. 2017  
**Sharifzadeh, Mohammad**, Masouleh, Mehdi Tale, and Kalhor, Ahmad. "On human-robot interaction of a 3-DOF decoupled parallel mechanism based on the design and construction of a novel and low-cost 3-DOF force sensor." Meccanica 52.10 (2017): 2471-2489.  
Doroudchi, Azadeh, Khodambashi, Roozbeh, **Sharifzadeh, Mohammad**, Li, Dongting, Berman, Spring, and Aukes, Daniel. "Tracking Control of a Miniature 2-DOF Manipulator with Hydrogel Actuators." IEEE Robotics and Automation Letters (2021)

## Conference Papers

Jiang, Yuhao, and **Sharifzadeh, Mohammad**, and Aukes, Daniel. “Reconfigurable Soft Flexure Hinges via Pinched Tubes,” IEEE IROS (2020).

**Sharifzadeh, Mohammad**, Jiang, Yuhao, Khodambashi, Roozbeh, and Aukes, Daniel. “Increasing the Life Span of Foldable Manipulators With Fabric.” ASME IDETC-CIE (2020).

**Sharifzadeh, Mohammad**, Khodambashi, Roozbeh, Zhang, Wenlong, and Aukes, Daniel. “On Locomotion of a Laminated Fish-inspired robot in a Small-to-size Environment.” ASME IDETC-CIE (2018)

**Sharifzadeh, Mohammad**, and Khodambashi, Roozbeh, and Aukes, Daniel. “An integrated design and simulation environment for rapid prototyping of laminate robotic mechanisms.” ASME IDETC-CIE (2018)

**Sharifzadeh, Mohammad**, Doroudchi, Azadeh, Masouleh, Mehdi Tale, and Kalhor, Ahmad. “Experimental identification of friction and dynamics of an overconstrained 3-DOF decoupled parallel mechanism.” IEEE ICROM (2016)

**Sharifzadeh, Mohammad**, Masouleh, Mehdi Tale, and Kalhor, Ahmad. “Design, construction & calibration of a novel Human-Robot Interaction 3-DOF force sensor.” IEEE ICROM (2015)

## Publication Under Preparation (Ph.D.)

**Sharifzadeh, Mohammad**, Jiang, Yuhao, Lafmejani, Amir Salimi, Nichols, Kevin, and Aukes, Daniel. “Maneuverable Gait Selection for a Novel Fish-Inspired Robot Using a CMAES-Assisted Workflow.” (Journal)

**Sharifzadeh, Mohammad**, Jiang, Yuhao, and Aukes, Daniel. “Compensating for Material Deformation in Foldable Robots via Deep Learning– A Case Study.” (Journal)

Jiang, Yuhao, **Sharifzadeh, Mohammad**, and Aukes, Daniel. “Shape Change Propagation Through Soft Curved Materials for Dynamically-Tuned Paddling Robots.” (Journal with Conference)

## Peer Reviewer

**Journals** Journal of Advanced Robotic Systems (2020), Journal of Mechanisms and Robotics (2020), Soft Robotics (2018)

**Conferences** ICRA (2020, 2019), RoboSoft (2020, 2019), IDETC (2020, 2018), ICROM (2016, 2015, 2014)

## Teaching Assistance Experience

*Spring 2015* Teaching assistant of Advanced Robotics, under supervision of Prof. Tale Masouleh, graduate-level course with 6 students.

*Fall 2014* Teaching assistant of Advanced Engineering Mathematics, under supervision of Prof. Tale Masouleh, graduate-level course with 25 students.

*Fall 2012* Teaching assistant of Instrumentation under supervision of Prof. Karim Aghaei, undergraduate course with over 30 students.

## Industrial Experiences (Internship)

*Spring & Summer 2013*                      **Shiraz Petrochemical Company (SPC)**, Shiraz, Fars, Iran.  
The company's activity is in producing Fertilizers. I spent 4 months in Utility department, especially in its Powerhouse. Collected information and data classification and PLC programming to renew the old water treatment alarm system with Siemens PLC (S7 Family). Participated in renewing generators' alarm System with Shinkawa PLC.

*Summer 2011*                                      **Noavaran Hooshmand Fars Co.**, Shiraz, Iran.  
The company's activities are focused on intelligent buildings and building management systems (BMS). Performing a comprehensive research into mechanisms of BMS subsystems. Collaborated with design and installation group to design a fire alarm system for a residential building.

## Honors

- Engineering Graduate Fellowship from Ira A. Fulton Schools of Engineering at ASU, 2018-2019.
- Best poster award of Southwest Robotics Symposium, ASU, 2019.
- Ranked 506 in National M.Sc. entrance exam of Electrical Engineers, Iran, 2013.
- Ranked 427 in National B.Sc. entrance exam of math and physics, Iran, 2008.
- Ranked 10 in Islamic Azad University's entrance exam, Iran, 2008.

## Programming skills

- **Programming languages:** MATLAB coding, Python, Qt programming, C++ programming, ROS, Arduino ide, Bascom (AVR), CodeVision (AVR)
- **Engineering Software:** SolidWorks, Abaqus, MATLAB (Simulink), M.Sc. PARTAN/NASTRAN, Altium Designer, LabVIEW, Pspice (Orcad Capture), Proteus
- **Office Software Suit:** L<sup>A</sup>T<sub>E</sub>X, Microsoft Office (Word, Excel and Power-point)

## Equipment

- **Academic grade:** Optitrack tracking system, ATI force sensors, Dynamixel DC servos, Arduino, Particle, Ultimaker 3D printer
- **Industrial grade:** UR-5 robotic arm, Epilog Laser cutter, Markforged 3D printer, Siemens PLC, Bonnet AC servos

## Press Coverage

- *Arizona PBS Jul. 11, 2018:* Catalyst: Keeping the Water Flowing with Robotic Fish
- *KJZZ Apr. 11, 2018:* Lifeblood Of The Desert: Salt River Project Teams Turn To ASU Robots To Maintain Canal System
- *ABC15 Nov. 21, 2017:* Robotic fish could help solve problem in Arizona canals
- *East Valley Tribune Nov. 12, 2017:* Polytechnic students try robots on real-world problems
- *The State Press Nov. 2, 2017:* ASU Polytechnic researchers are developing small robots from plastic
- *12 News Oct. 24, 2017:* ASU students are using robots to solve problems from health to public safety